Thesis

Four-Stroke, Internal Combustion Engine Performance Modeling

Submitted by

Richard C. Wagner

Department of Mechanical Engineering

In partial fulfillment of the requirements

For the Degree of Master of Science

Colorado State University

Fort Collins, Colorado

Fall 2017

Master's Committee:

Advisor: Allan Kirkpatrick

Xinfeng Gao
R. Steve Robinson

Copyright by Richard C. Wagner 2017

All Rights Reserved

Abstract

Four-Stroke, Internal Combustion Engine Performance Modeling

In this thesis, two models of four-stroke, internal combustion engines are created and compared. The first model predicts the intake and exhaust processes using isentropic flow equations augmented by discharge coefficients. The second model predicts the intake and exhaust processes using a compressible, time-accurate, Quasi-One-Dimensional (Q1D) approach. Both models employ the same heat release and reduced-order modeling of the cylinder charge. Both include friction and cylinder loss models so that the predicted performance values can be compared to measurements.

The results indicate that the isentropic-based model neglects important fluid mechanics and returns inaccurate results. The Q1D flow model, combined with the reduced-order model of the cylinder charge, is able to capture the dominant intake and exhaust fluid mechanics and produces results that compare well with measurement. Fluid friction, convective heat transfer, piston ring and skirt friction and temperature-varying specific heats in the working fluids are all shown to be significant factors in engine performance predictions. Charge blowby is shown to play a lesser role.

Acknowledgements

I wouldn't be Here (note the case) without My Lovely Bride, Catherine. She has supported me in trying to become the Engineer that I always wanted to be and was the one who said, "You have to go back to school." Once here at CSU, she made it possible for me to work 15 hour days and gave me hope when mine was exhausted. "Thanks" certainly doesn't express it. I hope "I love you" does. Thanks for putting up with Sheldon.

As a working Engineer, I have never been able to afford to come back to school. I wouldn't be at CSU if it weren't for the financial support of my Dad, Dick Wagner. I think he would be proud of me.

Thanks to my friends, John Waldron, Andy Toth, Glen Haydon and Rick Johnson, who have all understood my mania and offered their unrelenting support.

Thanks also to Dr. Xinfeng Gao, who championed me and got me into the CSU Mechanical Engineering graduate program. If it wasn't for you, I wouldn't be here.

And to Dr. Allan Kirkpatrick: thank you for your wisdom, knowledge, guidance and friendship. Our weekly meetings, where we not only talked about my research but All Things Engineering, kept my spirits high and my drive strong. It was great fun sharing the discoveries with you. I've learned a lot. And because of you, this has been fun.

Thanks to my committee members, Dr. Xinfeng Gao and Dr. Steve Robinson. Sorry about the length. I bit off a lot.

I did it, Dad.

Table of Contents

Nomenclature

Engine Specific:

AF	Air to Fuel Ratio (by mass)	
$ATDC$	After Top Dead Center of the Stroke	$\langle crankshaft^{\circ} \rangle$
A_v, A_{vc}	Valve Curtain Area	$\langle m^2 \rangle$
BDC	Bottom Dead Center of the Stroke	
$bmep$	Brake Mean Effective Pressure	$\langle Pa \rangle$
$BTDC$	Before Top Dead Center of the Stroke	$\langle crankshaft^{\circ} \rangle$
b	Cylinder Bore	$\langle m \rangle$
C_d	Intake or Exhaust Discharge Coefficient	
D_v	Valve Diameter	$\langle m \rangle$
$fmep$	Frictional Mean Effective Pressure	$\langle Pa \rangle$
h_d	Displacement Height	$\langle m \rangle$
h, H	Lubrication Gap Height	$\langle m \rangle$
$imep$	Indicated Mean Effective Pressure	$\langle Pa \rangle$
l_{cr}	Connecting Rod Length (center to center)	$\langle m \rangle$
L_v	Valve Lift	$\langle m \rangle$
$\dot{m}_b$	Blowby Mass Flow Rate	$\langle \frac{kg}{sec} \rangle$
$\dot{m}_e$	Exhaust Mass Flow Rate	$\langle \frac{kg}{sec} \rangle$
$\dot{m}_i$	Intake Mass Flow Rate	$\langle \frac{kg}{sec} \rangle$
MEP	Mean Effective Pressure	$\langle Pa \rangle$
$\dot{Q}_c$	Rate of Combustion Heat Added	$\langle W \rangle$
$\dot{Q}_T$	Rate of Heat Transfer from Charge to Cylinder	$\langle W \rangle$

r	Compression Ratio	
s	Piston Stroke	$\langle m \rangle$
TDC	Top Dead Center of the Stroke	
$\mathcal{V}_c$	Clearance Volume	$\langle m^3 \rangle$
$\mathcal{V}_d$	Displacement Volume	$\langle m^3 \rangle$
$\mathcal{V}_T$	Total Cylinder Volume	$\langle m^3 \rangle$
U_p, V_p	Piston Velocity	$\left\langle \frac{m}{sec} \right\rangle$
θ	Crankshaft Displacement	$\langle crankshaft^\circ \rangle$

General:

a	Speed of Sound	$\left\langle \frac{m}{sec} \right\rangle$
A	Duct Cross-Sectional Area	$\langle m^2 \rangle$
$\bar{A}$	Average Cross-Sectional Area of a Cell	$\langle m^2 \rangle$
A^*	Duct Throat (sonic) Area	$\langle m^2 \rangle$
c	Speed of Sound	$\left\langle \frac{m}{sec} \right\rangle$
C_D	Drag Coefficient	
c_p	Constant-Pressure Specific Heat	$\left\langle \frac{kJ}{kgK} \right\rangle$
$\bar{c}_p$	Mole-Specific Constant-Pressure Specific Heat	$\left\langle \frac{kJ}{kg-molK} \right\rangle$
c_v	Constant-Volume Specific Heat	$\left\langle \frac{kJ}{kgK} \right\rangle$
$\bar{c}_v$	Mole-Specific Constant-Volume Specific Heat	$\left\langle \frac{kJ}{kg-molK} \right\rangle$
C_x	Artificial Viscosity Multiplier	
e	Mass-Specific Internal Energy	$\left\langle \frac{J}{kg} \right\rangle$
F	Flux Value	$\left\langle \frac{kg}{m^2 sec}, Pa, \frac{W}{m^2} \right\rangle$
h	Mass-Specific Enthalpy	$\left\langle \frac{kJ}{kgK} \right\rangle$

$\bar{h}$	Mole-Specific Enthalpy	$\left\langle \frac{kJ}{kg-molK} \right\rangle$
$\bar{h}_f^0$	Mole-Specific Heat of Formation	$\left\langle \frac{kJ}{kg-molK} \right\rangle$
$\mathbf{h}$	Heat Transfer Coefficient (fluid)	$\left\langle \frac{W}{m^2K} \right\rangle$
H	Total Enthalpy	$\langle J \rangle$
J	Source Term	$\left\langle \frac{kg}{sec}, N, W \right\rangle$
k	Fluid Thermal Conductivity	$\left\langle \frac{W}{mK} \right\rangle$
m	Mass	$\langle kg \rangle$
M	Mach Number	
$\mathcal{M}$	Molar Mass	$\left\langle \frac{kg}{mol} \right\rangle$
n	Number of Moles	
P	Power	$\langle W, HP \rangle$
P	Pressure	$\langle Pa \rangle$
$\dot{q}$	Mass-Specific Rate of Heat Transfer	$\left\langle \frac{W}{kg} \right\rangle$
Q	Heat Energy	$\langle J \rangle$
R	Specific Gas Constant	$\left\langle \frac{kJ}{kgK} \right\rangle$
$\mathcal{R}$	Universal Gas Constant	$\left\langle \frac{kJ}{kg-molK} \right\rangle$
t	Time	$\langle sec \rangle$
T	Temperature	$\langle K \rangle$
$\vec{V}$	Velocity	$\left\langle \frac{m}{sec} \right\rangle$
ρ	Density	$\left\langle \frac{kg}{m^3} \right\rangle$
$\vec{S}$	Surface Unit Normal Vector	$\langle m^2 \rangle$
u	One-Dimensional Fluid Velocity	$\left\langle \frac{m}{sec} \right\rangle$
U	Flux Variable	$\left\langle \frac{kg}{m}, \frac{kg}{sec}, N \right\rangle$

W	Work	$\langle J \rangle$
$\dot{W}$	Power	$\langle W \rangle$
y	Mole Fraction	
δ	Finite Change	
Δ	Discrete Change	
γ	Ratio of Specific Heats	
μ	Dynamic Viscosity	$\left\langle \frac{Ns}{m^2} \right\rangle$
τ	Shear Stress	$\left\langle \frac{N}{m^2} \right\rangle$
τ	Torque	$\langle Nm, ft - lb \rangle$

Subscripts:

b	Blowby
b	"Burned"
c	Charge
e	Exhaust
i	Intake
p	Products
r	Reactants
u	"Unburned"

CHAPTER 1

Introduction

1.1. Background

At this point in time, when battery technology has reached a level where fully electric cars are becoming a possibility, it may seem misguided to pursue improvements in the internal combustion engine. But there are still many applications for which the piston engine is indispensable and will remain so for some time. That being the case, it is essential that we continue working to make engines more efficient. With a typical thermodynamic efficiency of only around 25%, there seems to be tremendous room for improvement: increasing specific power and efficiency while reducing fuel consumption and in turn, emissions. There may also be ways to make engines more carbon- or even resource-neutral, operating them on biofuels or even on solar- or wind-generated ammonia. But there is a problem. Our selection of modeling and analysis tools is limited. It restricts our ability to perfect current engine designs and obstructs our pursuit and evaluation of new ideas.

While we humans have been designing and building engines for over 100 years, our ability to create them has belied our limited understanding of the physics that occur within them. The four-stroke piston engine reached a point of mechanical maturity by 1913 with the Peugeot Grand Prix engine of Figure 1.1a. Building from that point, Vittorio Jano and Harry Miller took the engine to its ultimate, refined form by 1926 [1]. Figure 1.1b shows Miller with one of his 1.5 liter, straight-eights on the dynamometer. In 1926, this 330 lb. engine was producing 285 horsepower at 8,200 RPM. Nearly 100 years later, the highest

performance engines in our cars are indistinguishable from this engine. And their efficiency hasn't improved significantly.

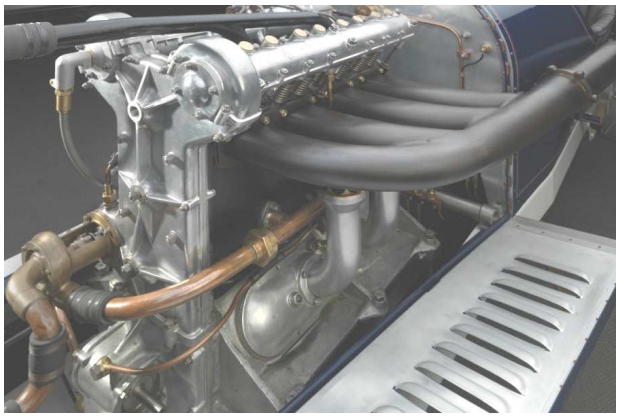

(A) The 1913 Peugeot Grand Prix Engine

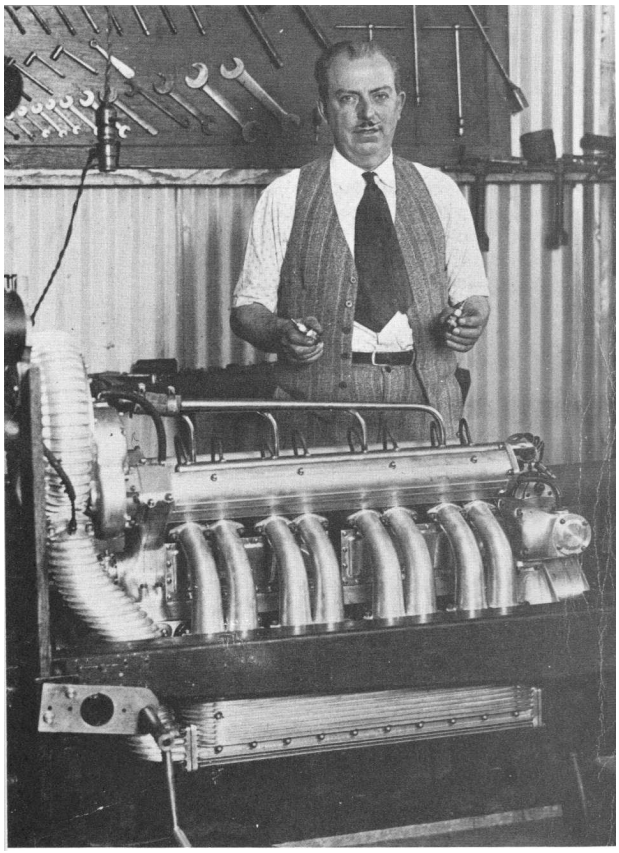

(B) Harry Miller with a 1.5 liter Straight-Eight

FIGURE 1.1. The Classic Pattern, Double Overhead Cam Engines from 1913 and 1926.

There has been a continuous effort over more than a century to demystify the physics of the engine, with some of the greatest names in science and engineering adding their contributions to the effort. The mechanics, structures, vibrational dynamics and thermodynamics of engines were identified, understood and reached a state of utility by the 1920's. Yet prior to, and surprisingly, since, engine designers have been baffled over and over by some engines' seeming refusal to perform as design rules of thumb and analytical tools say they should.

With all of the understanding that's been achieved, what is missing? Answer: an understanding of, and *ability to predict*, the physics of the charge inside of the cylinder and the flows in the intake and exhaust tracts. The science here has progressed along with the more recent development of the science of aerodynamics. The problems are the same: experimentally, attempting to observe the behavior of an invisible medium; analytically, attempting to apply equations that we can write but can't solve. And to make the process even more difficult, all of the physics are hidden from view and happen over astonishingly short timescales.

With the advent of computers and the application of Computational Fluid Dynamics (CFD) to the solution of fluid flows, researchers have been attempting to create systems that can predict the performance of an engine with its intake and exhaust systems before it is built. But as in all science and engineering, there are trade-offs. One obvious approach to simulating an engine's fluid flows is shown in Figure 1.2a, where the flow in a cylinder and its intake and exhaust tracts are modeled using three-dimensional CFD.

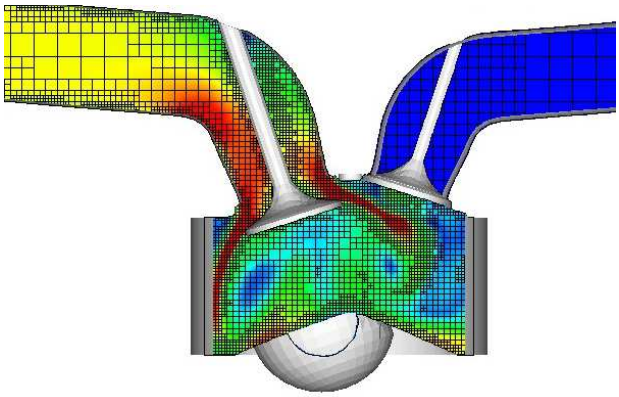

(A) An Engine Modeled with 3-D CFD

(B) The Cadillac V-16 (2002)

FIGURE 1.2. Computational Fluid Dynamics Applied to Engine Design

Cadillac used this approach to design a V16 (Figure 1.2b) in 2002 [2], with reportedly good results—the real engine performed about as predicted. But the utility of the approach is limited. Simulating this scenario, even by CFD standards, is very complicated. Cadillac

used a team of over 100 engineers and programmers to construct the simulation. And then, even running the simulation on their super computer, they waited...and waited...for the results. It took two months for the simulation to deliver the engine's power and torque curves. In that same amount of time, a prototype could have been fabricated and tested on a dynamometer, perhaps more than once. At the time of this writing, this approach doesn't lead to an effective design or research tool.

There are currently two commercial engine simulations on the market, from Ricardo and GT-Power. Both are based on reduced-order methods, although neither supplier divulges the internal algorithms of its system. In discussions with users (Dinan Corp., Edelbrock Corp., Continental Aircraft Engines, HyTech Exhaust Systems, Inc. and Rousch Performance), the author has received negative reports. The systems sometimes diverge, take too much time to deliver a solution and deliver inaccurate solutions. Dinan used Ricardo's Wave for a year before abandoning it and returning its engineers back to using their own intuition and established techniques, which yielded better products.

The published literature currently offers no "best approach" for modeling the charge, intake and exhaust flows of an engine. It is an unsolved problem and there is a healthy, active branch of research devoted to this endeavour. To speed the return of results and make an engine simulation a useful tool, the charge within the cylinder and, especially the intake and exhaust flows, must be modeled with some kind of reduced-order method. Predicting the flow dynamics has proved to be the technical bottleneck and much research is devoted to it. Three approaches are commonly used to model the intake and exhaust flows: a Helmholtz resonator model, an acoustic model or a one-dimensional CFD model.

1.2. Motivation and Focus

This thesis will focus on the derivation, construction and comparison of two reduced-order engine models. The first will model the intake and exhaust flows using an approach based on the isentropic flow equations. The second will model the intake and exhaust flows using a time-accurate, compressible, Quasi-One-Dimensional (Q1D) approach. In both cases, the intake and exhaust models will connect to a time-domain model of the cylinder and charge. Our motivation here is to see whether the dominant physics of the charge and the dominant physics of the intake and exhaust flows can be captured with either of these approaches. Researchers have identified and addressed many other factors that affect the real performance of an engine and, for verification and validation purposes must be included in an engine model. We will include a number of submodels so that we may evaluate the simulations' high-level predictions—power, torque, volumetric efficiency and Indicated Mean-Effective Pressure—and compare them to some real measurements. We will also turn these models on and off to see their effect on the simulations' predictions. In this way, we will be able to determine whether either of our modeling approaches is valid and suggest what is and what isn't dominant physics in the internal combustion engine.

1.3. Literature Review

A number of researchers have modeled the cylinder/intake/exhaust system as a Helmholtz resonator. Bortoluzzi et al. [3] found reasonable predictions modeling a single intake stroke. They also identified a significant weakness of the model, that it breaks down when stimulated with frequencies of shorter wavelength than the duct. It can't reproduce the organ pipe oscillations that come in that regime. Chapman et al. [4] created a Helmholtz model that

included viscous drag in the duct. Their development of the drag term could prove useful for this author in the future. They model the flow through the valves using an isentropic flow model, augmented by a discharge coefficient. They compare their results to those of a real, motored engine. The intake prediction is quite good. When compared to the measurements on the exhaust system of a firing engine, their results aren't good. Tabaczynski [5] discusses a number of closed-form approaches to predicting engine performance along with Helmholtz resonator theory. He suggests that the crankshaft speed for tuning is roughly one-half the Helmholtz frequency. He mentions organ pipe oscillations but adds their effect is unvalidated. He goes on to discuss method of characteristics and finite-difference approaches superficially. Hanriot et al. [6] performed experiments where they connected a Helmholtz resonator to a complete intake system and identified the parameters that maximized intake mass flow. Vorum [7] applies a two-state simulation that models intake and exhaust flows as Helmholtz resonators while the valves are open and as organ pipes when the valves are closed.

In their all-inclusive paper, Chalet et al. [8] test a Helmholtz model, a one-dimensional CFD model and an acoustic model on the flow through a pipe. The Helmholtz model breaks down when the pipe is stimulated at wavelengths shorter than the length of the pipe. The acoustic model, derived through the linearization of the one-dimensional Euler equations, breaks down any time shock waves or supersonic flow are present. The 1-D CFD model provides reasonable results throughout. Pearson and Winterbone [9] also take an acoustic approach to modeling the flow through an intake manifold. They connect their simulated intake runner to a cylinder model and compare the results to experiment. The correlation isn't very high. Mezher et al. [10] created another frequency-based approach where experiments were run on a simulated engine and shock tubes, using System Identification techniques to

create a transfer function describing an engine's overall performance. Harrison et al. [11] also created a linear acoustic model that estimated the time-varying intake pressure in a research engine. Their approach agrees fairly well with measurements made on the engine. Chalet et al. [12] attempted to create a frequency-domain acoustic analysis that doesn't assume small velocity or pressure perturbations, then they applied the model to the flow through an intake runner. Using an experimental setup, they studied the organ-pipe oscillations in a pipe, then, in System Identification style, attempted to "back out" the dominant parameters describing the fluid dynamics.

Much research has gone into applying Computational Fluid Dynamics techniques to the intake and exhaust flows. In an attempt to analyze exhaust flows, Benson et al. [13] applied an unsteady method of characteristics approach to model the flow through pipes with area contractions and expansions. Bulaty and Niessner [14] modeled the flows with one-dimensional governing equations, time-marching them using a Lax-Wendrof approach. Their time-domain results seemed reasonable, but of greatest importance was a section of their paper where they perform a magnitude analysis on the governing equations. They show that, for the momentum equation, the effect of artificial viscosity is insignificant compared to friction, a confirmation of the use of artificial viscosity to suppress oscillations in the solution. They also show that, for the energy equation, heat convection strongly dominates over conduction and viscosity. Chapman et al. [15] apply a finite difference approach to solve what are essentially the quasi-one-dimensional governing equations over the length of a pipe. They model intake and exhaust valves using an isentropic flow model with a discharge coefficient. They present an interesting approach to handling pipe junctions that the author will return to at a later date. Their results for a single engine RPM were good, but they

never compared predicted and real power and torque curves. Shimamoto et al. [16] solve the one-dimensional Euler equations using a method of characteristics approach and find an important result. Measuring curved pipe lengths by the shortest possible length, rather than by the centerline length, seems to provide the most accurate results. Takizawa et al. [17] solve the quasi-one-dimensional governing equations of fluid flow using a Lax-Wendroff approach. Their constant-RPM predictions are good, but they don't compare measured and predicted power, torque and volumetric efficiency over the engine's operating RPM range. Notably, they apply a "bend friction factor" that could prove useful for future work. Zhang and Assanis [18] created a quasi-one-dimensional simulation that they solved using a finite-volume approach which they claim to be Total Variation Diminishing. The TVD scheme employs a central differencing scheme when the flow is elliptic in space and a one-sided scheme when it is hyperbolic. They compare their results with Blair [19], which is also a computational prediction, and get varying levels of agreement. Stockar et al. [20] performed a comparison between three approaches to modeling a complete engine with intake and exhaust tracts: a finite-difference approach, a finite-volume approach and a reduced-order, spectral method. They model the valves as simple orifices with discharge coefficients. They show reasonable agreement between the three methods in time-domain pressure traces at the intake valve, and also characterize the relative computational cost of each method.

Researchers have recognized the need to replace empirical, steady-flow measurements of fluid drag in the intake and exhaust flows with more first-principles models. In an important paper, Chalet et al. [21] attempt to construct a reduced-order model that can account for the separation of a flow as it enters a straight pipe from the atmosphere. While not applied in

the current study, reduced-order models of flow separation are necessary to realize accurate, non-empirical results from an engine simulation. This is a rich field for future research.

In a more pure fluid dynamics study, Kim et al. [22] looked at the flow through a poppet valve using three-dimensional CFD. They compared the mass flow rate and downstream mixing to that of a surrogate, contracting-expanding nozzle of equal flow area and found that, functionally, they were identical. This provides strong footing for the use of such nozzles as valves in the present study.

CHAPTER 2

Cylinder Geometry

In this chapter, we derive the equations that describe the geometry of the cylinder and the collection of gases held within the cylinder, the charge. The cylinder model drives the engine simulation. Turning the virtual crankshaft causes the cylinder volume to change and the valves to open and close. When the valves are open, the cylinder model acts as a forcing function on the flows within the intake and exhaust tracts.

The cylinder model is largely a model of the charge *within* the cylinder. We'll consider the charge to be an isotropic, homogeneous mixture of gases. We'll model the charge as a single volume, neglecting the flow within the charge. In a four-stroke engine, the nearly complete displacement of the charge out of the cylinder on the exhaust stroke, followed by the positive inflow of new charge on the intake stroke, minimizes the effect of intracharge flow phenomena and fluid structures. This approach has been found to return reasonable results in closed-form gas cycle and four-stroke engine analyses [23] and it is one of the simplifications that we will test here. Will a time-domain, control-volume treatment of the charge encompass enough of the dominant physics to provide realistic results?

Figure 2.1 illustrates the charge, colored white, in the cylinder at bottom-dead-center (BDC) and top-dead-center (TDC) of the piston's stroke. Note how, at TDC, the charge has been highly compressed, leaving a very small volume, the clearance volume ($\mathcal{V}_c$), where combustion will take place. We need to establish a relationship between the volume of the charge and the angular displacement of the crankshaft.

Figure 2.2 illustrates the relevant dimensions that we'll use in deriving the cylinder model. These include the cylinder bore, the cylinder stroke and the length of the connecting rod.

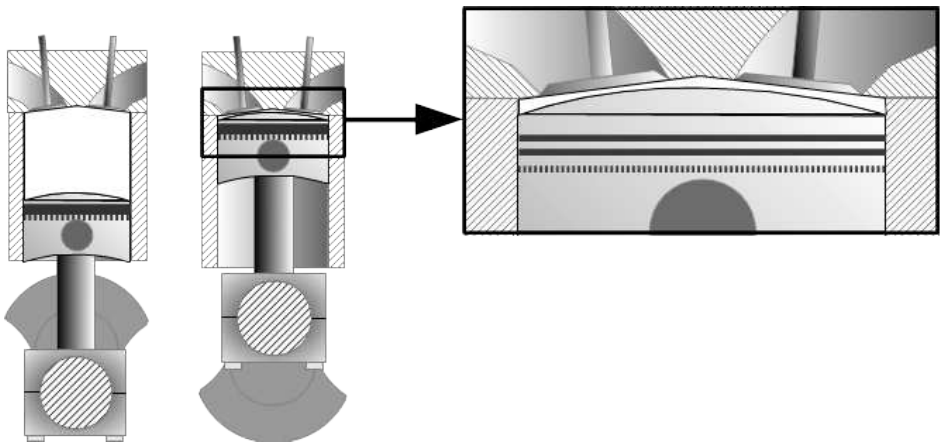

FIGURE 2.1. The charge in the cylinder at BDC and TDC

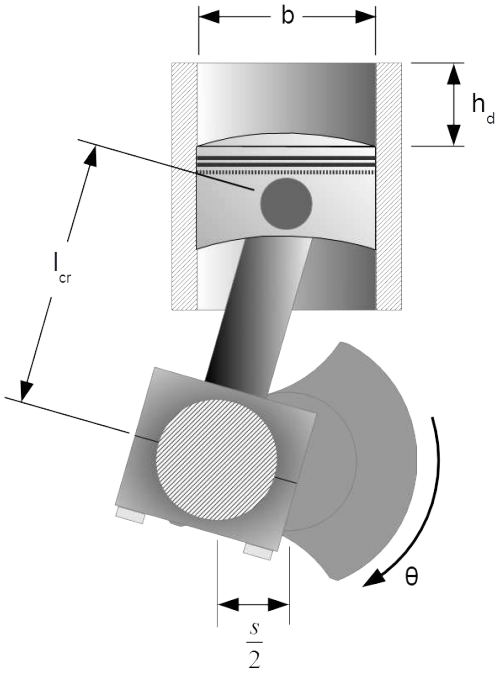

FIGURE 2.2. Cylinder Dimensions

We can envision the charge volume as being composed of two separate volumes, the clearance volume, which is constant, and the volume created as the piston rises and falls. We'll call that latter the "displacement volume", $\mathcal{V}_d$, of the charge. h_d is the height of the displacement volume. Rotation of the crankshaft, θ, is measured from TDC of the engine's compression stroke and ranges from zero to 4π, or 0 to 720°.

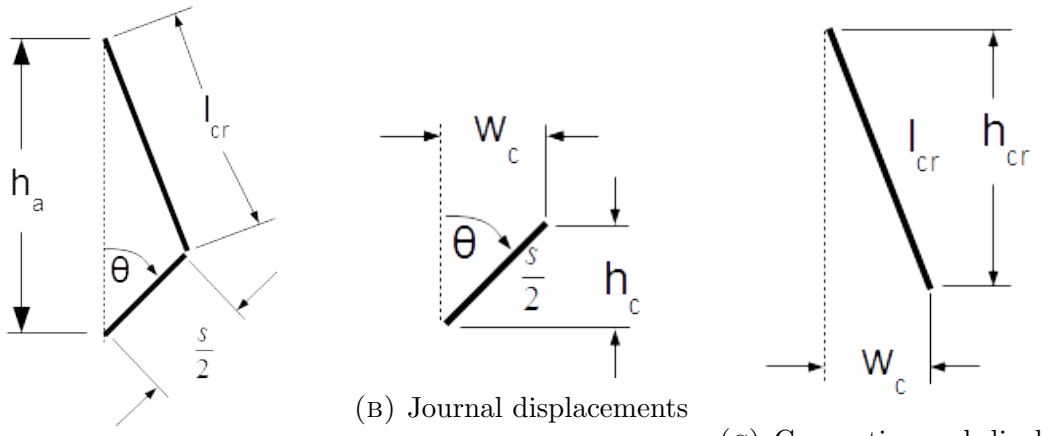

(A) Crankshaft/Connecting Rod Assembly

(B) Journal displacements

(C) Connecting rod displacements

FIGURE 2.3. Crankshaft/Connecting Rod Geometry

As the crankshaft rotates, the journal scribes a circular path in space. The vertical and horizontal displacements of the journal are illustrated in figure 2.3b and are given by:

$$h_c = \frac{s}{2}cos(\theta) \qquad w_c = \frac{s}{2}sin(\theta) \tag{2.1}$$

The large end of the connecting rod is connected to the crankshaft journal and translates with it. The overall lateral and vertical travel (width and height) of the connecting rod are illustrated in figure 2.3c and are related to its length by:

$$l_{cr}^2 = w_c^2 + h_{cr}^2 \qquad \text{or} \qquad h_{cr}^2 = l_{cr} - w_c^2$$

Based on the lateral displacement of the crankshaft journal, the height of the connecting rod is:

$$h_{cr} = \sqrt{l_{cr}^2 - \frac{s^2}{4} sin^2(\theta)} \tag{2.2}$$

The total height of the assembly as a function of crankshaft angle, as illustrated by figure 2.3a is then:

$$h_a = h_c + h_{cr} = \frac{s}{2} cos(\theta) + \sqrt{l_{cr}^2 - \frac{s^2}{4} sin^2(\theta)} \tag{2.3}$$

The maximum length of the assembly is

$$h_{a_{max}} = l_{cr} + \frac{s}{2} \tag{2.4}$$

Subtracting Equation 2.3 from Equation 2.4 gives us the distance between the transient height of the connecting rod small end and its maximum height. Since the piston is attached to the connecting rod small end, this also represents the distance between the piston's maximum height and its transient height. This is the displacement height of the cylinder volume.

$$h_d(\theta) = l_{cr} + \frac{s}{2} - \frac{s}{2} cos(\theta) - \sqrt{l_{cr}^2 - \frac{s^2}{4} sin^2(\theta)} \tag{2.5}$$

Multiplying by the circular area of the cylinder, $a_c = \pi r^2 = \pi \frac{b^2}{4}$, we have the displaced volume of the cylinder as a function of crankshaft angular displacement:

$$\mathcal{V}_d(\theta) = \pi\frac{b^2}{4}\left(l_{cr} + \frac{s}{2} - \frac{s}{2}cos(\theta) - \sqrt{l_{cr}^2 - \frac{s^2}{4}sin^2(\theta)}\right) \tag{2.6}$$

To determine the size of the clearance volume, we turn to the engine's compression ratio. The geometric compression ratio of the cylinder is equal to the maximum volume divided by the clearance volume. The maximum volume of the cylinder is the sum of the clearance volume and the maximum displacement volume,

$$\mathcal{V}_{max} = \mathcal{V}_c + \mathcal{V}_d$$

And the compression ratio is given by:

$$r = \frac{\mathcal{V}_{max}}{\mathcal{V}_c} = \frac{\mathcal{V}_c + \mathcal{V}_d}{\mathcal{V}_c} = \frac{\mathcal{V}_d}{\mathcal{V}_c} + 1 \qquad \text{or} \qquad \mathcal{V}_c = \frac{\mathcal{V}_d}{r-1}$$

The maximum displacement volume is the product of the stroke and the cylinder area:

$$\mathcal{V}_d = s\frac{\pi b^2}{4}$$

And so the clearance volume is:

$$\mathcal{V}_c = \frac{\pi s b^2}{4(r-1)} \tag{2.7}$$

And finally, the total volume of the charge in the cylinder, as a function of crankshaft angle, is the sum of the clearance volume, Equation 2.7, and the current displacement volume, Equation 2.6:

$$\boxed{\mathcal{V}(\theta) = \frac{\pi b^2}{4}\left(l_{cr} + \frac{s}{2} - \frac{s}{2}cos(\theta) - \sqrt{l_{cr}^2 - \frac{s^2}{4}sin^2(\theta)} + \frac{s}{r-1}\right)} \tag{2.8}$$

Note the data values required for this equation: cylinder bore, stroke, compression ratio and connecting rod length. All of these values except for connecting rod length are common engine specifications, available from all sources. The connecting rod length must either come from deeper sources or from actual measurement.

We'll also need the time-derivative of Equation 2.8. Without showing the manipulations, it is:

$$\boxed{\frac{d\mathcal{V}}{dt} = \frac{\pi b^2}{4}\left(\frac{s}{2}sin(\theta)\frac{d\theta}{dt} + \frac{s^2 sin(\theta)cos(\theta)}{4\sqrt{l_{cr}^2 - \frac{s^2}{4}sin^2(\theta)}}\frac{d\theta}{dt}\right)} \tag{2.9}$$

This equation, given crankshaft angle and crankshaft rotational velocity, provides the rate of change of the cylinder volume. It will be needed later in the governing equations of the charge.

The cylinder depicted in Figures 2.1 and 2.2 is a scale rendering of a cylinder from a real engine, an Alfa Romeo 2.5 liter V6, as found in the GTV6 and Milano models. Its dimensions are listed in Table 2.1.

TABLE 2.1. Cylinder Data

bore (b) (mm)	stroke (s) (mm)	connecting rod length (l_{cr}) (mm)	compression ratio
88	68	131	9.0

Table 2.2 lists a set of data derived from Table 2.1, the clearance volume, displacement volume, cylinder volume and the rate of change of the cylinder volume as the crankshaft passes through 90 degrees at 1,000 RPM.

TABLE 2.2. Derived Cylinder Data

clearance volume (cc)	displacement volume (cc)	cylinder volume (cc)	volume rate $\left(\frac{dV}{dt}\right)$ at 90° $\left(\frac{cc}{sec}\right)$
51.7	413.6	465.6	21,651

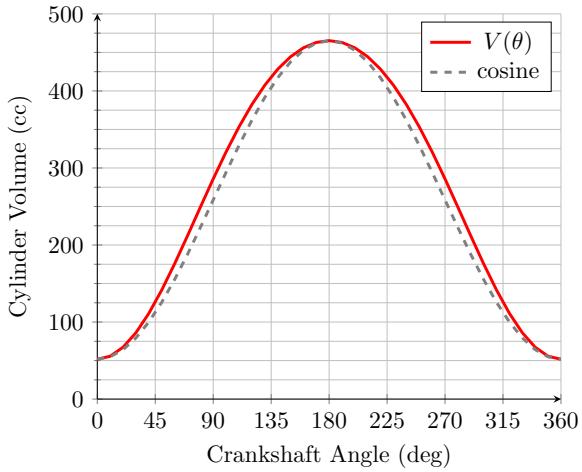

(A) $V(\theta)$

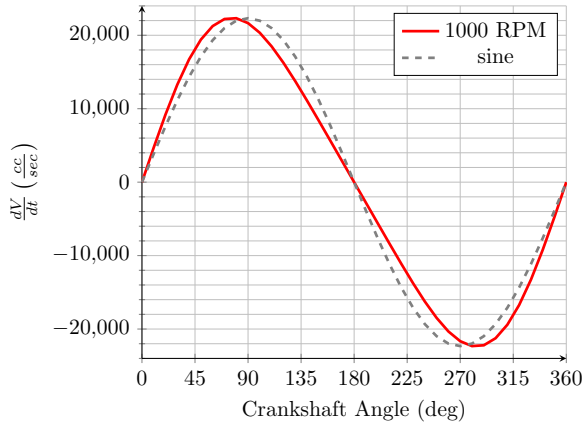

(B) $\frac{dV}{dt}$

FIGURE 2.4. Geometric Results for the Example Cylinder

Compare these results with the values in Figures 2.4a and 2.4b. Figure 2.4a illustrates the volume of the cylinder with respect to crankshaft angle, $\mathcal{V}_T(\theta)$. The values are generated by Equation 2.8, fed with the data from Table 2.1. We see the cylinder volume going from its minimum value, 51.7 cc, to its maximum value, 465.3 cc. Note how the minimum and

maximum values match those in Table 2.2. Also note the shape of the curve. A cosine curve of equal amplitude and phase is included for reference. Because of the linkage between the piston and the crankshaft, the piston's vertical position as the crankshaft rotates isn't sinusoidal, and therefore, neither is the volume of the cylinder.

Figure 2.4b illustrates the rate of change of the cylinder volume with respect to time, $\frac{d\mathcal{V}}{dt}$, at 1,000 RPM. The values here are generated by Equation 2.9 using the data from Table 2.1. At 90 degrees crankshaft angle, we see the volume rate, 21,655 $\frac{cc}{sec}$, essentially matching the value of Table 2.2. Also note the asymmetry in the curve. A sine curve with the same amplitude and phase is included for reference. Because of the piston-connecting rod-crankshaft linkage, the piston velocity in this engine reaches a maximum value at about 80 degrees. Piston velocity isn't sinusoidal.

These results give us confidence that our two equations, (2.8 and 2.9) are correct. This is crucial, as these equations drive the engine simulation.

Returning to Equation 2.3, we will need an equation describing the velocity of the piston. Without showing the manipulations, the time-derivative of Equation 2.3 is:

$$\boxed{\frac{dh_p}{dt} = V_p = -\frac{s_0}{2} sin(\theta) \frac{d\theta}{dt} - \frac{\frac{s_0^2}{4} sin(\theta) cos(\theta)}{\sqrt{l_{cr}^2 - \frac{s_0^2}{4} sin^2(\theta)}} \frac{d\theta}{dt}} \tag{2.10}$$

Using the values from table 2.1, with a crankshaft rotational speed of 1,000 RPM, Equation 2.10 generates the values shown in Figure 2.5. At 0 and 180° we should see values of 0. At 90° we should see a value of -3.56 $\frac{m}{sec}$ and at 270° we should see a value of 3.56 $\frac{m}{sec}$. These values all lie on the plot, giving us confidence that this equation is correct.

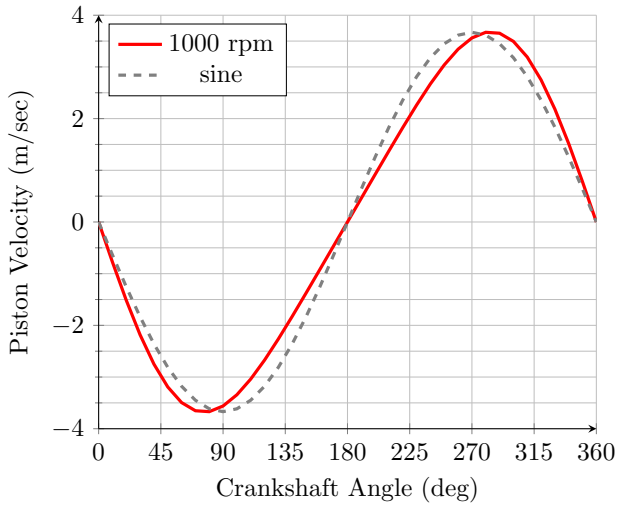

FIGURE 2.5. Piston Velocity

CHAPTER 3

Governing Equations of the Charge

With functions in hand that describe the volume and volume rate of the charge with respect to the crankshaft angle, we can now consider the aerodynamics and thermodynamics of the charge. In keeping with the motivation for this work given in the introduction, we're going to attempt to create a reduced-order model that will capture all of the dominant physics needed to provide a sufficient level of accuracy. For the cylinder model—the model of the charge—we'll consider the charge to be a homogeneous, isotropic mass of gas: density, pressure and temperature are constant across the charge. We'll assume that the gas is a mixture with static molecular weight and with mass fractions that are constant in both space and time. Finally, we'll assume that the gases comprising the charge are inviscid. In considering the charge to be a single mass of gas, we'll neglect any fluid motions or fluid structures that might exist within it. While they are certainly significant in analyses of combustion and in the detailed aerodynamics of the intake, exhaust and intra-cylinder flows, we hope to find that they aren't significant in the prediction of torque, power and volumetric efficiency in a four-stroke engine with poppet valves.

Figure 3.1 illustrates the charge in the cylinder as the piston is rising on the exhaust stroke. The charge has the properties volume, $\mathcal{V}$, rate of change of volume, $\frac{d\mathcal{V}}{dt}$, density, ρ, temperature, T, pressure, P, molecular weight, W, and specific heats c_p and c_v. Note that the exhaust valve is open, allowing fluid to flow out with mass flux $\dot{m}_e$. The intake valve is closed, blocking any fluid flow; $\dot{m}_i = 0$. There is also a mass flux across the piston skirt. This occurs because the piston and its rings don't create a perfect seal against the cylinder wall. This leakage through the rings is called "blowby". In reality, it is the result of many

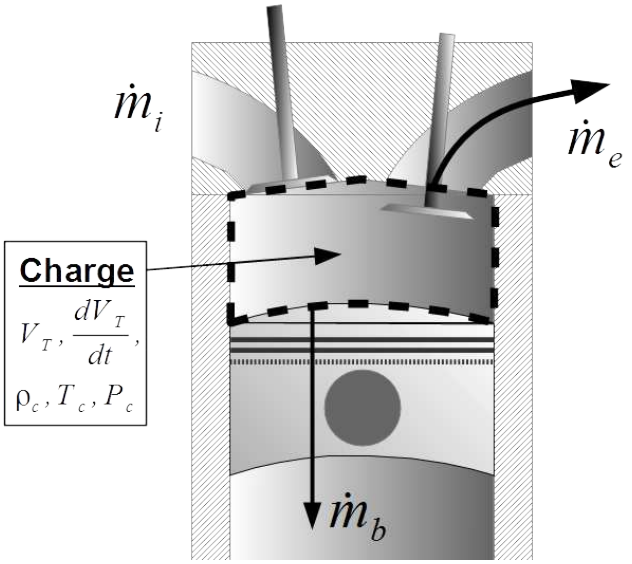

FIGURE 3.1. Charge Massflow

minute mass flows. We will consider it as a single flow, with mass flux $\dot{m}_b$. The cylinder, piston and cylinder head suggest a natural control volume surrounding the charge. It is indicated by the dashed, black line in the figure and we will refer back to it continuously as we derive the governing equations of the charge. The equations are derived by applying the laws of nature, in the form of the governing equations of fluid flow, to the control volume model.

3.1. The Continuity Equation

Physical principle applied here: mass is conserved. Since the charge is an inviscid fluid, we'll employ the continuity equation of the Euler Equations, [24] which is a refined statement of mass conservation for fluids:

$$\frac{\partial}{\partial t}\iiint_{\mathcal{V}} \rho d\mathcal{V} + \iint_{S} \rho \vec{V} \cdot d\vec{S} = 0 \tag{3.1}$$

Here $\mathcal{V}$ refers to a general volume of fluid, S under the double integral refers to the surface enclosing that volume, $\vec{V}$ is the velocity of the fluid crossing the surface and $\vec{S}$ is the unit surface normal vector pointing *out* of the volume.

Applied to the control volume surrounding the charge, illustrated in Figure 3.1, the volume integral (left-hand side) becomes:

$$\frac{\partial}{\partial t}\iiint_{\mathcal{V}} \rho d\mathcal{V} = \frac{d}{dt}\left(\rho_c \mathcal{V}\right)$$

where $\mathcal{V}$ on the right is the volume of the charge.

The right-hand term of Equation 3.1 is the integral of the incremental mass flow rate into or out of the control volume, increasing or decreasing the mass inside of the volume. Applying this term to the control volume surrounding the charge, we see that fluid can't cross its solid walls. Over all of those surfaces, $\vec{V} \cdot d\vec{S} = 0$. Fluid can enter or leave the control volume through three discrete paths, the open intake valve, the open exhaust valve, or through the imperfect seal between the piston and the cylinder wall, blowby. Considering massflow *out* of the cylinder as positive, the surface integral applied to the charge control volume becomes

$$\iint_{S} \rho\vec{V} \cdot d\vec{S} = \left(\rho\vec{V}A\right)_i + \left(\rho\vec{V}A\right)_e + \left(\rho\vec{V}A\right)_b$$

where ρ is the density of the fluid passing through the path, $\vec{V}$ is the velocity of the fluid in the intake, exhaust or blowby flow and A is the cross-sectional area of that flow.

Putting these two terms together, we can say that the rate of *decrease* of the mass of the charge, m_c,is:

$$-\frac{dm_c}{dt} = -\frac{d}{dt}(\rho_c \mathcal{V}) = \left(\rho \vec{V} A\right)_i + \left(\rho \vec{V} A\right)_e + \left(\rho \vec{V} A\right)_b \tag{3.2}$$

Performing the derivative of the product on the left hand side,

$$-\frac{d}{dt}(\rho_c \mathcal{V}) = -\frac{d\rho_c}{dt}\mathcal{V} - \rho_c \frac{d\mathcal{V}}{dt}$$

And so we have:

$$-\frac{d\rho_c}{dt}\mathcal{V} - \rho_c \frac{d\mathcal{V}}{dt} = \left(\rho \vec{V} A\right)_i + \left(\rho \vec{V} A\right)_e + \left(\rho \vec{V} A\right)_b \tag{3.3}$$

or,

$$\boxed{\frac{d\rho}{dt} = -\frac{1}{\mathcal{V}}\left[\left(\rho \vec{V} A\right)_i + \left(\rho \vec{V} A\right)_e + \left(\rho \vec{V} A\right)_b + \rho \frac{d\mathcal{V}}{dt}\right]} \tag{3.4}$$

Equation 3.4 is the continuity equation of the charge. Given the mass fluxes from the valve and blowby flow models, plus the volume and volume rate derived in the previous chapter, it provides the rate of change of the density of the charge in the cylinder. Note that velocity *out* of the control volume (cylinder) is positive.

3.2. The Momentum Equation

Physical principle applied here: Newton's Second Law. We'll employ a refined form of this concept, the momentum equation of the Euler equations,

$$\frac{\partial}{\partial t}\iiint_{\mathcal{V}} \rho\vec{V}d\mathcal{V} + \iint_{S}\left(\rho\vec{V}\cdot d\vec{S}\right)\vec{V} = \underbrace{-\iint_{S} Pd\vec{S}}_{a} \tag{3.5}$$

The assumption that the charge is isotropic combines with the surface pressure integral, term "a" of Equation 3.5, to reveal a surprising result. Figure 3.2 shows the pressure force on the surface of the control volume. Since the charge within the volume is isotropic, the pressure is the same throughout the charge. At the control volume surface, the pressure multiplied by the unit surface normal vector results in the force vectors pointing equally out in all directions. Integrated over the control volume surface, the forces cancel; the integral is zero. This means that there is no net pressure force on the charge, and it cannot accelerate in any direction.

The result is that the momentum of the charge is zero and therefore the charge has zero velocity. In reality, we know that the charge does move. The surface of the control volume in contact with the piston translates up and down with the piston. When the valves are closed, the surface of the control volume in contact with the cylinder head does not move. But we can see that the centroid of the charge must translate. This seems like a rather significant phenomenon to neglect. But closed-form engine analyses [23] making this same assumption seem to provide realistic and relatively accurate results. And so we will accept that the velocity of the charge is zero.

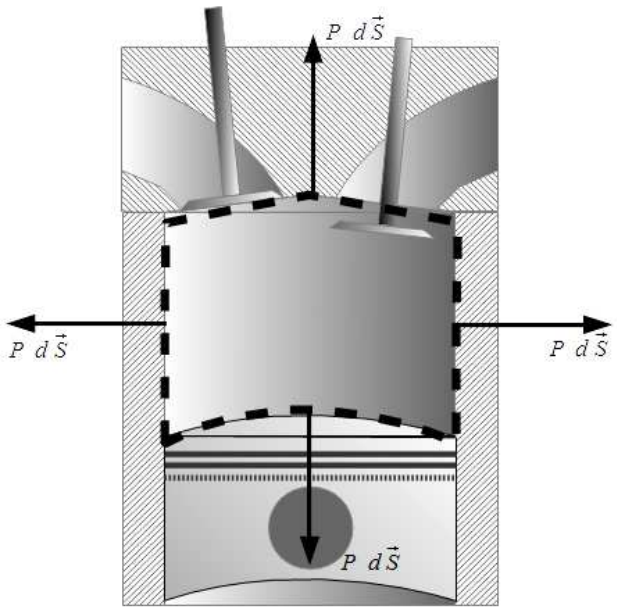

FIGURE 3.2. Pressure Force on the Charge

3.3. The Energy Equation

Physical principle applied here: energy is conserved. The energy equation is essentially a restatement of the first law of thermodynamics,

$$\delta q + \delta w = \delta e \tag{3.6}$$

saying that the increase in energy of a system is equal to the heat added plus the work done on the system. The charge being a fluid, we see that it can store energy kinetically, through pressure (work done) and as internal energy, a function of temperature. We're interested in the total energy of the fluid in the charge. Energy can enter or leave the charge through three mechanisms:

- δw, work done on the piston by the charge. This is the pressure-generated force on the piston, times the speed of the piston's withdrawal.
- δw, work done on the intake, exhaust and blowby flows. This is the pressure-generated force on those flows, times the outward speed of the flows.
- Mass transfer. As fluid leaves the charge through the valves and blowby, it carries its energy with it, decreasing the total energy of the charge.
- δq, heat loss from the charge to the cylinder walls, piston crown and cylinder head. This is heat transfered through convection and radiation.
- δq, heat addition (a negative value) through combustion of the reactants in the charge.

Since our system is a fluid, we'll employ the energy equation of the Euler Equations, which is itself a restatement of the First Law:

$$\underbrace{\frac{\partial}{\partial t}\iiint_{\mathcal{V}} \rho\left(e+\frac{\vec{V}^2}{2}\right)d\mathcal{V}}_{a}+\underbrace{\iint_{S} \rho\left(e+\frac{\vec{V}^2}{2}\right)\vec{V}\cdot d\vec{S}}_{b}=-\underbrace{\iiint_{\mathcal{V}} \rho\dot{q}d\mathcal{V}}_{c}-\underbrace{\iint_{S} P\vec{V}\cdot d\vec{S}}_{d} \tag{3.7}$$

Here, e is the internal energy of the charge,

$$e = c_v T \tag{3.8}$$

where T is the absolute temperature of the fluid and c_v is the constant-volume specific heat of the fluid.

The "a" term in Equation 3.7 represents the total energy contained in a volume of fluid. The "b" term represents the energy flux carried by fluid entering or leaving the volume. The "c" term represents heat added or lost from the mass of fluid contained in the volume and the "d" term represents work done on, or by, the fluid mass by pressure forces acting on the volume's surface. This equation embodies all of the processes listed above.

Applying the "a" term of Equation 3.7 to the control volume surrounding the charge in figure 3.1 it becomes:

$$\frac{\partial}{\partial t}\iiint_{\mathcal{V}} \rho\left(e + \frac{\vec{V}^2}{2}\right) d\mathcal{V} = \frac{d}{dt}\left(\rho e \mathcal{V}\right) \tag{3.9}$$

Where $\mathcal{V}$ on the right is the volume of the charge. Note that, since we have no momentum equation, we are assuming that the velocity of the charge is zero. Performing the derivative of the product on the right:

$$\begin{aligned}\frac{\partial}{\partial t}\iiint_{\mathcal{V}} \rho\left(e + \frac{\vec{V}^2}{2}\right) d\mathcal{V} &= \frac{d\rho}{dt}\mathcal{V}e + \rho\frac{d\mathcal{V}}{dt}e + \rho\mathcal{V}\frac{de}{dt} \\ &= \frac{d\rho}{dt}\mathcal{V}e + \rho\frac{d\mathcal{V}}{dt}e + \rho\mathcal{V}c_v\frac{dT}{dt}\end{aligned} \tag{3.10}$$

Applying the "b" term of Equation 3.7 to the control volume surrounding the charge in figure 3.1, we see that $\vec{V} \cdot d\vec{S}$ is zero at the cylinder walls. At the valves and the blowby, it is non-zero. And so the equation becomes:

(3.11)
$$\iint_S \rho\left(e+\frac{\vec{V}^2}{2}\right)\vec{V}\cdot d\vec{S} = \left[\rho\left(e+\frac{\vec{V}^2}{2}\right)\vec{V}A\right]_i + \left[\rho\left(e+\frac{\vec{V}^2}{2}\right)\vec{V}A\right]_e + \left[\rho\left(e+\frac{\vec{V}^2}{2}\right)\vec{V}A\right]_b$$

where ρ is the density of the fluid passing through the path, $e = c_v T$ where T is the temperature of the fluid passing through the path, $\vec{V}$ is the velocity of the fluid in the intake, exhaust or blowby flow and A is the cross-sectional area of that flow. Again, note that velocity *out* is positive.

Applying the "c" term of Equation 3.7 to the control volume surrounding the charge in figure 3.1 it becomes:

(3.12)
$$\iiint_{\mathcal{V}} \rho\dot{q}d\mathcal{V} = \rho\dot{q}\mathcal{V} = \dot{Q}$$

We see that this term represents a volumetric heating or cooling of the charge from unspecified sources. In our case, we will include a model for the convective and radiant heat transfer from the charge to the cylinder walls (and vice-versa). This c term will also be the conduit through which we add combustion heat to the charge.

(3.13)
$$\iiint_{\mathcal{V}} \rho\dot{q}d\mathcal{V} = \rho\dot{q}\mathcal{V} = \dot{Q}_T + \dot{Q}_c$$

Heat flow *out* of the control volume is positive.

Finally, term "d" of Equation 3.7 is a pressure-volume work term. (Actually, pressure-generated force times velocity, or power.) Applying it to the control volume surrounding the charge in figure 3.1 we see that $\vec{V} \cdot d\vec{S}$ is zero at the stationary cylinder walls and, since no fluid crosses the control surface at the piston crown, zero there also. It is non-zero at the valves and blowby. For our discrete control volume,

$$\iint_S P\vec{V} \cdot d\vec{S} = \left(P\vec{V}A\right)_i + \left(P\vec{V}A\right)_e + \left(p\vec{V}A\right)_b \tag{3.14}$$

Again, note that velocity *out* of the control volume is positive.

Assembling these four terms,

$$\begin{aligned} &\frac{d\rho}{dt}\mathcal{V}e + \rho\frac{d\mathcal{V}}{dt}e + \rho\mathcal{V}c_v\frac{dT}{dt} \\ &+ \left[\rho\left(e + \frac{\vec{V}^2}{2}\right)\vec{V}A\right]_i + \left[\rho\left(e + \frac{\vec{V}^2}{2}\right)\vec{V}A\right]_e + \left[\rho\left(e + \frac{\vec{V}^2}{2}\right)\vec{V}A\right]_b \\ &= -\dot{Q}_T - \dot{Q}_c - \left(P\vec{V}A\right)_i - \left(P\vec{V}A\right)_e - \left(p\vec{V}A\right)_b \end{aligned} \tag{3.15}$$

Subsuming the energy flux and pressure-volume power terms into sums,

$$\frac{d\rho}{dt}\mathcal{V}e + \rho\frac{d\mathcal{V}}{dt}e + \rho\mathcal{V}c_v\frac{dT}{dt} + \sum_{i=1}^{3}\left[\rho\left(e + \frac{\vec{V}^2}{2}\right)\vec{V}A\right]_i = -\sum_{j=1}^{3}\left(P\vec{V}A\right)_j - \dot{Q}_T - \dot{Q}_c \tag{3.16}$$

where 1 = intake, 2 = exhaust, 3 = blowby.

And finally, with some rearrangement,

(3.17)

$$\boxed{\frac{dT}{dt} = -\frac{1}{\rho \mathcal{V} c_v}\left\{\sum_{i=1}^{3}\left[\rho\left(e + \frac{\vec{V}^2}{2}\right)\vec{V}A\right]_i + \sum_{j=1}^{3}\left(P\vec{V}A\right)_j + \dot{Q}_T + \dot{Q}_c + \mathcal{V}e\frac{d\rho}{dt} + \rho e\frac{d\mathcal{V}}{dt}\right\}}$$

Equation 4.1 is the energy equation of the charge. Given the rate of change of density, from Equation 3.4, the energy fluxes from the valve and blowby flow models, the heat fluxes due to loss and combustion, the charge volume and volume rate, derived in the previous chapter, it provides the rate of change of the charge temperature.

$\frac{d\rho}{dt}$ and $\frac{dT}{dt}$ can be integrated to return the density and temperature of the charge. Given crankshaft rotational velocity, ω, and a rotational step size, $\Delta\theta$, we can calculate a timestep size:

(3.18)

$$\boxed{\Delta t = \frac{\Delta\theta}{\omega}}$$

To advance the solution of the charge state forward in time, we:

(1) Increment the crankshaft angle by $\Delta\theta$

(2) Advance the flow models forward in time by Δt

(3) Calculate values for the volume and volume rate at the new θ

(4) Calculate a density rate with the continuity equation and integrate the rate by Δt to find the density at the current timestep.

(5) With the new density value and rate, calculate a new temperature rate and integrate the rate by Δt to find the temperature at the current timestep.

(6) End the integration step by closing the system with the perfect gas equation of state:

$$P = \rho RT \tag{3.19}$$

With the density, temperature and pressure of the charge in hand, we are now ready to begin a new integration step by operating the flow models. In this manner, operating the charge and flow models in lockstep, we time-march the entire engine simulation into the future. Integration is done using a Runge-Kutta 4-stage integrator (RK4) that is fourth-order accurate in time.

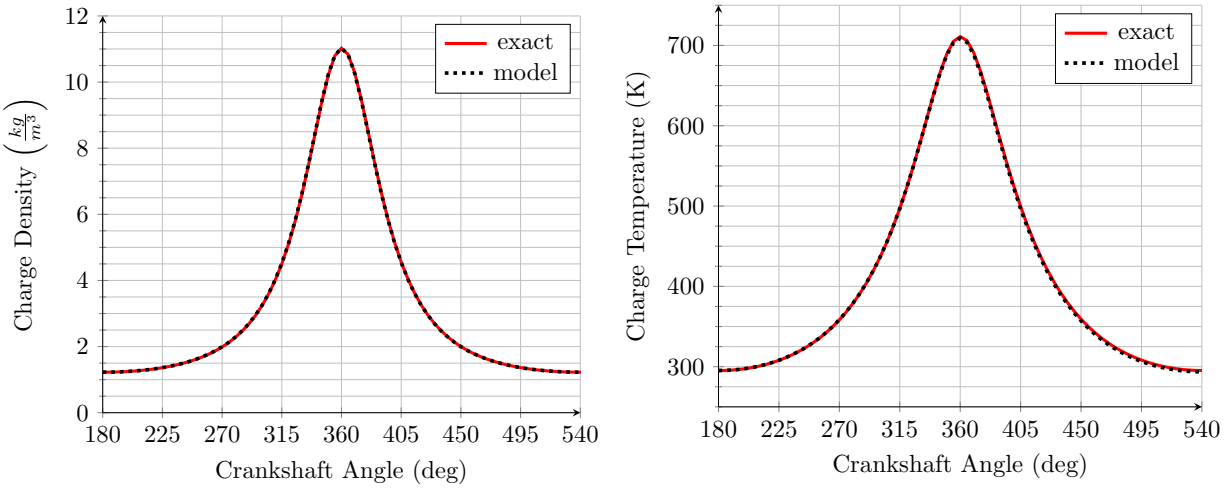

(A) Density from BDC to BDC

(B) Temperature from BDC to BDC

FIGURE 3.3. Model Results

Figure 3.3 shows the system in operation. With the piston beginning at BDC, the charge in the cylinder is assumed to be at ambient density and temperature. The crankshaft is then rotated one revolution. No mass is allowed to escape and there is no heat flow from the charge to the cylinder. Figure 3.3a illustrates the variation in density as the piston rises, reaches TDC at 360 degrees, then returns back down to BDC at 540 degrees. For

comparison, the density through this process can be modeled exactly using the isentropic gas relation,

$$\rho_2 = \rho_1 \frac{\mathcal{V}_1}{\mathcal{V}_2} \tag{3.20}$$

The exact relationship is given by the solid, red line, and the results of this model are given by the dashed black line. Figure 3.3b shows the temperature as the crankshaft is rotated one revolution and the piston cycles from BDC to TDC and back. The exact solution is calculated using the isentropic gas relation,

$$T_2 = T_1 \left(\frac{\mathcal{V}_1}{\mathcal{V}_2} \right)^{\gamma - 1} \tag{3.21}$$

Note how high the charge temperature rises as it is isentropically compressed to one-ninth of its original volume. The peak temperature is over 700 K.

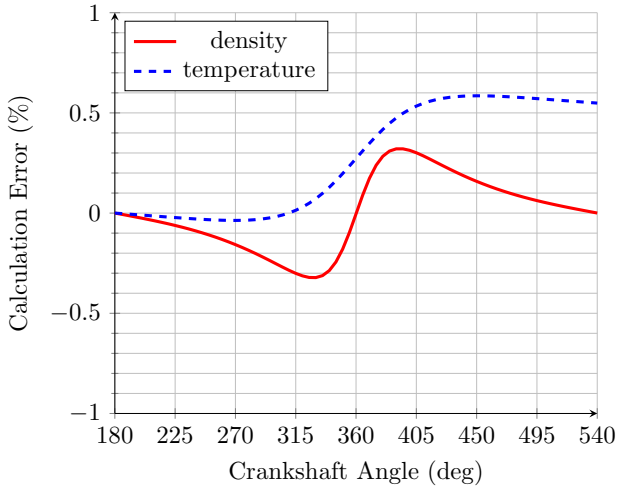

FIGURE 3.4. Calculation Error Over the Cycle

Figure 3.4 illustrates the calculation error in density and temperature over the cycle. The maximum error in density is about 0.27% and cyclic; it returns back to zero. Since the temperature calculation relies on density, the error there is compounded. The maximum error over the cycle is about 0.5% and accumulates. Since, in a typical power calculation, the model is advanced four revolutions, the error will be insignificant at the end of a simulation run.

Instantaneous power at the piston is measured by calculating the force on the piston and multiplying by its velocity, $P_i = F_p V_p$. To calculate the power over a full, two-revolution cycle, the instantaneous power is integrated with respect to time to give the total work over the cycle:

$$W_{cycle} = \int_0^{720^\circ} F_p V_p dt \tag{3.22}$$

This is also accomplished numerically using the RK4 integrator. After the engine has been advanced a full cycle, the work value is then divided by the time of the cycle to yield average power over the cycle:

$$P_{cycle} = \frac{W_{cycle}}{\Delta t_{cycle}} \tag{3.23}$$

Figure 3.5 illustrates the work performed as the crankshaft is rotated one revolution and the piston cycles from BDC to TDC and back. Note how the work value is negative. This means work is being done by the piston on the charge. A positive value would indicate work

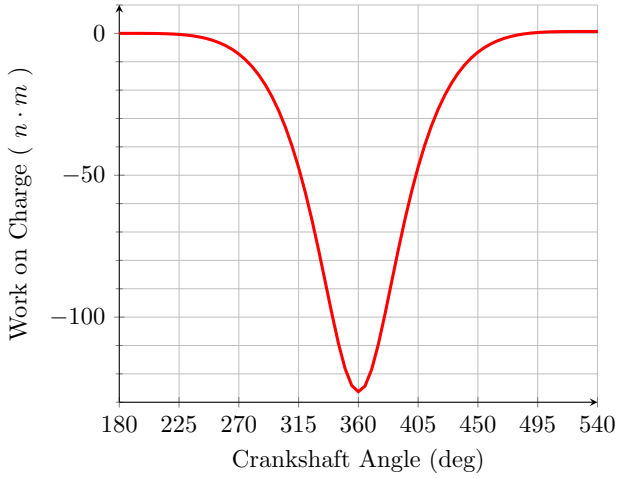

FIGURE 3.5. Work Performed Over the Cycle

done by the charge on the piston. Importantly, the value returns back to zero at the end of the revolution.

CHAPTER 4

Gas Values and Combustion

There is more than one way to account for the addition of energy to the charge by combustion. The energy equation of the charge,

(4.1)
$$\frac{dT}{dt} = -\frac{1}{\rho \mathcal{V} c_v}\left\{\sum_{i=1}^{3}\left[\rho\left(e + \frac{\vec{V}^2}{2}\right)\vec{V}A\right]_i + \sum_{j=1}^{3}\left(P\vec{V}A\right)_j + \dot{Q}_T + \dot{Q}_c + \mathcal{V}e\frac{d\rho}{dt} + \rho e\frac{d\mathcal{V}}{dt}\right\}$$

provides a term, $\dot{Q}_c$, allowing us to add combustion energy to the charge at a finite rate. But there is also the possibility of adding combustion energy to the charge instantaneously. We'll consider both approaches here.

4.1. Combustion Energy Release

In the engine, combustion energy comes from a fuel/air combustion reaction. Shortly before the beginning of the piston's intake stroke, the intake valve opens, allowing a mixture of air and gaseous fuel to enter the cylinder. Shortly after the end of the intake stroke, the intake valve closes, trapping the intake charge in the cylinder. The charge is compressed over the compression stroke and then ignited by a spark near the top of the stroke. Once ignited, the charge burns, releasing chemical energy as the mixture composition changes from reactants to products.

The magnitude of energy released is determined by the difference in enthalpy from the reactants to the products [25] [26] [27]:

(4.2) $$Q_c = H_p - H_r$$

and enthalpy,

(4.3) $$\bar{h} = \bar{c_p} T \qquad \text{(overbar = mole-specific)}$$

Gasoline is difficult to work with analytically. Rather than a compound, it is a mixture, typically of 40+ hydrocarbon compounds. Its makeup is largely determined by the crude oil from which it is refined. Its consistency is bounded by statistics, as the gas that comes out of a cracking tower today will be different from what came out yesterday. And so for analytical research we must substitute a compound that possesses as many of the characteristics of gasoline as possible. Here, we will use octane, C_8H_{18}, which is often used as a chemical surrogate, or simulant, for gasoline. And we will consider air a mixture of 78% nitrogen, 21% oxygen and 1% argon by volume. These volume fractions are equivalent to the mole fractions of the mixture:

(4.4) $$y_{N_2} = 0.78, \qquad y_{O_2} = 0.21, \qquad y_{Ar} = 0.01$$

or,

(4.5) $$y_{N_2} = 3.71\, y_{O_2} \qquad y_{Ar} = 0.0476\, y_{O_2}$$

The chemically balanced fuel/air reaction is then:

(4.6) $$C_8H_{18} + 12.5\, O_2 + (12.5)(3.71)\, N_2 + (12.5)(0.0476)\, Ar$$
$$\longrightarrow \quad 8\, CO_2 + 9\, H_2O + 46.375\, N_2 + 0.595\, Ar$$

From the balanced equation, we can establish the mole fractions for each of the species. The total moles of reactant species is 60.47. Then the mole fractions for the reactants, the intake charge, are:

(4.7) $$y_{C_8H_{18}} = 0.0165, \quad y_{O_2} = 0.2067, \quad y_{N_2} = 0.767, \quad y_{Ar} = 0.00983$$

Note how the mole fraction of each species in air has been reduced slightly by the addition of the gaseous fuel. The balanced equation also specifies an air/fuel ratio (by mass) of $AF = 15.07$. The molecular mass of the intake mixture is:

(4.8) $$\mathcal{M}_i = \sum_{i=1}^{n} y_i \mathcal{M}_i = 30.36 \frac{g}{mol} = 30.36 \frac{kg}{kmol}$$

We can find the enthalpy of each species in a mixture by multiplying its mole-specific enthalpy by the number of moles of the species. Then the total enthalpy of the mixture is the sum of the species enthalpies:

$$H_{mix} = \sum_{i=1}^{m} n_i \bar{h}_i \tag{4.9}$$

Enthalpies of elements and molecules are found experimentally and given at standard conditions of 298 K and 100 kPa. These are commonly called the "enthalpies of formation", and for the species in our air/fuel reaction are:

$$N_2 : \quad \bar{h}_f^0 = 0 \tag{4.10}$$

$$O_2 : \quad \bar{h}_f^0 = 0 \tag{4.11}$$

$$Ar : \quad \bar{h}_f^0 = 0 \tag{4.12}$$

$$C_8H_{18} : \quad \bar{h}_f^0 = -208447.0 \tag{4.13}$$

$$CO_2 : \quad \bar{h}_f^0 = -393522.0 \tag{4.14}$$

$$H_2O : \quad \bar{h}_f^0 = -241827.0 \tag{4.15}$$

with units $\left\langle \frac{kJ}{kg-mol \cdot K} \right\rangle$. Note that, since they exist without any reaction taking place, elemental gases have an enthalpy of formation of zero.

The gas mixtures that form the working fluid of the engine will almost never be at standard conditions. Certainly, we expect the combustion products to be far from those values.

Along with the enthalpies of formation, researchers have measured the constant-pressure specific heats of many elements and compounds and created polynomial approximations of c_p with respect to temperature. Remember that enthalpy, $\bar{h} = \bar{c_p}T$, and so these polynomials can be used to find non-standard enthalpies for elements and compounds. We will use the following polynomials [28, 27]:

$$N_2: \quad \bar{c_p} = 39.060 - 512,790\,T^{-1.5} + 1.0727x10^7\,T^{-2} - 8.204x10^8\,T^-3 \tag{4.16}$$

$$O_2: \quad \bar{c_p} = 37.432 + 2.0102x10^{-5}\,T^{1.5} - 178,570\,T^{-1.5} + 2.3688x10^6\,T^{-2} \tag{4.17}$$

$$Ar: \quad \bar{c_p} = 520.426 \tag{4.18}$$

$$C_8H_{18}: \quad \bar{c_p} = -323.5 + 36.98\,T^{0.5} - 0.4332\,T + 1.723x10^{-5}\,T^2 \tag{4.19}$$

$$CO_2: \quad \bar{c_p} = -3.7357 + 3.0529\,T^{0.5} - 0.041034\,T + 2.4198x10^{-6}\,T^2 \tag{4.20}$$

$$H_2O: \quad \bar{c_p} = 143.05 - 58.04\,T^{0.25} + 8.2751\,T^{0.5} - 0.036989\,T \tag{4.21}$$

The units on each polynomial are $\left\langle \frac{kJ}{kg-mol\cdot K} \right\rangle$. Figure 4.1 illustrates the C_p value of each gas species as a function of temperature.

Note how the value for Argon is constant. Argon, being a monatomic gas, doesn't store energy in molecular vibration, can't dissociate and up to 6,000 K, isn't ionized.

The non-standard enthalpy of an element or compound is found by adding the enthalpy of formation and the change in enthalpy from actual to standard temperature:

$$\bar{h} = \bar{h}_f^0 + \Delta\bar{h} \tag{4.22}$$

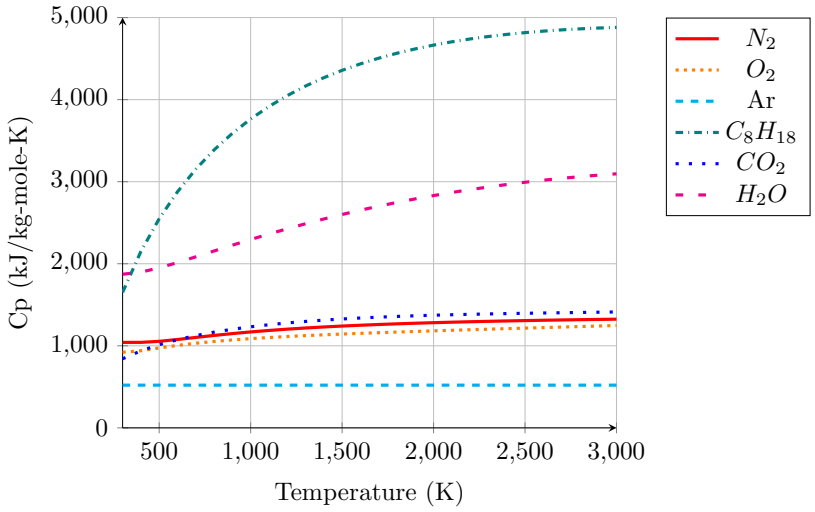

FIGURE 4.1. Cp Values

The $\Delta\bar{h}$ value is found by integrating $\bar{c_p}T$ from standard temperature to the actual temperature:

$$\Delta\bar{h} = \int_{T_0}^{T} \bar{c_p} dT \tag{4.23}$$

The c_p polynomials can be analytically integrated, yielding new polynomials for $\Delta\bar{h}$:

$$N_2: \quad \Delta\bar{h} = 39.06\,T + 1.0256x10^6\,T^{-0.5} - 1.0727x10^7\,T^{-1} + 4.102x10^8\,T^{-2}\Big]_{T_0}^{T} \tag{4.24}$$

$$O_2: \quad \Delta\bar{h} = 37.432\,T + 8.0x10^{-6}\,T^{2.5} + 357,140\,T^{-0.5} - 2.3688x10^6\,T^{-1}\Big]_{T_0}^{T} \tag{4.25}$$

$$Ar: \quad \Delta\bar{h} = 520.426\,T\Big]_{T_0}^{T} \tag{4.26}$$

$$C_8H_{18}: \quad \Delta\bar{h} = -323.5\,T + 24.65\,T^{1.5} - 0.2166\,T^2 + 5.74x10^{-6}\,T^3\Big]_{T_0}^{T} \tag{4.27}$$

$$CO_2: \quad \Delta\bar{h} = -3.7357\,T + 2.0353\,T^{1.5} - 0.02052\,T^2 + 8.0x10^{-7}\,T^3\Big]_{T_0}^{T} \tag{4.28}$$

(4.29) $$H_2O: \quad \Delta\bar{h} = 143.05\,T - 46.43\,T^{1.25} + 5.5167\,T^{1.5} - 0.01849\,T^2\Big]_{T_0}^{T}$$

with units $\left\langle \frac{kJ}{kg-mol} \right\rangle$. Finally, the energy provided by the combustion of the charge is calculated by returning to Equation 4.2:

(4.30)
$$\begin{aligned}
H_p(T_p) &= (8)\left[-393,522 + \Delta\bar{h}(T_p)_{CO_2}\right] + (9)\left[-241,827 + \Delta\bar{h}(T_p)_{H_2O}\right] \\
&\quad + (46.375)\left[\Delta\bar{h}(T_p)_{N_2}\right] + (0.595)\left[\Delta\bar{h}(T_p)_{Ar}\right] \\
H_r(T_r) &= (1)\left[-208447 + \Delta\bar{h}(T_r)_{C_8H_{18}}\right] + (12.5)\left[\Delta\bar{h}(T_r)_{O_2}\right] \\
&\quad + (12.5)(3.71)\left[\Delta\bar{h}(T_r)_{N_2}\right] + (12.5)(0.0476)\left[\Delta\bar{h}(T_r)_{Ar}\right] \\
Q_c &= H_p(T_p) - H_r(T_r) \qquad \langle kJ \rangle
\end{aligned}$$

where T_p is the temperature of the products and T_r is the temperature of the reactants. This gives us the total energy released by the reaction, where 1 mole of fuel has been burned with 12.5 moles of air. Per stoichiometric mole of fuel, the energy release is:

(4.31) $$\bar{q}_{c_{fuel}} = \frac{Q_c}{n_{f_s}} = \frac{H_p(T_p) - H_r(T_r)}{1}$$

The simulation is marched forward in time by calculating the density of the charge at each timestep. We also know the volume of the charge at each timestep, so we can calculate the mass of charge in the cylinder. The total mass of the charge is:

$$m_T = m_{air} + m_{fuel} \tag{4.32}$$

And the air-to-fuel ratio is:

$$AF = \frac{m_{air}}{m_{fuel}} \rightarrow m_{air} = AF\, m_{fuel} \tag{4.33}$$

Substituting Equation 4.33 into Equation 4.32,

$$m_T = AF\, m_{fuel} + m_{fuel} = m_{fuel}(AF + 1) \longrightarrow m_{fuel} = \frac{m_T}{AF + 1} \tag{4.34}$$

Then the number of moles of fuel in the charge is:

$$n_f = \frac{m_{fuel}}{\mathcal{M}_{fuel}} = \frac{m_T}{(AF + 1)\mathcal{M}_f} \tag{4.35}$$

Note that this is not the stoichiometric number of moles of fuel. This is the number of moles of fuel actually introduced into the cylinder. Finally, based on the mass of charge in the cylinder, we have the energy released by combustion of the intake charge:

$$\boxed{Q_c = \bar{q}_{c_{fuel}} n_f = [H_p(T_p) - H_r(T_r)]\, \frac{m_T}{(AF + 1)\mathcal{M}_f}} \tag{4.36}$$

Equation 4.36 gives the total energy added to the charge due to the combustion of its reactants.

We're left with the question of how to determine T_p and T_r. T_p is the temperature of the products of combustion. For this value, we'll use the temperature of the charge. This is interesting, for as we add combustion energy to the charge, its temperature rises. This in turn affects the enthalpy of the product gases and the amount of energy added to the charge. The relationship is nonlinear. For the temperature of the reactants, consider that, as combustion progresses, there are burned and unburned fractions of the charge [23]. At ignition, the unburned fraction is 1. At completion of combustion, the unburned fraction is 0.

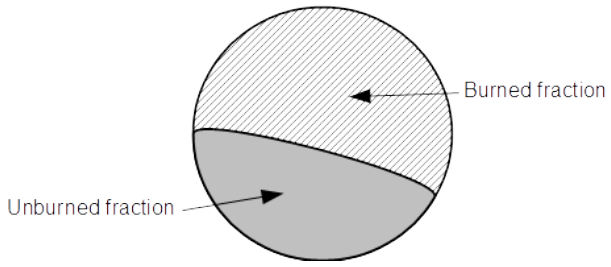

FIGURE 4.2. Burned and Unburned Fractions of the Charge

Figure 4.2 illustrates the burned and unburned fractions as distinct volumes within the charge [23]. As the burned fraction grows the temperature of the charge rises. The pressure of the charge rises in response. Thus even though the unburned fraction isn't reacting, it's temperature is still rising from isentropic compression. We model this by storing the temperature and pressure of the charge at ignition, the start of the combustion process. These are the initial temperature and pressure of the unburned fraction, the initial temperature and pressure of the reactants:

$$T_s = T_{\text{charge @ ignition}} \tag{4.37}$$

$$P_s = P_{\text{charge @ ignition}} \tag{4.38}$$

Then as the simulation advances, the temperature of the reactants is calculated by:

$$T_u = T_s \left(\frac{P_s}{P} \right)^{\frac{\gamma-1}{\gamma}} \tag{4.39}$$

4.2. Finite-Rate Combustion

Equation 4.36 provides the total energy that will be added to the charge. But the energy equation (4.1) is time-relative and only offers a *rate*-of-combustion-energy-added term. We must find a way to supply the energy of combustion as a rate. Ideally, we could define the combustion reaction with a full reaction mechanism consisting of hundreds of intermediate species undergoing hundreds of sub-reactions, each with a known, finite reaction rate. This non-equilibrium approach would provide the greatest level of accuracy and has been applied in many computational combustion and reduced-order analyses [29, 30, 23, 27]. But it requires a great deal of development and is very computationally expensive. It is too demanding for our purposes.

A number of finite-rate energy release models have been developed in the past [23]. These are based on differential equations, typically with respect to crankshaft angle. The models are based on experimentation and observation and exhibit the three phases of combustion,

ignition development (after the spark plug has been fired), rapid burning and burning completion. Wiebe [23, 31] developed a widely-used finite-rate heat release correlation based on high-level modeling of combustion reaction mechanisms. He then estimated values of the free parameters in his resulting equations using published experimental data.

The Wiebe function is:

$$x_b = 1 - exp\left[-a\left(\frac{\theta - \theta_s}{\theta_d}\right)^n\right] \tag{4.40}$$

where,

x_b = fraction of energy released and mixture burned

θ = crankshaft angle

θ_s = crankshaft angle at start of energy release (spark)

θ_d = duration of energy release

a = form factor (typically, a = 5)

n = efficiency factor (typically, n = 3)

Wiebe's function provides the fraction of energy released. We can model the energy input as a function of crankshaft angle by:

$$Q_c(\theta) = Q_c x_b \tag{4.41}$$

But we want the *rate* of energy released. So we will take the derivative of Equation 4.40 with respect to θ:

$$\boxed{\frac{dx_b}{d\theta} = \frac{an}{\theta_d}\left(\frac{\theta - \theta_s}{\theta_d}\right)^{n-1} exp\left[-a\left(\frac{\theta - \theta_s}{\theta_d}\right)^{n}\right]} \tag{4.42}$$

Then, the heat released with respect to time is:

$$\boxed{\frac{dQ}{dt} = Q_c \frac{dx_b}{d\theta}\frac{d\theta}{dt}} \tag{4.43}$$

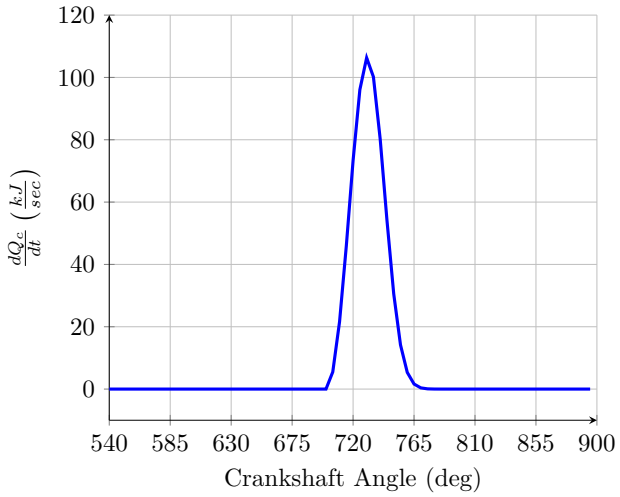

FIGURE 4.3. Combustion Energy Release

Figure 4.3 is a plot of Equation 4.43 with respect to crankshaft angle for an engine speed of 3,000 rpm. Here, ignition is begun at a crankshaft angle of 700° and combustion duration is 60°. This value is substituted into Equation 4.1 for the $\dot{Q}_c$ term.

Figure 4.4 illustrates the result. The piston begins at BDC of the stroke with the charge at ambient temperature and pressure. The crankshaft is turned one revolution, taking the

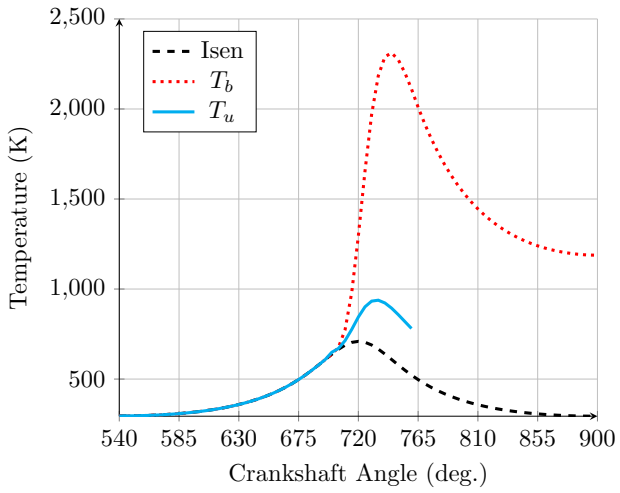

FIGURE 4.4. Unburned Fraction Temperature

piston to TDC and back. Ignition and combustion progress as above. The dashed, black line illustrates the temperature of the charge without combustion. The red, dotted line is the temperature of the burned fraction of the charge and the solid, blue line is the temperature of the unburned fraction. The curve ends at the point where the unburned fraction is consumed. Without the added pressure generated by the burning fraction, the unburned fraction temperature would follow the no-combustion curve. Combustion pressures raise the unburned fraction temperature significantly above the no-combustion values. This two-zone model provides a vitally important piece of information. Note the peak unburned fraction temperature of about 950 K. The autoignition temperature of the octane/air mixture is about 1,300 K. We can see here that the charge will burn to completion without detonating, without "knock". If the engine had a higher compression ratio we would see the unburned temperature coming closer to the 1,300 K mark, indicating that the unburned fraction could detonate, a condition that reduces performance in, and can even destroy, spark-ignition engines.

4.3. Instantaneous (Infinite-Rate) Combustion

It is also useful to model combustion occurring instantaneously. If we consider the charge as the piston reaches TDC of the compression stroke, we can imagine the charge suddenly going from reactants to products instantaneously. This would mean that the reaction rate is infinite. In going from reactants to products instantly, there is no time for heat loss and the reaction leaves the product gases at the adiabatic flame temperature of the mixture.

To determine the adiabatic flame temperature, we return to the First Law of thermodynamics:

$$Q - W = H_p(T) - H_r(T) \tag{4.44}$$

There is no heat loss and no work being done on the mixture over this instant, so the left-hand side is zero. We're left with:

$$H_p(T) = H_r(T) \tag{4.45}$$

Just as before, we calculate the enthalpies using equations 4.30. We know the temperature of the reactants. It is the temperature of the charge when the piston arrives at TDC. We need to find a temperature where the enthalpy of the products is equal to the enthalpy of the reactants. This is the adiabatic flame temperature. We find the value by applying a Newton-Raphson method, successively iterating until the change in flame temperature is below a minimum. For example, using a reactant temperature of 700 K, which is typical

for an engine with a compression ratio of 9, we calculate an adiabatic flame temperature of 2,734 K.

Once the value of the adiabatic flame temperature is found, we directly set the temperature of the charge to the new value and reset the pressure of the charge using the known density and the perfect gas equation of state, $P = \rho RT$. The charge is now in the post-combustion state.

Instantaneous combustion provides an ideal situation where no heat is lost while the reaction is occurring and where ignition advance plays no role. It provides a theoretical ideal which can't be reached in reality but to which we can compare more realistic calculations. The power the engine makes using this approach is the most it could possibly make.

If, in simulating an engine, the real ignition advance is unknown, instantaneous combustion can be employed to sidestep the issue and make comparisons as other values are adjusted.

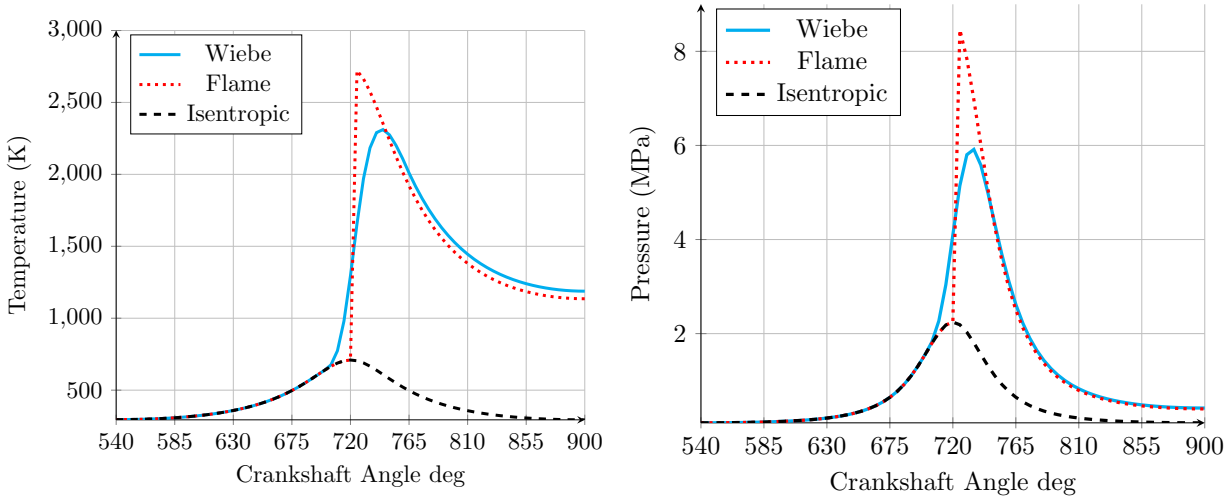

(A) Combustion Temperatures

(B) Combustion Pressures

FIGURE 4.5. Combustion Model Results

Figure 4.5 shows the two combustion models in operation. We begin again with the piston at BDC and the charge at ambient density and temperature. The crankshaft is rotated one revolution and the piston rises from BDC to TDC and back. The Wiebe model activates at 700° and combustion completes at 760°. The instantaneous model activates at 720°. Figure 4.5a shows the effect on charge temperature. The black, dashed line, included for reference, is the temperature of the charge with no combustion. The shape of the curve is a result of isentropic compression of the charge. Without combustion, peak compression temperature is around 700 K. Finite-rate combustion takes the peak temperature to about 2,300 K and instantaneous combustion takes the temperature to about 2,700 K. Note how close the curves fall during the expansion stroke. Notionally, we should be adding the same amount of energy in either case, so it seems reasonable that the curves should overlap at a certain point. Figure 4.5b shows the pressures caused by both combustion models. Peak pressures are 60 and 85 atmospheres. Note again that the two curves merge on the expansion stroke.

4.4. Gas Values

The working fluid in the engine can be modeled in numerous levels of detail. At a macroscopic level, in the simplest case, air can be used as the working fluid. Air is drawn in, combustion energy is added to air during combustion, air is exhausted from the cylinder [23]. For more detail, a mixture of air and gaseous fuel can be used as the working fluid until combustion occurs, then, from combustion to the intake stroke, the fluid can be switched to a mixture of the exhaust products. At intake, the mixture is switched back to air and fuel.

At the next lower scale, we can consider the gas properties of whatever working fluid is chosen. In a real engine, a mixture of air and gaseous fuel is drawn in during the intake

stroke. At ambient temperatures, the gas mixture stores energy internally in the translation and rotation of its molecules. Over a small temperature range, temperatures below those of combustion and velocities below about Mach 5, internal energy and enthalpy can both be considered linear functions of temperature. But during the compression stroke, if the compression ratio of the engine is high enough, the composition of the mixture can change as high isentropic compression temperatures cause the fuel molecules to dissociate. Once combustion begins, dissociation, vibrational stimulation and ionization occur. Energy is stored in new, "extended" modes and internal energy and enthalpy can no longer be considered linear functions of temperature. For accurate calculations we expect that energy storage in the extended modes must be taken into account. High-temperature gas dynamics would have us track vibrational, dissociative and electronic energy for each species in the gas, and apply rate constants to calculate the rates of storage or loss in each mode [29]. But this approach takes us into the high-demand realm again. Instead, we can create a lower-order model by turning to the c_p functions listed above. Each function is a curve fit to experimental measurements of the real responses of each species [28]. Each takes into account the energy storage into the extended modes as temperature increases. Using the c_p functions, we can treat each species as a perfect gas, calculating internal energy, enthalpy and pressure as functions of temperature.

We know the mole fractions, y_i, of each species in air, and with the balanced, stoichiometric chemical equation of the combustion reaction, we know the mole fractions of each species in the intake and exhaust mixtures. We also know the molecular masses, $\mathcal{M}_i$, of each species. The molecular masses of the mixtures are found by:

$$\mathcal{M}_{mix} = \sum_{i=1}^{n} \mathcal{M}_i \, y_i \tag{4.46}$$

which yields

$$\mathcal{M}_{air} = 28.97 \qquad \mathcal{M}_{intake} = 30.38 \qquad \mathcal{M}_{exhaust} = 28.72$$

The universal gas constant is invariant with temperature and pressure. Using it and the molecular weight of each mixture, the specific gas constant for each mixture is:

$$R_i = \frac{\mathcal{R}}{\mathcal{M}_i} \tag{4.47}$$

which yields:

$$R_{air} = 287.0 \qquad R_{intake} = 273.7 \qquad R_{exhaust} = 289.5$$

The constant-pressure specific heat of each mixture is calculated using the c_p function for each species:

$$\boxed{c_{p_{mix}}(T) = \sum_{i=1}^{n} c_{p_i}(T) \, y_i} \tag{4.48}$$

With the mixture c_p values, we calculate the constant-volume specific heats, c_v, of the mixtures by:

(4.49)
$$\boxed{c_{v_{mix}}(T) = c_{p_{mix}}(T) - R_{mix}}$$

And the ratio of specific heats for each mixture is:

(4.50)
$$\boxed{\gamma_{mix}(T) = \frac{c_{v_{mix}}(T)}{c_{p_{mix}}(T)}}$$

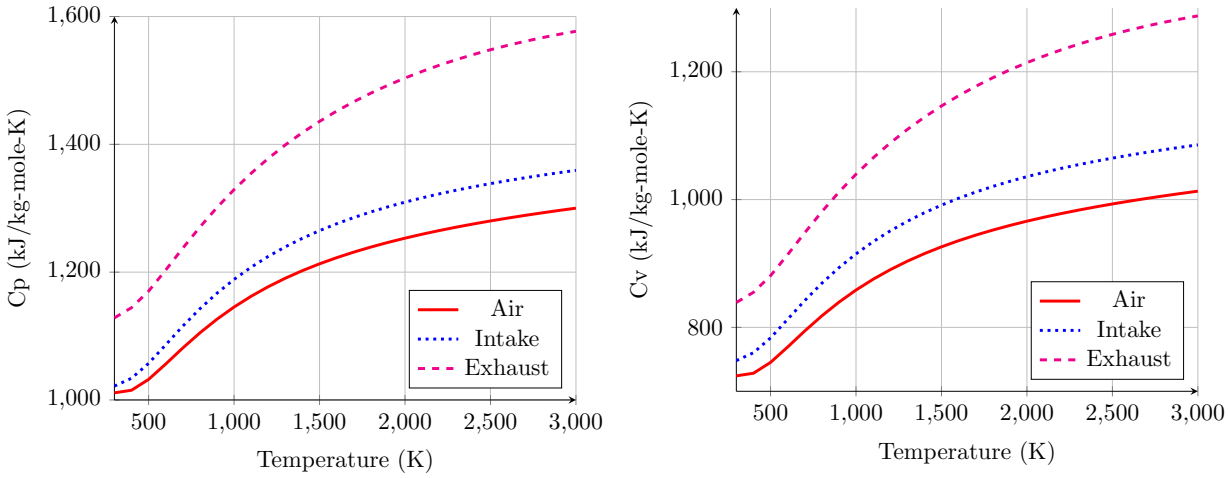

(A) Mixture c_p Values

(B) Mixture c_v Values

FIGURE 4.6. Mixture Specific Heats

Figure 4.6 shows the specific heats of each mixture and the way they respond to increasing temperature. Note the decrease in slope with increasing temperature. This implies that as temperature rises, temperature itself,

$$T = \frac{e}{c_v} \qquad T = \frac{h}{c_p}$$

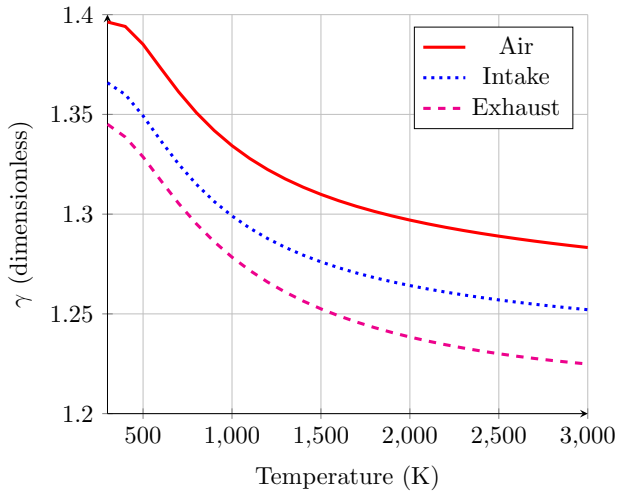

FIGURE 4.7. Mixture γ Values

is no longer a linear function of internal energy or enthalpy, and some of the internal energy is being stored in the extended modes. Figure 4.7 illustrates the ratio of specific heats for each mixture.

In modeling the engine's working fluids in this manner, we will model the realistic physics of employing the three mixtures as engine working fluids and also capture the realistic changes in gas properties with increasing temperature [32]. The main drawback of using this reduced-order model is that we don't capture the temporal nature of the storage and release of energy from the extended modes. That only comes with the full, non-equilibrium model. Our model assumes that energy transitions between modes at infinite rate. Thus, we are employing an equilibrium model.

Figure 4.8 illustrates the difference in gas responses using the different mixtures. We have again begun with the piston at BDC and with the charge at ambient conditions. The crankshaft is rotated one revolution taking the piston to TDC and back. In Figure 4.8a we see the temperatures of frozen air, equilibrium air and equilibrium intake/exhaust gases. Note that frozen air has the largest temperature response. All of the energy being put into

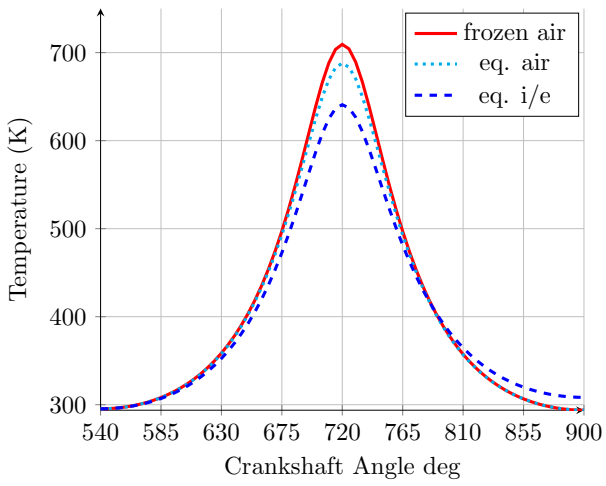

(A) Mixture Temperature Response

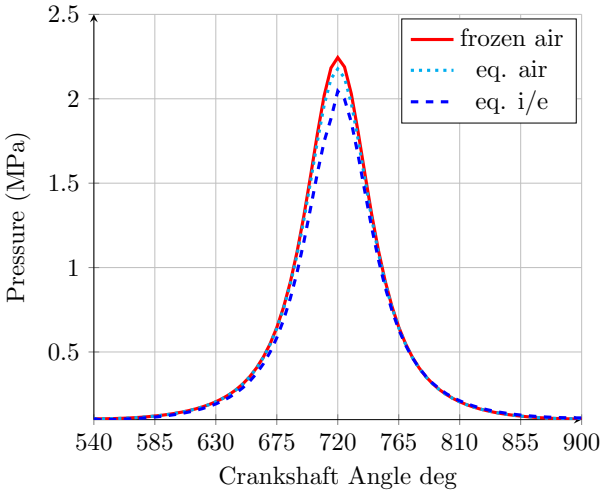

(B) Mixture Pressure Response

FIGURE 4.8. Mixture Responses

the charge through the work of the piston is manifest in the temperature of the gas. In the equilibrium air and equilibrium intake/exhaust curves, some of the energy is being stored in the extended modes, resulting in lower temperatures. In Figure 4.8b we see the pressure response of each mixture. Since $P = \rho RT$ and the difference in the specific gas constant, R, is small from mixture to mixture, the differences we see here are largely driven by the temperature responses of the mixtures.

CHAPTER 5

Loss Modeling

While some of the physics that occur within an engine are hidden from view and can be non-intuitive, other phenomena are so palpable that they are obvious to anyone who has built or worked on an engine. Engines get hot. They have to be cooled to opearate for any length of time. It's clear that heat escapes from the hot charge in the cylinders and flows out through the block and head. Also, turning the crankshaft of an engine by hand, one feels resistance. When the rotating moment is taken away, the crankshaft doesn't coast. It stops immediately. So it's clear that there is significant friction in the rotating and sliding components of an engine. When turning over an engine by hand, one can also hear gases escaping from the compressed charge through the small gaps between the piston rings and the cylinder walls. If the crankshaft is turned slowly, the gases escape completely and there is no resistance as the piston passes TDC of the compression stroke. It's clear that the pistons aren't perfectly sealed in their cylinders and blowby occurs, causing loss of useful charge. Are these phenomena dominant physics? We will find out by modeling them.

5.1. Blowby

Because of its obvious presence, blowby has been recognized as an issue from the earliest days of engine development. It is assumed to play a role in engine performance and emissions [23, 33–35]. Physically, blowby is composed of the passage of gas through the gaps between the ends of the piston rings and through many small leaks where the rings form an imperfect seal with the cylinder wall and with the piston ring grooves [36]. We can model blowby by

condensing these small leaks into a single flowpath with an equivalent total cross-sectional area, as illustrated in Figure 5.1.

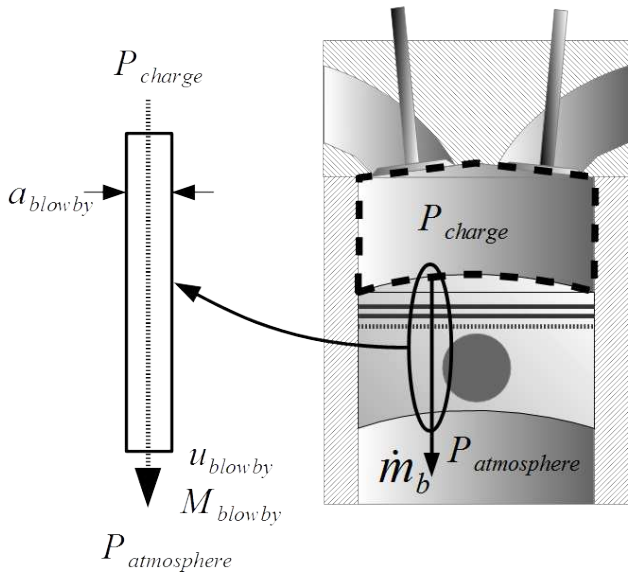

FIGURE 5.1. Modeling Blowby

We will assume that the flow through the single, unified blowby passage is isentropic and driven by the difference in pressure from the charge to the atmosphere. We can employ the isentropic flow equations [29, 23, 37] as simple flow models. The isentropic flow equation for pressure is,

$$\frac{P_0}{P} = \left[1 + \left(\frac{\gamma - 1}{2}\right) M^2\right]^{\frac{\gamma}{\gamma-1}} \tag{5.1}$$

Here, P_0 is the total pressure, the pressure we would measure if the flow was brought to rest isentropically from a Mach number of M. P is the static pressure of the flow, the pressre where the flow is moving with Mach number M. Since the total pressure is the pressure anywhere the flow is brought to rest isentropically, or is *already* at rest, the air at the upstream end of the flowpath, which has a velocity of zero just a short distance from the

flowpath entrance, has a pressure of P_0. Given the total pressure and the Mach number at a given point in the flow, this equaton allows us to calculate the static pressure at that same point in the flow. We can invert Equation 5.1:

$$M = \sqrt{\left[\left(\frac{P_0}{P}\right)^{\frac{\gamma-1}{\gamma}} - 1\right]\frac{2}{\gamma-1}} \tag{5.2}$$

or,

$$\boxed{M_b = +\sqrt{\left[\left(\frac{P_c}{P_a}\right)^{\frac{\gamma-1}{\gamma}} - 1\right]\frac{2}{\gamma-1}} \quad \text{or,} \quad M_b = -\sqrt{\left[\left(\frac{P_a}{P_c}\right)^{\frac{\gamma-1}{\gamma}} - 1\right]\frac{2}{\gamma-1}}} \tag{5.3}$$

Equations 5.3 allow us to calculate the Mach number of the blowby flow based on the pressure of the charge, P_c and atmospheric pressure, P_a. We will consider flow *out* of the cylinder as positive, and so if $P_c > P_a$, M is positive. If $P_c < P_a$, M is negative.

With the Mach number at the downstream end of the blowby flowpath in hand, we can calculate the temperature and density of the flow at that end:

$$\boxed{\begin{aligned} T_b &= T_0\left[1 + \left(\frac{\gamma-1}{2}\right)M^2\right]^{-1} \\ \rho_b &= \rho_0\left[1 + \left(\frac{\gamma-1}{2}\right)M^2\right]^{\frac{1}{1-\gamma}} \end{aligned}} \tag{5.4}$$

We can calculate the velocity at the downstream end with:

(5.5) $$\vec{V}_b = M_b\sqrt{\gamma R T_b}$$

and then the mass flow rate through the blowby is:

(5.6) $$\boxed{\dot{m}_b = \rho_b A_b \vec{V}_b}$$

Where A_b is the specified cross-sectional area of the blowby flowpath. We couple the blowby model to the model of the charge by inserting the mass flow rate value into the charge continuity equation (5.7, repeated here for convenience) as $\left(\rho\vec{V}A\right)_b$.

(5.7) $$\frac{d\rho}{dt} = -\frac{1}{\mathcal{V}}\left[\left(\rho\vec{V}A\right)_i + \left(\rho\vec{V}A\right)_e + \left(\rho\vec{V}A\right)_b + \rho\frac{d\mathcal{V}}{dt}\right]$$

The values of ρ_b, T_b and $\vec{V}_b$ are also used for the first two terms of the charge energy equation (5.8, also repeated here) where $e = c_v T_b$ in term 1 and the pressure in term 2 is P_{charge}. In both terms the area is A_b.

(5.8)
$$\frac{dT}{dt} = -\frac{1}{\rho\mathcal{V}c_v}\left\{\underbrace{\sum_{i=1}^{3}\left[\rho\left(e + \frac{\vec{V}^2}{2}\right)\vec{V}A\right]_i}_{1} \underbrace{+\sum_{j=1}^{3}\left(P\vec{V}A\right)_j}_{2} + \dot{Q}_T + \dot{Q}_c + \mathcal{V}e\frac{d\rho}{dt} + \rho e\frac{d\mathcal{V}}{dt}\right\}$$

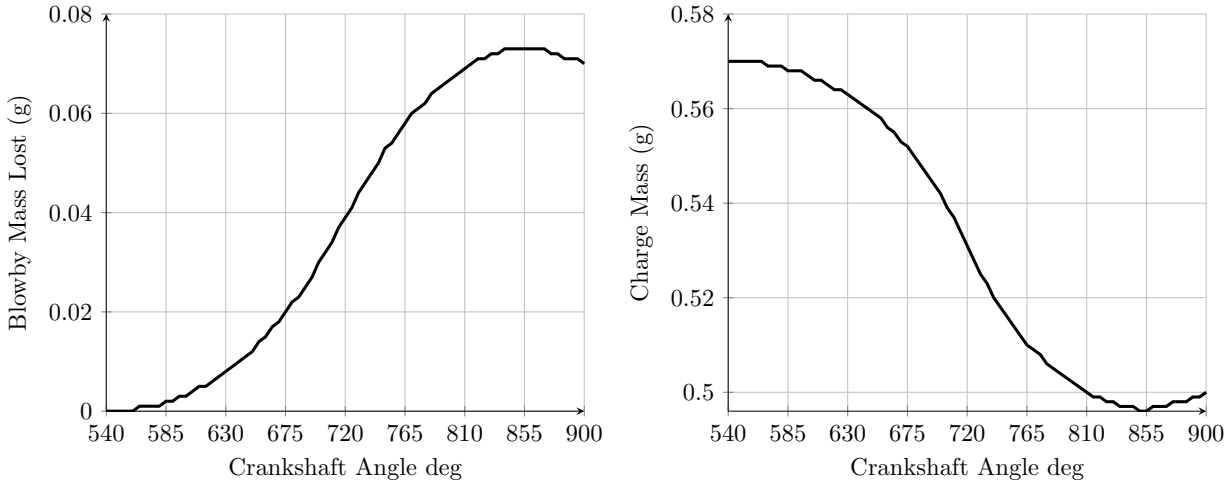

(A) Blowby Mass Lost (B) Charge Mass

FIGURE 5.2. Effect of Blowby on Charge Mass

Figure 5.2 shows the blowby model in operation. We begin the test with the cylinder at BDC and the charge at ambient conditions. We rotate the crankshaft one revolution, taking the piston to TDC and back. Combustion is turned off to simplify the results and the crankshaft speed is set to a low 750 rpm to magnify the effect. In Figure 5.2a, as the piston rises and the pressure in the cylinder increases, mass flows out the blowby path. The rate of mass loss increases, reaching a maximum at TDC (720°), then decreases. With the loss of mass, on the downstroke, the pressure in the cylinder drops to ambient before the piston reaches BDC. Then the pressure in the cylinder goes below ambient and the flow reverses, with mass flowing *into* the cylinder through the blowby passage. Figure 5.2b shows the mass of gas in the cylinder over the same test. Mass is lost as the piston and charge pressure both rise. Near BDC on the downstroke mass flows back into the cylinder.

Figure 5.3 shows the effect of blowby on the charge properties. In Figure 5.3a the black, dashed line marks the density of the charge with no blowby. No mass is lost and we see nothing but the effect of the isentropic compression and expansion of the charge. The solid, red line shows the density with blowby. As mass is lost the density drops continuously

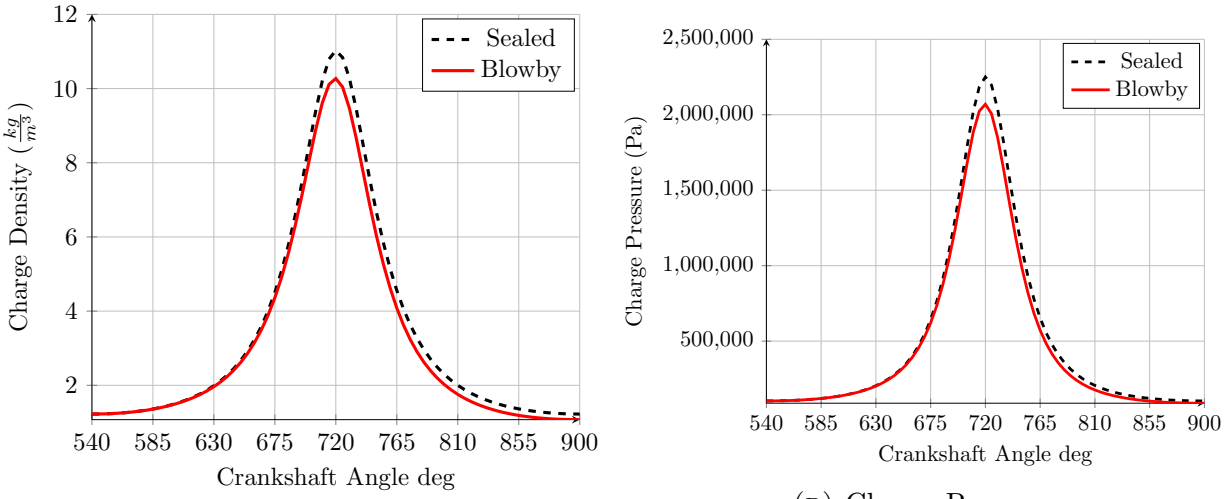

(A) Charge Density

(B) Charge Pressure

FIGURE 5.3. Effect of Blowby on Charge

throughout the cycle. Figure 5.3b shows that, as mass is lost, the charge pressure drops. This will affect power output, as power is directly related to the cylinder pressure.

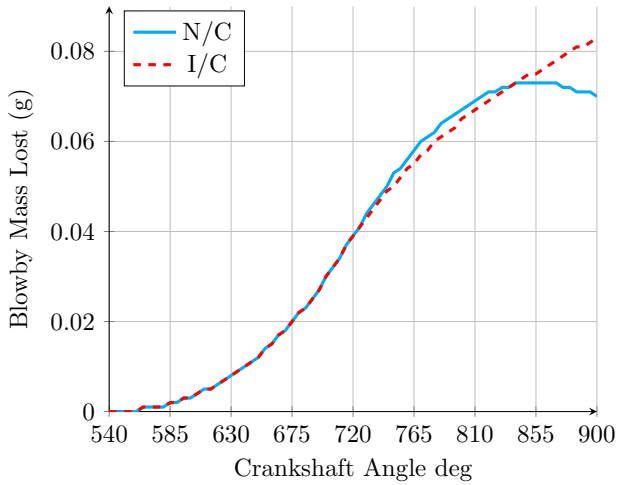

FIGURE 5.4. The Effect of Combustion on Blowby

In the previous test there was no combustion. Figure 5.4 shows the same test with instantaneous combustion. Combustion increases charge pressure, so we expect to see a higher rate of mass loss. Interestingly, we see a slight decrease in the rate of mass loss because of the increase in charge temperature and resulting reduction of density at the

blowby exit. But the increased pressure does cause mass to flow out the blowby passage even after the piston has reached BDC.

Rose and Stahman [35] made measurements of blowby on a variety of cars operating at a cruise speed of 40 mph and under road load. They found the average blowby volume rates given in table 5.1. These values compare well with Kirkpatrick [23].

TABLE 5.1. Measured Blowby

Engine	Blowby $\dot{\mathcal{V}}$ $\frac{ft^3}{min}$	Exhaust $\dot{\mathcal{V}}$ $\frac{ft^3}{min}$	% Blowby
6 cyl	0.95	44.8	2.12
8 cyl	1.55	45.9	3.4

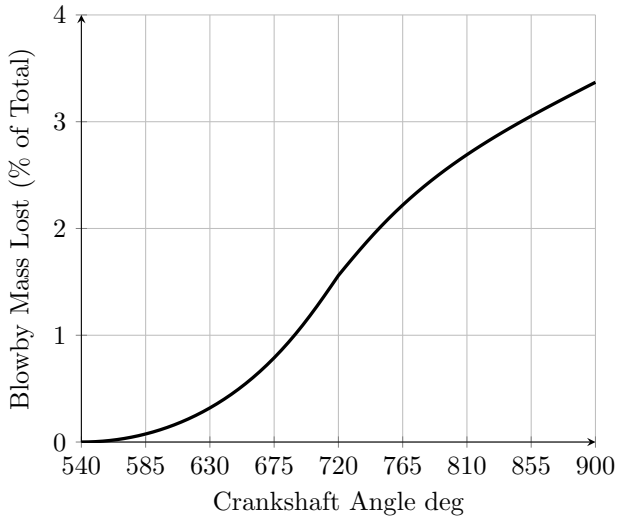

FIGURE 5.5. Percentage of Mass Lost

Figure 5.5 shows the mass loss through the blowby as a percentage of total mass in the cylinder. This test is identical to the test above with instantaneous combustion, but with a crankshaft rotational speed of 2,500 rpm. With a blowby cross-sectional area of 1.5 mm^2, we see a maximum mass loss of about 3.2%. Since this matches Rose and Stahlman, we'll use 1.5 mm^2 as the value for blowby area in our future studies. A typical specification on the ring end-gap for a piston ring is 0.8 mm. And the typical specification on piston clearance

is 0.04 mm. Multiplying these together, we get a flowpath area of 0.032 mm^2 through the ring end-gap. This means that leaks between the ring and the cylinder wall total about 1.46 mm^2.

5.2. Heat Transfer

Like blowby, heat transfer from the hot charge to the cylinder walls is a phenomenon so obvious it can't be missed. As quickly as engines heat up and as hot as they get, even with active cooling, heat loss seems likely to be dominant physics. To find out, we'll examine three heat transfer models to determine their effect on engine performance and whether heat transfer is indeed dominant physics in engine modeling.

For greatest realism and accuracy, we'd like to employ a first-principles approach in modeling heat transfer. This can be done if the charge is modeled using 3-dimensional Computational Fluid Dynamics. But this again is too demanding for our purposes. Researchers have developed reduced-order models that are based on the macroscopic physics expected in heat transfer, calibrated using measurements from real engines. Our models are three of these correlations.

Heat transfer in engines is understood to be a function of both the Nusselt number,

$$Nu = \frac{\boldsymbol{h}b}{k} \tag{5.9}$$

(Where $\boldsymbol{h}$ is the macroscopic heat transfer coefficient of the gas, b is the cylinder bore and k is the thermal conductivity of the gas.)

and the Reynolds number which, for the purposes of engine heat transfer calculations is calculated using mean piston speed, $\bar{U}_p$, for the velocity term and cylinder bore, b, as the characteristic length:

(5.10) $$\boxed{\bar{U}_p = 2sN}$$

(5.11) $$Re = \frac{\vec{V}x}{\nu} = \frac{\rho\vec{V}x}{\mu} = \frac{\rho\bar{U}_p b}{\mu}$$

(5.12) $$\boxed{Re = \frac{2\rho bsN}{\mu}}$$

The Nusselt number is the ratio of convection to conduction in a fluid and the Reynolds number is the ratio of inertial to viscous forces in a fluid. The heat transfer coefficient of the Nusselt number, $\boldsymbol{h}$, represents convective heat transfer and is proportional to the velocity and turbulence of the fluid. In an engine, during combustion, velocities and turbulence grow rapidly. $\boldsymbol{h}$ grows in response. Some correlations take this into account. Some don't.

The heat transfer correlations are all built on a variation of the relation

(5.13) $$Nu = f(Re)$$

Annand's correlation [38, 23] is the simplest we will employ here. It was developed using instantaneous cylinder head heat flux measurements and is based on the relation:

$$Nu = a_1 Re^{a_2} \tag{5.14}$$

The heat transfer coefficient, $\boldsymbol{h}$, is considered constant. Filling in the details,

$$\boxed{\dot{q} = \underbrace{a_1 \frac{K}{b} Re^{0.7} \left(T - T_w\right)}_{1} + \underbrace{a_2 \sigma \left(T^4 - T_w^4\right)}_{2} \qquad \left\langle \frac{W}{m^2} \right\rangle} \tag{5.15}$$

where:

$0.35 < a_1 < 0.8$ depending on charge motion intensity. (We use the average, 0.575.)

$a_2 = 0.58$ (diesel) $\quad a_2 = 0.075$ (spark)

σ = Stefan-Boltzman constant = $5.67x10^{-8} \left\langle \frac{W}{m^2 K^4} \right\rangle$

Term 1 represents the convective heat flux between the charge and the cylinder wall. Term 2 represents the radiant heat flux between the charge and the cylinder wall. Spark ignition engines produce less carbon soot than diesels, thus the much lower radiant transfer coefficient. Note the units. Equation 5.15 provides a power density. We must multiply this by the total exposed area of the cylinder to get the heat transfer in the units of power. The height of the exposed cylinder wall is:

$$y = l_{cr} + \frac{s}{2} - \left(l_{cr}^2 - \frac{s^2}{4} sin^2\theta \right)^{-\frac{1}{2}} - \frac{s}{2} cos\theta \tag{5.16}$$

And the total wall area surrounding the charge is:

$$A_w = \pi by + \pi \frac{b^2}{2} \tag{5.17}$$

Then the total heat transfer is given by:

$$\boxed{\dot{Q} = \dot{q} A_w \quad \langle W \rangle} \tag{5.18}$$

This value is entered into the charge energy equation (5.8) for the $\dot{Q}_T$ term.

Woschni [39, 23] created a more complex heat transfer correlation based on a heat balance analysis of an engine, where he measured the heat fluxes into and out of an operating engine. The Woschni correlation is based on the relation:

$$Nu = 0.035 Re^{0.8} \tag{5.19}$$

and assumes that $\boldsymbol{h}$ varies with charge velocity and turbulence. The heat transfer coefficient is:

(5.20) $$\boxed{\boldsymbol{h} = 3.26 P^{0.8} U^{0.8} b^{-0.2} T^{-0.55} \qquad \left\langle \frac{W}{m^2 K} \right\rangle}$$

U is a gas velocity term. It has two definitions, depending on whether the valves are open or closed. If the valves are open,

(5.21) $$U = 6.18 \bar{U}_p$$

If the valves are closed,

(5.22) $$U = 2.28 \bar{U}_p + 0.00324 T_{ic} \frac{\mathcal{V}_d}{\mathcal{V}_{ic}} \frac{P - P_m}{P_{ic}}$$

where:

(5.23) $T_{ic} =$ the charge temperature at intake valve closure

(5.24) $\mathcal{V}_{ic} =$ the charge volume at intake valve closure

(5.25) $P_{ic} =$ the charge pressure at intake valve closure

(5.26) $\mathcal{V}_d =$ the displacement volume of the cylinder

(5.27) $P =$ the current pressure of the charge

(5.28) $P_m =$ the motored (non-firing) pressure of the charge

We can calculate a value for P_m by noting the charge volume and pressure at intake valve closure (ic), then calculating P_m using the isentropic gas relation:

$$P_m = P_{ic}\left(\frac{\mathcal{V}}{\mathcal{V}_{ic}}\right)^{\gamma} \tag{5.29}$$

Then the Woschni heat flux is calculated by:

$$\boxed{\dot{Q}_W = \boldsymbol{h} A_w \left(T_g - T_w\right) \qquad \langle W \rangle} \tag{5.30}$$

This value is entered into the charge energy equation (5.8) for the $\dot{Q}_T$ term.

Chang et al. [23] produced a set of modified parameters for the Woschni equation based on measured instantaneous heat flux data for a Homogeneous Charge Compression Ignition engine. Their modified Woschni equation is:

$$\boxed{\boldsymbol{h} = 3.4 P^{0.8} U^{0.8} y^{-0.2} T^{-0.73} \qquad \left\langle \frac{W}{m^2 K} \right\rangle} \tag{5.31}$$

where y is the height of the exposed cylinder wall. And they offer a modified valves-closed velocity equation:

$$U = 2.28\bar{U}_p + \frac{0.00324}{6} T_{ic} \frac{\mathcal{V}_d}{\mathcal{V}_{ic}} \frac{P - P_m}{P_{ic}} \tag{5.32}$$

As above, the total heat transfer rate is:

(5.33)
$$\boxed{\dot{Q}_W = \boldsymbol{h} A_w \left(T_g - T_w\right)}$$

This value is entered into the charge energy equation (5.8) for the $\dot{Q}_T$ term.

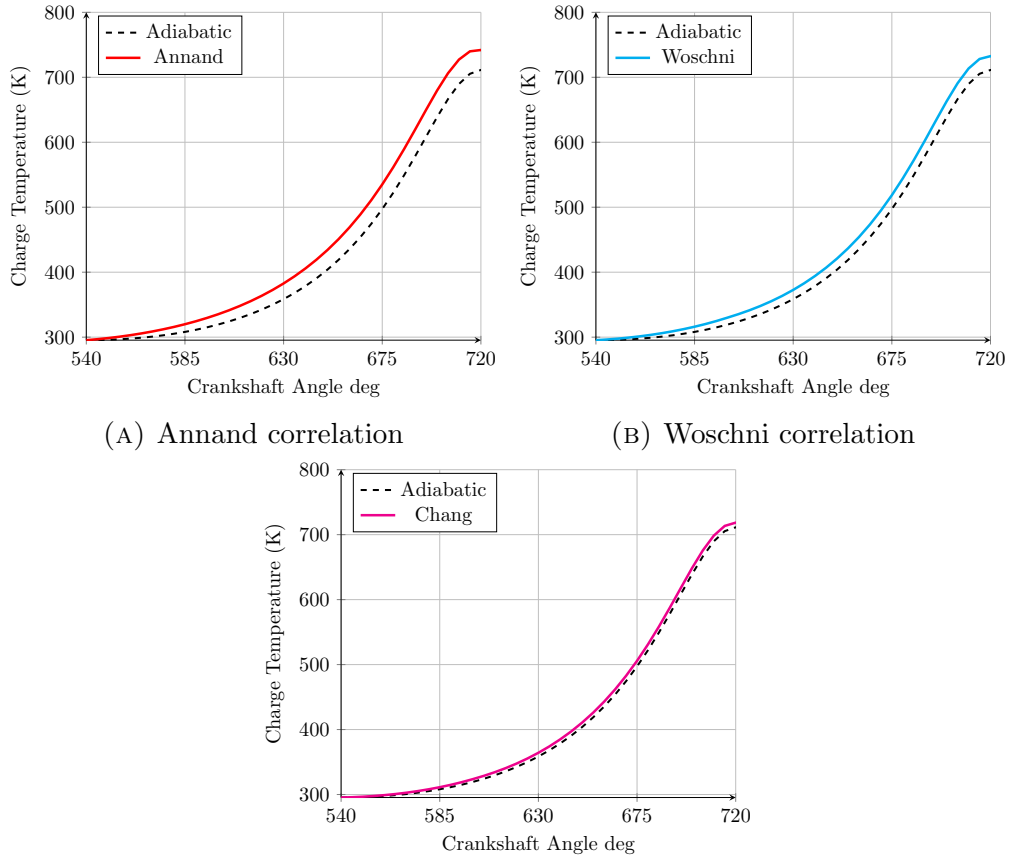

(A) Annand correlation

(B) Woschni correlation

(C) Chang correlation

FIGURE 5.6. Heat Transfer Models–No Combustion

Figure 5.6 shows these three heat transfer models in operation. The test is begun with the cylinder at BDC and the charge at ambient conditions. The crankshaft is then rotated half a revolution, taking the piston to TDC through the compression stroke. There is no combustion, but the temperature of the cylinder walls is 500 K, much hotter than the initial charge temperature. Crankshaft speed is 3,000 rpm. The dashed, black curve is

the temperature with no heat transfer. We see that the three models predict different rates of heat gain through the compression stroke. Chang predicts the least, followed by Woschni and then Annand.

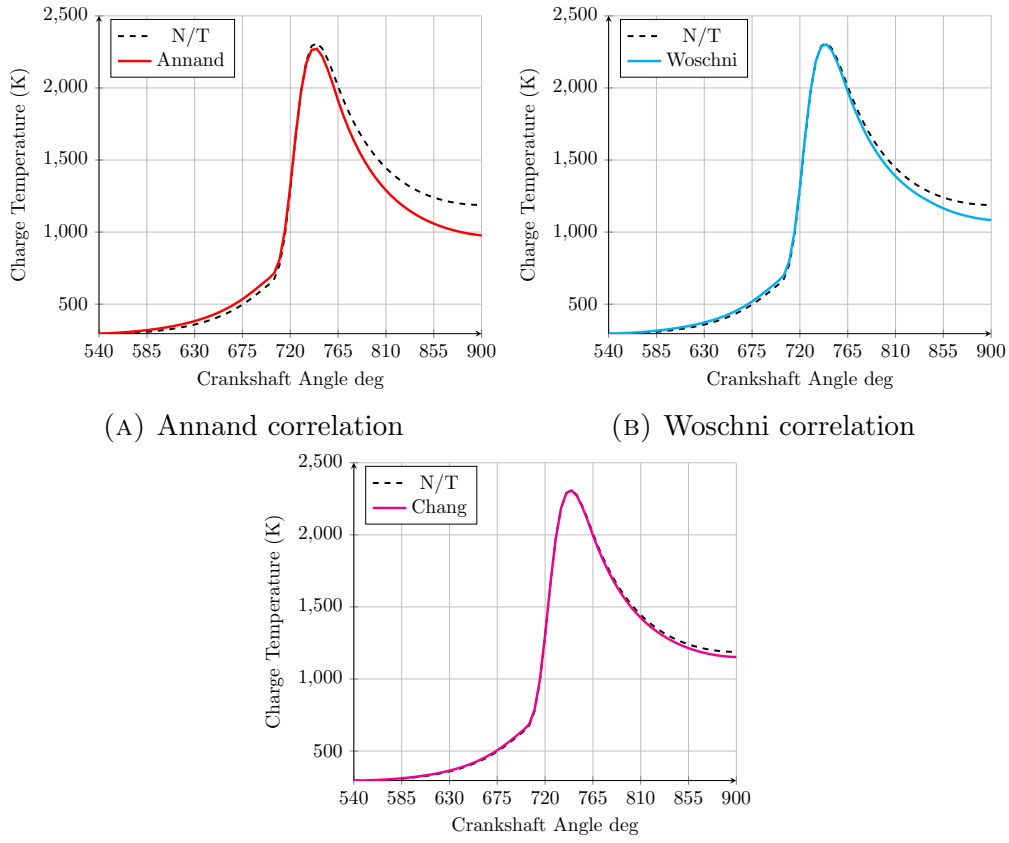

(A) Annand correlation

(B) Woschni correlation

(C) Chang correlation

FIGURE 5.7. Heat Transfer Models–Finite-Rate Combustion

In Figure 5.7 we see the same test, but this time with finite-rate combustion. Note that each model predicts the charge heating up during the compression stroke due to heat transfer from the hot walls. Combustion takes the charge in all three cases to about 2,200 K. During the expansion stroke, each model predicts a different rate of heat loss to the cylinder wall. Again we see Chang predicting the least followed by Woschni and then Annand. That the models predict heat transfer from the walls to the charge when the charge is cooler and heat transfer from the charge to the walls when the charge is hotter is a good physical result. We

may only be able to state which model is most accurate when they are tested in the complete engine model and the results compared to measured data.

5.3. Friction

Engine designers have known for a long time that internal friction results in significant losses of power. Friction also causes wear and limits engine life. Engineers have dedicated great levels of effort to understand where friction is generated inside engines and to minimize its effects. With its noted significance, we must consider it here and determine what effect it has on the modeling of an engine.

Engineers and scientists who work with engines classify friction into three main categories:

(1) Mechanical friction

(2) Accessory work

(3) Pumping work

To those of us outside of the engine research circle, items 2 and 3 seem rather misplaced as they don't fit our typical definition of friction. To the Aerodynamicist, the flows into and out of an engine may be viscous and may exhibit significant losses. But these effects don't fit well under the common definition of "friction", which we think of as a mechanical contact phenomenon. Indeed, item 3 will not be examined in this section at all. Instead, the model we're creating here will explicitly calculate flow or pumping work and its associated losses. That modeling will be covered in another chapter. We will however examine item 2 here, as we're curious about its level of significance: must it be included for realistic results?

Friction, the mechanical variety, is commonly broken down into three regimes [23, 40, 41]:

- Boundary, or surface-to-surface contact.

- Hydrodynamic, or non-contact, fluid supported, viscous drag.
- Mixed, where both of these phenomena occur.

Engines possess a variety of rotating and translating components that are all subject to friction. Engineers have made efforts to characterize and understand where and at what levels friction is generated, but teasing out this information hasn't been easy. We're faced again with the problem of seeing what is going on inside of the engine, when its necessary design and construction precludes just such an examination. Bishop [40], working at Ford Motor Company, pioneered a very interesting technique. First, he identified specific foci of friction, like the crankshaft main bearings, piston rings, camshaft followers, etc. Then, with the understanding of what regimes of friction occur at each location, plus the physics of each sliding or rotating contact surface, he derived equations that described the general form of the frictional physics at each location. Using a motoring dynamometer, he measured the actual power consumed in turning over a real engine. Then he disassembled sections of the engine to eliminate specific assemblies and retested. The difference in power input from one run to the next indicated the power consumed by the removed component and its level of friction. Doing this for a number of engines, he was able to adjust the parameters of his equations to his measured data, creating a set of friction correlations. With these, a designer can use the design data from a given engine and get estimates of the frictional losses that the engine would exhibit in use.

Bishop decomposed overall engine friction into functional groups that are still commonly recoginzed today [23, 40–42]:

- Crankshaft bearings (including connecting rod bearings) and seals
- Pistons (including piston skirts and piston rings)

- Valve train (Camshaft bearings and seals and camshaft followers)
- Accessories (oil and coolant pumps)
- Pumping (intake and exhaust flows)

Bishop's techniques are still in common use and have been revised and modified by other researchers, like Patton, et al. [41] and Sandoval, et al. [42].

One universal measure of engine performance is to take the work an engine can do over one thermodynamic cycle and divide that by its displacement. This work per unit displacement results in units of pressure and is called the Mean Effective Pressure of the engine:

$$mep = \frac{W_{cycle}}{\mathcal{V}_d} \tag{5.34}$$

If we measure the engine's power output on a dynamometer (or engine "brake"), we can calculate the brake mep (bmep) using power:

$$bmep = \frac{\dot{W}_{brake} 60\alpha}{\mathcal{V}_d N} \tag{5.35}$$

where α is the number of crankshaft revolutions in a thermydynamic cycle and N is the crankshaft speed in rpm. Likewise, if we measure or calculate the work or power lost through friction, we can calculate a frictional mep (fmep):

$$fmep = \frac{W_{friction}}{\mathcal{V}} = \frac{\dot{W}_{friction} 60\alpha}{\mathcal{V}_d N} \tag{5.36}$$

Thus, we have bmep representing the engine's power output and fmep representing its losses.

The following correlations, representing each of the functional groups above, are from Patton and Sandoval [41, 42] all $fmep$ units are in kPa:

- Crankshaft:

$$fmep_{cs} = 1.22x10^{5}\left(\frac{D_b}{b^2 s n_c}\right) + 3.03x10^{-4}\left(\frac{N D_b^3 L_b n_b}{b^2 s n_c}\right) + 1.35x10^{-10}\left(\frac{D_b^2 N^2 n_b}{n_c}\right) \tag{5.37}$$

- Piston (including skirt, ring tension and ring pressure):

$$fmep_p = 294\left(\frac{\bar{U}_p}{b}\right) + 4.06x10^{4}\left(1 + \frac{500}{N}\right) + 6.89\left[0.88r + 0.182r^{\left(1.33-2k\bar{U}_p\right)}\right] \tag{5.38}$$

where $k = 2.38x10^{-2}$.

- Valvetrain (including cam, cam followers and valves):

$$fmep_v = 244\frac{N n_b}{b^2 s n_c} + C_{ff}\left(1 + \frac{500}{N}\right)\frac{n_v}{S n_c} + C_{rf}\left(\frac{N n_v}{s n_c}\right) + C_{oh}\left(\frac{L_v^{1.5} N^{0.5} n_v}{b s n_c}\right) + C_{om}\left(1 + \frac{500}{N}\right)\frac{L_v n_v}{s n_c} \tag{5.39}$$

- Accessories (including oil and coolant pumps and alternator):

$$fmep_a = 8.32 + 1.86x10^{-3}N + 7.45x10^{-7}N^2 \tag{5.40}$$

- Pumping:

$$fmep_{i/o} = (p_a - p_i) + 4.12x10^{-3}\left(\frac{p_i}{p_a}\right)^2\left(\frac{\bar{U}_p^2}{n_v^2 r_i^4}\right) + 0.178\left(\frac{p_i}{p_a}\bar{U}_p\right)^2 + 4.12x10^{-3}\left(\frac{p_i}{p_a}\right)^2\left(\frac{\bar{U}_p^2}{n_v^2 r_e^4}\right) \tag{5.41}$$

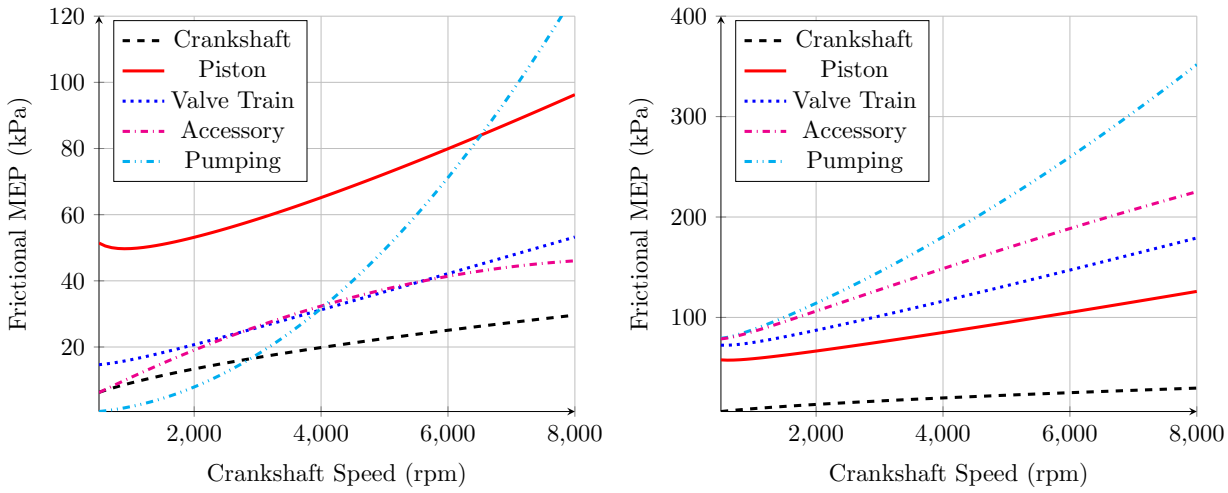

(A) Component Frictional Power Losses (B) Totalled Frictional Power Loss

FIGURE 5.8. Frictional Losses

(Some of the constant values have been left out to avoid clutter. See Sandoval for more detail.)

Figure 5.8 illustrates their output, the fmep of the frictional components of a six cylinder engine with a 100 mm bore and stroke and compression ratio of 11. Figure 5.8a shows the fmep of each component with respect to crankshaft speed and provides a good comparison of each component's significance. Note how the power consumed by each component increases with rpm. This means that, as rpm increases, the engine loses more power to friction. Pumping losses are included here for illustration, but we will address them later. The

pistons are the largest contributor of engine friction, and therefore the largest consumer of engine power. Clearly, if we want to account for dominant physics, we will need to model at least piston friction. Figure 5.8b shows the curves in stacked form. The "pumping" curve represents the total for all of the components. With its 11:1 compression ratio, this engine has a theoretical, or indicated mep (imep) of 1,582 kPa. We see that, at 3,000 rpm, this engine has an fmep of about 150 kPa, so friction consumes about 9.5% of the engine's power at 3,000 rpm.

The correllations seem to provide realistic results. But one has to wonder, are they accurate for *any* engine? Are there first-principles approaches to modeling friction for these components that might be accurate for the general case?

5.3.1. Piston Friction

Figure 5.8a presents a single curve for piston friction, but its value actually represents a total. Bishop, Patton and Sandoval [40–42] identified two distinct sources of friction associated with the piston: the piston skirt and piston rings.

Figure 5.9 shows the piston in its cylinder with a magnification of the piston skirt and cylinder wall. Typically, there is a clearance of about 0.05 mm between the skirt and the wall. When the engine is running, the clearance is filled with oil to lubricate the two surfaces hydrodynamically. In the magnified view the piston is depicted as moving downward. The cylinder wall is stationary and the oil layer between them forms what is essentially a combination Couette/Poiseuille flow. The no-slip condition creates a velocity gradient between the two surfaces that results in viscous shear. Motor oils are considered Newtonian fluids, and so the shear stress through the oil, and on the surface of the piston skirt is:

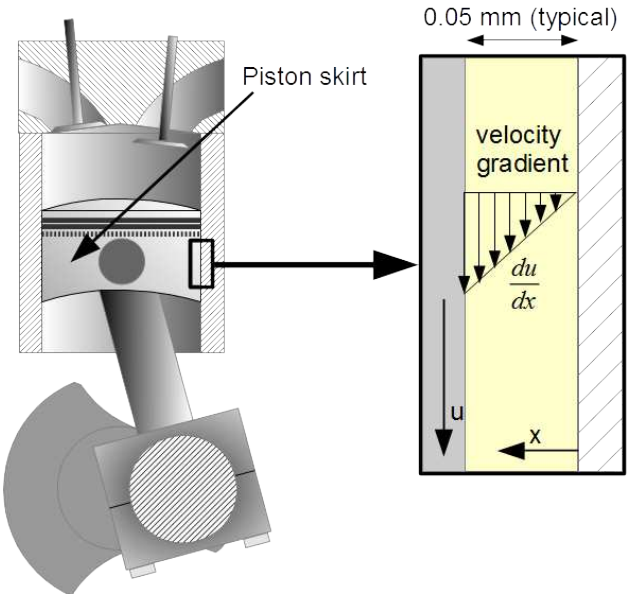

FIGURE 5.9. Piston Skirt Magnified

$$\tau_s = \mu \frac{du}{dx} \qquad \left\langle \frac{N}{m^2} \right\rangle \tag{5.42}$$

If we multiply the shear stress applied to the skirt by the area of the skirt, A_s, we have the shear force on the piston. This is the piston skirt "friction":

$$F_{f_{ps}} = A_s \mu \frac{du}{dx} \tag{5.43}$$

Since oil is Newtonian, the velocity gradient will be linear and we can approximate it with a simple spatial difference:

$$\boxed{F_{f_{ps}} = A_s \mu \frac{U_p}{\Delta x} \qquad \langle N \rangle} \tag{5.44}$$

The piston skirt imposes a shear force on the fluid at a given velocity, and thus is imparting power into the oil film. This raises the temperature of the film [29, 24, 37]. The temperature of the oil, with regard to x-position is [43]:

$$T(x) = -\frac{\mu}{2k}\left(\frac{u}{H}\right)^2 x^2 + \left[\frac{T_{ps} - T_{wall}}{H} + \frac{\mu}{2k}\left(\frac{u}{H}\right)^2 H\right] x + T_{ps} \tag{5.45}$$

Where H is the "height" or thickness of the oil film, T_{wall} is the temperature of the cylinder wall and T_{ps} is the temperature of the piston skirt. Integrating this equation analytically and dividing by H, we can calculate a space-average, instantaneous temperature of the oil film:

$$\boxed{\bar{T} = \frac{1}{12}\frac{\mu}{k}u^2 + \frac{1}{2}\left(T_{wall} - T_{ps}\right) + T_{ps}} \tag{5.46}$$

One might ask whether accounting for the increase in temperature of the oil in the lubrication gap is necesssary, whether it is dominant physics. In the course of this research we've found that it is, and it is something that Bishop, Patton and Sandoval erroneously neglected.

Motor oil viscosity is sensitive to temperature. For SAE (Society of Automotive Engineers) rated motor oils, Kirkpatrick [23] offers the relationship:

$$\mu = c_1 \exp\left(\frac{c_2}{1.8T + 127}\right) \tag{5.47}$$

where μ is the dynamic viscosity, temperature, T, is in $^{\circ}C$ and c_1 and c_2 are given in Table 5.2.

TABLE 5.2. SAE Viscosity Constants

SAE grade	c_1 $\left(\frac{Ns}{m^2}\right)$	c_2 $(^{\circ}C)$
10	$1.09x10^{-}4$	1157.5
20	$9.38x10^{-}5$	1271.6
30	$9.73x10^{-}5$	1360.0
40	$8.35x10^{-}5$	1474.4

So as piston velocity rises, temperature in the oil film rises and viscosity drops. This causes the skirt friction term to decrease in slope slightly with increasing rpm.

Calculating piston skirt friction is straight-forward. But because of its more complicated physics, calculating piston ring friction isn't. It's been long recognized that engine cylinders wear more quickly at the top and bottom, indicating that there is metal-to-metal contact, "boundary-lubricated" wear, at the top and bottom of the stroke. Meanwhile, through the mid-stroke, wear seems to be minimal, indicating hydrodynamic lubrication is occuring there. Engineers surmised that the piston rings, which are in place to seal the clearance gap between the piston and the cylinder wall, may be floating on a film of oil where the piston speed is high enough, and settling onto the cylinder walls when the speed drops below a certain level.

Figure 5.10 shows the piston rings nested in their grooves in the piston. The rings have an outer diameter that is larger than the cylinder bore and must be compressed to fit into the cylinder. Thus, they exert a constant pressure against the cylinder wall to aid in sealing. The static tension typically results in a pressure of between 120 kPa to 250 kPa (1.2 to 2.5 atm) between the ring and the wall [34]. Note that the rings don't fill the piston groove from top to bottom or front to back. During combustion and the power stroke, this small

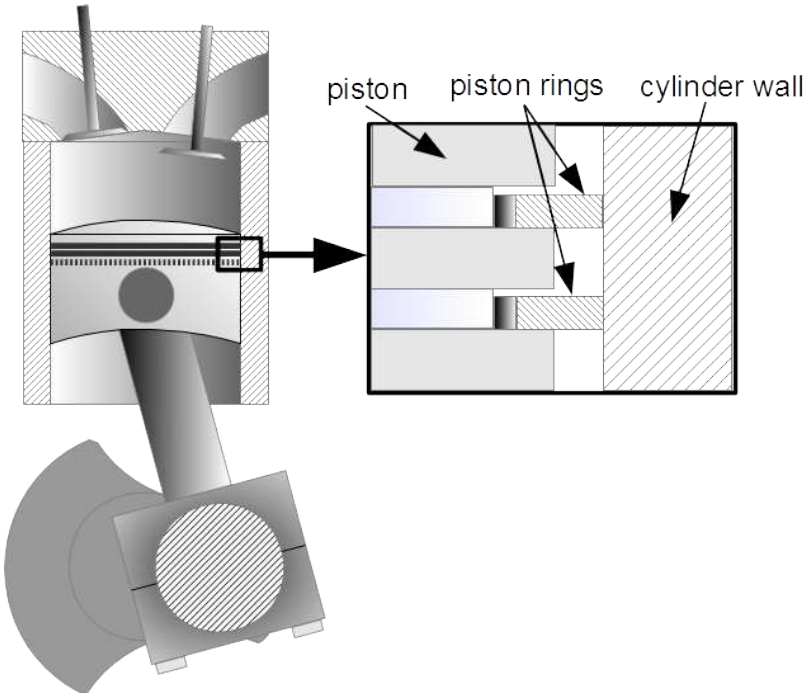

FIGURE 5.10. Piston and Piston Rings

clearance allows high pressure cylinder gases in the cylinder to flow behind the ring and drive it into the cylinder wall with even greater force.

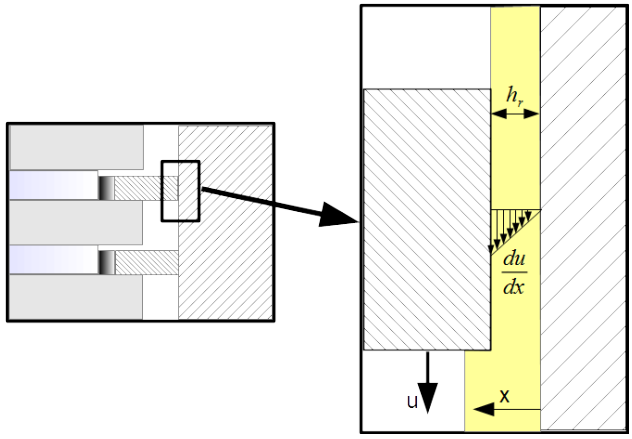

FIGURE 5.11. Ring, cylinder wall and oil film

Figure 5.11 is an even more magnified view of the ring and cylinder wall. The ring is moving down with respect to the stationary wall and there is a film of oil between the ring and the wall. As with the skirt, the oil film forms a combination Couette/Poiseuille flow,

with the oil film in viscous shear. The clearance behind the ring allows the ring to float on the oil film, so that when the pressure behind the ring is low enough and the piston speed high enough, the ring makes no actual contact with the cylinder wall. But when pressures rise high enough and piston speeds drop low enough, the rings sink and make metal-metal contact. Thus, piston rings operate in the mixed lubrication regime. Calculating the friction force is difficult because the height of the ring must be estimated accurately. With a given piston speed, a change in height creates a change in the velocity gradient across the gap, a resulting change in the shear stress throughout the film, and a change in the shear load on the piston ring. Also, when the height drops low enough, asperities, microscopic peaks in the finely machined surfaces of the ring and cylinder wall, begin to make contact [44, 45, 23]. From the low-friction realm of fluid drag proportional to piston velocity, the ring enters the true realm of mechanical friction, where the tangential force is proportional to the normal force. If the ring height is estimated poorly, then the extent of the stroke where boundary contact occurs, and where the frictional forces on the rings are magnified by orders of magnitude, will also be estimated poorly, yielding great errors in the calculation of piston ring friction.

Researchers have made in situ measurements of the size of the ring lubrication gap, the "ring height", h_r, between the piston ring and the cylinder wall. Sherrington et al. [46] describe a series of both optical and electrical techniques for making ring height measurements. Furuhama et al. [47] made measurements on an operating engine using a capacitance technique. Their results are quite noisy, but do show the kind of general trends that researchers intuitively expected. The ring height grows through the middle of the stroke and drops at the top and bottom. All through the power stroke, where cylinder pressures are high and the rings are strongly driven into the cylinder wall, heights are lower. They measured maximum

heights on the order of 10 μm, and minimum heights on the order of 0 μm. Figure 5.12 shows some of their results.

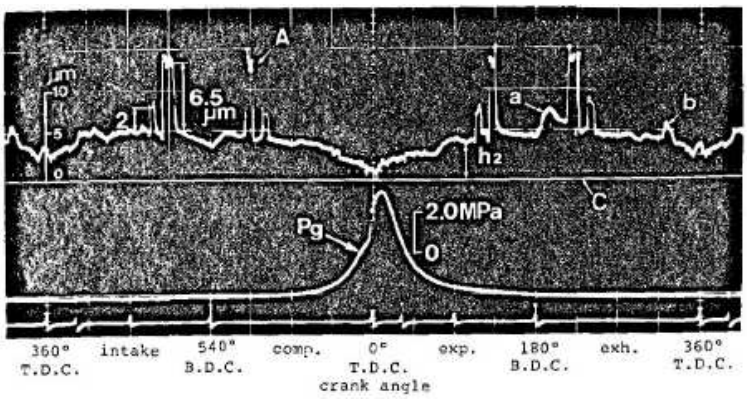

FIGURE 5.12. Ring Height and Cylinder Pressure from Furuhama

Söderfjäll et al. [48] have made direct friction measurements on a motored, instrumented test rig with a piston running in a production engine block. Wakuri et al. [49] have made friction measurements on a purpose-designed, firing test engine with a floating cylinder liner. Both have been able to measure real values of friction force and confirm the mixed lubrication theory for the piston rings, showing the greatly increased forces that are generated when the rings make contact at the top and bottom of the stroke. In the Wakuri case, they have also been able to show the massively increased friction values at the begining of the power stroke, when cylinder pressures are high and piston speeds low.

The piston ring height, h_r, is controlled by a balance of forces, the ring's built-in tension plus the gas pressure load, balanced by hydraulic pressure created in the oil film by the motion of the piston and by differential pressure across the ring. The thin, viscous oil film of figure 5.11 has been studied by researchers since the late 1800s [50] and their work forms the backbone of lubrication theory. In 1886 Osborne Reynolds applied the Navier-Stokes

equations to a model of flow through a channel of extremely small height and great length, between parallel plates, as in Figure 5.13:

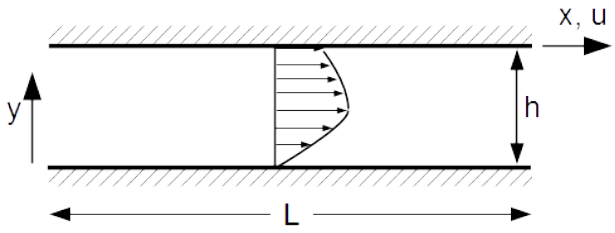

FIGURE 5.13. Flow Between Parallel, Flat Plates

He was able to eliminate lower-order terms, leaving only terms of the same order as h. The result is the Reynolds Equation, which forms the basis for much lubrication theory [51, 50, 52]:

$$\frac{d}{dx}\left(\frac{\rho h^3}{\mu}\frac{dP}{dx}\right) = 6u\frac{d}{dx}(\rho h) \tag{5.48}$$

where:

h = the height of the fluid film (5.49)

ρ = the density of the fluid (5.50)

μ = the viscosity of the fluid (5.51)

u = the velocity of the upper wall (5.52)

Note that the lower wall is stationary. Also note that u refers to the velocity of the upper wall, *not* the velocity of the fluid. Note, in fact, that there are no inertial terms in this

equation. They have all been eliminated at this tiny scale. The only physics left is viscosity. This means that this flow will exhibit physics that we are not familiar with.

The equation says that, given an upper wall velocity and height derivative at a point along the flow, we can calculate a second derivative of pressure at that same point. Solving the equation results in a fluid pressure profile down the length of the flow, $P(x)$. The term on the right contains a $\frac{dh}{dx}$ term. This provides a profile for the height of the film, $h(x)$. Unfortunately, it also typically introduces terms that make the equation nonlinear and very difficult to solve analytically. There are a few simple cases of straight profiles, flat and linear incline, with equal fluid pressures on both sides, that can be solved analytically. But for the general case of a curved profile with differential pressure across the length of the flow $[P(0) \neq P(n)]$, the equation can't be solved analytically.

If we work the derivative through on the left, we have:

$$\boxed{\frac{d^2P}{dx^2} + \frac{3}{h}\frac{dh}{dx}\frac{dP}{dx} - \frac{6\mu u}{h^3}\frac{dh}{dx} = 0} \tag{5.53}$$

This equation is parabolic in space. This makes sense as viscous flows are expected to be mathematically parabolic in nature. Perhaps, for the general case, we can solve the equation using a numerical technique. Note that there is no time derivative available, so we can't solve the equation using a time-marching technique. And because it is parabolic, a space marching technique won't offer a properly posed solution. But since it is parabolic, we should be able to solve it using a relaxation technique.

We'll use a finite-difference approach, replacing the spatial derivatives of Equation 5.53 with the finite differences:

(5.54)
$$\boxed{\begin{aligned}\left(\frac{dh}{dx}\right)_i &= \frac{h_{i+1} - h_{i-1}}{2\Delta x} \\ \left(\frac{dP}{dx}\right)_i &= \frac{P_{i+1} - P_{i-1}}{2\Delta x} \\ \left(\frac{d^2P}{dx^2}\right)_i &= \frac{P_{i+1} - 2P_i + P_{i-1}}{(\Delta x)^2}\end{aligned}}$$

The finite differences discretize the continuous oil film between the ring and cylinder wall into a compuational domain, as illustrated in Figure 5.14. Here, the ring and cylinder wall have been turned 90° for greater clarity. The piston ring is above the cylinder wall and moves horizontally. The oil film fills the gap between the ring and wall.

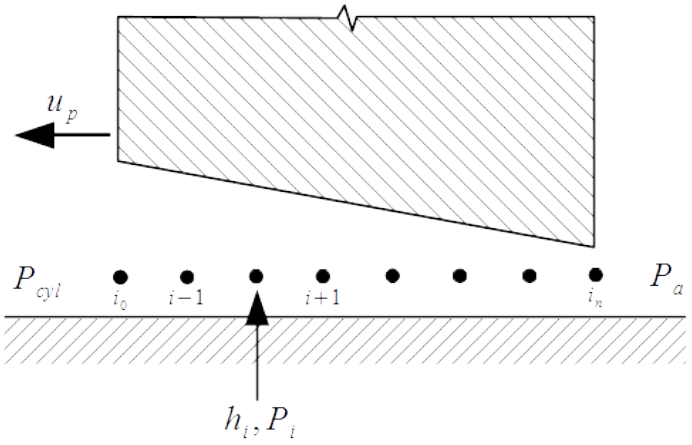

FIGURE 5.14. Piston Ring Computational Domain

Substituting the finite differences into Equation 5.53, we see that our carefull selection of a central, second-difference equation provides us with a P_i that we can isolate on the left:

(5.55)
$$\boxed{P_i = \frac{P_{i+1} + P_{i-1}}{2} + \frac{3}{8h_i}(h_{i+1} - h_{i-1})(P_{i+1} - P_{i-1}) - \frac{3\mu u \Delta x}{2h^3}(h_{i+1} - h_{i-1})}$$

Equation 5.55 is the equation we will solve across the domain. Note its structure: it gives us the value of the pressure at any point in the domain using the pressure at the two neighboring points. We must supply the height of the lubrication gap at each point, which is just what we're looking for, a general solution. We must also supply the distance between points, Δx. Note that we can't apply this equation at the endpoints. There are no neighbors above and below. But since the equation is parabolic, we must specify the pressure at the endpoints (the boundaries) to have a well-posed solution. We will know the pressures at those points from the start. To get the solution–to solve the pressure at all of the field points in the domain–we will set the pressures of the endpoints, then use Equation 5.55 to calculate the pressure at point 1. With that saved, we will repeat at point 2 and so-on to point n. Each sweep of the domain "relaxes" the solution toward a final, converged result. The Reynolds equation allows the use of "successive overrelaxation" in the relaxation of the solution. After solving for the pressure at point i, we subtract the new pressure from that of the previous iteration, multiply by the overrelaxation factor, then add this value to the pressure value from the previous iteration:

$$P_i^{n+1} = (P_i - P_i^n)\,\omega + P_i^n \tag{5.56}$$

With an overrelaxation factor of 1.8, the solution is stable under all tested scenarios and the pressure converges on its final distribution in *one-tenth* the number of iterations required with no overrelaxation. This speeds up the simulation by a factor of nearly 10.

Figure 5.14 depicts the ring in cross-section as a scraper or "inclined slider bearing", in the lubrication lexicon. This is a shape for which the Reynolds equation can be solved

analytically. Figure 5.15 shows Hamrock's [50] closed-form solution for the inclined slider compared with the current numerical solution. They are identical.

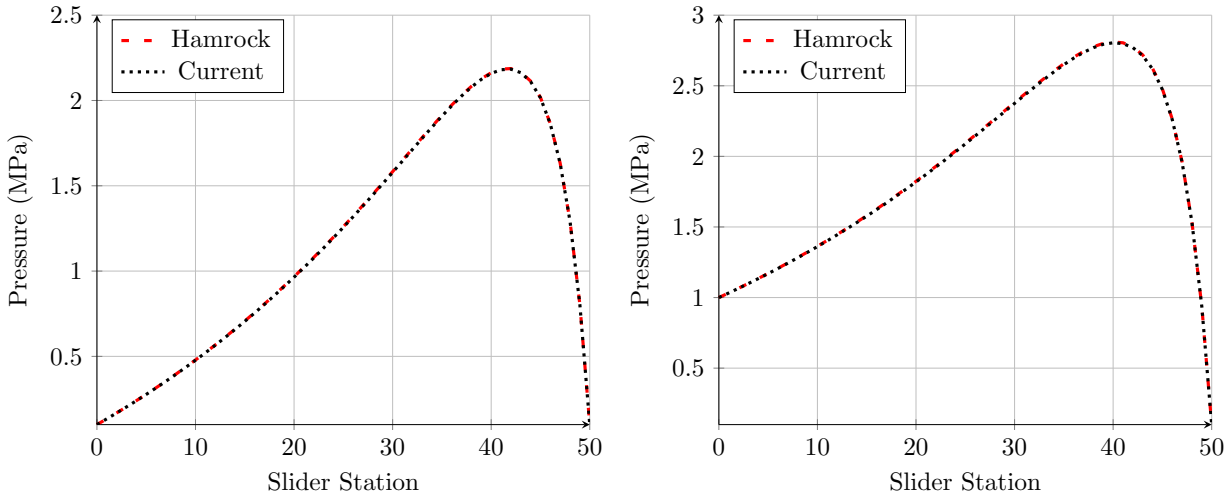

(A) Comparison with Analytical Result (B) Comparison with Differential Pressure

FIGURE 5.15. Reynolds Equation Solution

In Figure 5.15a the pressure at both ends of the fluid film is 100,000 Pa, the slider is moving from right to left at 5 $\frac{m}{s}$, the oil film is 16 μm thick on the left side of the slider and 4 μm thick on the right. Note the massive increase in pressure caused by the slider's motion over the film. Figure 5.15b shows the same scenario with differential pressure. The pressure on the left side of the slider is at 1 MPa. The numerical solution is identical to the closed-form solution.

As the ring moves closer to the cylinder wall, the amplification in pressure increases. Figure 5.16a shows the variation in the film pressure as the ring height is increased from 2 microns to 8. The response is nonlinear, with the pressure amplification growing greatly when the ring nears the cylinder wall.

Figure 5.16b shows the fluid's response as the speed of the ring across the cylinder wall is increased from 2 m/s to 8. Here, we see a linear increase in pressure amplification with

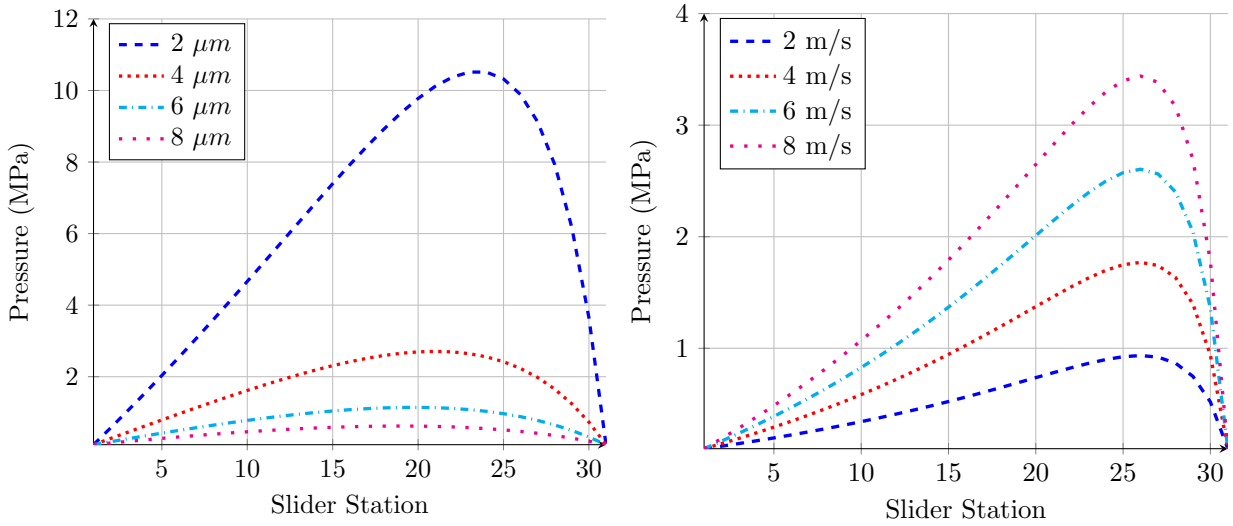

(A) Pressure Variation with Height

(B) Pressure Variation with Speed

FIGURE 5.16. Fluid Film Pressure Variation

speed. These two figures show the most important physics of ring hydrodynamic lubrication, that the pressure under the ring decreases with height and increases with speed. Thus we see why the ring drops to the surface at the top and bottom of the stroke and we can also envision that the height of the ring is self-stabilizing. As cylinder pressure increases and drives the ring into the cylinder wall, the pressure under the ring will rise and eventually match the combined pressure/tension load and the ring will be "flying" on the oil.

To calculate the fluid dynamic drag on the ring, at each crankshaft timestep, we add the cylinder pressure and ring tension, then use a Newton-Raphson technique to find the ring height where the integrated fluid pressure under the ring matches the total pressure being applied. With the height in hand, we can then find the shear stress in the fluid and on the ring and then, with the ring's area, find the shear load on the ring–the friction. We're assuming that the pressure distribution under the ring adjusts from timestep to timestep with infinite rate. We're also neglecting the mass of the ring and assuming that the ring

settles at its stabilized height with infinite rate, and so this is actually an equilibrium solution of ring height.

When the ring height drops below 2.25 μm, we assume there is asperity contact. Rather than calculating the hydrodynamic drag on the ring, we sum the gas and tension pressure and multiply by the face area of the ring for a total normal force. Then, using the coefficient of friction for steel on steel, we calculate the friction force on the ring.

With all of this physics and math embodied in the full engine model, including simple, dynamic models of the intake and exhaust flows (to be covered in the next chapter), we can see the results.

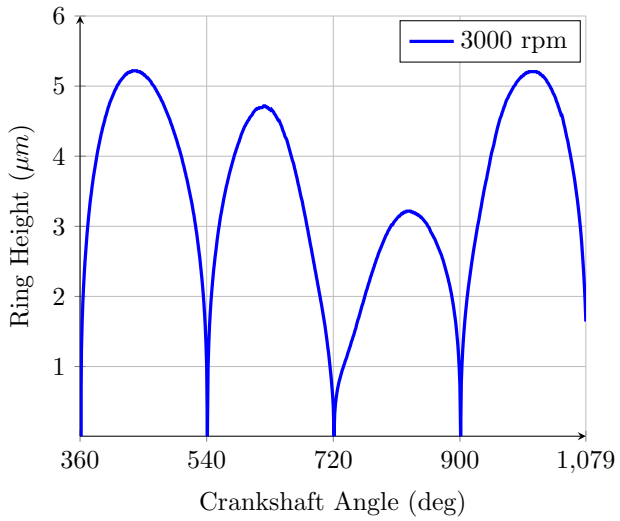

FIGURE 5.17. Cycle Ring Height

Figure 5.17 shows the ring height over the two-revolution cycle for the engine of Chapter 2. (The piston ring face profile is changed from the inclined slider, above, to a "crown face", or circular profile. This is a commonly used ring profile for production engines [34] and is part of the motivation for finding a numerical solution for a complex-shaped lubrication gap.) Here, each value on the x-axis represents a top- or bottom-dead-center point. From left to right, we see the intake, compression, power and exhaust strokes. Note how, at TDC

and BDC the ring height goes to zero and the ring makes contact with the cylinder wall. Then, at mid-stroke, we see the largest height values because the piston velocity is greatest there. Through the intake and exhaust strokes the cylinder pressure is low, near atmospheric, and we see large and nearly equal ring height profiles. On the compression stroke, cylinder pressure increases across the stroke, and so the ring height decreases more rapidly through the stroke than through intake or exhaust. On the power stroke, the ring is being driven into the cylinder wall by the high pressure combustion gases, resulting in the lowest ring heights of the cycle. But as long as the piston is moving, the ring still finds a height where the oil film pressure balances the forces driving it into the wall.

Finally, Figure 5.18 shows the result we've been pursuing. Here we see predictions for the skirt and ring friction over a single engine cycle. Figure 5.18b illustrates the friction force on the piston skirt at 3,000 rpm. We see that friction is proportional to piston speed and reaches a peak value of almost 40 N. Figure 5.18a illustrates the friction force on the piston rings at 3,000 rpm. Each x-axis value marks a TDC or BDC point, with the engine strokes between. Over the strokes we see the same sinusoid-like variation present in the piston skirt curve. But at the ends of the stroke we see sudden spikes. At TDC of the compression/power strokes we see a set of massive spikes. These are caused by the rings making boundary contact with the cylinder wall. Under compression pressure, when the rings make contact, we see about 500 N of force resisting the piston's motion into the cylinder. Ignition begins, raising cylinder pressures dramatically, driving the rings into the cylinder walls and as the piston reverses and begins to descend we see a frictional force of about 800 N resisting its motion. When the piston speed rises enough and the rings begin to float, the friction drops by orders of magnitude.

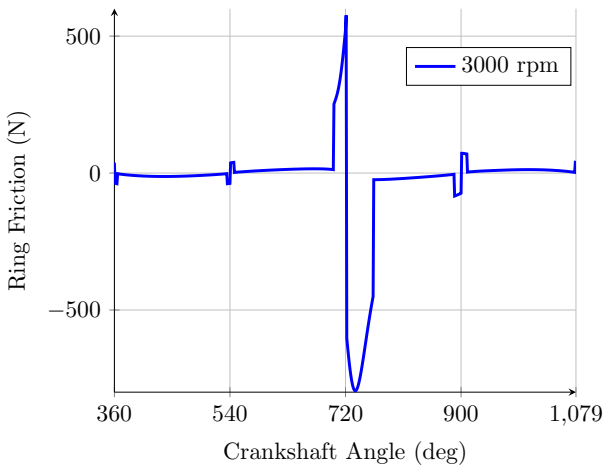

(A) Cycle Ring Friction

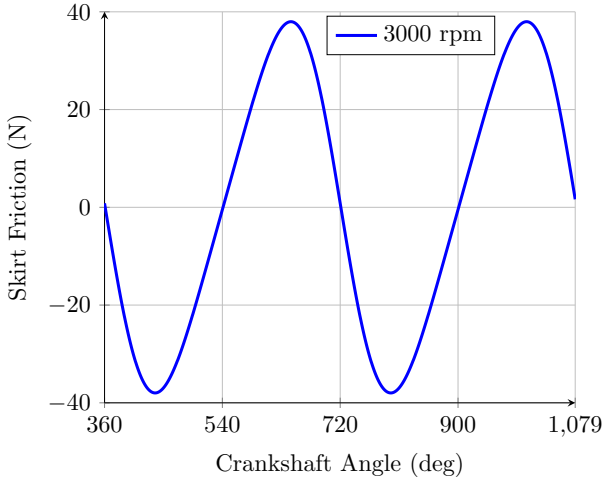

(B) Cycle Skirt Friction

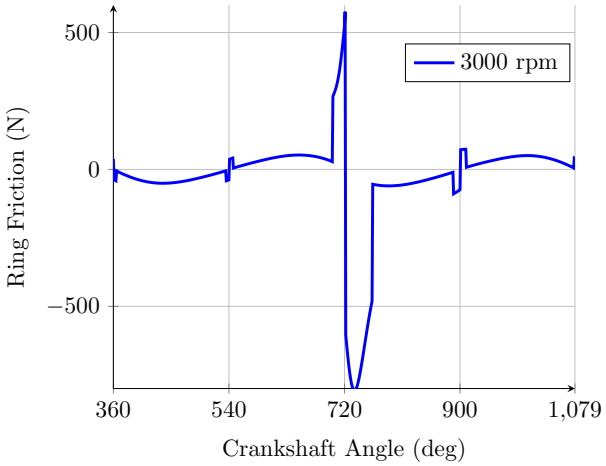

(C) Cycle Total Friction

FIGURE 5.18. Cycle Piston Friction

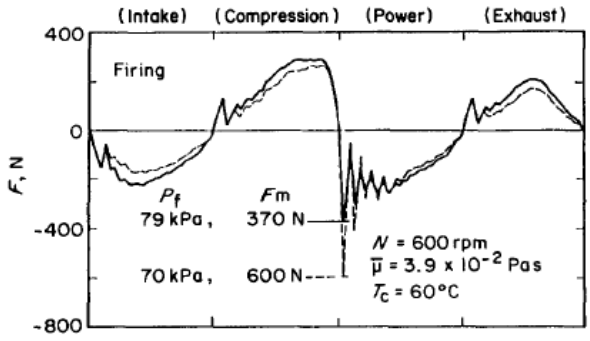

FIGURE 5.19. Piston Friction Measured on Running Engine (Wakuri [49])

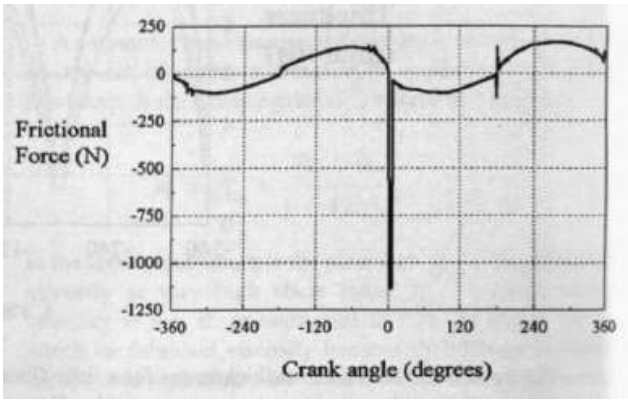

FIGURE 5.20. Predicted Piston Friction (Taylor)

Compare the total friction of Figure 5.18c with Figure 5.19, a plot of piston friction measured by Wakuri et al. on a real, running engine. They made direct measurements of friction by employing a floating cylinder liner held in place by load cells–the load cells measuring piston friction loads directly. Note the spikes at TDC and BDC of the engine's strokes and the sinusoid-like hydrodynamic values in between. Their meausrements have a bit of noise at TDC and BDC caused by "ringing" of the free cylinder liner. Their forces are also higher, as their measurements are on a diesel engine with more rings in its piston and much higher cylinder pressures. But there is strong qualitative agreement between these real measurements and those produced by the engine model. Figure 5.18c also compares very well with the results of Taylor et al., Figure 5.20 [53], which they generated using an analytical technique.

One very important thing to note is the ring friction values through the strokes. Figure 5.21 is an enlargement of the intake stroke from Figure 5.18a. It shows a peak friction value of about 12 N. Compare this with the friction loads on the piston skirt, almost 40 N. What we're seeing here is the difference in area between the rings, which are narrow (about 1.5 mm) and the skirt, which is centimeters in length. The hydrodynamic friction forces on the

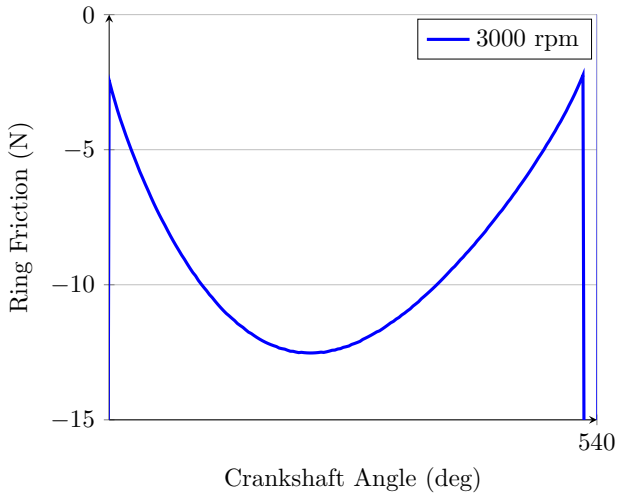

FIGURE 5.21. Intake Stroke Ring Friction

skirt actually pose a much greater loss than those of the rings. We can conclude that, if the piston skirt could be made with narrow "contact" bands at top and bottom, we might be able to significantly reduce the friction in the engine and raise its efficiency.

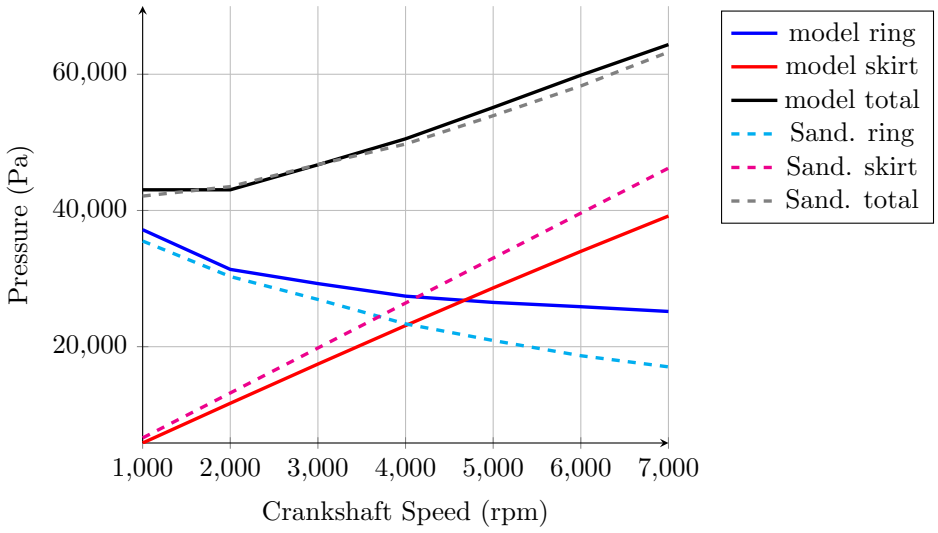

FIGURE 5.22. FMEP: Current Model Compared to Sandoval Correlation

Figure 5.22 shows the final results. The curves show the skirt and ring fmep predicted by our current model and those of Sandoval's [42] correlation. There are two significant points to note here. First, compare the total fmep curves. The current model's result comes very close

to matching the Sandoval correlation and provides strong validation for our first-principles approach. This suggests we now have a technique for estimating piston friction that may be more accurate and more general than the prior correlations. The second point to note is that neither of the component fmep curves fall on the Sandoval curves. As we stated earlier, Sandoval's correlations make no accomodation for the reduction in oil viscosity with piston speed. The Sandoval skirt curve is a straight line. But we can show that it shouldn't be. Instead, the slope of the skirt fmep curve should reduce gently with increasing piston speed, as the model's curve does. The physics here is simple enough to say that this must happen, and that the model's curve is correct. Sandoval's equations are calibrated using real engine measurements and his data included the piston speed/viscosity relationship. But Sandoval's math model for skirt friction can't assimilate that data. Instead, we believe the results of that data went into the ring fmep equation. And this is also the reason for the difference between the two ring friction curves. Sandoval's accounts for the reduction in viscosity with piston velocity for the ring *and* for the skirt. The result is that the total fmep comes out correct, but the component fmep values are incorrect.

One last point for this section: When the ring height decreases to the point where asperitiy contact is made, around 2.25 microns, then the ring friction switches from hydrodynamic to boundary friction. The shear force on the ring is:

$$\tau_{pr} = \eta_k F_N \tag{5.57}$$

where η_k is the kinetic friction coefficient and F_N is the ring normal force. References list the friction coefficient for steel-to-steel contact from 0.41 – 0.57. When a value in this

range is used, the friction force on the piston comes out much higher than predicted by the Patton/Sandoval correlation. To match their estimates, a value of about 0.2 must be used. This suggests that, in the case of ring–cylinder contact, we aren't seeing true steel-to-steel contact. It appears that some amount of oil adsorption must take place, limiting the dry contact seen between the ring and cylinder wall.

5.3.2. Journal Bearing Friction

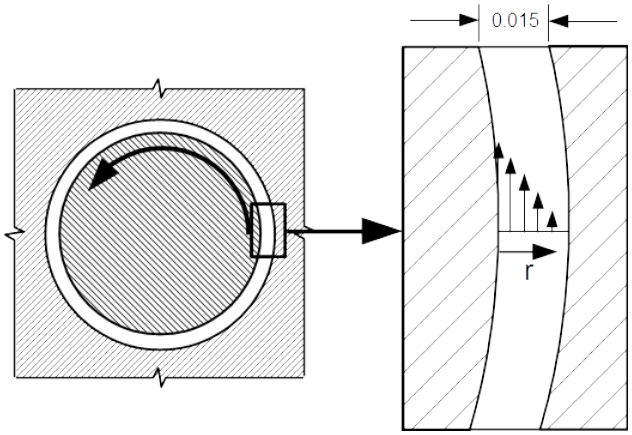

Figure 5.23. Journal Bearing Magnified

Like modeling friction for the piston skirt, modeling journal bearing friction is quite straight-forward. Figure 5.23 shows a journal bearing in cross section. The bearing consists of a circular shaft surrounded by a circular support. A small clearance between the two surfaces provides an anular lubrication gap where oil circulates. The gap clearance is typically on the order of 0.015 mm. In practice, when it is supporting a load, the shaft runs slightly eccentrically in the bearing, the lubrication gap slightly narrower opposite the load. This change in gap height provides the same hydraulic pressure amplification that we saw under the sliding ring, maintaining hydrodynamic lubrication between the two surfaces and supporting the load. Like in the case of the piston ring, the shaft essentially "flies" on the

oil film and finds a stabilized height where the fluid pressure exactly counters the load. For our purposes, we will consider the shaft to be concentric, with the lubrication gap height constant around the shaft. In the gap, we see the same velocity gradient and shear flow that we saw around the piston skirt, except that, where the flow past the skirt is axial, in the bearing it is radial. The shear stress through the film of fluid and on the surface of the shaft is:

$$\tau_b = \mu \frac{du}{dr} \tag{5.58}$$

The radius of the shaft is many orders of magnitude larger than the clearance gap, so we can "unroll" the bearing and ignore the effects of curvature. Since the oil is a Newtonian fluid, the velocity gradient across the gap will be linear and we can represent it with a simple difference. Keeping in mind that the outer surface is stationary:

$$\tau_b = \mu \frac{u}{\Delta r} \tag{5.59}$$

And $u = \omega r$, so,

$$\tau_b = \mu \frac{\omega \frac{D_b}{2}}{\Delta r} = \mu \frac{D_b}{2\Delta r} \omega \tag{5.60}$$

The shear force on the shaft is equal to the shear stress times the area over which it is applied. The area of the bearing is:

$$A_b = \pi D_b L_b \tag{5.61}$$

where D_b is the diameter of the bearing surface and L_b is the length of the bearing surface. Then the force applied to the shaft surface is:

$$F_\tau = \pi\mu \frac{D_b^2 L_b}{2\Delta r}\omega \tag{5.62}$$

The moment created about the shaft by the shear force is:

$$\boxed{M_\tau = F_\tau r = F_\tau \frac{D_b}{2} = \pi\mu \frac{D_b^3 L}{4\Delta r}\omega} \tag{5.63}$$

This is the equation we will apply in the engine model, as there, we sum forces and moments. But for component-level comparisons, we can continue on here and get a closed-form result. The power consumed by the hydrodynamic friction is:

$$P_\tau = \omega M_\tau = \pi\mu \frac{D_b^3 L_b}{4\Delta r}\omega^2 \tag{5.64}$$

For convenience, we'd like to see rotational velocity in rpm, rather than radians per second, $\omega = N\frac{2\pi}{60} = N\frac{\pi}{30}$:

(5.65)
$$P_\tau = \frac{\pi^3 \mu}{3600} \frac{D_b^3 L_b}{\Delta r} N^2$$

And for comparison to the Patton/Sandoval correlation, we'd like an fmep value:

(5.66)
$$\boxed{fmep_b = \frac{120\dot{W}}{\mathcal{V}_d N} = \frac{\pi^3 \mu}{30} \frac{D_b^3 L_b}{\Delta r} \frac{N}{\mathcal{V}_d}}$$

Viscosity is sensitive to temperature and so, for accuracy, we must again include the temperature of the oil film, Equation 5.46 and the SAE viscosity equation, 5.47. There is some disagreement on the operation of shaft seals, with Patton/Sandoval claiming that they operate in the boundary friction regime, while DICHTA [54], a seal manufacturer, claims they operate in the hydrodynamic regime with an oil film height of about 3μm. Here, we will assume the latter and apply Equation 5.66 for the crankshaft main bearings, connecting rod bearings and shaft seals.

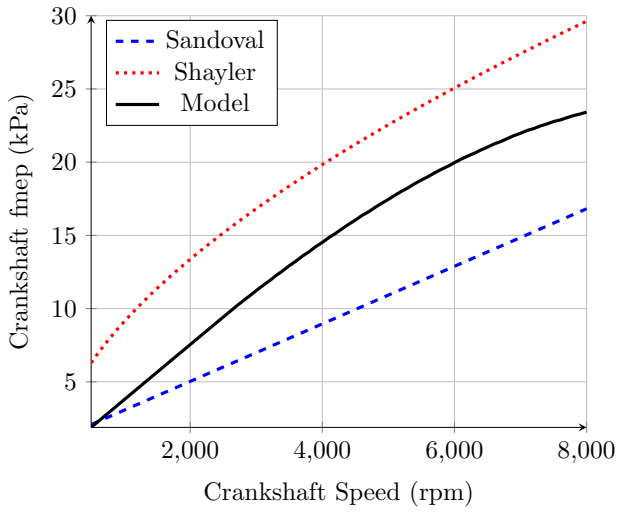

FIGURE 5.24. Crankshaft Friction Model Comparison

Figure 5.24 shows the results. The blue, dashed curve is the Patton/Sandoval correlation. The red, dotted curve is the correlation of Shayler [23]. The black, solid curve is for the present model. Each result is calculated for the same engine, with:

- six cylinders
- 100 mm bore and stroke
- seven main bearings, 54 mm diameter, 21.6 mm length
- six connecting rod beaings, 49 mm diameter, 21.4 mm length
- For the present model:
  - two crankshaft seals, 1.0 mm wide with 3 μm clearance
- SAE 30 oil at 90° C

There is a significant difference in the predictions. Shayler and Sandoval are correlations and aren't guaranteed to be accurate for every engine. It should also be noted that the Sandoval results seem to underpredict real measurements in that paper. The current model falls between the Sandoval and Shayler predictions, and has a similar shape to Shayler's. This at least provides a level of confidence that the current model and its derivation are correct and may be valid.

CHAPTER 6

Simple Intake and Exhaust Flow Modeling

6.1. Valves

The most commonly used valve in piston engines is the poppet valve. Figure 6.1a shows a poppet valve situated in its place in a cylinder head with its port visible in cross section above it. The valve is open and flow is free to move in or out. If this were an intake valve, an intake "runner" would be connected to the atmospheric end of the port. If this were an exhaust valve, an exhaust "header" pipe would be connected to the atmospheric end. When closed, the valve rests on its seat, sealing the port, preventing gas from moving either in or out. Figure 6.1b shows just the valve and its seat. The seat and the valve's matching contact surface are finely machined so that, when in contact, a perfect seal is formed and no fluid can pass. (With use, the seat and the valve's seating surface both wear and the perfect seal is lost. Gases begin to leak out during the compression and power strokes, decreasing the engine's efficiency.) The seat is made of hardened steel and is retained in the cylinder head by a strong interference fit. The seat is illustrated in-place in Figure 6.1a.

Figure 6.1b illustrates the pertinent dimensions associated with a valve, its diameter and its lift. The lift isn't really a valve property, but instead is determined by the geometry of the cam that actuates the valve. The cross-sectional area of the port, the area of the flowpath, is easy to envision and measure. But the area of the flowpath through the valve is a bit more complicated. Typically, two measures are used.

Figure 6.2 shows, on the left, the valve seat area. This is the cross-sectional area of the valve seat at its outer edge:

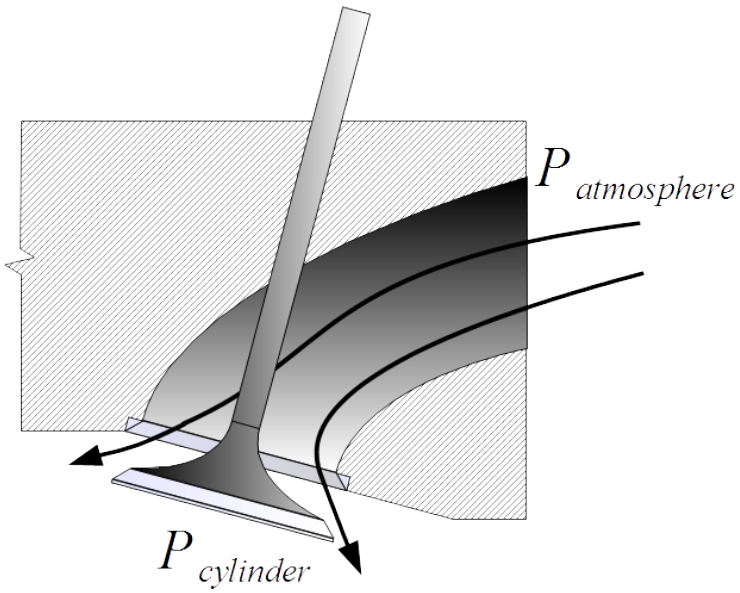

(A) Open Poppet Valve

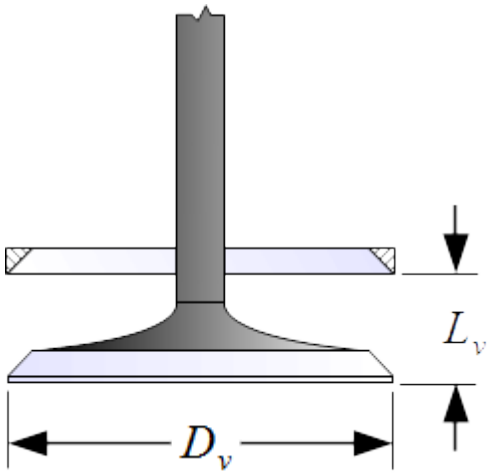

(B) Valve Dimensions

FIGURE 6.1. Valve Geometry

$$A_{vs} = \pi \frac{D_v^2}{4} \tag{6.1}$$

On the right, the horizontally hatched area is the "curtain area" of the valve flowpath. It is a short, concentric cylinder of area:

$$\boxed{A_{vc} = \pi D_v L_v} \tag{6.2}$$

Here, we will represent the flowpath cross-sectional area using the valve curtain area.

The valves are actuated by a camshaft. The eccentric cams on the shaft push on the end of the valve "stem", forcing the valve open against spring force. As the camshaft rotates, the cam opens the valve and then, as the cam lobe passes, the valve's return spring forces it closed and against its seat. The geometry of a cam, defined by its opening and closing points,

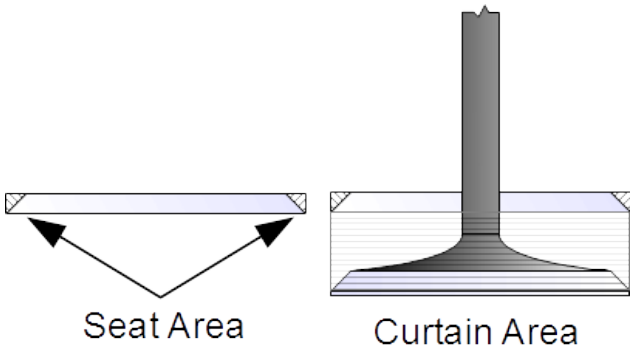

FIGURE 6.2. Valve Flow Area

its maximum lift and the profile over which it goes from zero to maximum lift, all affect the performance of an engine. To be useful, any engine analysis technique, from closed-form to simulation, must be sensitive to changes in cam geometry. Three lift profiles are commonly used in the manufacture of cams, simple harmonic, cycloidal and catenoidal. Each lifts the valve at a slightly different rate over its opening duration, affecting the forces on the valve and the airflow past the valve in its own, individual manner. Here, we will only study the simple harmonic profile:

$$L_v = L_{v,max} \frac{1 - cos\left[2\pi\left(\frac{\theta-\theta_o}{\theta_c-\theta_o}\right)\right]}{2} \tag{6.3}$$

where $L_{v,max}$ is the maximum lift, θ_o is the crankshaft angle where the valve begins to open, θ_c is the crankshaft angle where the valve is fully closed and θ is the current crankshaft angle. Figure 6.3a shows the result, the lift profiles for the engine of chapter 2. The cam geometry is:

- Intake $\theta_o = 323°$
- Intake $\theta_c = 600°$

- Intake $L_{v,max} = 9.0$ mm
- Intake $D_v = 40.9$ mm
- Exhaust $\theta_o = 120°$
- Exhaust $\theta_c = 384°$
- Exhaust $L_{v,max} = 6.4$ mm
- Exhaust $D_v = 36.6$ mm

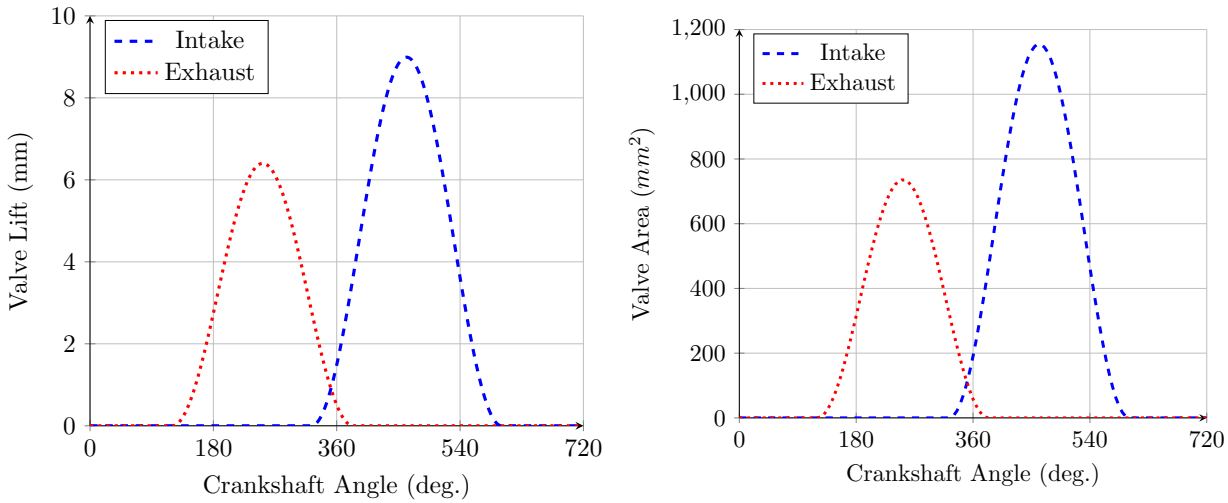

(A) Valve Lift Profiles

(B) Valve Area Profiles

FIGURE 6.3. Valve Profiles

Figure 6.3a shows the lift profiles of both the intake and exhaust valves with respect to crankshaft angle. TDC of compression is at 0°. Each vertical grid line marks a TDC or BDC point. The areas between the grid lines represent the four strokes of the engine: power, exhaust, intake and compression, from left to right. Note how both valves are open at TDC of the exhaust stroke (360°). This "valve overlap" is a non-intuitive, beneficial design feature that was discovered through experimentation. Figure 6.3b shows the valve curtain area with respect to crankshaft angle. Note how there is less flowpath area on the exhaust side. The hot exhaust gases have a much higher speed of sound, and so a smaller area can

be used without the threat of choking. Also, the pressure on the cylinder side of the valves is controlled by the piston rising, and so, even when choked, the mass flow rate can still rise due to supply-side pressure. Choking through the intake valve is especially detrimental and by minimizing the size of the exhaust valve, more real estate is made available in the head and the intake valve can be made larger.

6.2. Isentropically-Based Flow Model

The simplest model of intake and exhaust flow begins with an isentropic model. Here, we employ the isentropic flow equations [29, 23, 37], applying them to two regions, that outside of the valve and that inside of the valve:

$$\frac{P_0}{P} = \left[1 + \left(\frac{\gamma - 1}{2}\right) M^2\right]^{\frac{\gamma}{\gamma-1}} \tag{6.4}$$

$$\frac{T_0}{T} = \left[1 + \left(\frac{\gamma - 1}{2}\right) M^2\right] \tag{6.5}$$

$$\frac{\rho_0}{\rho} = \left[1 + \left(\frac{\gamma - 1}{2}\right) M^2\right]^{\frac{1}{\gamma-1}} \tag{6.6}$$

Equation 6.4 can be inverted for Mach number and the other equations solved for their static values:

$$\boxed{M = +\sqrt{\left[\left(\frac{P_c}{P_a}\right)^{\frac{\gamma-1}{\gamma}} - 1\right]\frac{2}{\gamma - 1}} \quad \text{or,} \quad M = -\sqrt{\left[\left(\frac{P_a}{P_c}\right)^{\frac{\gamma-1}{\gamma}} - 1\right]\frac{2}{\gamma - 1}}} \tag{6.7}$$

(6.8)
$$\boxed{\begin{aligned} T &= T_0 \left[1 + \left(\frac{\gamma - 1}{2}\right) M^2\right]^{-1} \\ \rho &= \rho_0 \left[1 + \left(\frac{\gamma - 1}{2}\right) M^2\right]^{\frac{1}{1-\gamma}} \end{aligned}}$$

Here, P_c is pressure inside of the cylinder and P_a is atmospheric pressure. When cylinder pressure is higher, the left equation 6.7 is used, yielding a positive Mach number, or flow *out* of the cylinder. When atmospheric pressure is higher, the right Equation 6.7 is used, yielding a negative Mach number or flow *into* the cylinder.

With the Mach number in hand, equations 6.8 are used. Here, the subscript 0 applies to the high-pressure or upstream side of the valve. The result is then the temperature and density of the fully expanded flow on the downstream side of the valve where the Mach number is given by equations 6.7.

We calculate the velocity on the downstream side with:

(6.9)
$$\boxed{\vec{V} = M\sqrt{\gamma RT}}$$

and then, with the valve's current curtain area, we calculate the mass flow rate through the valve:

(6.10)
$$\boxed{\dot{m} = \rho \vec{V} A_{vc}}$$

We couple the intake/exhaust model to the model of the charge by inserting the mass flow rate value into the charge continuity equation (6.11, repeated here for convenience) as $\left(\rho\vec{V}A\right)_i$ and $\left(\rho\vec{V}A\right)_e$.

$$\frac{d\rho}{dt} = -\frac{1}{\mathcal{V}}\left[\left(\rho\vec{V}A\right)_i + \left(\rho\vec{V}A\right)_e + \left(\rho\vec{V}A\right)_b + \rho\frac{d\mathcal{V}}{dt}\right] \tag{6.11}$$

The values of ρ, T and $\vec{V}$ are also used for the first two terms of the charge energy equation (6.12, also repeated here) where $e = c_v T$ in term 1 and the pressure in term 2 is P_{charge}. In both terms the area is A_{vc}. In the sums, the intake values correspond to subscript 1, exhaust values to subscript 2 and blowby values to subscript 3.

$$\frac{dT}{dt} = -\frac{1}{\rho\mathcal{V}c_v}\left\{\underbrace{\sum_{i=1}^{3}\left[\rho\left(e + \frac{\vec{V}^2}{2}\right)\vec{V}A\right]_i}_{1} \underbrace{+\sum_{j=1}^{3}\left(P\vec{V}A\right)_j}_{2} + \dot{Q}_T + \dot{Q}_c + \mathcal{V}e\frac{d\rho}{dt} + \rho e\frac{d\mathcal{V}}{dt}\right\} \tag{6.12}$$

These isentropic flow equations don't specify the process that is used to expand the intake and exhaust flows to the downstream pressures. But they do envision a flowpath and they do envision the flow being accelerated down that flowpath. The cross-sectional area of the flowpath has a perfect profile that delivers the flow at the downstream end at downstream pressure. We need to add just a bit of non-theoretical reality to this model, however. When we envision the flowpath, it will have some finite area profile down its length. It could be constant area or it could have a minimum area at some point along its length. In that case, when the pressure differential is high enough, we will see the flow reach Mach 1 at that point

and the flow will be choked. We need to include this behavior, so we'll say that the flowpath area will reach a minimum value at the downstream end; the throat of the flowpath is at the exit. Then we know that the Mach number there must never exceed 1. We can test for this condition by looking at the pressure differential:

$$\frac{P_0}{P} = \left[1 + \left(\frac{\gamma - 1}{2}\right) M^2\right]^{\frac{\gamma}{\gamma-1}} \tag{6.13}$$

$$\frac{P_0}{P} = \left[1 + \left(\frac{\gamma - 1}{2}\right) (1)\right]^{\frac{\gamma}{\gamma-1}} \tag{6.14}$$

(6.15)

For a ratio of specific heats of 1.4, this gives a value of:

$$\frac{P_0}{P} = 1.893 \tag{6.16}$$

and,

$$T = 0.833 T_0 \tag{6.17}$$

$$\rho = 0.634 \rho_0 \tag{6.18}$$

Note then, that on the intake stroke, since P_0 is fixed, the velocity on the downstream side will have a limit and, for a given valve opening, so will mass flow rate. For the exhaust stroke, P_0 is unbounded. If the flow chokes the pressure will continue to rise as the piston

compresses the charge and the downstream density and temperature will rise along with it, increasing the mass flow rate. So we see that an engine's performance is limited by choking through the intake tract. In the engine model, we'll make these calculations with frozen or equilibrium gas values, as discussed earlier.

Real flow through the intake and exhaust tracts is viscous. It has drag, imposed by the viscous boundary layer and by any separation that may occur as the flow proceeds through the tract. Even though we're modeling the flow isentropically, we can account for drag by taking a page from the experimentalists.

FIGURE 6.4. A Cylinder Head Flow Bench

Racers, engine builders and engine designers have been using a device called a cylinder head flow bench (Figure 6.4) for years. This device draws a vacuum on the cylinder side of the head, measuring the mass flow rate of air passing from the atmosphere through the engine's tracts and into the bench's vacuum chamber. A lift adjusting screw is used to open the valve a precisely measured amount so that the relationship between lift and mass flow rate can be built. Given the measured mass flow rate and the isentropic mass flow rate for the same pressure differential and valve area, they calculate a "discharge coefficient":

$$C_d = \frac{\dot{m}_{meas}}{\dot{m}_{isen}} = \frac{A_f}{A_{vc}} \tag{6.19}$$

Then, we can say that there is an effective flowpath area, based on the discharge coefficient:

$$\boxed{A_f = C_d A_{vc}} \tag{6.20}$$

The discharge coefficient isn't constant across engine operating conditions or even across the valve open duration. It changes with valve lift and with flow Reynolds number. For the intake flow, Kirkpatrick [23] offers the equation:

$$\boxed{C_{di} = -0.798\left(\frac{L_v}{D_v}\right)^2 - 0.860\frac{L_v}{D_v} + 0.850} \tag{6.21}$$

And for the exhaust:

$$\boxed{C_{de} = -3.6975\left(\frac{L_v}{D_v}\right)^2 + 1.0585\frac{L_v}{D_v} + 0.6499} \tag{6.22}$$

We'll use these equations to calculate the effective areas of the intake and exhaust valves, completing the flow model. Note that, with the discharge coefficients added, the intake and exhaust flows are no longer isentropic; instead, they are adiabatic. With this flow model

added to the overall engine model, we finally reach our first major milestone. We have a complete, operating simulation of an engine.

6.3. Preliminary Results

For the following discussion, to avoid complicating the technical picture, we'll operate the complete simulation with all of the loss models turned off. There will be no blowby, heat transfer or friction. The results we present will be driven only by the fluid dynamics and thermodynamics of the complete model.

Figure 6.5 shows the results, the properties of the charge across the engine's two-revolution cycle. The solid, vertical grid lines indicate the TDC and BDC points of the engine cycle. The red, dash-dotted grid lines indicate the opening and closing points of the intake and exhaust valves. Each is labeled on the bottom plot. Begin observing this figure at 0 degrees crankshaft angle. This is TDC of the compression stroke. As the crankshaft angle increases, ignition has occurred and the charge is burning. The piston is moving downward on the power stroke. Note how the density decreases as the piston drops and the volume of the trapped charge increases. Temperature and pressure drop as the density decreases. At 120° the exhaust valve opens. The pressure in the cylinder is about 5 atmospheres and with the valve opening, the hot, high-pressure gases begin to rush out in what is called the "blow-down" phase. Note the inflection of all three curves at this point as, with mass now flowing out of the cylinder, the density decreases even more rapidly. The exhaust valve continues to open as the crankshaft rotates. Just after 180°, BDC of the power stroke, blowdown ends as the charge pressure equalizes with ambient. The piston begins to move upward and the charge is pumped out of the cylinder. With the valve fully open and the volume of the

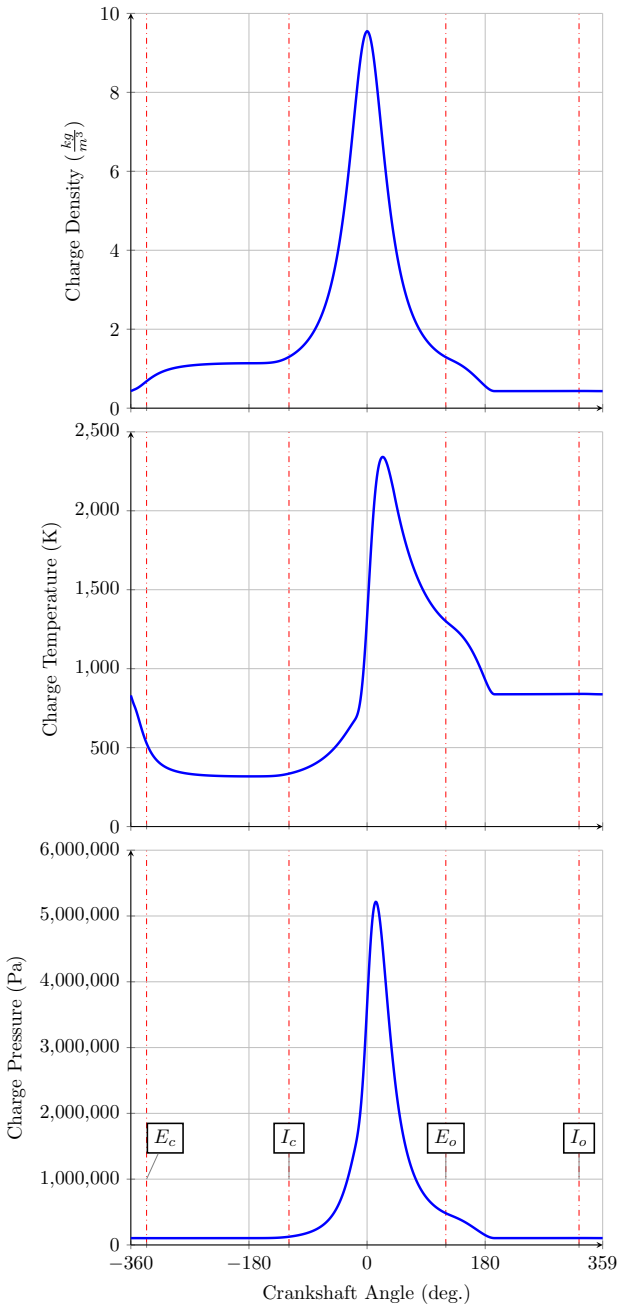

FIGURE 6.5. Cycle Charge Properties, 3,000 rpm

cylinder decreasing, the charge pressure remains at ambient and the density and temperature remain essentially constant. At 323°, with the piston still rising, the intake valve begins to open. At 359° the piston has arrived at TDC of the exhaust stroke. It now begins moving downward again on the intake stroke. Follow the plot around to the left, where we continue

at the beginning of the intake stroke. The exhaust valve is now nearly closed and the intake valve is opening wider. With the intake valve open, the pressure of the charge remains at ambient. The piston is now drawing cool fuel/air mixture into the cylinder. Note how the temperature of the charge decreases as the cool intake charge mixes with the residual, hot exhaust gases. Also note how the density increases as the cool, dense intake charge mixes with the hot, low density residual gases. The intake valve closes at -119°, sealing the cylinder, trapping the intake charge. With the piston rising on the compression stroke, the density, temperature and pressure of the charge all increase. Ignition starts at -20°. Note the slight discontinuity of the temperature plot at this point. As the charge begins to burn, the piston passes 0°, TDC of compression, and we begin the cycle over again.

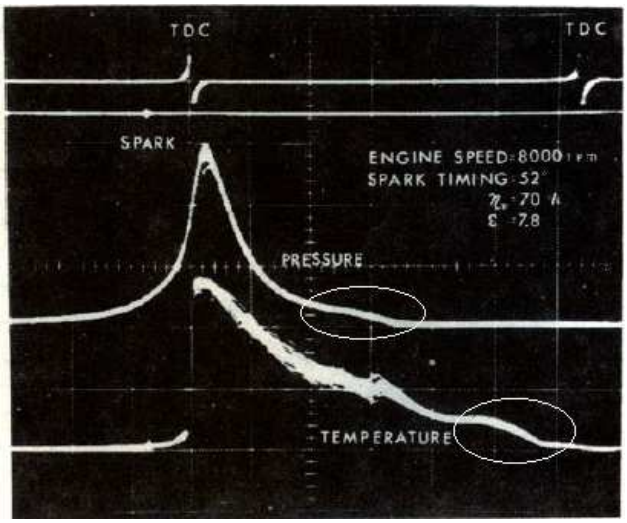

FIGURE 6.6. Measured Charge Pressure and Temperature

Figure 6.6 shows the pressure and temperature measured inside of an operating engine cylinder by Yagi et al. [55]. These measurements are made on a four-stroke engine of unspecified displacement at 8,000 rpm. While we can't compare the results directly, there is good qualitative agreement between the measurements and the model's calculations. In

particular, note the blowdown section visible in the pressure plot and the drop in temperature as the cool intake charge is drawn in (both circled).

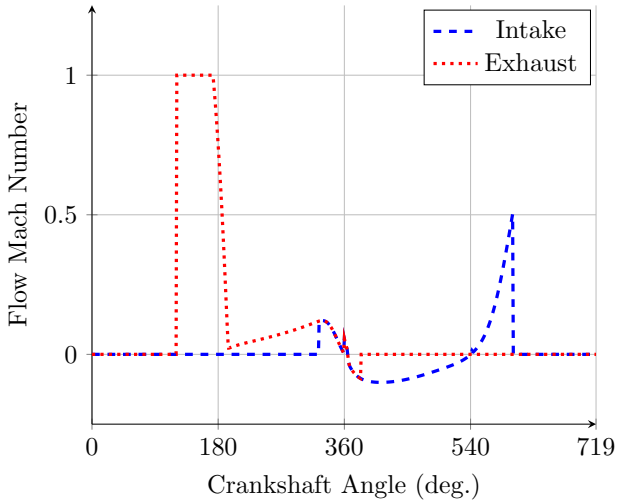

FIGURE 6.7. Intake and Exhaust Flow Velocities

Figure 6.7 illustrates the velocities of the intake and exhaust flows as they pass through the valves. Here, TDC of compression has been moved to the left to increase clarity. Positive velocity is flow out of the cylinder. Negative velocity is flow in. It is easy to see where the valves open and close. At 120° the exhaust valve opens. We see blowdown occurring, with the flow through the valve choked. As the piston passes through BDC, the cylinder pressure equalizes and the velocity drops to nearly zero. Then as the piston rises we see the velocity grow and stay in the low, subsonic regime. In the center of the figure we see the overlap region. When the intake valve opens, hot exhaust gases actually flow *out* for a short period of time. Then, as the piston passes through TDC, some air is drawn *in* through the exhaust valve. Note that these are velocities. The valve areas are changing continuously from left to right. So the values here don't reflect mass flux.

In Figure 6.8 we do see mass flux. At the top of the figure, we repeat the valve area profile, for convenience. Below it, we see the mass flow rates through the two valves. Positive

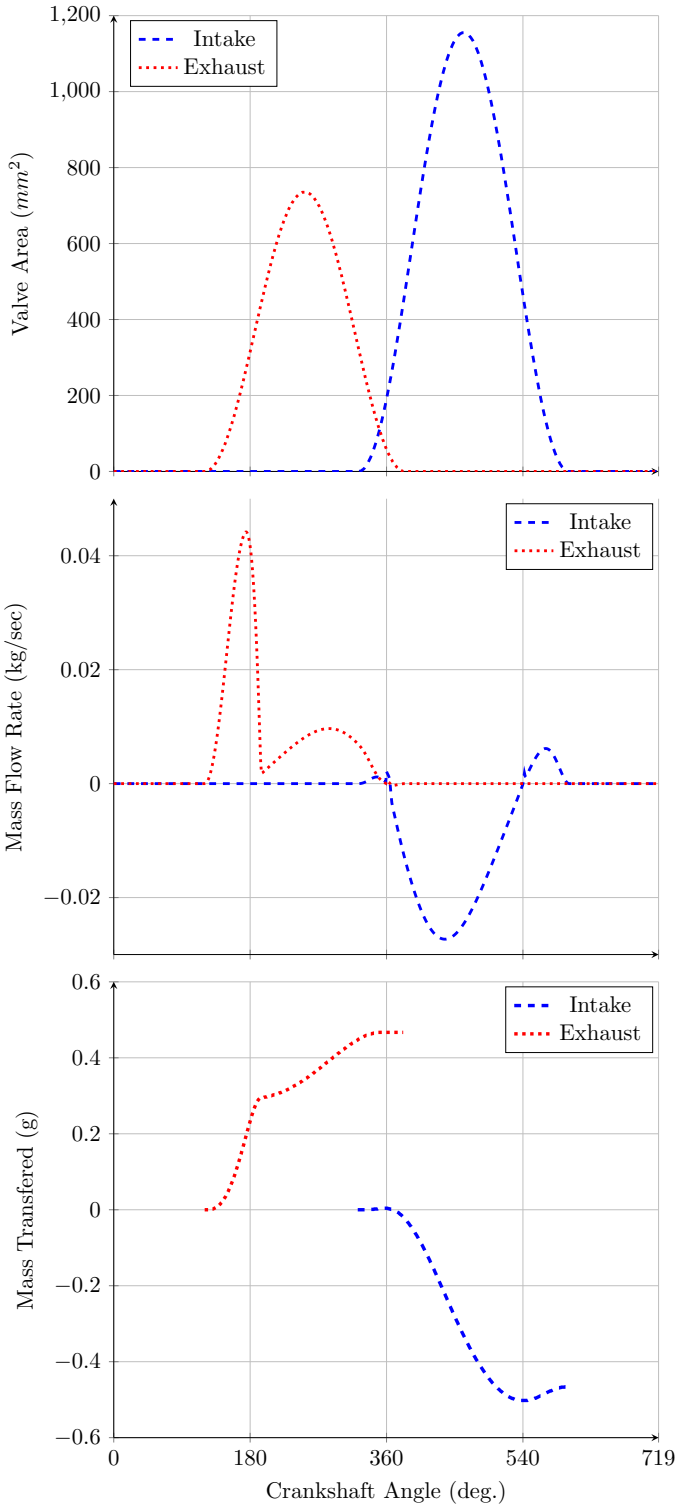

FIGURE 6.8. Mass Inducted and Exhausted

is flow out and negative is flow in. The exhaust flux curve clearly shows blowdown. Note that the curve isn't discontinuous, as is the velocity. This is because the rate is controlled by the varying pressure of the charge on the upstream end. After blowdown, we see the flow being pumped out by the piston. Note the overlap region. While the velocities were significant through this range, the mass flow rates are quite modest. Also note the flow reversal at the end of the intake valve's duration. Here, we see that we're actually losing some useful intake charge, as it flows back out the intake tract, and we note that, if the valve were to close a few degrees earlier, we might gain some power. This is something that is difficult to measure on a real engine, and is validation of the effort in creating an engine model. The bottom plot in the figure shows the integrated mass inducted into and exhausted out of the cylinder. On the exhaust curve, we again see the blowdown phase. On the intake curve, we can easily see the intake charge escaping before the valve closes. Note that the total mass exhausted is equal to the total mass inducted, another sign that the model is working as designed.

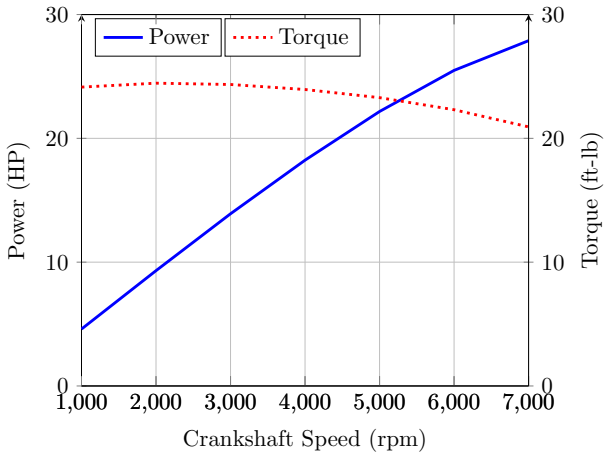

(A) Engine Power and Torque

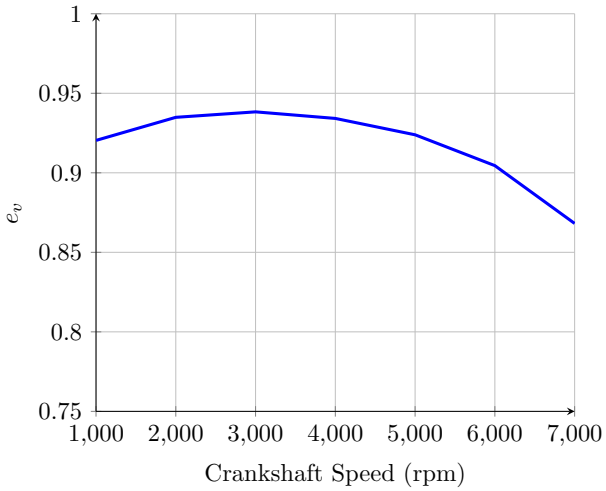

(B) Engine Volumetric Efficiency

FIGURE 6.9. High-Level Results

Figure 6.9a is arguably the most important result the simulation can produce. To an engine designer, vehicle or equipment engineer, or intake and exhaust system designer, the power the engine generates and the character of its delivery is of greatest importance. The power is calculated as described in Chapter 3. It is a high-level result, as it isn't revealed by basic data. Instead, pressure must be integrated over the engine's two-revolution cycle. The values predicted here are in line with what would be expected from the real engine of Chapter 2. Note that the curve is not linear. It appears there may be a peak at a higher rpm. This is a normal characteristic of engine power delivery; there is always a power peak. The torque curve is calculated from the power values by:

$$\tau = \frac{P}{\omega} \tag{6.23}$$

where τ is torque, P is power and ω is the rotational velocity of the crankshaft. Figure 6.9b shows the "volumetric efficiency" of the engine. This is a measure of how much the cylinder fills with charge over the intake stroke. A value of 1 indicates that the density of the charge is equivalent to the ambient air density at intake valve closure. This curve also typically has a peak value.

Remember that these results include no loss modeling. They represent only the fluid dynamics and thermodynamics active in the engine.

Experience shows that real engines are sensitive to changes in cam timing. To be accurate, an engine model must also be sensitive to such changes. Figure 6.10 shows the model's power, torque and volumetric efficiency predictions when the intake cam is advanced and retarded 5°. Figure 6.10a shows that power increases slightly over the entire rpm range when the

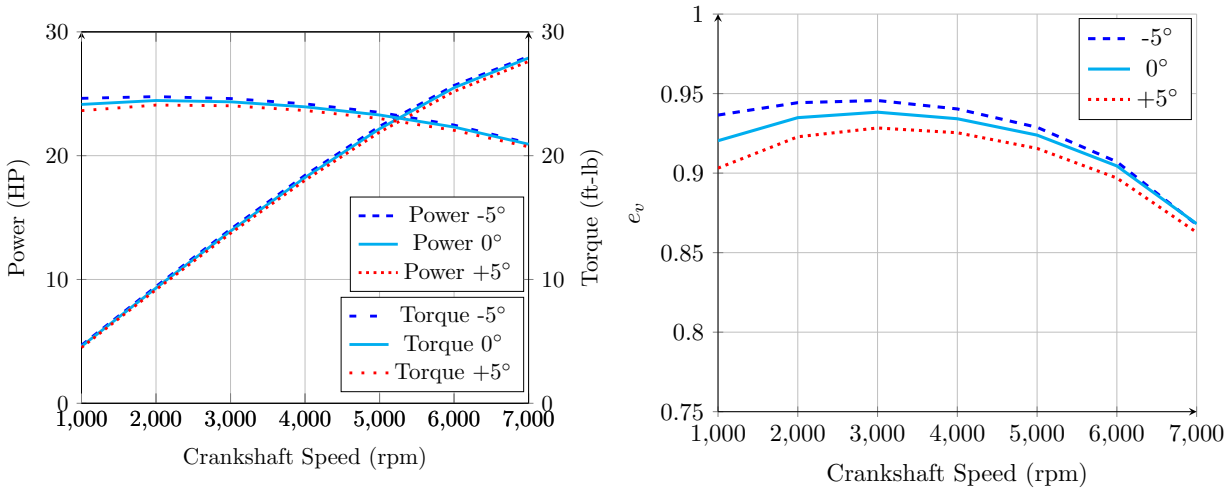

(A) Power and Torque Variation

(B) Volumetric Efficiency Variation

FIGURE 6.10. Model Sensitivity to Cam Timing

intake timing is advanced (-5°) and decreases slightly when the timing is retarded (+5°). Torque follows the same pattern, with the variation greatest at low rpm. Figure 6.10b shows the variation in volumetric efficiency as the intake timing is varied. E_v increases, especially at low rpm, when the intake timing is advanced and drops when the timing is retarded. So we do see that the model is sensitive to changes in valve timing.

We've skipped one key question: how do we start the simulation? For measuring power and for observing the charge and flow values over the engine's two revolution cycle, it's most convenient to start the simulation with the piston at TDC of the compression stroke. Then the simulation is advanced 720° into the future, completing one cycle and arriving at the beginning of another. But does this work? Figure 6.11a shows how charge pressure responds to such a strategy.

Here, the charge is initialized to ambient density, pressure and temperature at TDC of the compression stroke. The simulation begins marching forward from 0°. The pressure is low and begins to rise due to combustion. The simulation advances through the power and

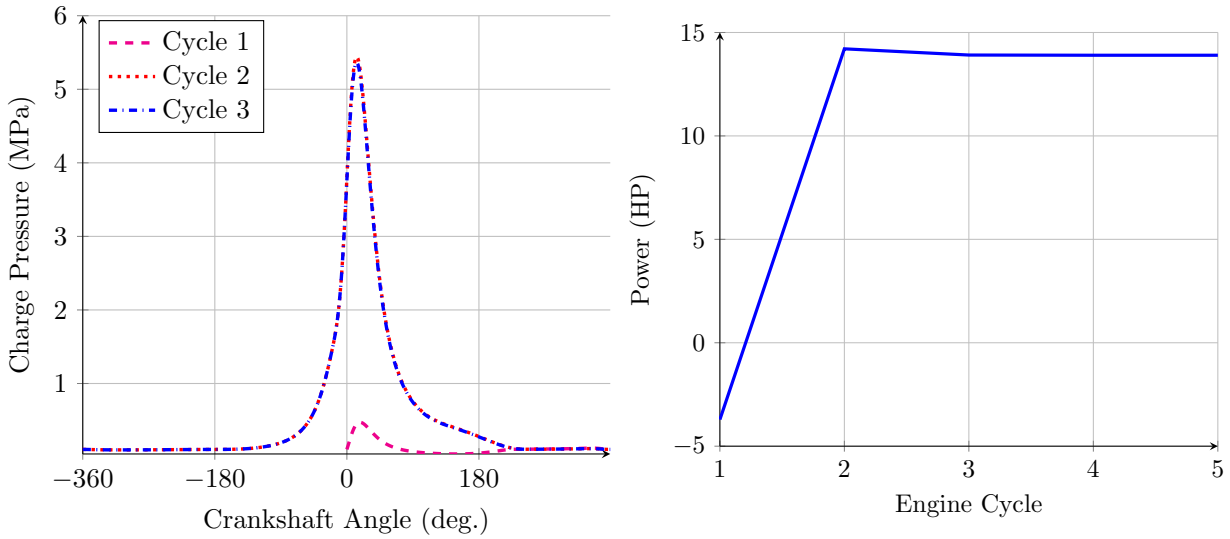

(A) Charge Pressure Converging

(B) Power Converging

FIGURE 6.11. Simulation Convergence, 3,000 rpm

exhaust strokes, arriving at the right-hand side of the plot at the top of the exhaust stroke. We follow around to -360° and watch as we advance through the intake and compression strokes, the pressure following a very different path as the engine begins a second cycle. Note how, by the third cycle, the pressure converges on a final, repetitive curve. Figure 6.11b shows the power predicted by the simulation, given the same startup strategy, over a succession of cycles. Note how the measurement converges on a final value over three cycles. The convergence indicates that this is a valid approach to starting the simulation. But we need to keep in mind that the simulation must be cycled through two thermodynamic cycles–four crankshaft revolutions–before the physics settle and we can consider the data accurate. All of the figures above are generated with this in mind.

CHAPTER 7

Quasi-One-Dimensional Intake and Exhaust Flow Modeling

Modeling the intake and exhaust flows with the isentropic flow equations, as in the previous chapter, is a reasonably simple solution that, combined with the model of the charge in the cylinder, provides a very realistic simulation of a piston engine in operation, with a high degree of functionality and realism. But it has clear shortcomings. At each timestep, when the intake and exhaust Mach numbers are calculated, there is an implicit assumption that the velocity, density and temperature of the flows instantaneously arrive at the new values. But air has mass, and so we know that, even if the rate of acceleration is very high, it is still finite. Also, the intake and exhaust tracts of a real, installed engine—the flowpaths from the cylinder to the atmosphere—are often quite long and enclose a significant mass of air, which must flow and stop cyclically. The simple model doesn't account for the inertia or momentum of the air in those flows. We ask, "are those physics important?" To find out, will compare the simple-flow results to those of a higher-order, higher-fidelity model.

Again, a three-dimensional CFD model would be the most desirable for realism and accuracy. But that approach is far too computationally expensive for our purposes. Instead, we will take the next step up in realism, and unfortunately, a great step up in complexity, from the simple approach and model the intake and exhaust flows using a Quasi-One-Dimensional (Q1D) approach. In a Q1D model, the assumption is that the flow is enclosed in a conduit or duct of unspecified cross-sectional shape but of known cross-sectional area. The sectional

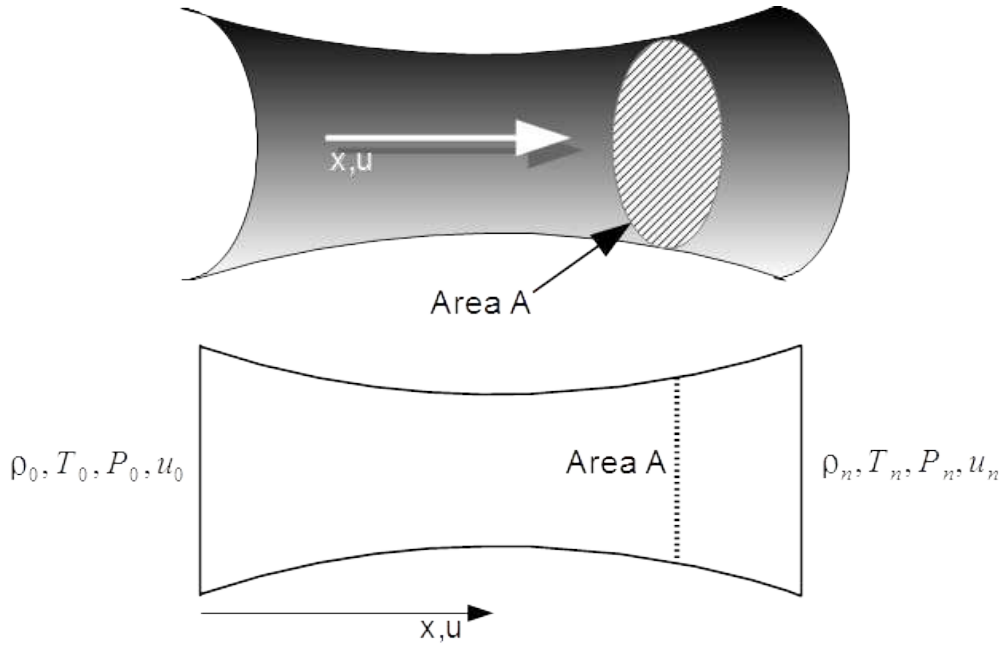

FIGURE 7.1. A Quasi-One-Dimensional Duct

shape of the duct isn't a factor in the final equations, and can therefore be thought of as any arbitrary shape. But usually, for simplicity in derivation and thought experiment, the conduit is assumed to be circular.

Figure 7.1 shows a duct in cross section. At any point along the duct we can measure or specify a cross-sectional area, A. For the Q1D model, we specify that there is only one dimension, x. Even though the duct is, in our imagination, a three-dimensional object, we will say that there is no measurement in the y- and z-dimensions and, importantly, *there is no flow in the y- or z-directions.* Velocities v and w are both zero. We also specify that fluid properties—velocity, density, temperature and pressure are constant across any cross section. In reality this assemblage of requirements is impossible. If the duct changes area, there must be flow in three dimensions. But if the area change is gradual and smooth, and if the velocity in the x-direction is an order or two of magnitude larger than the transverse velocities would be, this is actually not a bad approximation. Closed-form and computational Q1D analyses

show surprisingly good agreement with flow through real nozzles [56, 29, 24]. Note that the duct doesn't go to infinity in either direction. There will always be two ends separated by a finite length of duct. We will be modeling a non-isentropic flow, and so the values of the fluid properties will be known, specified, at each end.

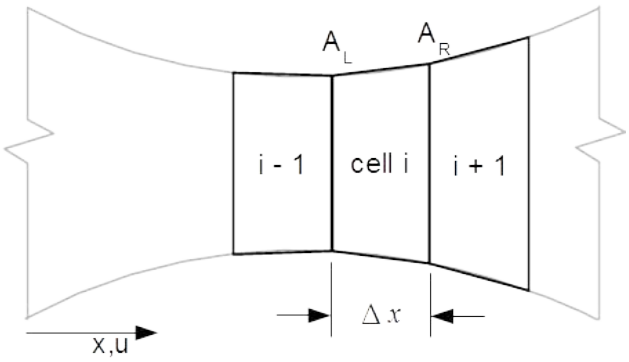

FIGURE 7.2. Q1D Duct Discretized into Cells

Figure 7.2 shows a schematic of a duct in cross-section. The duct is divided into discrete volumes or cells, with the cell of interest labeled i. The cell in the negative x-direction is labeled i - 1 and the cell in the positive x-direction is labeled i + 1. Cell i is enclosed by a control volume that is bounded on the left by the fully permeable cross-sectional area A_l and on the right by the permeable cross-sectional area A_r. At top and bottom, the control volume is bounded by solid, non-permeable walls. We will assume that those walls are linear, connecting A_l to A_r. The length of each cell is Δx and we will assume that the cell lengths are *not* equal. We'll call the collection of cells that comprise a duct a "mesh". And Δx along the mesh will be non-uniform. It is clear from the figure that the straight control volume walls don't perfectly match the smooth curve of the duct. But as Δx gets smaller the approximation gets better and better.

We're going to apply the integral form of the Euler Equations [29, 24, 37] to the control volume of cell i. In doing so, we will be developing what is commonly called a "Finite Volume" approach to solving the flow along the duct.

7.1. The Continuity Equation

The continuity equation of the Euler Equations is:

$$\frac{\partial}{\partial t}\iiint_{\mathcal{V}} \rho d\mathcal{V} + \iint_{S} \rho \vec{V} \cdot d\vec{S} = 0 \tag{7.1}$$

Expanding the dot product and noting that v and w are zero,

$$\frac{\partial}{\partial t}\iiint_{\mathcal{V}} \rho d\mathcal{V} + \iint_{S} \rho \left(u\, dS_x + \cancelto{0}{v\, dS_y} + \cancelto{0}{w\, dS_z} \right) = 0 \tag{7.2}$$

gives us the continuity equation specialized to one-dimensional flow:

$$\underbrace{\frac{\partial}{\partial t}\iiint_{\mathcal{V}} \rho\, d\mathcal{V}}_{1} + \underbrace{\iint_{S} \rho u\, dS_x = 0}_{2} \tag{7.3}$$

Figure 7.3 is a schematic of cell i. The cell has volume $\mathcal{V}$ and the fluid in the cell has the properties velocity, u; density, ρ; temperature, T and pressure, P. The control surface surrounding the cell encloses volume $\mathcal{V}$ and has four discrete surfaces, each with its own

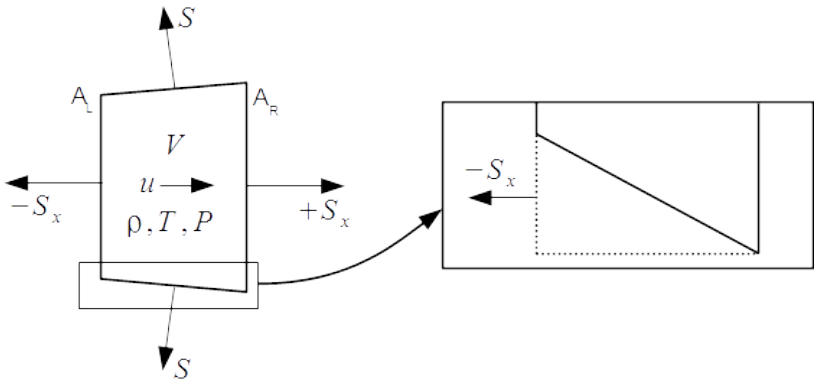

FIGURE 7.3. Cell i Surface Areas

surface normal vector, S. Term 1 of Equation 7.3 is the rate of change of mass in the cell. Applied to cell i, it becomes:

$$\frac{\partial}{\partial t}\iiint_{\mathcal{V}} \rho d\mathcal{V} = \frac{d}{dt}\left(\rho \mathcal{V}\right) \tag{7.4}$$

Term 2 represents the integrated mass flux across the control surface. dS_x is the surface unit normal vector pointing *out* of the volume in the x-direction. Integrated, the unit surface normal vectors become the x-areas of each discrete surface of the cell, S_x. Because of the cell's discrete surfaces, we can convert the integral to a sum. The fluid properties can vary in the x-direction and so we must perform the product, $\rho u S_x$, to form the integrand at each surface location. On the left side of the cell the product becomes $-\rho u A_l$, the negative associated with the negative-pointing area vector. On the right side, we have $\rho u A_r$ and at the walls, since there is no flow across them, we have 0. Term 2 becomes:

$$\iint_{S} \rho u \, dS_x = \sum_{S} \rho u S_x \tag{7.5}$$

And the discretized continuity equation is:

$$\frac{d}{dt}\left(\rho\mathcal{V}\right) + \sum_{S} \rho u S_x = 0 \tag{7.6}$$

For the mass flux term, term 2, the flow properties are evaluated at the surface of the cell. But exactly where are the values defined? We will stipulate that the primitive values are defined at the *center* of each cell, the point equidistant from the left and right faces, creating a "cell-centered" approach [57, 58]. With the values defined at the cell centers, we must find some way of approximating the values at the cell faces. We will employ the simplest approach, a linear interpolation between cell i and its neighbors. Keeping in mind that we've declared the mesh to be non-uniform, for cell i's right-hand face a general property value, F, is:

$$F_r = F_i + \left(\frac{\Delta x_i}{\Delta x_i + \Delta x_{i+1}}\right)\left(F_{i+1} - F_i\right) \tag{7.7}$$

$$= F_i + Z_r\left(F_{i+1} - F_i\right) \tag{7.8}$$

And for a value at cell i's left face:

$$F_l = F_i - \left(\frac{\Delta x_i}{\Delta x_{i-1} + \Delta x_i}\right)\left(F_i - F_{i-1}\right) \tag{7.9}$$

$$= F_i - Z_l\left(F_i - F_{i-1}\right) \tag{7.10}$$

or, using the mass flux (ρu) from Equation 7.6 as an example:

$$(\rho u)_r = (\rho u)_i + Z_r \left[(\rho u)_{i+1} - (\rho u)_i\right] \tag{7.11}$$

$$(\rho u)_l = (\rho u)_i - Z_l \left[(\rho u)_i - (\rho u)_{i-1}\right] \tag{7.12}$$

This approach to approximating the values at the cell faces provides a solution that is second order-accurate in space [59, 57, 58]. Note how the quantity with the cell lengths, which we will call Z, is a proportioning term. When cell i and its neighbor are the same length, the approximation becomes a simple average.

There is no flow across the cell (duct) walls, and so ρu is zero there. We can now write the continuity equation in semi-discrete form:

$$\frac{d}{dt}\underbrace{(\rho \mathcal{V})}_{a} - \underbrace{A_l \left\{(\rho u)_i - Z_l \left[(\rho u)_i - (\rho u)_{i-1}\right]\right\}}_{b} + \underbrace{A_r \left\{(\rho u)_i - Z_r \left[(\rho u)_{i+1} - (\rho u)_i\right]\right\}}_{c} = 0 \tag{7.13}$$

Note the form of terms b and c in Equation 7.13. They are the mass flux through the left and right cell boundaries, respectively. That the difference between them is equal to the rate of change of mass within the cell makes complete sense and gives us some confidence that the derivation is correct. We can approximate the volume of the cell by taking the average area and multiplying by the length:

$$\mathcal{V}_i = \frac{A_l + A_r}{2} \Delta x = \bar{A} \, \Delta x \tag{7.14}$$

But we must consider a subtle issue: these equations are derived from the conservation form of the Euler Equations. Term a of Equation 7.13, which is the mass within a given cell along the duct, is considered a "conserved value" across the domain. Under steady-state conditions, the mass flow rate will be constant across the domain, even across shock waves, if they exist. But the inclusion of Δx in this term stipulates that Δx is also conserved. And we've already stated that it isn't. This means that, when Δx changes along the domain, the conserved value being constant, we will see a compensating change in ρ, a mathematical artifact. So we must remove Δx from this term. Since it doesn't change with time, we can move it out from the time derivative:

$$\frac{\partial}{\partial t}\iiint_{\mathcal{V}} \rho d\mathcal{V} = \Delta x \frac{d}{dt}\left(\rho \bar{A}\right) \tag{7.15}$$

(7.16)

$$\Delta x \frac{d}{dt}\left(\rho\bar{A}\right) - A_l\left\{(\rho u)_i - Z_l\left[(\rho u)_i - (\rho u)_{i-1}\right]\right\} + A_r\left\{(\rho u)_i - Z_r\left[(\rho u)_{i+1} - (\rho u)_i\right]\right\} = 0$$

In an attempt to minimize algebraic complexity, let's call:

$$\boxed{U_1 \equiv \rho\bar{A} \qquad \text{and} \qquad F_1 \equiv \rho u} \tag{7.17}$$

Finally then, the semi-discrete, quasi-one-dimensional continuity equation is:

$$\boxed{\left(\frac{dU_1}{dt}\right)_i = \frac{1}{\Delta x_i}\left\{A_l\left[F_{1_i} - Z_l\left(F_{1_i} - F_{1_{i-1}}\right)\right] - A_r\left[F_{1_i} + Z_r\left(F_{1_{i+1}} - F_{1_i}\right)\right]\right\}} \tag{7.18}$$

7.2. The Momentum Equation

The momentum equations of the Euler Equations are:

$$\frac{\partial}{\partial t}\iiint_{\mathcal{V}} \rho\vec{V}d\mathcal{V} + \iint_S \left(\rho\vec{V}\cdot d\vec{S}\right)\vec{V} = -\iint_S P d\vec{S} + F_{viscous} \tag{7.19}$$

This is a vector equation that expands into three velocity components. Keeping in mind that $\vec{V}\cdot d\vec{S} = u\,dS_x + \cancelto{0}{v}\,dS_y + \cancelto{0}{w}\,dS_z = u\,dS_x$, the equation becomes:

$$\frac{\partial}{\partial t}\iiint_{\mathcal{V}} \rho u d\mathcal{V} + \iint_S (\rho u)\,u dS_x = -\iint_S P dS_x + F_{vx} \tag{7.20}$$

$$\frac{\partial}{\partial t}\iiint_{\mathcal{V}} \cancelto{0}{\rho v}d\mathcal{V} + \iint_S \cancelto{0}{\left(\rho v\right)}u dS_x = -\iint_S \cancelto{0}{P dS_y} + \cancelto{0}{F_{vy}} \tag{7.21}$$

$$\frac{\partial}{\partial t}\iiint_{\mathcal{V}} \cancelto{0}{\rho w}d\mathcal{V} + \iint_S \cancelto{0}{\left(\rho w\right)}u dS_x = -\iint_S \cancelto{0}{P dS_z} + \cancelto{0}{F_{vz}} \tag{7.22}$$

The u and v equations disappear completely and we're left with a single momentum equation, specialized to one-dimensional flow:

$$\underbrace{\frac{\partial}{\partial t}\iiint_{\mathcal{V}} \rho u \, d\mathcal{V}}_{1} + \underbrace{\iint_{S} \rho u^2 \, dS_x}_{2} = -\underbrace{\iint_{S} P \, dS_x}_{3} + F_{vx} \tag{7.23}$$

Applied to cell i of Figure 7.3, term 1 of Equation 7.23 becomes:

$$\frac{\partial}{\partial t}\iiint_{\mathcal{V}} \rho u d\mathcal{V} = \rho u \mathcal{V} \tag{7.24}$$

As in the continuity equation, term 2 of Equation 7.23 becomes:

$$\iint_{S} \rho u^2 \, dS_x = \sum_{S} \rho u^2 \, S_x \tag{7.25}$$

Like term 2, term 3 operates over each of the cell faces and in discrete form becomes:

$$\iint_{S} P \, dS_x = \sum_{S} P S_x \tag{7.26}$$

We will leave the viscous term undefined for now. But with the terms defined as above, the semi-discrete, one-dimensional form of the momentum equation is:

$$\frac{d}{dt}\left(\rho u \mathcal{V}\right) + \sum_{S} \rho u^2 \, S_x = -\sum_{S} P S_x + F_{vx} \tag{7.27}$$

The momentum flux term, term 2 of Equation 7.23, is evaluated as the mass flux term is for the continuity equation. We will estimate the values of ρ and u at the left and right cell boundaries using a linear interpolation with the neighboring values.

$$\left(\rho u^2\right)_r = \left(\rho u^2\right)_i + Z_r \left[\left(\rho u^2\right)_{i+1} - \left(\rho u^2\right)_i\right] \tag{7.28}$$

$$\left(\rho u^2\right)_l = \left(\rho u^2\right)_i - Z_l \left[\left(\rho u^2\right)_i - \left(\rho u^2\right)_{i-1}\right] \tag{7.29}$$

Term 3 is a force term; we are calculating the force on the fluid, applied at the boundaries of the cell. Since the surface integrand doesn't contain a velocity value, all four surfaces enter into the discrete sum, unlike in term 2. We will evaluate it at the left and right cell faces and at the solid cell walls. At the left and right faces, we'll interpolate the pressure. At the walls, we can envision that the center of each wall aligns with the center of the cell. And so we'll say that the pressure at the cell center acts there. Observing Figure 7.3, we see that the pressure doesn't simply act on the area of each wall. Instead, it acts on the *x-oriented area*, S_x of each wall. And looking at the Figure, we can see that there are two S_x areas, at top and bottom. Then the total x-area presented by the walls is equal to $A_l - A_r$. If A_l is greater than A_r, the area vector is positive. If A_l is smaller than A_r the vector is negative.

Assembling each of these terms into a single equation:

(7.30)

$$\frac{d}{dt}\left(\rho u \mathcal{V}\right) + A_r \left\{\left(\rho u^2\right)_i + Z_r \left[\left(\rho u^2\right)_{i+1} - \left(\rho u^2\right)_i\right]\right\} - A_l \left\{\left(\rho u^2\right)_i - Z_l \left[\left(\rho u^2\right)_i - \left(\rho u^2\right)_{i-1}\right]\right\}$$
$$= -A_r \left\{P_i + Z_r \left[P_{i+1} - P_i\right]\right\} + A_l \left\{P_i - Z_l \left[P_i - P_{i-1}\right]\right\} - P_i \left(A_l - A_r\right) + F_{vx}$$

Combining the flux and pressure terms,

$$\begin{aligned}\frac{d}{dt}\left(\rho u\mathcal{V}\right) = &-A_r\left\{\left(\rho u^2+P\right)_i + Z_r\left[\left(\rho u^2+P\right)_{i+1} - \left(\rho u^2+P\right)_i\right]\right\} \\ &+A_l\left\{\left(\rho u^2+P\right)_i - Z_l\left[\left(\rho u^2+P\right)_i - \left(\rho u^2+P\right)_{i-1}\right]\right\} \\ &-P_i\left(A_l - A_r\right) + F_{vx}\end{aligned} \tag{7.31}$$

As above, we can approximate the left-hand side of Equation 7.31 with:

$$\frac{d}{dt}\left(\rho u\mathcal{V}\right) = \frac{d}{dt}\left(\rho u\bar{A}\Delta x\right) \tag{7.32}$$

And since Δx isn't conserved,

$$\frac{d}{dt}\left(\rho u\mathcal{V}\right) = \Delta x\frac{d}{dt}\left(\rho u\bar{A}\right) \tag{7.33}$$

Then, if we call,

$$\boxed{U_2 \equiv \rho u\bar{A} \qquad \text{and} \qquad F_2 \equiv \rho u^2 + P \qquad \text{and} \qquad J_2 \equiv -P\left(A_l - A_r\right) + F_{vx}} \tag{7.34}$$

the semi-discrete, quasi-one-dimensional momentum equation is:

(7.35)

$$\boxed{\left(\frac{dU_2}{dt}\right)_i = \frac{1}{\Delta x_i}\left\{A_l\left[F_{2_i} - Z_l\left(F_{2_i} - F_{2_{i-1}}\right)\right] - A_r\left[F_{2_i} + Z_r\left(F_{2_{i+1}} - F_{2_i}\right)\right] + J_{2_i}\right\}}$$

7.3. The Energy Equation

The energy equation of the Euler Equations is:

(7.36)

$$\frac{\partial}{\partial t}\iiint_{\mathcal{V}} \rho\left(e + \frac{\vec{V}^2}{2}\right) d\mathcal{V} + \iint_S \rho\left(e + \frac{\vec{V}^2}{2}\right)\vec{V}\cdot d\vec{S} = \iiint_{\mathcal{V}} \rho\dot{q} d\mathcal{V} - \iint_S P\vec{V}\cdot d\vec{S} + \dot{W}_{viscous}$$

Expanding the dot products and noting that $\vec{V} = u$, we have the energy equation specialized to one-dimensional flow:

(7.37)

$$\underbrace{\frac{\partial}{\partial t}\iiint_{\mathcal{V}} \rho\left(e + \frac{u^2}{2}\right) d\mathcal{V}}_{1} + \underbrace{\iint_S \rho\left(e + \frac{u^2}{2}\right) u\, dS_x}_{2} = \underbrace{\iiint_{\mathcal{V}} \rho\dot{q} d\mathcal{V}}_{3} - \underbrace{\iint_S Pu\, dS_x}_{4} + \dot{W}_{vx}$$

Term 1 of Equation 7.37, applied to Figure 7.3 is:

(7.38)

$$\frac{\partial}{\partial t}\iiint_{\mathcal{V}} \rho\left(e + \frac{u^2}{2}\right) d\mathcal{V} = \frac{d}{dt}\left[\rho\left(e + \frac{u^2}{2}\right)\mathcal{V}\right] = \Delta x \frac{d}{dt}\left[\rho\left(e + \frac{u^2}{2}\right)\bar{A}\right]$$

To reduce algebraic clutter, let's call,

$$e' \equiv e + \frac{u^2}{2} \tag{7.39}$$

Then,

$$\frac{\partial}{\partial t} \iiint_{\mathcal{V}} \rho \left(e + \frac{u^2}{2} \right) d\mathcal{V} = \Delta x \, \frac{d}{dt} \left(\rho e' \bar{A} \right) \tag{7.40}$$

Discretized, term 2 of Equation 7.37 becomes:

$$\iint_{S} \rho \left(e + \frac{u^2}{2} \right) u \, dS_x = \iiint_{S} \rho e' u \, dS_x = \sum_{S} \rho e' u S_x \tag{7.41}$$

And evaluating the sum,

(7.42)

$$\sum_{S} \rho e' u S_x = A_r \left\{ (\rho e' u)_i + Z_r \left[(\rho e' u)_{i+1} - (\rho e' u)_i \right] \right\} - A_l \left\{ (\rho e' u)_i - Z_l \left[(\rho e' u)_i - (\rho e' u)_{i-1} \right] \right\}$$

Term 3 of Equation 7.37 is:

$$\iiint_{\mathcal{V}} \rho \dot{q} d\mathcal{V} = \rho \dot{q} \mathcal{V} = \rho \dot{q} \bar{A} \Delta x \tag{7.43}$$

In practice, $\dot{q}$ would be a function expressing the rate of conductive and convective heat transfer from the fluid within a cell to the cell's walls, or vice-versa. While it's depicted

as a source term here, it could easily contain surface and volume integrals of its own. And incorporating it could, itself, prove a significant line of research. For the sake of brevity in an already very full study, we are going to neglect this piece of complex physics and leave it to be added as future research. So at this point, now that we have identified and defined it, we will drop term 3.

And finally, in discretized form, term 4 of Equation 7.37 is:

$$\iint_S Pu\, dS_x = \sum_S Pu\, S_x \tag{7.44}$$

While term 4 resembles the pressure term of the momentum equation, the velocity value makes it go to zero at the walls; we only evaluate the sum at the left and right boundaries of cell i:

$$\sum_S Pu\, S_x = A_r \left\{ (Pu)_i + Z_r \left[(Pu)_{i+1} - (Pu)_i \right] \right\} - A_l \left\{ (Pu)_i - Z_l \left[(Pu)_i - (Pu)_{i-1} \right] \right\} \tag{7.45}$$

We can combine terms 2 and 4, Equations 7.42 and 7.45:

(7.46)

$$\iint_S \rho\left(e + \frac{u^2}{2}\right) u\, dS_x + \iint_S Pu\, dS_x$$

$$= A_r\left\{(\rho e'u)_i + Z_r\left[(\rho e'u)_{i+1} - (\rho e'u)_i\right]\right\} - A_l\left\{(\rho e'u)_i - Z_l\left[(\rho e'u)_i - (\rho e'u)_{i-1}\right]\right\}$$

$$+ A_r\left\{(Pu)_i + Z_r\left[(Pu)_{i+1} - (Pu)_i\right]\right\} - A_l\left\{(Pu)_i - Z_l\left[(Pu)_i - (Pu)_{i-1}\right]\right\}$$

$$= A_r\left\{(\rho e'u + Pu)_i + Z_r\left[(\rho e'u + Pu)_{i+1} - (\rho e'u + Pu)_i\right]\right\}$$

$$- A_l\left\{(\rho e'u + Pu)_i - Z_l\left[(\rho e'u + Pu)_i - (\rho e'u + Pu)_{i-1}\right]\right\}$$

For now, we'll leave the viscous work term undefined.

To reduce algebraic clutter, we'll say:

(7.47)

$$\boxed{U_3 \equiv \rho e' \bar{A} \qquad F_3 \equiv \rho e'u + Pu \qquad J_3 \equiv \dot{W}_{vx}}$$

and collecting all of the terms above the semi-discrete quasi-one-dimensional energy equation is:

(7.48)

$$\boxed{\left(\frac{dU_3}{dt}\right)_i = \frac{1}{\Delta x_i}\left\{A_l\left[F_{3_i} - Z_l\left(F_{3_i} - F_{3_{i-1}}\right)\right] - A_r\left[F_{3_i} + Z_r\left(F_{3_{i+1}} - F_{3_i}\right)\right] + J_{3_i}\right\}}$$

7.4. The Equations Collected

Finally, we have the semi-discrete, finite-volume governing equations of quasi-one-dimensional flow, all in one place:

(7.49)

$$\left(\frac{dU_1}{dt}\right)_i = \frac{1}{\Delta x_i}\left\{A_l\left[F_{1_i} - Z_l\left(F_{1_i} - F_{1_{i-1}}\right)\right] - A_r\left[F_{1_i} + Z_r\left(F_{1_{i+1}} - F_{1_i}\right)\right] + J_{1_i}\right\}$$

$$\left(\frac{dU_2}{dt}\right)_i = \frac{1}{\Delta x_i}\left\{A_l\left[F_{2_i} - Z_l\left(F_{2_i} - F_{2_{i-1}}\right)\right] - A_r\left[F_{2_i} + Z_r\left(F_{2_{i+1}} - F_{2_i}\right)\right] + J_{2_i}\right\}$$

$$\left(\frac{dU_3}{dt}\right)_i = \frac{1}{\Delta x_i}\left\{A_l\left[F_{3_i} - Z_l\left(F_{3_i} - F_{3_{i-1}}\right)\right] - A_r\left[F_{3_i} + Z_r\left(F_{3_{i+1}} - F_{3_i}\right)\right] + J_{3_i}\right\}$$

(7.50)

$$\boxed{\begin{aligned} Z_r &= \frac{\Delta x_i}{\Delta x_i + \Delta x_{i+1}} \\ Z_l &= \frac{\Delta x_i}{\Delta x_{i-1} + \Delta x_i} \end{aligned}}$$

We can write a single, generic equation to represent this system,

(7.51)

$$\boxed{\left(\frac{dU}{dt}\right)_i = \frac{1}{\Delta x_i}\left\{A_l\left[F_i - Z_l\left(F_i - F_{i-1}\right)\right] - A_r\left[F_i + Z_r\left(F_{i+1} - F_i\right)\right] + J_i\right\}}$$

where U, F and J are the vectors,

(7.52)

$$\boxed{U = \begin{bmatrix} \rho\bar{A} \\ \rho u\bar{A} \\ \rho e'\bar{A} \end{bmatrix} \begin{matrix} U_1 \\ U_2 \\ U_3 \end{matrix} \qquad F = \begin{bmatrix} \rho u \\ \rho u^2 + P \\ \rho u e' + Pu \end{bmatrix} \begin{matrix} F_1 \\ F_2 \\ F_3 \end{matrix} \qquad J = \begin{bmatrix} 0 \\ -P\left(A_l - A_r\right) + F_{vx} \\ \dot{W}_{vx} \end{bmatrix} \begin{matrix} J_1 \\ J_2 \\ J_3 \end{matrix}}$$

and,

(7.53)
$$\boxed{e' = c_v T + \left(\frac{u^2}{2}\right)}$$

The U values are called the "flux variables". They constitute the solution vector for the problem but are fluxes, not the primitive variables of density, temperature, pressure and velocity. The F values are called the "flux terms". They are also fluxes, of mass, momentum and energy, into a given cell. The J values are source terms, adding or removing mass, momentum or energy from a given cell.

Equations 7.49 allow us to calculate the time-rates of change of the flux variables for any cell in the domain given the flux values of that cell and those of its neighbors. If we integrate the flux variable rates with respect of time, we can obtain the flux variables for the cell. Doing this for each cell in succession, we solve the equations of Q1D flow across the domain. But our true interest is in the primitive variables in each cell. They are the physical values that describe the state of the flow. We also need them to construct the flux and source terms. So we will need to "decode" the flux variables to get to the primitive variables:

(7.54)
$$\boxed{\begin{aligned} \rho &= \frac{U_1}{\bar{A}} \\ u &= \frac{U_2}{U_1} \\ e' &= \frac{U_3}{U_1} \\ T &= \frac{\gamma - 1}{R}\left[\frac{U_3}{U_1} - \frac{1}{2}\left(\frac{U_2}{U_1}\right)^2\right] \end{aligned}}$$

Note that pressure isn't returned among the flux variables. But density and temperature are. We can construct pressure using the perfect gas equation of state, then decode the flux variables for pressure:

$$\boxed{\begin{aligned} P &= \rho R T \\ P &= \frac{\gamma - 1}{\bar{A}} \left(U_3 - \frac{1}{2} \frac{U_2^2}{U_1} \right) \end{aligned}} \tag{7.55}$$

This closes the system of equations. We now have four equations in four unknowns.

7.5. Time-Marching the Q1D Governing Equations

Now we must ask, "How will we march the solution of the Q1D governing equations forward in time?" This is determined by the mathematical nature of the governing equations and by the finite-volume discretization we have created. On a uniform mesh, the linear interpolation we use to approximate the flux values at the cell faces reduces to a central, finite-difference scheme, with the right-hand side of each equation becoming a central, first-difference equation. We've derived the Q1D governing equations from the Euler equations, and so they contain no viscous—physically diffusive or numerically dissipative—terms; they are pure convection equations. They are also nonlinear and their nonlinearity makes it very difficult to study the stability of a solution that marches them forward in time. Researchers have studied Time Marching Methods (TMMs) for space-discretized equations by applying modal analyses to model equations, then examining the amplification factors that drive the transient portion of the solution to grow or decay [59, 58, 60, 61]. For a *linear* convection model equation, discretized using central, first-differences for the spatial derivative, applied

to a 1-dimensional domain with periodic boundaries, we find that the *system* of equations has a set of eigenvalues that are purely imaginary. (Inclusion of viscosity in the governing equations would give the eigenvalues a negative-real component.) Since they are pure convection equations, the Q1D governing equations will also have purely imaginary eigenvalues and behave like the model equation. To march the solution of the equations forward in time, we must choose a Time Marching Method (TMM) that includes at least some of the imaginary axis in its stability region. If a TMM is used that doesn't include part of the imaginary axis, then the eigenvalues of the system won't fall inside of the TMM's stability region and the solution will diverge as it is advanced forward in time.

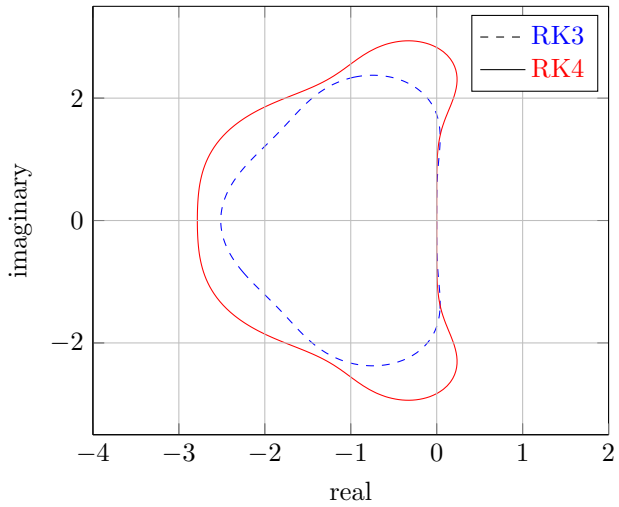

FIGURE 7.4. Runge-Kutta TMM Stability Contours

Figure 7.4 shows the stability contours for the Runge-Kutta RK3 and RK4 TMMs when applied to the central-differenced, linear convection model equation. These TMMs both include part of the imaginary axis in their stability regions and for this reason are commonly used to time-march the Euler and Navier-Stokes equations [58, 60, 57]. For our finite-volume approach, the RK3 and RK4 methods will both produce a solution that is conditionally stable—provided that the timestep is made small enough to keep the system's eigenvalues

within the TMM's stability contour. The RK4 method's stability region extends farther up and down the imaginary axis than that of the RK3 method, and Jameson and Hirsch [57, 58] point out that this allows the use of a Courant-Friedrichs-Lewy (CFL) factor, which multiplies the calculated timestep, of up to $2\sqrt{2}$ or about 2.8 times while still providing a stable solution. This implies that, when a simulation is being time-marched to the steady state, the RK4 method will allow for a larger CFL, less timesteps and faster convergence than the RK3 method. But our application is unsteady, and must match, temporally, the physics that occur in the cylinder. So we will always use a timestep that provides a time-accurate solution, with a CFL value of 1. The author has already shown that the RK3 TMM is sufficient for this application [62], providing stability in all tested conditions. But here, for comparison, we will use the RK4 TMM. Implementations vary. Here, denoting a general variable to be integrated as u and denoting a time derivative of the variable as u', the method is given as [57, 58]:

$$u_0 = u_n \tag{7.56}$$

$$u_1 = u_0 + \frac{1}{2}\Delta t u'_0 \tag{7.57}$$

$$u_2 = u_0 + \frac{1}{2}\Delta t u'_1 \tag{7.58}$$

$$u_3 = u_0 + \Delta t u'_2 \tag{7.59}$$

$$u_{n+1} = u_n + \frac{1}{6}\Delta t \left[u'_0 + 2u'_1 + 2u'_2 + u'_3\right] \tag{7.60}$$

This is just a mathematical description of the method. The process for implementing the scheme is:

(1) Store the current u value for each cell in a safe location, which we'll call u_0.

(2) With the u values for the current timestep still in place, advance the system in time, to sub-timestep u_1, using the current and saved u values and Equation 7.57. For each cell, save a copy of the time derivative for later use.

(3) With the original u_0 values still in place, but with new u values created by the previous operation, advance the system again using Equation 7.58 to sub-timestep u_2. Save a copy of the time derivative for each cell for later use.

(4) Using Equation 7.59, repeat the process again, advancing the system to sub-timestep u_3. Again, save a copy of each time derivative.

(5) Finally, using the stored u_0 value, along with the saved time derivative values, calculate the value of u_{n+1} for each cell using Equation 7.60. The system is now advanced one timestep and the values of u_0 and the stored derivatives can be overwritten.

To facilitate the RK4 operations, we'll need the following data values at each cell:

- The primitive variables, ρ, u, T and P.
- The flux variables U_1, U_2 and U_3.
- The saved flux variable values from the current timestep, U_{1_0}, U_{2_0} and U_{3_0},
- The time-derivatives u'_0, $\left(\frac{dU_1}{dt}\right)_0$, $\left(\frac{dU_2}{dt}\right)_0$ and $\left(\frac{dU_3}{dt}\right)_0$, the flux variable rates from sub-timestep 1.
- The time-derivatives u'_1, $\left(\frac{dU_1}{dt}\right)_1$, $\left(\frac{dU_2}{dt}\right)_1$ and $\left(\frac{dU_3}{dt}\right)_1$, the flux variable rates from sub-timestep 2.
- The time-derivatives u'_2, $\left(\frac{dU_1}{dt}\right)_2$, $\left(\frac{dU_2}{dt}\right)_2$ and $\left(\frac{dU_3}{dt}\right)_2$, the flux variable rates from sub-timestep 3.

- The time-derivatives u_3', $\left(\frac{dU_1}{dt}\right)_3$, $\left(\frac{dU_2}{dt}\right)_3$ and $\left(\frac{dU_3}{dt}\right)_3$, the flux variable rates from sub-timestep 4.
- The cell left and right cross-sectional areas, A_l and A_r.
- The cell average area, $\bar{A}$.
- The artificial viscosity values for each flux variable, S_1, S_2 and S_3.
- The length of the cell, Δx.
- The interpolation proportioning terms, Z_l and Z_r.

The size of the timestep, Δt, is critical to the stability of the solution. If the timestep selected is too large, the eigenvalues of the system move above or below the stability region on the imaginary axis and the solution diverges. To select the correct timestep size we can turn to the characteristics of the system, its eigenvalues.

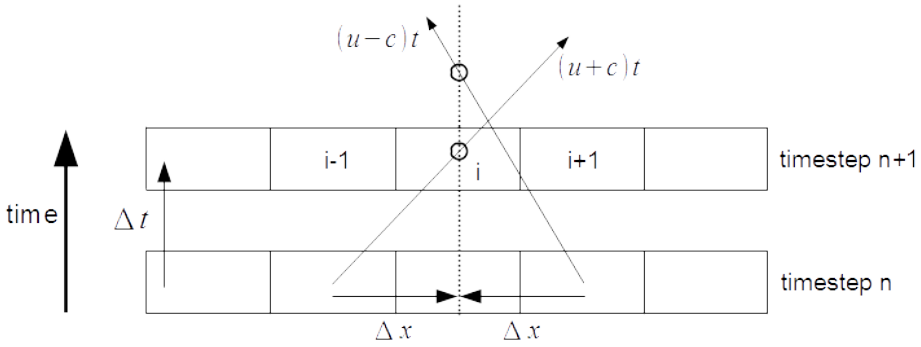

FIGURE 7.5. Propagation of Influences with Time

Figure 7.5 illustrates a segment of the finite-volume mesh centered on cell i. From cell $i-1$, characteristic $u+c$ carries influences through the domain to the right. From cell $i+1$, characteristic $u-c$ carries influences through the domain to the left. As time passes, the influences from each neighbor cell travel through time and space along the characteristic lines $(u+c)t$ and $(u-c)t$. Physically, we must size the timestep so that influences can reach the center of cell i from both of its neighbor cells. From cell $i-1$ it takes,

$$\Delta t = \frac{\Delta x}{u + c} \tag{7.61}$$

for an influence to propagate the distance Δx and reach the center of cell i. From cell $i + 1$ it takes,

$$\Delta t = -\frac{\Delta x}{u - c} \tag{7.62}$$

for an influence to reach the center of cell i. To ensure that influences propagate from both neighbor cells to the center of cell i, we must make both calculations, then take the smaller as the correct timestep. Note that it's possible, when the flow goes supersonic, for either calculation to go undefined or negative. We must trap this condition and avoid making the calculation in that case. We must make these calculations for each cell in the domain, selecting the smaller of the two Δt values as correct for that cell. Then, scanning down the entire domain, we must select the smallest cell Δt value as the Δt for the domain. Doing otherwise would result in one or more cells exceeding its maximum allowable timestep. This calculation is made at the beginning of each RK4 procedure, then the whole system is marched forward one timestep, Δt.

Using the prescribed timestep, which will always be quite small, we can march the whole domain forward in time a prescribed number of seconds—many timesteps. We simply decrement the specified time by ΔT each timestep, marching one final, short timestep at the end. This is necessary since the overall engine model is advanced based on the time required

to move the crankshaft a specified angle. At the top level, we advance the crankshaft one "tick", then advance the Q1D model the equivalent length of time.

7.6. Stability and Accuracy Considerations

Surprisingly, one very demanding task for the Q1D model comes when a valve is closed and the flow in the intake or exhaust tract progresses toward quiescence. At 3,000 rpm the intake valve is closed for about 25 msec. The *largest* Δt we can expect is on the order of 1 μsec, and so the CFD model will be marched ahead at least 25,000 steps with ever-decreasing property value rates that will ultimately be of the same order as the computer's truncation errors. At low RPM this stress grows worse, as the number of timesteps grows with decreasing engine speed.

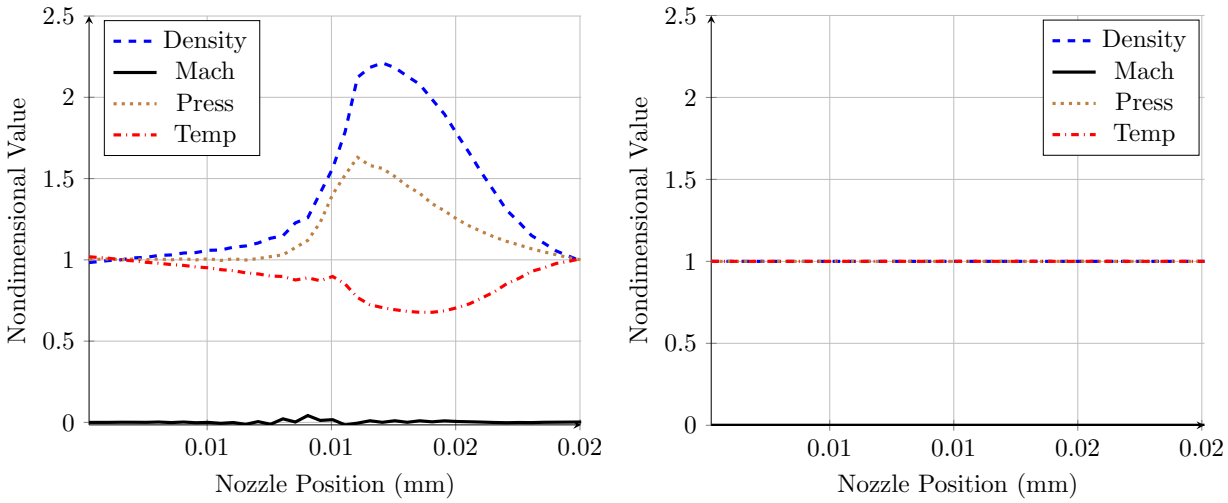

(A) A Valve Quiescently Diverging (B) A Valve Remaining Quiescently Stable

FIGURE 7.6. Mesh-Independence and Stability

Figure 7.6a shows what happens when a valve is closed, initialized to zero velocity and ambient fluid values and marched forward in time 25,000 steps. The velocity should be zero across the duct and the other values should all measure 1.0. Note how density, temperature

and pressure are all diverging from their correct values and causing the velocity to become non-zero. If the number of cells in the duct is reduced, this effect grows. A 19-cell duct can completely diverge, with its properties reaching machine infinity after being advanced 25,000 timesteps.

It turns out that this test is a good measure of "mesh-independence". If a CFD mesh is too coarse, the simulation can't resolve phenomena and flow structures that should be present in the flow and the solution loses accuracy. As more cells are added and the mesh becomes finer, the solution will converge on a final result that includes all of the phenomena and structure that can be modeled by the CFD physics. When the mesh gets extremely coarse, the model can diverge. In our case, with the valve closed, these two results happen at about the same time. As we add cells to the valve, we find a point—46 cells—where grid-independence is reached. The quiescent solution no longer diverges. Figure 7.6b shows the result. Here, a valve with 46 cells is initialized to zero velocity and ambient fluid values and marched 25,000 timesteps into the future with no hint of divergence. We must use at least 46 cells in each 2 cm valve.

While considering stability and accuracy, we must recognize another subtle but important point. In section 7.5 we said that we would find the appropriate Δt value for each cell in the numerical domain, then use the smallest value as the overall Δt in the RK4 timestep. This ensures the system will stay stable, but only a single cell in the entire domain will be marched forward at its optimal rate. All of the other cells in the domain will be marched forward at a sub-optimal Δt. What happens?

Figure 7.7 illustrates a mesh that has been marched one timestep into the future. Because of the governing equations and the discretization we've used, cell i receives information from

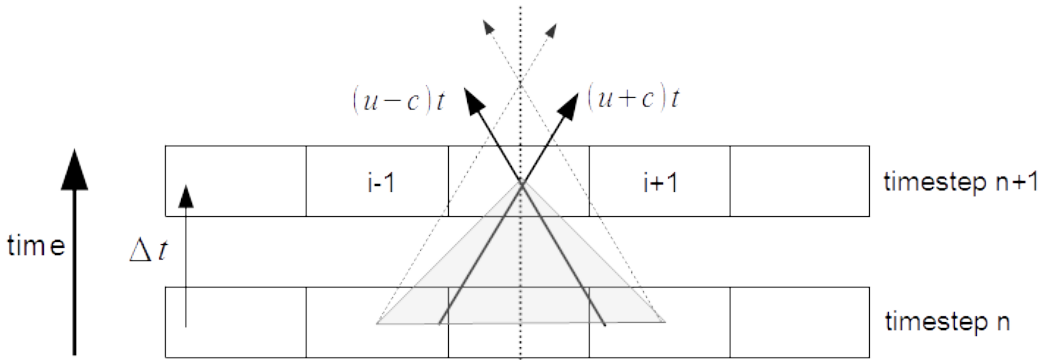

FIGURE 7.7. A Sub-Optimal Timestep

cells $i-1$ and $i+1$. Those cells and cell i itself form cell i's computational "domain of dependence", which is marked by the shaded triangle. The characteristic lines extending from the neighboring cells intersect at the optimal timestep for cell i. If the domain were advanced this far into the future, influences from the centers of the neighboring cells would be carried exactly to the center of cell i and cell i's domain of dependence and the characteristics would coincide. But let's say that, due to conditions at another cell, the actual timestep is smaller. Note where the characteristics drawn through cell i's center (parallel to the characteristics from the neighboring cells) now fall. In this case, cell i's *physical*, or analytical domain of dependence lands somewhere between the neighboring cell centers. But we're still feeding the math with data from the cell centers. This causes the calculation of cell i's flux variable rates to become less accurate. In a simulation marching to a steady-state solution, this isn't as big a problem. Each cell can be advanced at its optimal rate. But in a time-accurate simulation, all of the cells in the domain must be advanced the same timestep. We're saddled with some level of inaccuracy that we must accept. And that's the good news. The bad news is that this introduction of error exacerbates the quiescent flow condition discussed above. By introducing error *and* requiring more timesteps to advance a given time increment, a short timestep causes any marginally stable cell to diverge farther during valve closure. We

must do whatever we can to minimize this condition. In testing, when a valve diverges, it is clear that the intake valve always diverges first. Why? Consider the difference in typical flow temperatures. The intake tract operates at around ambient temperature, 300 K. But the exhaust tract operates at temperatures of 800 K and above. Timestep size is a function of the speed of sound, which is a function of temperature. The calculated timestep for the exhaust tract will always be a fraction of the proper timestep for the intake tract. If both tracts are advanced together, the intake tract will see far more error build-up, causing the intake valves to diverge more rapidly. To combat this, we will model the two tracts as separate domains, each with its own calculated timestep size. Both tracts will be advanced into the future a specified time using the procedure given in section 7.5. This strategy makes the simulation more robust and reduces the possibility of a flow calculation diverging.

7.7. Artificial Viscosity

There is a notable difference between the Q1D equations and the model convection equation used for the modal analyses: the model equation is linear and the Q1D equations are nonlinear. In our analysis, when and where the flow through the duct is smooth, the Q1D equations will exhibit a more linear behavior, and we can expect to see stable predictions of the flow state into the future. But Hirsch [58] points out that when we pair a central-difference spatial discretization with the RK4 TMM, high frequency waves passing through the domain will see amplification factors approaching 1. This can cause the solution to become poorly posed and marginally stable around sharp changes in flow properties or duct areas.

To reduce this tendency, we will employ artificial viscosity terms. These are source terms that are designed to act at points of high pressure gradient in the domain and are dissipative; they consume small amounts of momentum and energy and introduce a negative-real eigenvalue component to the governing equations. This helps to damp-out the oscillations around high-frequency features in the flow and leads to a stable solution. The artificial viscosity is non-physical, and therefore adds error into the solution. Being dissipative, it also causes flow structures to soften. But the artificial viscosity terms are derived to be fourth-order in space and thus are two orders of magnitude below the accuracy of the solution. As long as their influence is kept to a low level, their introduction of error can be kept to acceptable levels. We'll calculate artificial viscosity using the empirical equation provided by Anderson [59]:

$$S_i = C_x \frac{|P_{i+1} - 2P_i + P_{i-1}|}{P_{i+1} + 2P_i + P_{i-1}} (U_{i+1} - 2U_i + U_{i-1}) \tag{7.63}$$

where P is the pressure within a cell, U is the vector of flux variables above and C_x is an adjustable proportioning term that is set through trial and error. To apply artificial viscosity to the Q1D governing equations, we simply add the term to the flux value in each cell after it has been advanced forward in time:

$$(U)_i^{n+1} = \int_n^{n+1} \left(\frac{dU}{dt}\right)_i^n dt + S_i \tag{7.64}$$

The artificial viscosity terms are computationally expensive to calculate. Notionally, we would apply them at the end of each RK4 sub-timestep. But researchers have found that they can be applied at the end of a full RK4 timestep with good results and a significant reduction in computational load [57]. Here, we are applying artificial viscosity once each timestep, after the RK4 process has been completed but before the flux variables have been decoded. This provides very acceptable results.

7.8. Boundary Handling

At the high-level, our problem is an Initial, Boundary-Value Problem. We must specify an initial value for each cell in the domain and, directed by the characteristics of the flow at the cylinder and atmospheric boundaries, also specify certain values there while calculating others. If the boundaries aren't handled correctly, the solution will become ill-posed and we can expect it to diverge. The simplest approach for handling the boundaries is to apply Dirichlet boundary conditions, specifying or calculating the primitive fluid values, by way of the flux variables. For the simulation of external flows, this technique provides a well-posed and stable solution. For unsteady internal flows, the picture isn't so clear. The numerical dissipation of the external solution's large domain softens and damps waves as they travel. And the large, open boundaries of the external flow allow the highest wavelength disturbances to exit the domain. Internal flows like ours have physically smaller domains which dissipate less and walls that reflect and trap disturbances, leading to the buildup of waves that travel back and forth between the boundaries. In the engine simulation at high RPM, the violent stimulation at the cylinder boundary, especially when the valve is just barely open, leads to a buildup of wave fronts with extremely large gradients that eventually cause a cell to

diverge, typically taking its temperature negative. After the first cell diverges, the rest of the cells in the domain diverge in a cascade. After only a few timesteps, the primitive fluid values across the domain go to machine infinity.

To combat this problem, we need to apply some form of boundary handling that allows waves to exit the domain. That is precisely the behavior of "non-reflective" boundary handling. There is no better reason to apply non-reflective boundary handling than to provide a stable solution. But it also offers some other major benefits, providing for greater realism than the pressure-based, "hard" Dirichlet boundary handling.

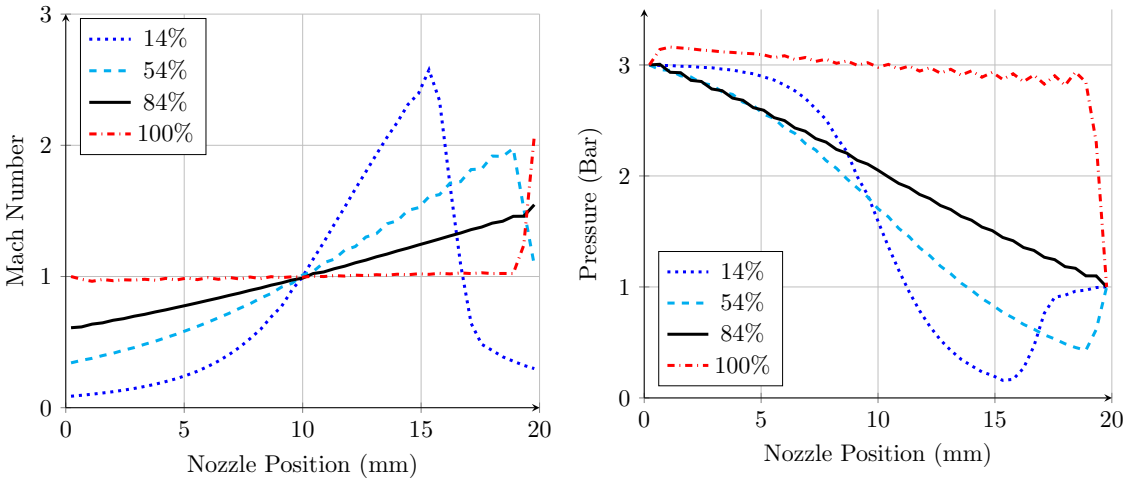

(A) Velocity

(B) Pressure

FIGURE 7.8. A Nozzle Operating at Various Throat Areas with Hard Boundary Handling

Figure 7.8 shows the Q1D model operating with hard boundary handling. The system is solving the flow through a nozzle operating at a number of selected throat areas. The pressure on the 0th end of the nozzle is 3 times atmospheric and the pressure on the Nth end is one atmosphere. At 84% opening, the nozzle is operating at its design operating condition. Figure 7.8a shows the velocity of the frozen, standard air in the 84%-open nozzle accelerating from subsonic to supersonic, and exiting the nozzle supersonically, at atmospheric pressure.

The entire flow through the nozzle is isentropic. Figure 7.8b shows the pressure of the air passing through the nozzle decreasing steadily from 3 atmospheres to 1. When the nozzle is open 14% the air accelerates to about Mach 2.5, then decelerates to subsonic velocity through a shock wave. The air continues to decelerate through the expanding portion of the nozzle and exits subsonically at 1 atmosphere. These are both valid and correct results. But observe the 54% solution. The flow accelerates to supersonic speed through the nozzle, then suddenly drops to lower supersonic speed through a shock wave before exiting. In Figure 7.8b, the pressure drops below atmospheric through the nozzle, then suddenly rises to atmospheric at the exit. This is a correct result up until the exit. At 54%, the nozzle is operating overexpanded. In a real nozzle, the flow would be brought to atmospheric pressure through a train of shock waves *outside of the nozzle exit.* And so the velocity at the exit should be supersonic. Because the "hard" boundary handling imposes atmospheric pressure at the exit, we get an erroneous, non-physical result. With the nozzle 100% open, the flow at the exit should be underexpanded, exiting at about Mach 1 but at greater than atmospheric pressure. In a real nozzle, an annular expansion fan forms outside of the nozzle exit, accelerating the flow to supersonic speed and atmospheric pressure. With the hard boundary handling, we see this happening inside of the nozzle, over a small set of cells. The hard boundary handling can only provide a correct result when the flow at the exit is naturally at atmospheric pressure, that is, subsonic or at the design supersonic velocity.

The hard boundary handling also misses a very important transient result. Figure 7.9 shows a set of Schlieren photographs from Blair [19]. They show the tip of an engine's exhaust pipe as the engine is just beginning its exhaust stroke. Under most conditions, the pressure in the cylinder of an engine is above atmospheric when the exhaust valve opens.

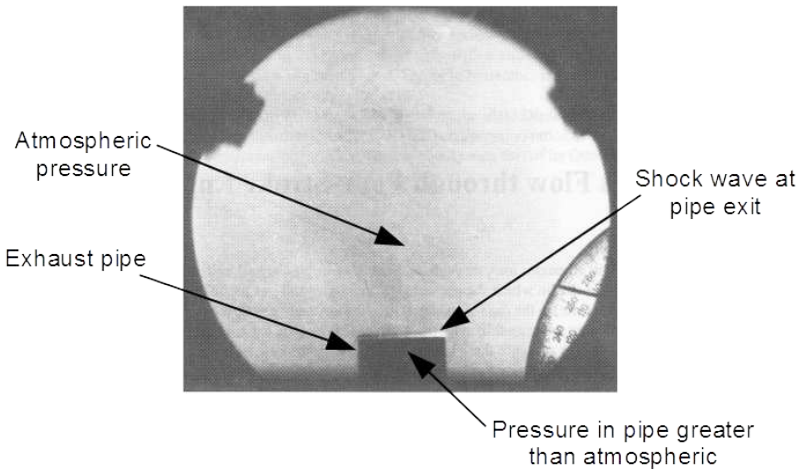

(A) Shock Wave at Exhaust Pipe Exit

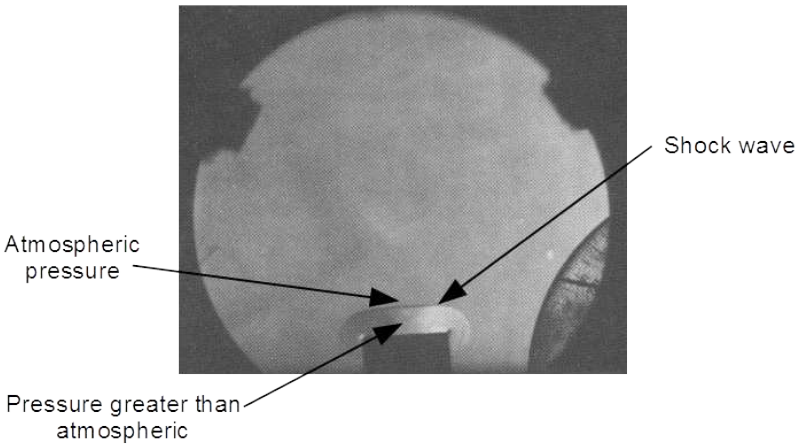

(B) Shock Wave Outside of Pipe Exit

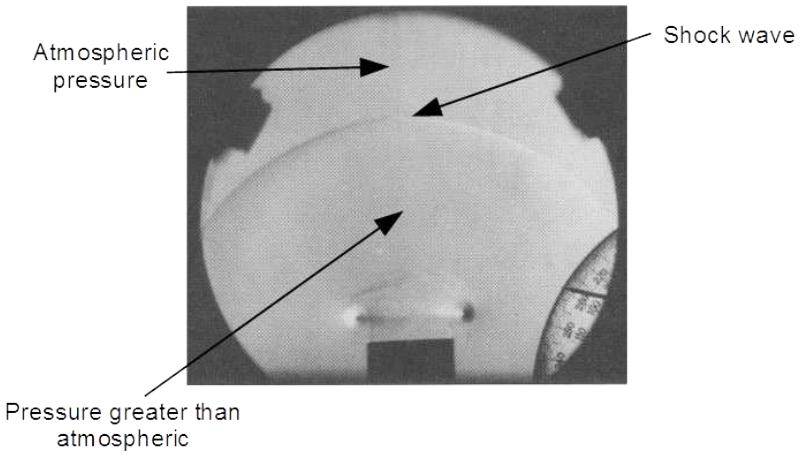

(C) Shock Wave Expanding Three-Dimensionally

FIGURE 7.9. A Shock Wave Exiting an Exhaust Pipe

This results in a shock wave forming and propagating down the pipe. Figure 7.9a shows the shock wave at the pipe exit. We need to observe this photo and think for a minute. What is the pressure at the exit of the pipe? The shock wave is an almost infinitesimally thin discontinuity. We can see from the figure that the pressure in front of the wave is atmospheric. The pressure behind the shock *must* be above atmospheric. Otherwise, the wave would dissipate; it wouldn't be there. So we're looking at a scenario where the pressure at the atmospheric end of the pipe *isn't* atmospheric. It's a physical scenario which the constant-pressure boundary handling can't reproduce. Note the one-dimensionality of the shock wave. This gives a good bit of credence to the notion that we can simulate pipe flow using the Q1D approach. In Figure 7.9b the shock wave has exited the pipe and is beginning to expand three-dimensionally into the atmosphere. What is the pressure at the pipe exit now? The pressure in front of the shock is still atmospheric. And since the shock wave still exists, we know the pressure behind the shock is still above atmospheric, but likely decreasing as the shock wave expands into the atmosphere. Figure 7.9c shows the shock wave a short distance from the pipe exit, and becoming nearly spherical as it expands. At this point, we still can't apply atmospheric pressure to the Nth cell of the pipe and get a correct physical result. Even though the shock wave has exited the pipe, the pressure at the exit takes a finite length of time to return to atmospheric.

The derivation and application of non-reflective boundary handling to the Q1D model is a non-trivial task. To help maintain the flow of this chapter, we will include it as Appendix A. For now, let's simply say that the non-reflective approach creates a set of Neumann boundary conditions that we apply to the 0th and Nth cells of the complete tract. The Neumann conditions specify the time-rates of change of the flux variables. The rates are

calculated in step with the rates for the field cells and marched forward in time along with the field cells using the RK4 integration. While the non-reflective calculations add many lines of code to the model, their application removes all of the characteristic-based logic required to operate Dirichlet boundary handling. Conceptually, the model gets a bit simpler.

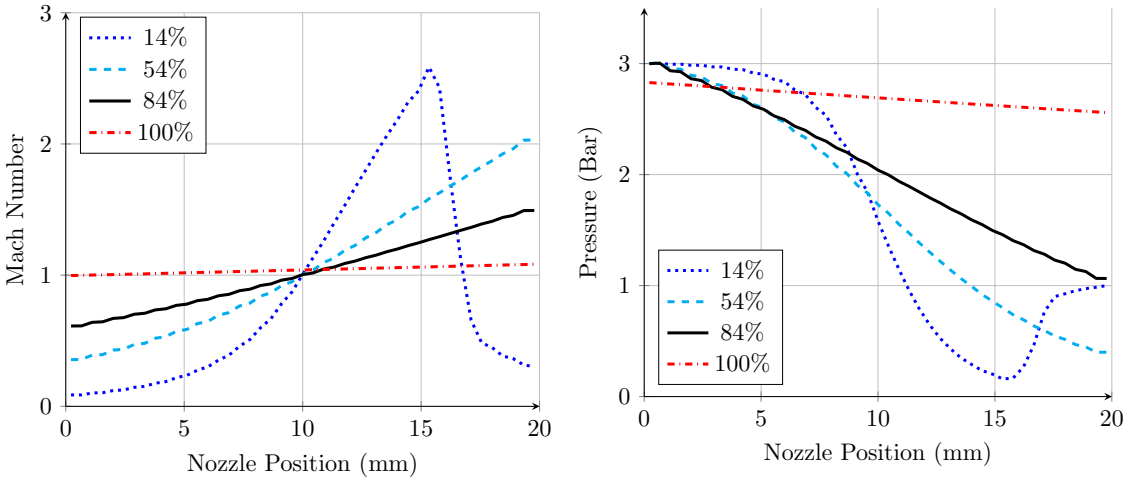

(A) Velocity

(B) Pressure

FIGURE 7.10. A Nozzle Operating at Various Throat Areas with Non-Reflective Boundary Handling

Figure 7.10 shows the same test that was performed above, with the nozzle operating at a 3:1 pressure ratio and four different throat areas. This time, both boundaries are handled non-reflectively. Compare Figure 7.10a with Figure 7.8a. There is a significant, and importantly, realistic difference in the results. At 14% and 84% opening, the curves are identical to above. However, at 54%, the overexpanded case, there is no shock wave in the domain. The flow is exiting the domain at the correct supersonic speed. At 100%, the underexpanded case, we no longer see the flow accelerating over the final few cells. Instead, it is exiting at just over Mach 1. We see even more satisfying results in Figure 7.10b. Now, for the 54%, overexpanded case, we indeed see that the exit pressure is below atmospheric.

And for the 100%, underexpanded case, we see that the exit pressure is above atmospheric. The CFD model is now *solving for* the exit pressure.

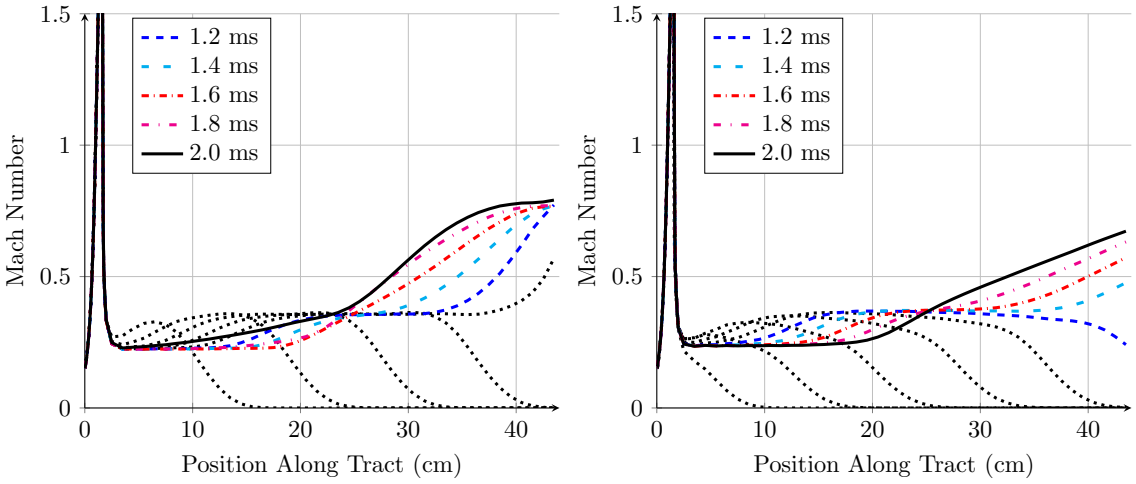

(A) Shock Wave Reflecting off of Hard Boundary

(B) Shock Wave Exiting through Non-Reflecting Boundary

FIGURE 7.11. The Effect of Hard and Non-Reflecting Boundary Handling

Figure 7.11 compares the results of the Q1D model simulating the passage of a shock wave through a valve with a connected, straight pipe. Figure 7.11a is a sequence of snapshots as a shock wave passes from left to right. The shock wave induces the flow to accelerate to the right (positive velocity) as it passes. When the wave reaches the Nth cell of the pipe, instead of the cell's pressure suddenly going from atmospheric to the pressure behind the shock, the pressure in cell Nth simply stays atmospheric. This causes the physics of the Q1D governing equations to instantaneously generate an expansion wave that returns back down the pipe, from right to left, (the curves with associated time values) inducing even higher velocity in the positive direction and taking the pressure in the pipe to atmospheric. This doesn't happen in a real pipe; it is a mathematical artifact. Figure 7.11b shows exactly the same scenario with non-reflective boundary handling on the Nth end. Now, when the shock wave reaches the Nth boundary, the pressure in cell N spikes, just as it does in the field cells,

allowing the shock to exit the domain, as it would in a real pipe. The pressure in cell N then decreases at a finite rate to atmospheric, generating an infinite series of infinitesimal expansion waves that slowly bring the pressure in the pipe back to atmospheric.

These results are far closer to reality than we can get using the simpler, hard boundary handling. For the cost of adding non-reflective boundary handling, we get a solution that is physically accurate across the domain. But importantly, it also solves the problem we talked about earlier: it allows shock waves to pass through the pipe exit, rather than reflecting back and forth, causing non-physical artifacts and possibly destabilizing the CFD solution. The simulation will remain stable, even at extremely high RPM.

7.9. Preliminary Results

With all of these details embodied in software, we can present the following preliminary results. For each of these tests, the gas used is exhaust gas, a mixture of CO_2, H_2O, N_2 and Ar. The gas has the composition described in Table 7.1 and has the properties listed in Table 7.2.

Table 7.1. Exhaust Gas Mixture

Constituent Gas	Mole Ratio
N_2	0.725
H_2O	0.141
CO_2	0.125
Ar	0.00930

Table 7.2. Exhaust Gas Properties at 800 K

Molecular Mass	28.72	$\frac{g}{mol}$
Specific Gas Constant (R)	289.5	$\frac{kJ}{kg-K}$
Specific Heat (C_p)	1,270	$\frac{kJ}{kg-K}$
Specific Heat (C_v)	981.0	$\frac{kJ}{kg-K}$
Ratio of Specific Heats (γ)	1.295	

Figure 7.12 illustrates the sudden initiation of flow in a straight duct that is initially quiescent. The duct is 2 cm long, 7.355 cm^2 in cross-sectional area and runs left-to-right in the figure. The duct contains 46 cells with the 0th cell at the left and the 45th cell at the right.

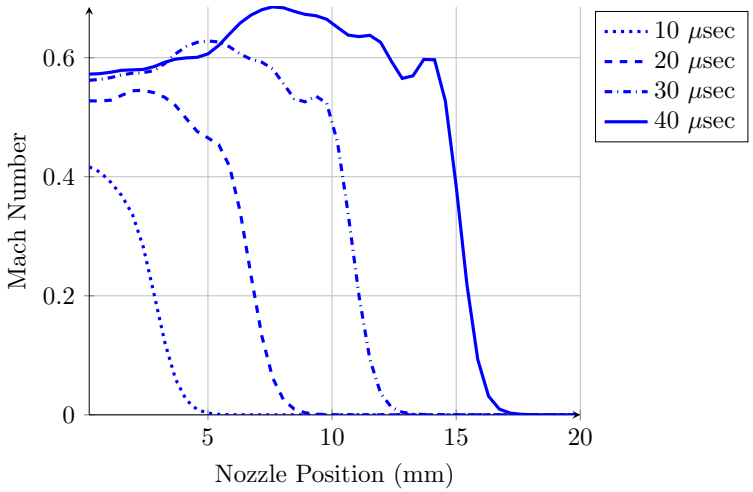

FIGURE 7.12. Shock Wave Transiting a Straight Pipe

A high-pressure reservoir of exhaust gas at three atmospheres and 800 K is positioned at the 0th boundary and the Nth boundary is open to the atmosphere. When the simulation is begun, cells 1 through 45 are initialized to atmospheric conditions. Cell 0 is initialized with the high-pressure gas. When time-marching is begun, the discontinuous pressure gradient between cells 0 and 1 creates a shock wave which advances into the lower pressure gas and induces a positive velocity in the gas as it passes. The figure presents the velocity of the flow as four snapshots, 10 μsec apart. The shock wave is denoted by the steep rise in velocity, with zero velocity ahead of it and relatively high velocity behind it. Note how the shock wave is transiting from left to right as the flow is time-marched into the future. This is physically correct behavior and shows how well the system can handle strong shock waves. Note the absence of oscillations in the velocity.

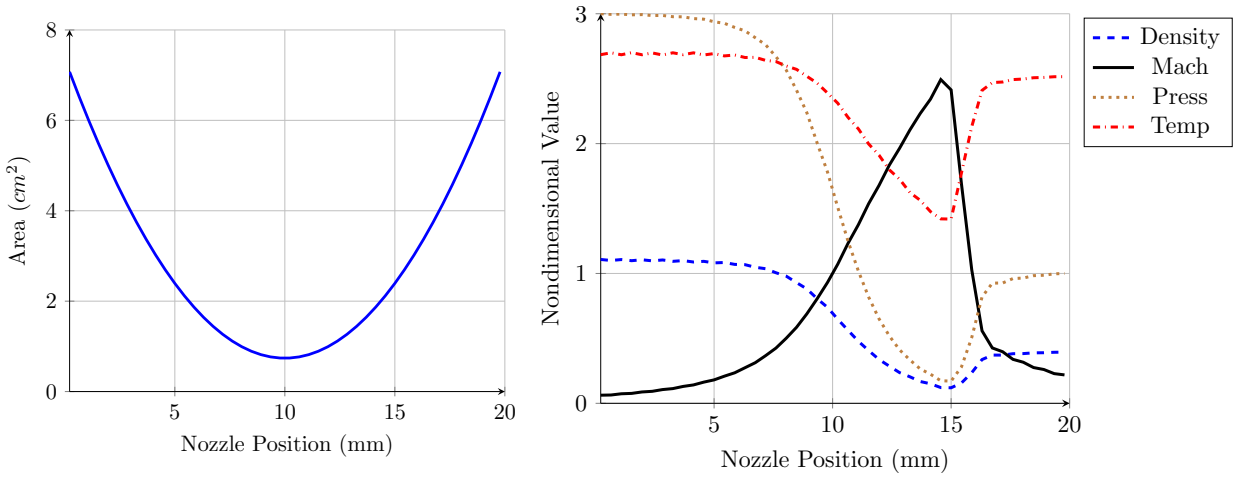

(A) Nozzle Area Profile

(B) Nozzle Flow Properties

FIGURE 7.13. Q1D Nozzle Flow Steady State Results

Figure 7.13 shows a more detailed example. Here, exhaust gas is flowing steadily from left to right through a converging/diverging nozzle. The nozzle is 2 cm long and has the area profile given by Figure 7.13a. The minimum duct area, A^*, is one-tenth the maximum area. The 0th boundary connects to a reservoir of exhaust gas at 3 atmospheres and 800 K; the Nth boundary is open to the atmosphere. The flow through the nozzle is started in the same manner as that in Figure 7.12, then time-marched to the steady state. Figure 7.13b shows the values of the primitive flow variables when steady flow is reached. Note how the velocity is positive, indicating flow from left-to-right through the duct. The gas accelerates through the converging section of the nozzle, reaching Mach 1 at the throat. Then it continues accelerating through the diverging section of the nozzle until reaching Mach 2.37. There, a shock wave forms, taking the flow to subsonic speed. Across the shock, density, temperature and pressure all increase. Downstream of the shock wave, the flow decelerates through the final, divergent section of the nozzle, exiting at Mach 0.23. With a C_x value of 0.9, the velocity break at the beginning of the shock wave is quite sharp, yet we see only very minor

oscillations in the result. Note the appropriate behavior of the density, temperature and pressure values across the domain.

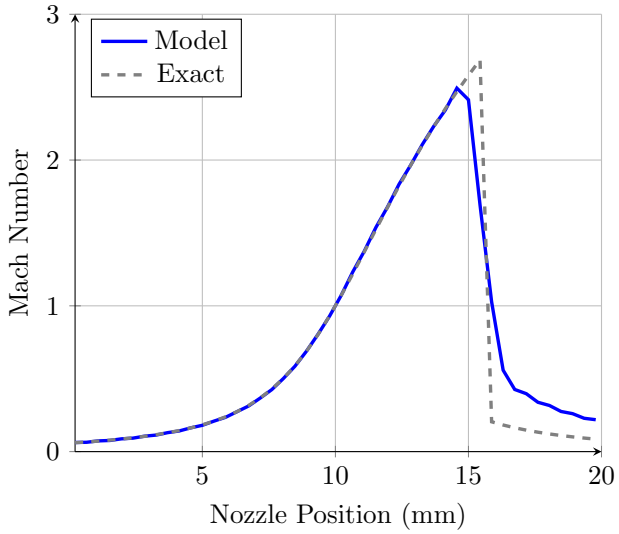

FIGURE 7.14. Computed and Exact Mach Numbers

Figure 7.14 compares the computed Mach number for this example with the exact Mach number, generated using a separate program that applies closed-form, quasi-one-dimensional theory. (For a nozzle operating in the non-isentropic regime, generating these results proves to be a surprisingly non-trivial task on its own.) The CFD model does a very good job of matching theory from the reservoir to the shock wave. There, we note differences. By always summing a cell's flux values on both the left and right faces, we have created a "non-upwind" solution. In the supersonic region of the flow, we're taking information from downwind of the cell when influences can't come from that side. As a result, the calculation of the shock wave is smudged out across a number of cells, reducing the maximum Mach number slightly and affecting the point where isentropic flow resumes. Note that the exact shock wave is discontinuous, and the flow through the duct is composed of two isentropic flows joined by a discontinuity. The computed shock wave is has finite thickness, intruding into both of

the isentropic regions, truncating the upstream isentropic flow slightly and displacing the return to isentropic flow slightly down the duct. The result is still accurate enough for our purposes. Also note how accurately the CFD model is able to capture the location of the shock wave—identical to the exact location.

7.10. Additional 0th End Boundary Handling

As discussed in the previous chapter, the engine has poppet valves that open and close to control the flows in the intake and exhaust tracts and to seal the cylinder so the charge can be compressed and contained. Kim et al. [22] showed that the poppet valves in an engine can be validly replaced by convergent-divergent nozzles of equal flowpath area. The fluid drag, downstream velocities, mass flow rates and fluid structures are unaltered. And so we will replace the intake and exhaust poppet valves with nozzles of time-varying, parabolic cross-sectional area profile, given by:

$$A(x) = 4\,(A_0 - A^*)\,\frac{x^2}{L^2} - 4\,(A_0 - A^*)\,\frac{x}{L} + A_0 \tag{7.65}$$

Where x is the axial station along the nozzle, A_0 is the non-varying area at either end of the nozzle and A^* is the variable area of the throat.

Figure 7.15 shows the nozzle-valve at four stages of closure, wide open, 75% open, 50% open and 1% open. Flow through the valve is from left to right and vice-versa. The valve is modeled using a duct of 46 cells. The 0th end of the duct always connects to the cylinder, making positive duct velocity equate to flow *out* of the cylinder. The Nth end of the duct connects to the atmosphere or to another duct that represents either an intake runner or

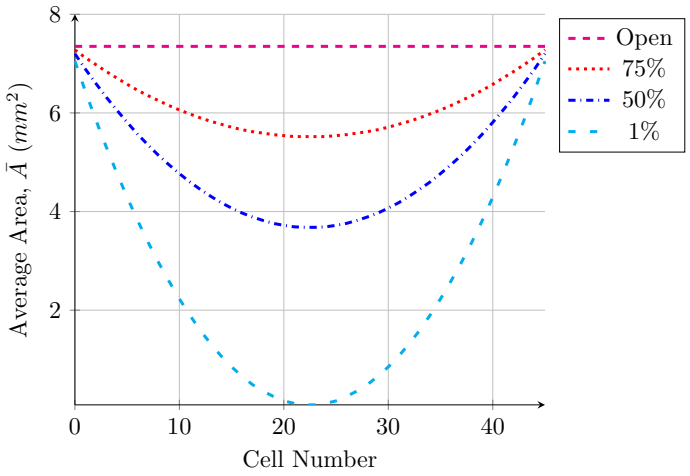

FIGURE 7.15. Nozzle-as-Valve Profile at Selected Percentages of Opening

exhaust header. The ends of the valve are set to the area of the intake or exhaust port and the throat area is slaved to the skirt area of the modeled valve, dictated by the cam timing and cam profile in the cylinder model. As the crankshaft is stepped forward in time, the valve lift is updated at each step. Returning to the flux variable decode equations, Equations 7.54, we see that density and pressure both have $\bar{A}$ in their denominators. Reducing the throat area to zero will cause those calculations to fail at the throat cell. And so the valve's minimum throat area, A^*, will be limited to 1% of A_0. As the valve opens and closes, the simulated flow sees the cross-sectional area growing and shrinking while, at the same time, the cylinder acts as a forcing function on the valve's 0th end. While 1% cross-sectional area is small, it doesn't stop the fluid from flowing. Some mechanism is still required to fully stop the flow when the valve is closed. For that, we can apply another boundary condition to the zeroth end of the valve, making that end of the duct a solid boundary.

Figure 7.16 shows the characteristics at the 0th duct boundary when the flow there is stopped. There is a single characteristic entering the domain. This means that we must specify a flux variable there while letting two float. We're already specifying velocity, zero,

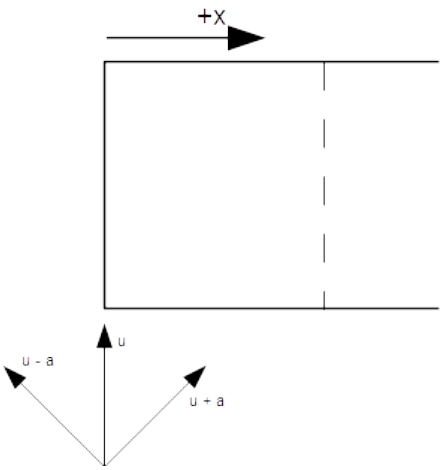

FIGURE 7.16. Characteristics for the Closed 0th End

so we'll allow density and temperature to float. We can extrapolate the values of U_1 and U_3 from the interior cells, but we get a better result if we calculate the F_1 and F_2 values, associated $\frac{dU_1}{dt}$ and $\frac{dU_2}{dt}$ rates and time-step this cell along with the field cells. But there is no neighboring cell to the left, so how do we estimate the flux values at the left cell face? We won't have to. If we consider the velocity in cell 0 to be zero, we can validly specify that the velocity at the left cell face is also zero. Therefore, the fluxes within cell 0 and at its left face are zero. And so, applying the semi-discrete Q1D equations to the cell, we get a new set of finite volume equations. The generic equation for cell 0 becomes,

$$\boxed{\left(\frac{dU}{dt}\right)_0 = -\frac{1}{dx}\left[A_r Z_r (F)_1 + (J)_0\right]} \tag{7.66}$$

with the vectors,

$$(7.67)\quad \boxed{U = \begin{bmatrix} \rho\bar{A} \\ 0 \\ \rho c_v T\bar{A} \end{bmatrix} \begin{matrix} U_1 \\ U_2 \\ U_3 \end{matrix} \qquad F = \begin{bmatrix} \rho u \\ \rho u^2 + P \\ \rho u e' + P u \end{bmatrix} \begin{matrix} F_1 \\ F_2 \\ F_3 \end{matrix} \qquad J = \begin{bmatrix} 0 \\ PA_r + F_{vx} \\ \dot{W}_{vx} \end{bmatrix} \begin{matrix} J_1 \\ J_2 \\ J_3 \end{matrix}}$$

This complicates the boundary handling for Cell 0. Now, when the valve is open, we calculate the flux variable rates using non-reflective handling. When the valve is closed, we calculate the flux variable rates for as above. In both cases, we integrate the rates with those of the field cells.

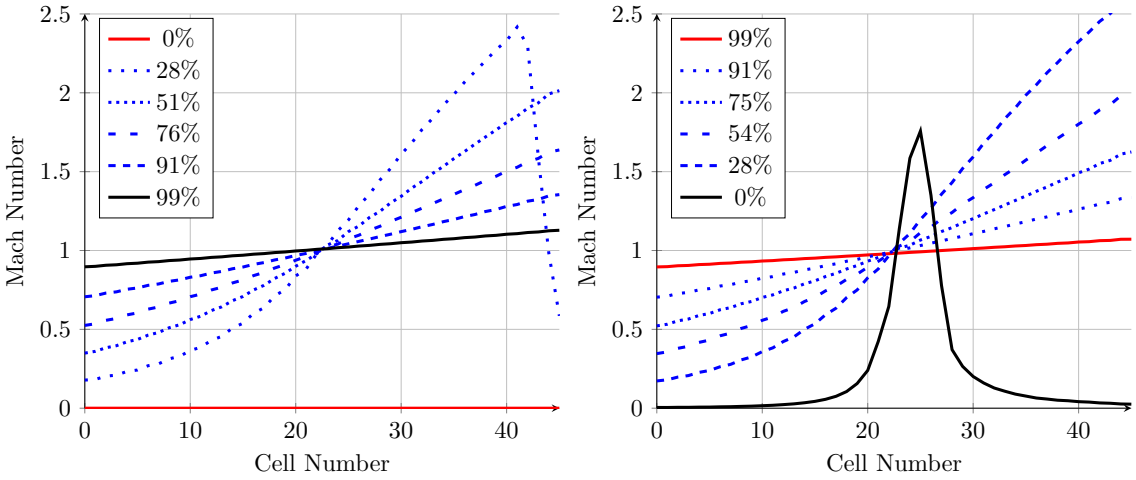

(A) Velocities as the Valve Opens (B) Velocities as the Valve Closes

FIGURE 7.17. Flow Through the Moving Valve

Figure 7.17 shows the additional 0th boundary handling in operation. Here, the valve is bounded on the 0th end by a reservoir of exhaust gas at three atmospheres and is open to the atmosphere at the Nth end. The valve starts closed, then opens and closes again sinusoidally over a period of 14 msec. This simulates the exhaust valve opening and closing at a crankshaft speed of 3,000 rpm. In Figure 7.17a, the valve starts out with zero velocity

throughout. At 28% opening there is a shock wave around cell 42. As the valve continues to open, the shock wave moves downstream, exiting the domain. At 99% opening, the flow through the entire valve is near Mach 1.

Figure 7.17b picks up where Figure 7.17a leaves off. As the valve closes, a shock wave forms at the exit, and with further closure, travels upstream. There is hysteresis in the reverse sequence, so we don't see the shock wave enter until the valve is closed below 28%. The final curve shows the valve at 1% minimum throat area, with the closed-end handling active. In the compressible flow, while fluid at the 0th end is stopped, fluid through the rest of the valve is still moving to the right. The very small throat area results in deceptively large velocity there.

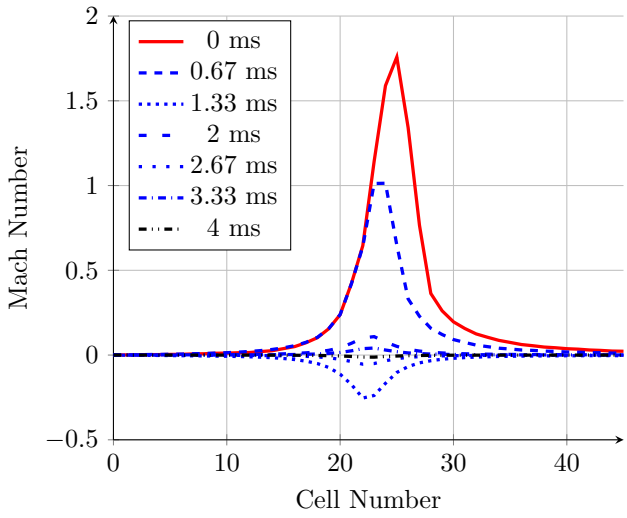

FIGURE 7.18. Velocities After Valve Closure

Figure 7.18 picks up where Figure 7.17b leaves off. The valve is now closed, with closed 0th-end handling active. The velocity is positive at first, then drops to near zero, then reverses. Note that the velocity of cell 0 is always zero. The velocity oscillation in the body of the valve continues for a number of cycles with decreasing amplitude, as the flow decays toward quiescence. This is organ pipe oscillation, what one hears when patting the open

end of a pipe with the opposite end closed, and importantly, is physically accurate behavior. This is again good validation that the model is working correctly and that the assumptions we made for the 0th-end handling are both valid and correct.

7.11. Connected Ducts

The intake and exhaust systems of engines are composed of valves, intake and exhaust ports, intake runners and exhaust headers, plus other piping. Computationally, it's not convenient to create a long string of cells with varying area, varying Δx and, to top it off, one set of cells whose area changes temporally. Instead, it's easier to create individual ducts and connect them together end-to-end to form an entire intake or exhaust tract. Then, each duct can have a distinct identity and behavior. For example, a valve duct can have time-varying area. But accomplishing this requires yet another set of boundary handling algorithms.

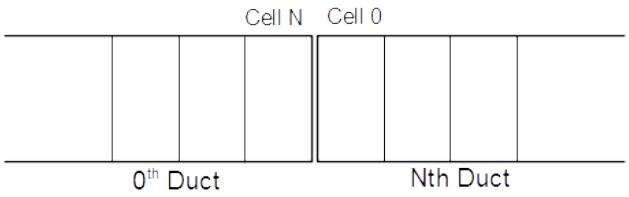

Figure 7.19. Connected Ducts

Figure 7.19 shows two ducts connected end-to-end. For the left duct, the duct to its right is its Nth duct. For the right duct, the duct to its left is its 0th duct. It's clear from the illustration that we must make sure the touching face areas of the Nth and 0th cells are equal. Otherwise we have an ambiguous face area at the interface. Applying the generic equation to the connected cells is straight forward. If we call the Nth cell of the 0th duct N' and the 0th cell of the Nth duct $0'$, then for the 0th cell:

$$\left(\frac{dU}{dt}\right)_0 = -\frac{1}{\Delta x_0}\left\{A_l\left[F_0 - Z_l\left(F_0 - F_{N'}\right)\right] - A_r\left[F_0 + Z_r\left(F_1 - F_0\right)\right] + J_0\right\} \tag{7.68}$$

And for the Nth cell:

$$\left(\frac{dU}{dt}\right)_N = -\frac{1}{\Delta x_N}\left\{A_l\left[F_N - Z_l\left(F_N - F_{N-1}\right)\right] - A_r\left[F_N + Z_r\left(F_{0'} - F_N\right)\right] + J_N\right\} \tag{7.69}$$

where the vectors are given by Equations A.8.

But this provides yet another boundary handling requirement. On the 0th end of a duct, we must test for three possible conditions: Open to the cylinder, closed or connected to another duct. On the Nth end, we must test for connected and not connected. Then the boundary handling rules become:

TABLE 7.3. 0th Cell Boundary Handling Rules

Open	Closed	Connected
Calculate U_1, U_2 and U_3 rates using non-reflective handling	$U_2 = 0$, Calculate U_1 and U_2 according to Equations 7.66 and 7.67	Calculate U_1, U_2 and U_3 rates according to Equations 7.68 and A.8

TABLE 7.4. Nth Cell Boundary Handling Rules

Open to the Atmosphere	Connected
Calculate U_1, U_2 and U_3 rates using non-reflective handling	Calculate U_1, U_2 and U_3 rates according to Equations 7.69 and A.8

With these additions to the model, Figure 7.20 presents the initiation of flow in a straight tract composed of a wide-open valve, 2 cm long, connected to a straight pipe 20 cm long. Δx in the valve is 0.435 mm and in the pipe, 5 mm. So this is a good test of both the connected-end handling and the Δx-based flux proportioning Z terms. The figure is again

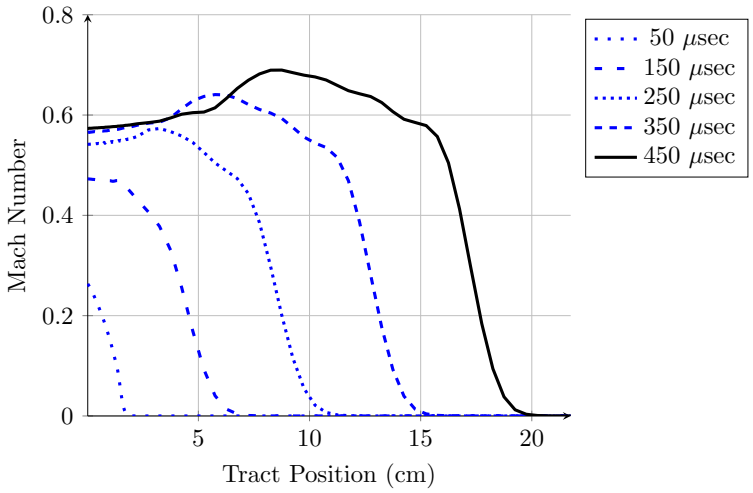

FIGURE 7.20. Shock Wave Transiting Connected Pipes

a collection of snapshots, each 100 μsec apart. Like in Figure 7.12, we see the shock wave transiting through the initially quiescent flow, inducing positive velocity. The shock wave advances across the duct connection without any distortion, indicating that the algorithm and software are both correct.

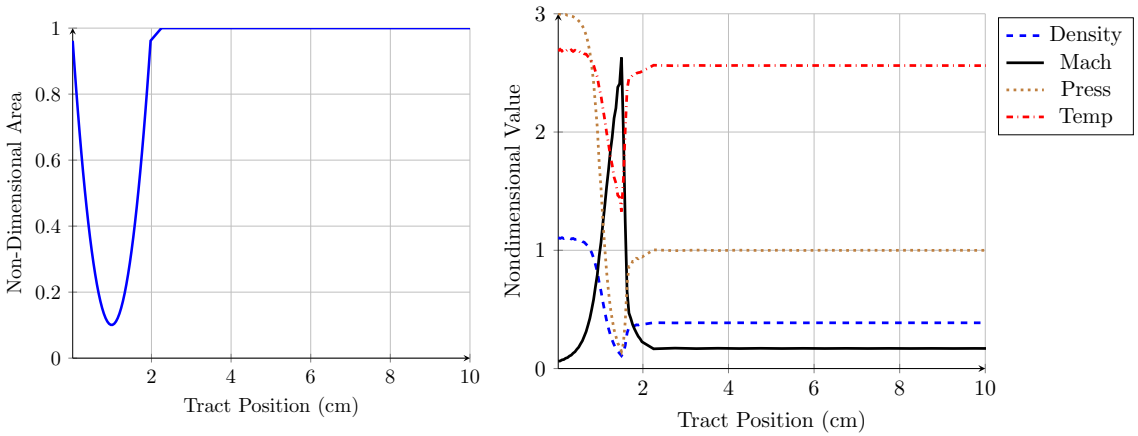

(A) Tract Area Distribution

(B) Tract Flow Properties

FIGURE 7.21. Q1D Tract Flow Steady-State Results

Figure 7.21 shows exhaust gas flowing through a combined valve/pipe tract. The valve, 2 cm long, is connected to a straight pipe, 20 cm long, at its Nth end. The overall area profile of the tract is shown in Figure 7.21a. The valve is open 10% and exhaust gas is supplied at 3

atmospheres and 800 K at the left. The right end of the pipe is open to the atmosphere. The flow was started as above, with the passage of a shock wave, then marched forward in time to the steady state. Compare the flow through the valve section with Figure 7.13b. The results are identical. Downstream of the valve exit, the flow remains constant through the pipe to the atmosphere. (The pipe section has been truncated to make the curves through the valve easier to see.) The curves are all smooth where the two ducts connect, again indicating that the algorithm and software are correct.

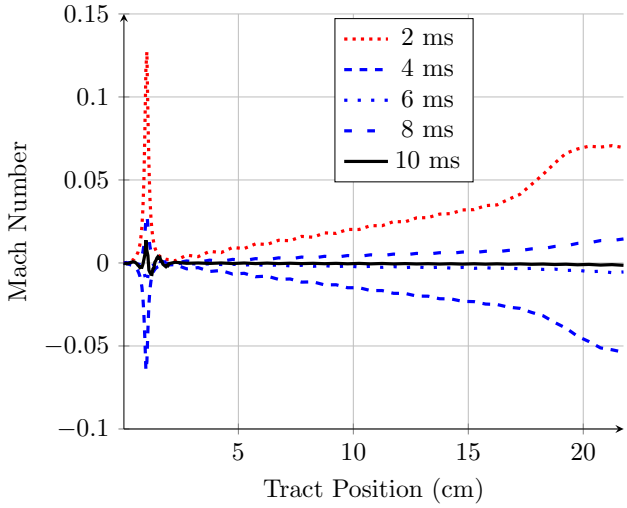

FIGURE 7.22. Closed-End Fluid Response

From the fully developed, steady-state flow presented above, we can slam the valve shut instantaneously, stopping the flow at the left end of the tract. This is a very violent event and stresses the simulation. What happens? Figure 7.22 shows the results; the fluid oscillates as it does in an organ pipe. Here, oscillations of the fluid in the tract are very visible. Because of the length of the tract, the frequency is lower than in Figure 7.18 and the oscillations decay more slowly. Each curve is plotted 2 msec from the last.

Figures 7.13b, 7.14 and 7.21b show that the Q1D model is accurate in predicting steady-state results. But what about time-accuracy? For us, it's just as important for the Q1D

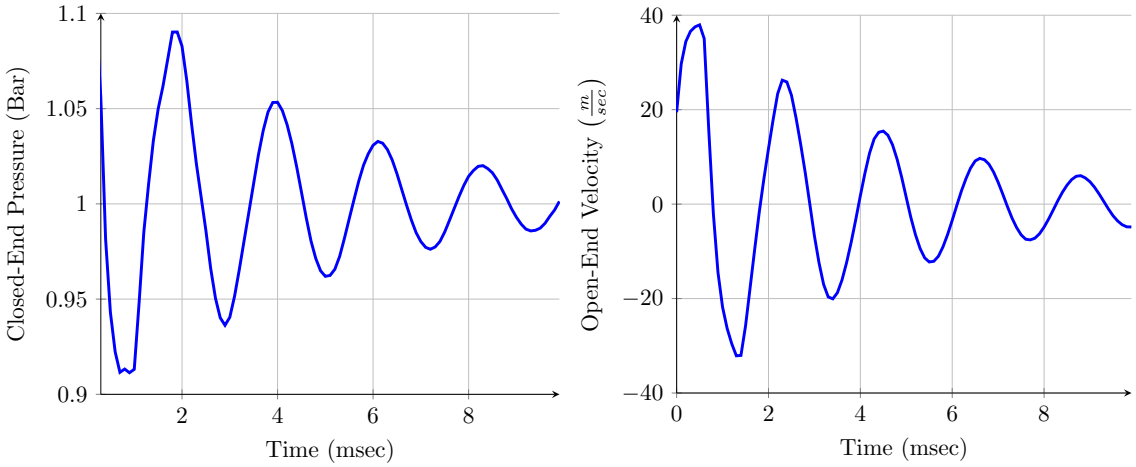

(A) Pressure Oscillations at the Closed End (B) Velocity at the Open End

FIGURE 7.23. Organ Pipe Oscillations

model to be able to predict *when* an event will occur as it is to predict how and where it will occur. Luckily, we're dealing with pipes, which have acoustic responses. We can take advantage of that. We use the same setup as above, a tract composed of a valve with attached pipe. The test begins with the valve closed and the tract filled with standard, frozen air at ambient temperature and 1.1 atmospheres. The simulation is advanced forward and the effect is as if a membrane over the open end of the pipe, retaining the lightly compressed air, has suddenly ruptured. The tract goes into organ pipe oscillations. Figure 7.23 shows the result. The total length of the tract is 0.022 m and acoustic theory says the oscillations should occur at a frequency of 430 Hz. Figure 7.23a shows the pressure experienced at the closed end of the tract. The wavelength of the oscillations is about 2.3 msec, for a frequency of 435 Hz, very close to the theoretical value. Figure 7.23b shows the velocity of the air column at the open end of the pipe. Note how the velocity leads the pressure by 270 degrees. That the predicted and theoretical frequencies are close provides additional confidence that the Q1D model and software are correct.

7.12. Fluid Friction

Now that we have an operating Q1D fluid flow model, we can think about adding more physics. The governing equations of Q1D flow were derived from the Euler equations and are therefore inviscid. Without the inclusion of fluid viscosity, it would seem we are stuck with an ideal model that doesn't include the important phenomenon of fluid drag. But this is precisely why we included the viscous work terms in the J_2 and J_3 terms of the generic equation.

In an external flow over a body, like the flow over an airframe, we're very concerned with estimating the force of drag imparted to the body by the air. In an internal flow, we're more interested in estimating the drag imparted on the *fluid* by the walls. Returning to our original Q1D assumptions, the properties across any given fluid cross section are constant. There is no boundary layer at the walls, no transverse velocity gradient. But we can still model the viscous drag on the fluid by applying a source term reflecting the drag force at a point along the flow, averaged out over the cross sectional area of the flow.

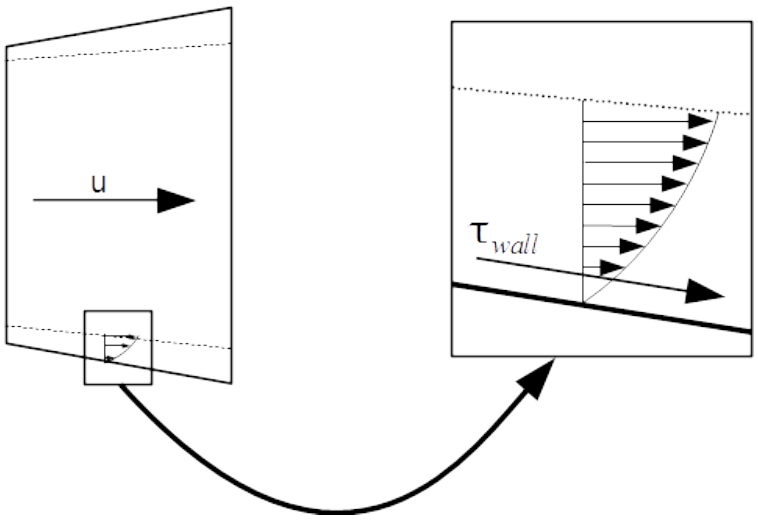

Figure 7.24. The Boundary Layer and its Viscous Shear Stress

Figure 7.24 shows one cell of a duct. If the duct had a three-dimensional, viscous flow inside of it, we could envision an annular boundary layer along the wall, indicated by the area between the wall and the dashed lines, where the fluid is in viscous shear. The enlargement at the right shows the parabolic velocity distribution through the boundary layer. The no-slip condition at the wall dictates that the fluid there has a velocity of zero and the fluid at the edge of the boundary layer has free-steam velocity. The retardation of the flow at the surface results in a shear stress, τ, applied to the wall:

$$\tau = \nu \frac{\partial u}{\partial r} \qquad \left\langle \frac{N}{m^2} \right\rangle \tag{7.70}$$

where ν is the viscosity of the fluid and r is the radius from the centerline of the duct. We can integrate the shear stress over the surface of the cell—the area of the wall—arriving at the viscous force applied to the cell wall:

$$F_{wall} = \int_S \tau dS \qquad \langle N \rangle \tag{7.71}$$

where S is the surface of the cell wall. According to Newton's third law, this same force acts on the fluid itself, and so $F_{wall} = -F_{fluid}$, and the force we calculate is *the total drag force on the fluid passing through this cell.* Note that the drag we've calculated is a single, vector value applying to all of the fluid in the cell. Since it is a single value, we can apply it to the flow in the cell as a source term, drag, D.

For a Newtonian, viscous flow, the force of drag increases with the square of velocity. It is common to non-dimensionalize the drag force by the dynamic pressure times a reference area, resulting in a drag coefficient:

$$C_D = \frac{D}{\frac{1}{2}\rho u^2 S} \tag{7.72}$$

or,

$$D = \frac{1}{2}\rho u^2 S C_D \tag{7.73}$$

If we assume a circular duct and a cell with conical section,

$$S = 2\Delta x\sqrt{\pi \bar{A}} \tag{7.74}$$

then, using the area of the cell wall as the reference area,

$$\boxed{D = \rho u^2 \Delta x \sqrt{\pi \bar{A}} C_D} \tag{7.75}$$

From experiment, for a Reynolds number, $Re > 10^5$ and a surface roughness of $0.0005\bar{r}$, researchers have found, [29],

(7.76) $$\boxed{C_D = 0.005}$$

That is the surface roughness of a smooth but unpolished pipe. A typical, cast intake runner or exhaust header has a surface roughness of about an order of magnitude higher, and so we can expect to use a value significantly higher than $C_D = 0.005$ for realistic results.

To apply drag to the momentum equation, we remind ourselves that the momentum equation is a force equation. Therefore, drag gets added to the J_2 term as a force. Drag is also opposite in sense to velocity, so:

(7.77) $$\boxed{J_2 = -P\left(A_l - A_r\right) - \text{sgn}(u)\rho u^2 \Delta x \sqrt{\pi \bar{A}} C_D}$$

To apply drag to the energy equation, we remember that the energy equation actually employs power. And so we need to add the *power* lost to drag to the equation. The power of drag is equal to the drag force times velocity:

(7.78) $$\dot{W}_{drag} = Du = \rho u^3 \Delta x \sqrt{\pi \bar{A}} C_D$$

Drag always *consumes* power, and so the drag power term is always negative. The J_3 term of the generic equation becomes:

(7.79)
$$\boxed{J_3 = -\left|\rho u^3 \Delta x \sqrt{\pi \bar{A}} C_D\right|}$$

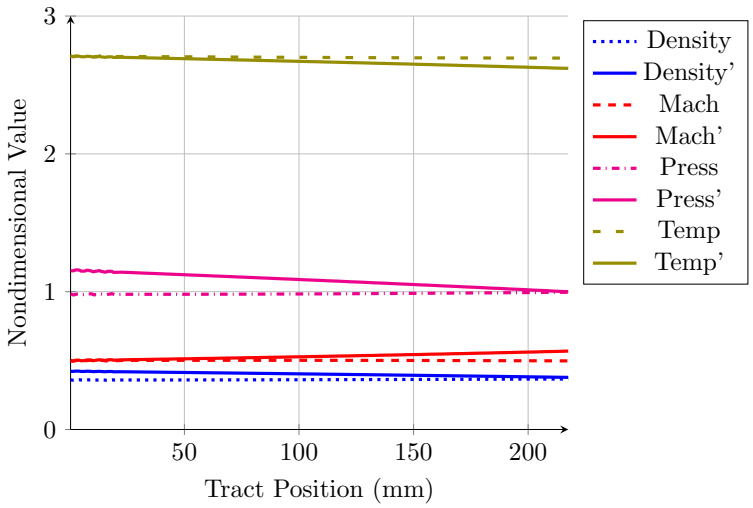

FIGURE 7.25. The Effect of Friction on Subsonic Flow

With these new source terms added to the Q1D generic equation, Figure 7.25 shows the result for subsonic flow. A wide-open valve is attached to a 20 cm long straight pipe, forming a pipe 22 cm long. The velocity (U_2) at the inflow (left side of the figure) is specified, with respect to temperature, at 0.5 Mach, density (U_1) is allowed to float and U_3 is specified with respect to temperature and velocity. A first run is made with C_D set to 0 (non-solid lines), then a second run is made with C_D set to 0.005 (solid lines and primed labels). With friction, Mach number increases from inflow to outflow. Temperature drops from inflow to outflow. Because the flow is subsonic, outflow pressure is equal between the two runs, but when friction is added, it is clear that pressure decreases from inflow to outflow. Last, density also decreases from inflow to outflow. These trends each match the closed-form results for a Fanno flow [29, 24, 63].

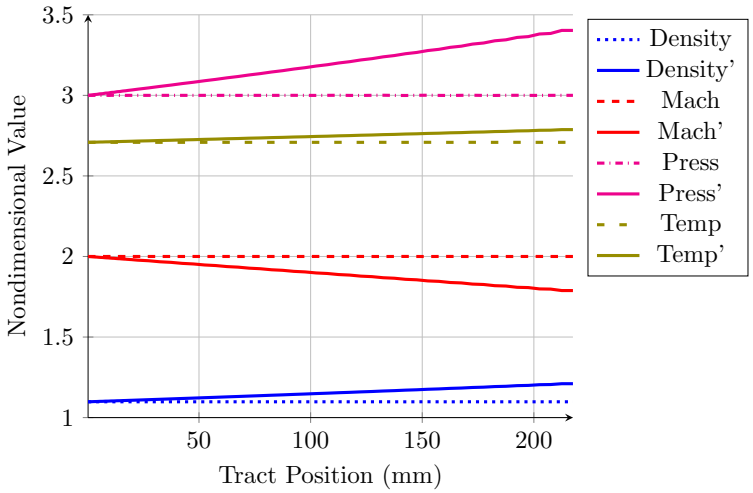

FIGURE 7.26. The Effect of Friction on Supersonic Flow

Figure 7.26 shows the effect of friction on a supersonic flow. The same duct is used but now all three flux variables are specified at the inflow (for supersonic inflow, three characteristics enter the domain) with velocity specified at Mach 2. An initial run with no viscosity is represented by the non-solid lines. A second run with $C_D = 0.005$ is represented by the solid lines. In this flow regime, viscosity makes the Mach number decrease, the temperature increase, pressure increase and density increase. These trends again match the closed-form results for Fanno flow.

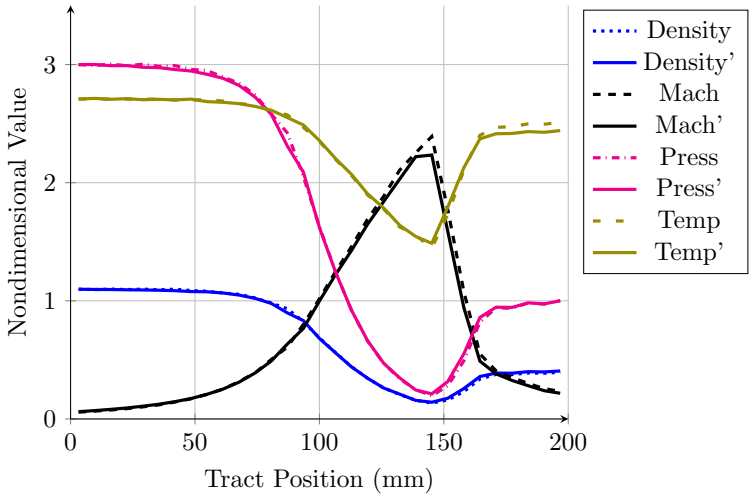

FIGURE 7.27. The Effect of Friction on Flow Through a Nozzle

Figure 7.27 shows the effect of friction on the flow through a nozzle. The nozzle tested is 20 cm long, to magnify the effect of friction (more total wall area). Again, a first run was made with no friction (non-solid lines), then a second run was made with $C_D = 0.005$ (solid lines). As the velocity increases through the nozzle the effect of friction becomes more evident. This makes sense, since the force of friction is proportional to the square of velocity. With friction it appears that, rather than reaching Mach 1 at the nozzle throat, the flow instead reaches Mach 1 slightly downstream of that point. Additionally, after the throat, the velocity is lower and the shock wave moves slightly upstream. The Mach number downstream of the shock is decreased, as is temperature. Pressure and density both appear to increase.

Unless we're simulating viscous flow through the ducts with a three-dimensional CFD model, there is no way to accurately estimate the drag on the fluid, and so we must turn to the common aerodynamic practice of using an empirical drag coefficient. In chapter 6, we showed the use of an empirical discharge coefficient. That can also be used here. The discharge coefficient is taken to relate the *effective* flowpath area through a valve to the valve's geometric flowpath area based on the current lift/diameter ratio. From Kirkpatrick [23]:

$$C_d = -0.798\left(\frac{l}{d}\right)^2 - 0.86\,\frac{l}{d} + 0.85 \qquad \text{(Intake)} \tag{7.80}$$

$$C_d = -3.6975\left(\frac{l}{d}\right)^2 + 1.0585\,\frac{l}{d} + 0.6499 \qquad \text{(Exhaust)} \tag{7.81}$$

Unfortunately, drag coefficient and discharge coefficient are commonly expressed with the same letters. Note we are using capital D for drag and lower-case d for discharge. The effective flowpath area through the valve is then:

$$A_{eff} = A_{skirt} C_d \tag{7.82}$$

And so we can simply modify the valve skirt area using C_d and use the effective area as the throat area for our computational valve.

7.13. Connecting the Intake and Exhaust Flow Models: Preliminary Results

We now have a fairly complete model of Q1D flow through ducts. We can create two valves, connect them each to a straight duct to form a complete intake or exhaust tract, then connect each tract to the cylinder model.

Figure 7.28 shows the intake and exhaust tracts in place in a complete engine. Note how the Q1D nozzles take the place of the engine's valves. The pipes connected to the nozzle's Nth ends form the intake and exhaust ports. We can connect more pipes to the end of the ports as intake runners and exhaust headers. We specified previously that the 0th cell of each valve is connected to the cylinder. The Nth cell is either open to the atmosphere or, more likely, connected to the 0th cell of a straight pipe. The outermost Nth cell of a complete tract connects to the atmosphere.

We can couple the Q1D intake/exhaust tracts to the model of the charge by calculating the mass fluxes, energy fluxes and pressure-work values at each valve's 0th cell. Then

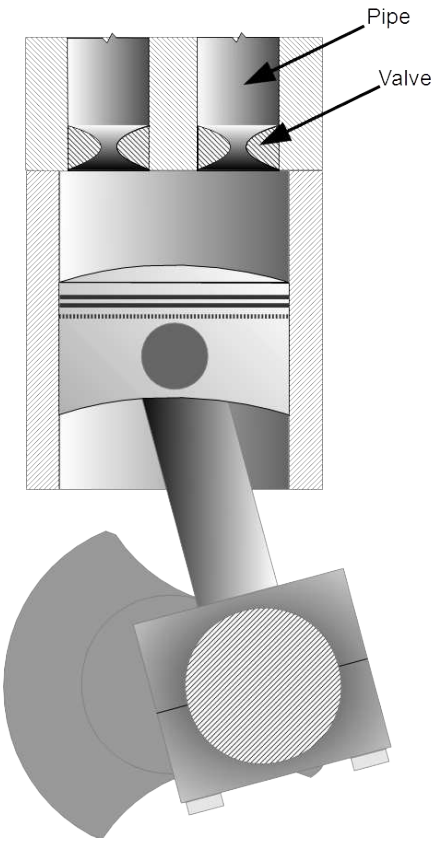

FIGURE 7.28. The Engine with Q1D Intake and Exhaust Tracts

we insert the mass flux value into the charge continuity equation (7.83, repeated here for convenience) as

$$\left(\rho\vec{V}\bar{A}\right)_0 = \left(\rho\vec{V}A\right)_i \qquad \text{or} \qquad \left(\rho\vec{V}\bar{A}\right)_0 = \left(\rho\vec{V}A\right)_e$$

(7.83)
$$\frac{d\rho}{dt} = -\frac{1}{\mathcal{V}}\left[\left(\rho\vec{V}A\right)_i + \left(\rho\vec{V}A\right)_e + \left(\rho\vec{V}A\right)_b + \rho\frac{d\mathcal{V}}{dt}\right]$$

And we insert the energy flux and pressure-work values into the charge energy equation (7.84, also repeated here), as

$$\left(\rho e' \vec{V} \bar{A}\right)_0 + \left(P \vec{V} \bar{A}\right)_0 = \left[\rho \left(e + \frac{\vec{V}^2}{2}\right) \vec{V} A\right]_i + \left(P \vec{V} A\right)_j$$

For the sums, the intake values correspond to subscript 1, exhaust values to subscript 2 and blowby values to subscript 3.

(7.84)

$$\frac{dT}{dt} = -\frac{1}{\rho \mathcal{V} c_v} \left\{ \underbrace{\sum_{i=1}^{3} \left[\rho \left(e + \frac{\vec{V}^2}{2}\right) \vec{V} A\right]_i}_{\text{energy flux}} \underbrace{+ \sum_{j=1}^{3} \left(P \vec{V} A\right)_j}_{\text{pressure work}} + \dot{Q}_T + \dot{Q}_c + \mathcal{V} e \frac{d\rho}{dt} + \rho e \frac{d\mathcal{V}}{dt} \right\}$$

Thus, we have a complete, integrated engine model with cylinder and tract submodels. But how do we know whether the integrated charge and flow models are working correctly? A good, comprehensive test technique is to set the system up to model a Helmholtz resonator. If we set the crankshaft rotational speed to zero, position the piston at the bottom of its stroke and open one valve fully, the open volume of the cylinder, combined with the flow path of a single tract (one must be kept closed) forms a Helmholtz resonator. With the charge initialized to slightly over atmospheric pressure, as the simulation is marched forward in time, the system should oscillate. One theory, based on the isentropic flow relations, provides the angular frequency of oscillation [64]:

(7.85)

$$\omega = c \sqrt{\frac{A}{L \mathcal{V}}}$$

where A is the cross-sectional area of the intake or exhaust tract, L is the length of the tract, $\mathcal{V}$ is the volume of the cylinder and c is the speed of sound in the fluid. From the engine we've been using through the thesis, table 7.5 provides the pertinent data.

TABLE 7.5. Helmholtz Oscillator Values

L (valve only)	0.02 m
L (valve and pipe)	0.32 m
A	0.001155 m^2
V	465.3 cc = 0.0004653 m^3
c	344.5 $\frac{m}{s}$

Figure 7.29 shows the results. The cylinder is filled with frozen, standard air with a density of 1.1 times ambient, resulting in a cylinder pressure of 1.1 atmospheres. The single, wide-open valve is initialized to zero velocity and ambient conditions. Then the simulation is marched forward in time with the timestep of the cylinder model, $\Delta t = 0.00005s$. The Q1D flow model sets its own, much smaller Δt value and, as described above, cycles as many times as necessary to march forward with the cylinder timestep.

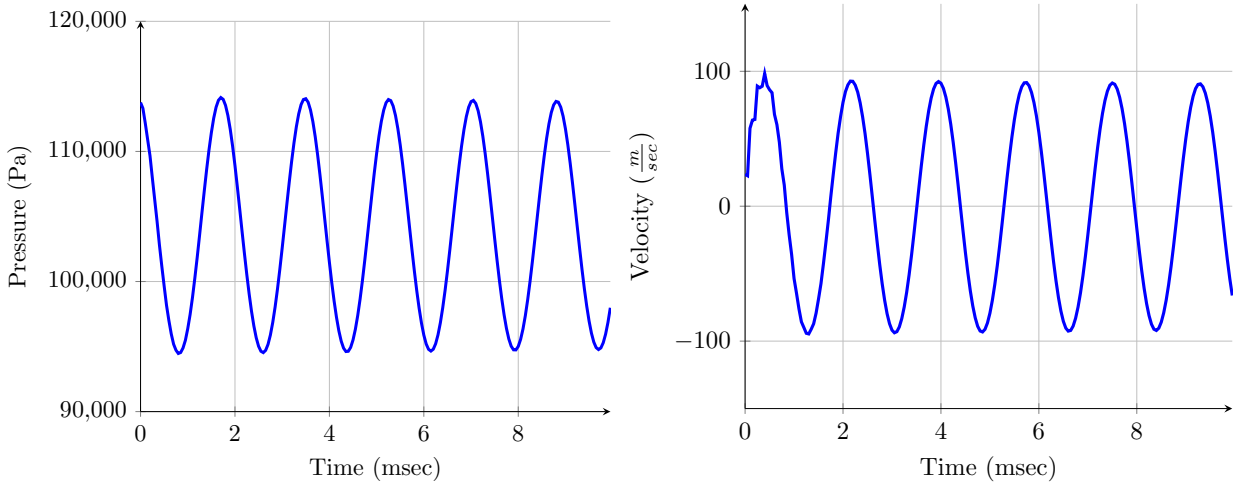

(A) Cylinder Pressure

(B) Valve 0th Cell Velocity

FIGURE 7.29. Cylinder/Valve Helmholtz Response

Figure 7.29a shows the pressure response of the charge in the cylinder. The pressure rises and falls just as we expect it to. The pressure response shows a period of 1.75 msec, for a frequency of 571 Hz. The theoretical frequency is 611 Hz. Figure 7.29b shows the velocity of the flow through the valve measured at its 0th cell. Flow out is positive. Note how the velocity leads the pressure by 90°, which makes sense.

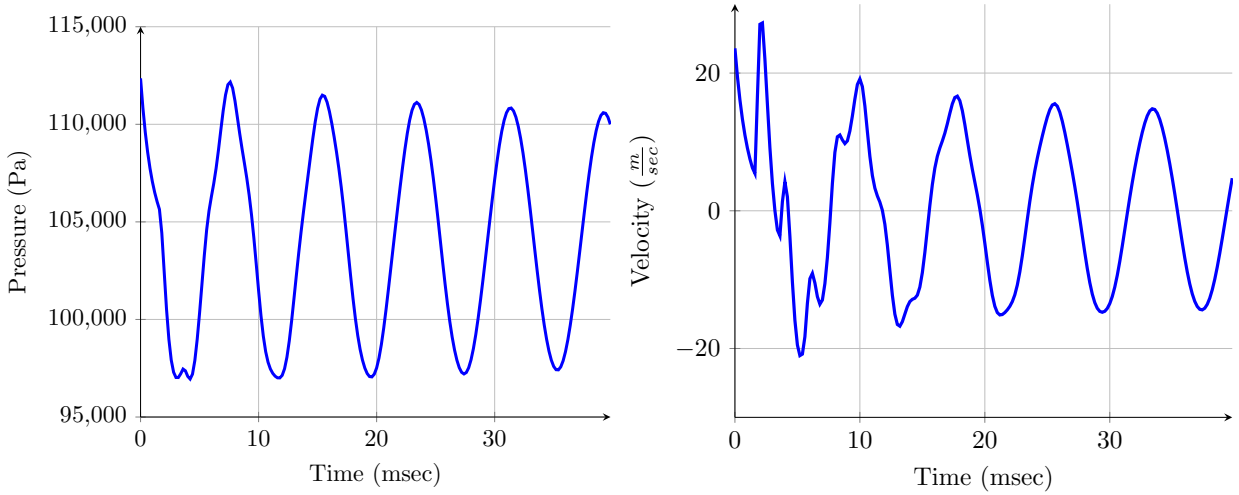

(A) Cylinder Pressure

(B) Valve 0th Cell Velocity

FIGURE 7.30. Cylinder/Tract Helmholtz Response

Figure 7.30 shows the same test done with a pipe connected to the valve for a total length of 22 cm. For this test, the system timestep is set to 0.002 seconds. Figure 7.30a shows the pressure response of the charge. Note the significantly longer wavelength. The period of the response is 7.8 msec for a frequency of 128 Hz. Theory predicts a frequency of 153 Hz. Figure 7.30b shows the velocity response leading the pressure response by 90°.

Performed with hard boundary handling (not shown here), the results come out to within 5 Hz of the theoretical values. Apparently, non-reflective boundary handling has an effect on the Helmholtz responses. This is concerning and is an issue that will be pursued at a later date.

7.14. The Fully Operational Simulation

Now that we've satisfied ourselves that the integrated cylinder and Q1D flow models form a harmonious system that can make accurate predictions, it's time to turn them loose as a complete engine simulation. We're continuing with the same engine we've used through the thesis (described in Chapter 2). In this case, the cylinder is outfitted with bare Q1D intake and exhaust valves. There is no port, intake runner or exhaust header attached to either valve. This arrangement allows a direct comparison with the results from Chapter 6, where the engine is modeled with simple valves. The following comparisons are made at 3,000 rpm, with all of the loss models turned off and C_D set to zero so that we're only observing thermodynamic and inviscid aerodynamic physics. The working fluid is frozen, standard air.

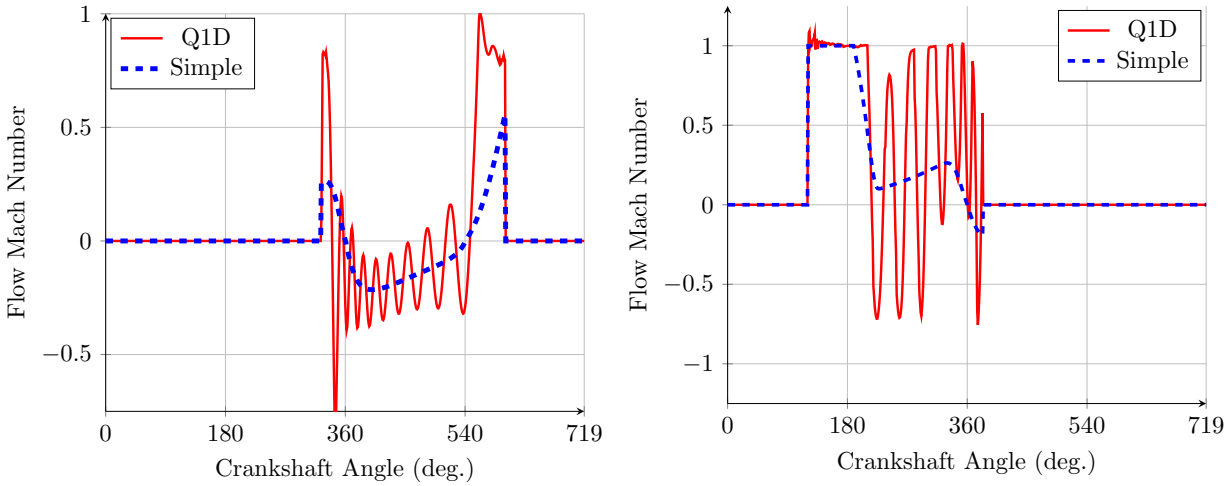

(A) Intake Velocity

(B) Exhaust Velocity

Figure 7.31. Intake and Exhaust Flow Velocities

Let's begin by studying the intake and exhaust flows. Figure 7.31 presents the velocity of the flows through the intake and exhaust valves. For each plot, TDC of compression is at the left (0°). The plots display the velocity through the valves over the engine's two-revolution cycle. In Figure 7.31a it's very easy to see where the intake valve opens and

closes. The solid, red curve is the velocity through the Q1D intake valve and the dashed, blue curve is the velocity through the simple valve with the discharge coefficient set to zero. The first thing we notice is that the Q1D flow is oscillating wildly, while the simple flow is well behaved. What is going on here? Observe the oscillations beginning at 360°, then follow them to the right. The wavelength of the oscillations is growing as the piston drops from TDC to BDC of the intake stroke. Following to the left of 360° we see the same trend. These are Helmholtz oscillations. With the intake valve open and the exhaust valve closed, we have a Helmholtz resonator, just like above. While the initial reaction is that there may be something wrong, after some consideration, we may be seeing correct, physical behavior. Note how the average Q1D value follows the isentropic curve. Figure 7.31b Shows the velocity through the exhaust valve. Note the level of correlation in the predicted duration of choked flow through the valve during blowdown. After the blowdown phase is complete, the Q1D model shows strong oscillations. Note how the wavelength decreases as the piston rises from 180° to 360° through the exhaust stroke. Again, Helmholtz oscillations. Note again how the average Q1D value tracks the simple value. Notionally, the appearance of Helmholtz oscillations in the Q1D results makes sense. We can picture the volume of the cylinder and the short duct that is the valve connected together and we can picture the momentum in the valve flow creating an over- and underpressure in the charge. It's also clear that the simple model, lacking any modeling of momentum, shouldn't be able to produce these kinds of phenomena.

Figure 7.32 shows the mass flow rate through both valves. Note how the average value of the Q1D flows tracks the value from the simple model. On inspection, it perhaps seems

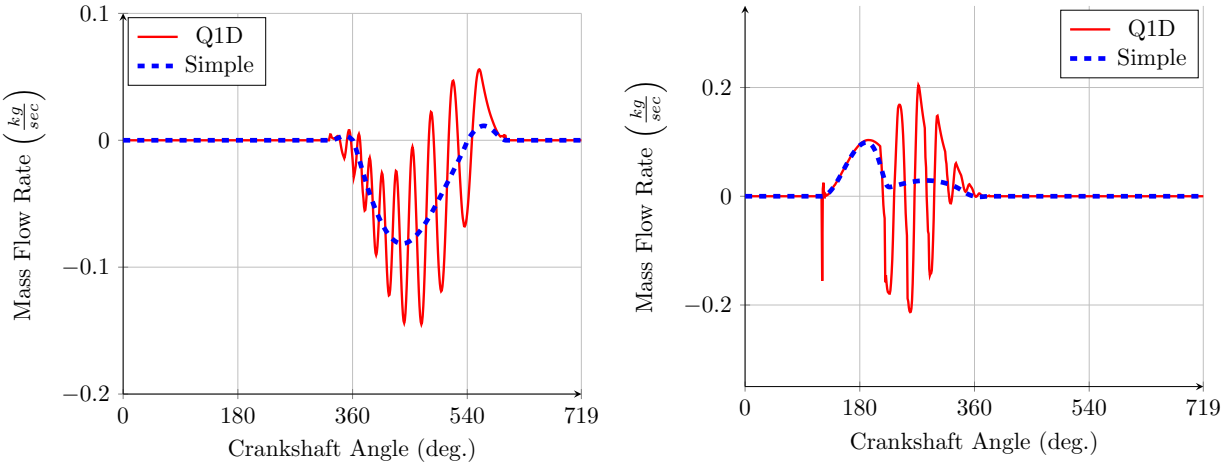

(A) Intake Mass Flow Rate

(B) Exhaust Mass Flow Rate

FIGURE 7.32. Intake and Exhaust Mass Fluxes

unlikely that the high-level results from the Q1D model would come close to matching the results from the simple model. But Figure 7.33 tells a different story.

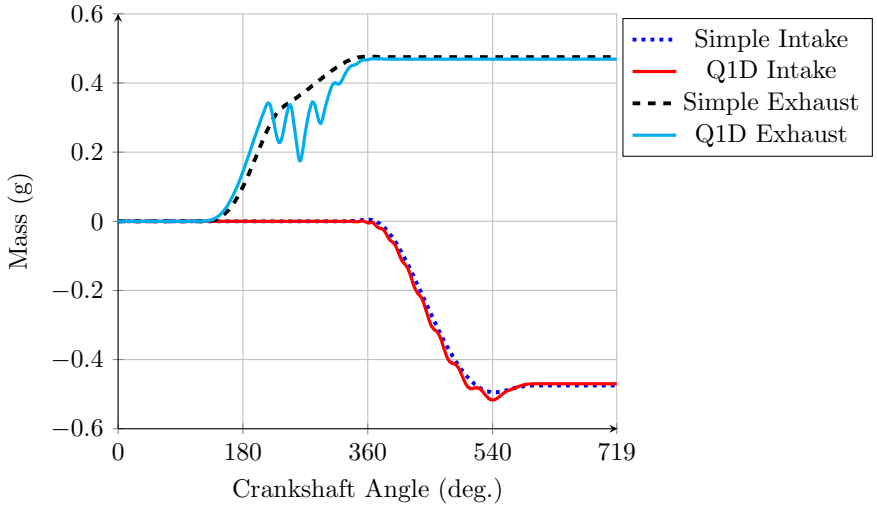

FIGURE 7.33. Total Mass Inducted and Exhausted

Here, we see the total mass of air inducted into the engine (flow in is negative) and the total mass of air expelled. Note how closely the totals from both models match. The intake curves are almost coincident, with some gentle oscillations visible toward the bottom of the Q1D curve. In the Q1D exhaust curve, the strong Helmholtz oscillations are quite evident,

but they damp out as the piston rises and the Q1D and simple curves also become nearly coincident. What at first looked like a disaster has begun to look far more promising. Let's look at some higher level results.

Figure 7.34 shows the density, temperature and pressure of the charge in the cylinder over the engine's two-revolution cycle. TDC of the compression stroke (0°) has been moved to the center of each plot for clarity. The opening (I_o, E_o) and closing (I_c, E_c) points of the intake and exhaust valves are indicated by the vertical lines. In the density curve, note the strong correlation between the two models until blowdown ends. Then the strong oscillations in the Q1D model are evident. Because of the short length of the exhaust valve, only 2 cm, when the flow reverses, cold, dense, atmospheric air is brought into the cylinder. This raises the density of the charge, oscillation after oscillation, until the valve closes. On the temperature plot, we see the same physics in play. As the flow oscillates, hot exhaust charge is pumped out and cold, atmospheric air is drawn back in, reducing the temperature of the charge. Since the isentropic flow model neglects momentum, there is no flow reversal and the density and temperature curves follow a more constrained path. But observe the result in the pressure curve. The Q1D and isentropic models are almost identical, with the two curves nearly coincident. There are some small pressure oscillations in the Q1D curve over the exhaust stroke (180° – 360°).

Figure 7.35 is of greatest interest to an engine designer. It presents the engine's power and torque predicted using the two models. In Figure 7.35a, note how close the two power curves are. They are nearly linear and exhibit no peak value in the engine's operating range; they appear to extend to infinity. The torque curves of Figure 7.35b are fairly flat, exhibiting very mild peaks. The form of the power and torque curves is actually unrealistic—real power and

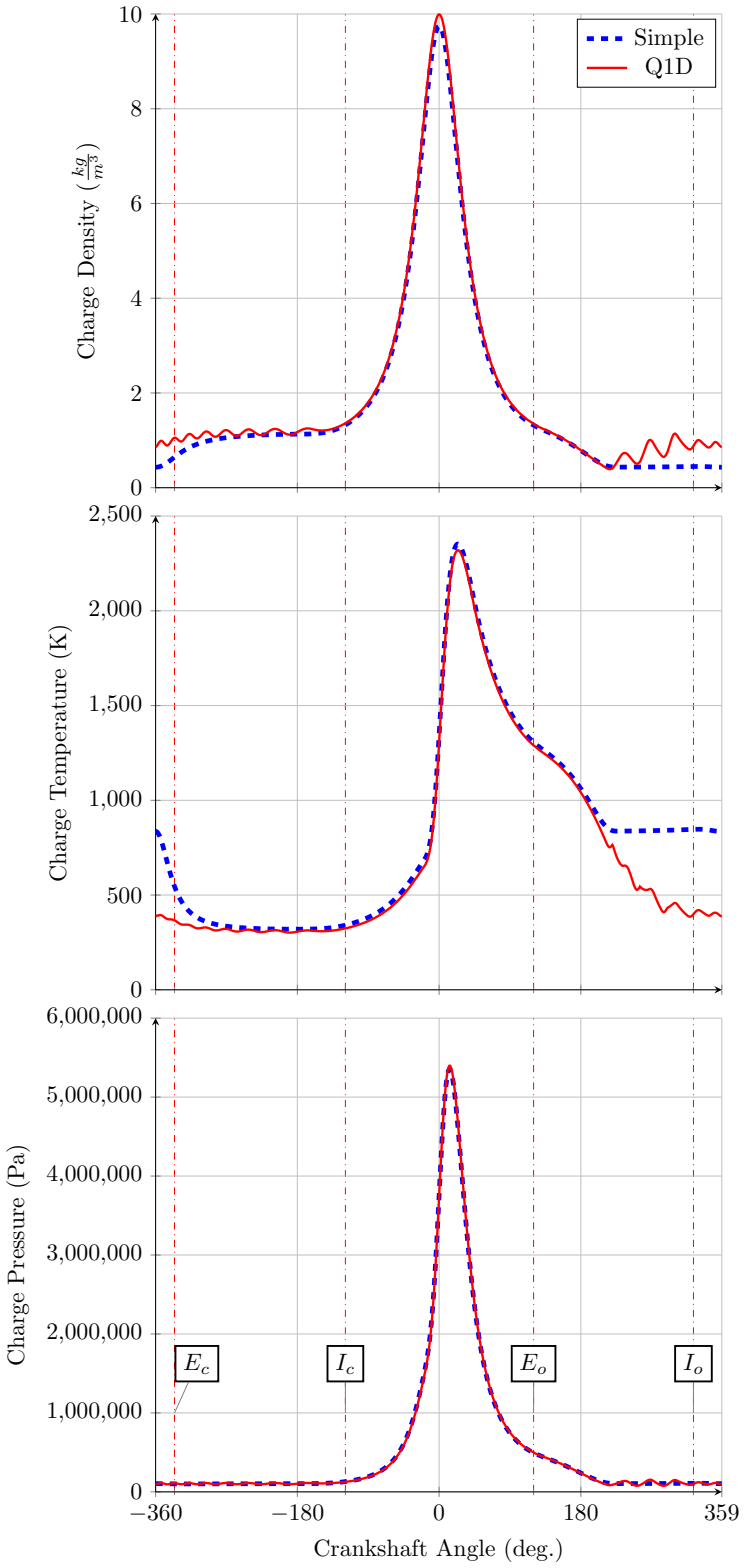

FIGURE 7.34. Charge Properties

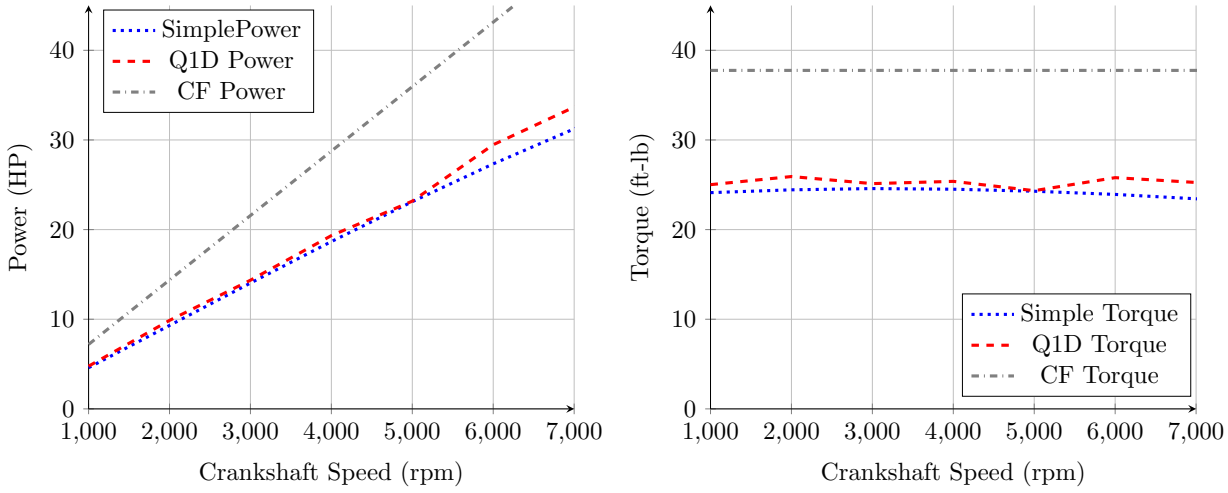

(A) Engine Power

(B) Engine Torque

FIGURE 7.35. Valve-Only Engine Performance Predictions

torque curves always exhibit a peak value–but the fact that the predictions are nearly equal provides a good bit of confidence that the Q1D model is working correctly. The dot-dashed curves present the results from a closed-form technique, included for comparison. The closed-form technique overlays the Otto gas cycle on the four-stroke cycle of the engine, applying isentropic compression and expansion, plus constant-volume combustion to make a prediction of power and torque. The closed-form approach includes no concept of valves, intake flows or exhaust flows, and therefore can't account for any of the engine's fluid dynamics. It predicts a constant torque across the rpm range, which in turn produces a linear power curve extending to infinity. The difference between the closed-form and the current models is due to choking. The current models predict choking of the flow through the valves and account for the power expended as the piston pumps the exhaust gases through the choked valve. This happens, to some degree, at all engine speeds, and is the main reason for the difference between the closed-form and current models across the rpm range. At extremely high RPM the intake flow will also begin to choke, introducing additional pumping losses and reducing the total mass inducted into the cylinder. The Q1D model adds momentum to

the physics. But with only 2 cm of flowpath, the actual momentum of the flows is minimal and at these engine speeds the Q1D model essentially reverts to the simple model. In fact, that the isentropic and Q1D results in this scenario are nearly identical may be showing us the limit that is reached when a real engine is made with intake and exhaust flowpaths of essentially zero length.

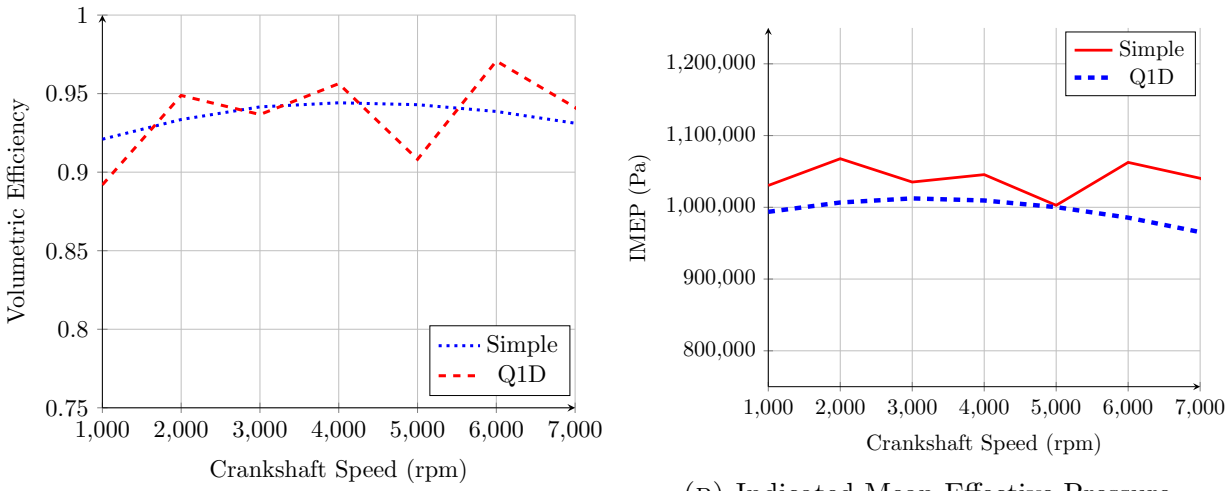

(A) Volumetric Efficiency

(B) Indicated Mean Effective Pressure

FIGURE 7.36. High-Level Performance Parameters

Figure 7.36 provides a comparison of two high-level performance parameters. Figure 7.36a shows the predicted volumetric efficiency for the engine. This is the percentage of mass that actually flows into the cylinder during the intake valve duration, divided by the mass of atmospheric air the cylinder can hold. Figure 7.36b shows the predicted Indicated Mean Effective Pressure for the engine. The IMEP is the average pressure in the cylinder over the engine's two-revolution cycle. Again, we see strong correlation between the two models for both parameters.

7.15. Intake and Exhaust Flows with Drag

Prior to this section, every simulation run was done without discharge or drag coefficients. Since discharge coefficients are measured with a bare cylinder head—no intake runner or exhaust header—we'll set the Q1D model up as before, with only intake and exhaust valves. Figure 7.37a shows the effect of adding discharge coefficients to both the simple and Q1D models. The loosely marked curves are the power curves from Figure 7.35a (no discharge coefficients), expanded out to 15,000 RPM. The densely marked curves are the simulation's predictions for the models with discharge coefficients turned on. Note how the power peaks have moved down and left significantly. These two curves look much more like real engine power curves, with a smooth rise to a peak, then a drop as RPM increases. Both peaks even fall at realistic values, around 9,000 RPM. This comparison makes it very clear that the drag experienced by the intake and exhaust flows is dominant physics. For reasonable, realistic results, drag can't be neglected.

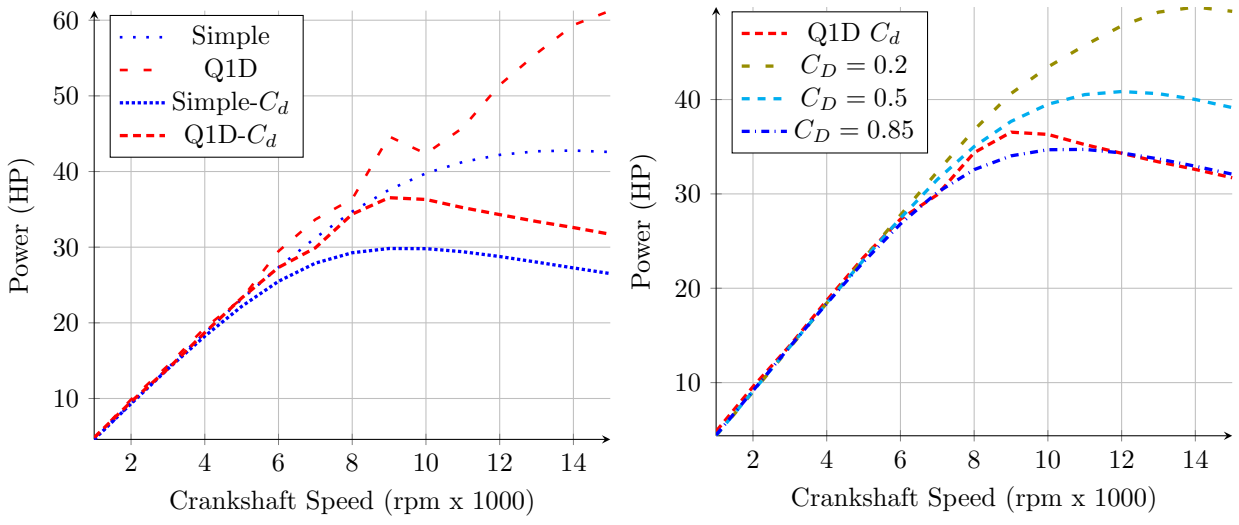

(A) Power Predictions With and Without Discharge Coefficients

(B) Q1D Power Predictions with a Drag Coefficient

Figure 7.37. The Effect of Drag on Engine Power

In section 1.12 (Friction), we noted that researchers have established a value of $C_D = 0.005$ for a smooth, straight pipe. We need to establish a C_D value for the flow through the valves, which aren't straight pipes. The discharge coefficient is actually a measure of the drag through the valves and we can use it to calibrate the valve C_D. Figure 7.37b shows the effect of applying drag to the valves-only Q1D model. The curve labeled "Q1D C_d" is the Q1D power curve from Figure 7.37a, with discharge coefficients applied. For the other curves, the discharge coefficient is turned off and the value of the drag coefficient is being increased. Note the effect as C_D is raised from 0.2 to 0.85. The power peak moves down and to the left. At a value of $C_D = 0.85$ the result is quite similar to the model with discharge coefficients applied. The C_D value is constant and doesn't vary with valve $\frac{L}{D}$, so the power curve doesn't have an identical shape. But this still allows us to establish a reasonable value for the drag coefficient through the valves.

A ballpark C_D value for a cast pipe is 0.05. The fact that C_D must be increased to a value of 0.85, a value *17 times* that of a cast, straight pipe, is a clear indication that the drag through the valves isn't caused by laminar, viscous drag. Instead, it's caused by separated flow. This makes a good bit of sense. At the throat of the valve, velocities are very high. Downstream of the throat, in the subsonic case, the flow is advancing into a strong adverse pressure gradient. In the supersonic case, the flow is advancing through a shock wave and entering an even more powerful adverse pressure gradient. Both cases are a prescription for separation and its associated high drag. From this point on, we'll apply a value of $C_D = 0.85$ through the valve and use a value of $C_D = 0.05$ for straight pipes. When simulating the complete engine, even when using discharge coefficients, we'll apply a value of $C_D = 0.05$ to the straight pipes.

7.16. Final Results: Modeling a Complete Engine

And *finally*, after all of this preparation, we can use the system to model a complete engine. Let's begin with a validation case. We'll model the engine from Chapter 2: cylinder, intake and exhaust valves, intake and exhaust ports, intake runner and exhaust header. The working fluids are equilibrium intake and exhaust mixtures. Discharge coefficients are as specified above. The valve drag coefficient is set to $C_D = 0.85$ and the straight pipe $C_D = 0.05$. Combustion is Wiebe finite rate. Blowby, as well as ring and skirt friction, are turned on. Heat transfer is Woschni. The engine's specifications are repeated in Table 7.6 for convenience.

Table 7.6. Engine Data: Alfa Romeo GTV6 (one cylinder)

bore (b) (mm)	stroke (s) (mm)	connecting rod length (mm)	compression ratio
88	68	131	9.0

clearance volume (cc)	displacement volume (cc)	cylinder volume (cc)	intake runner length (cm)	exhaust header length (cm)
51.7	413.6	465.6	22.0	38.0

Intake Valve Diameter (mm)	Intake Valve Lift (mm)	Intake Valve Opens (°BTDC)	Intake Valve Closes (°ABDC)
40.89	9.0	36.9	119.2

Exhaust Valve Diameter (mm)	Exhaust Valve Lift (mm)	Exhaust Valve Opens (°ATDC)	Exhaust Valve Closes (°ATDC)
36.58	6.4	120.0	23.9

We will continue using the engine in this configuration from this point forward.

Figure 7.38 shows the results: the predicted power, torque and E_v curves for the fully modeled engine. Each graph contains a curve generated using discharge coefficients (C_d) and another using drag coefficients (C_D). We don't have complete dynamometer data for the

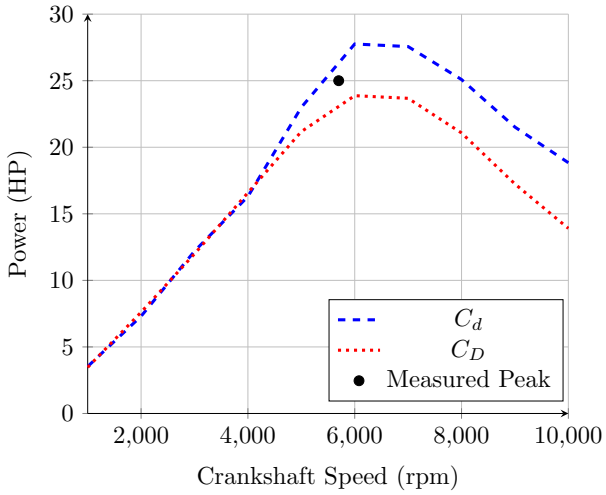

(A) Predicted Power

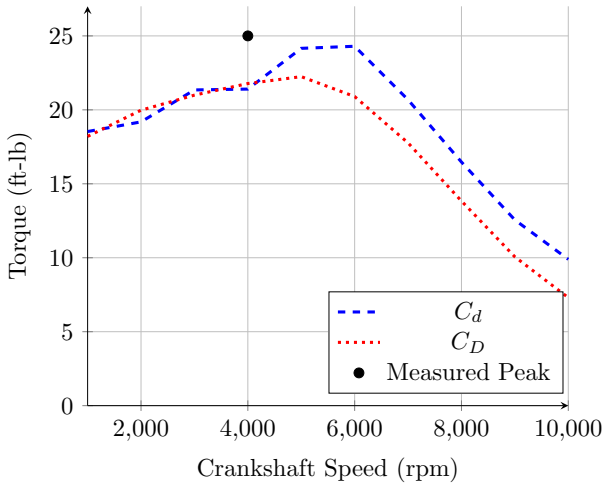

(B) Predicted Torque

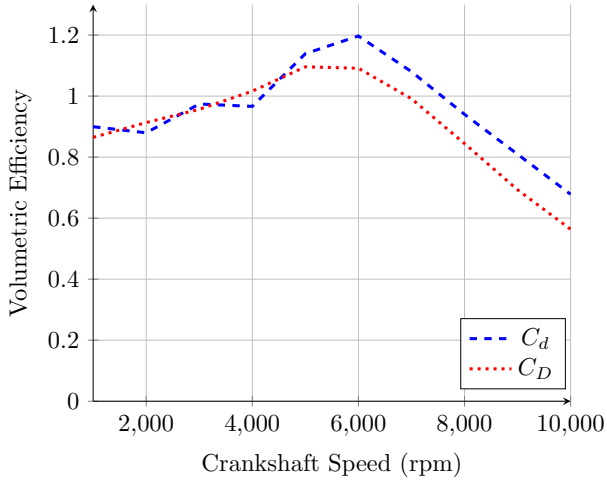

(C) Predicted Volumetric Efficiency

FIGURE 7.38. Predicted Performance, Alfa Romeo GTV6 (One Cylinder)

engine, but from the manufacturer's literature, maximum power is listed as 25 HP at 5,700 RPM. Note how close the two power curves of Figure 7.38a come to that value. Maximum torque is listed as 25 ft-lb at 4,000 RPM. The Torque curves of Figure 7.38b are also not far off. These are exciting results. The predictions are far better than, as Anderson says, "on the same sheet of graph paper", and this without making any specific adjustments to the models! Clearly, parameters like drag or discharge coefficient can be changed to bring the prediction even closer to the actual measurements. We're also not modeling the full intake

or exhaust systems, just the primary flowpaths. Adding the intake plenum and snorkel, plus the full exhaust system, could bring the predictions even closer to reality.

These results confirm that the engine model, as designed, with a time-domain cylinder model connected to finite-volume-based Q1D models of the intake and exhaust flows, accounts for much of the physics of a four-stroke engine. In addition, these results give us a good bit of confidence that the simulation's modeling is realistic and fairly accurate. It's predictions can be given a reasonable level of trust.

The simulation generated the curves of Figure 7.38 in about *10 minutes* on a single processor of an Intel P6200-powered, 2.14 GHz laptop. While this isn't instantaneous, it begins to provide the kind of rapid turnaround that is needed for a designer to go through an effective edit/test cycle and understand the engine's responses, or to iterate on a design until it meets his requirements.

Yin [65] and Sammut et al. [66] both mention Engleman's equation for approximating the location of the E_v peak from intake runner length:

$$N = \frac{13.5c}{k}\sqrt{\frac{A}{L\mathcal{V}_d}}\sqrt{\frac{r-1}{r+1}} \; = 5,900 - 7,400 \text{ RPM} \tag{7.86}$$

where c is the speed of sound in the intake mixture, k is a value between 2 and 2.5, A is the cross sectional area of the intake runner, L is the length of the runner, $\mathcal{V}_d$ is the displacement volume of the cylinder r is the compression ratio and N is RPM. For the engine above, this predicts the torque peak between 5,900 and 7,400 RPM. The 5,900 value doesn't compare too badly to the predicted discharge coefficient peak but it's some distance from

the measured peak of 4,000 RPM. The 7,400 RPM figure is almost on another sheet of graph paper.

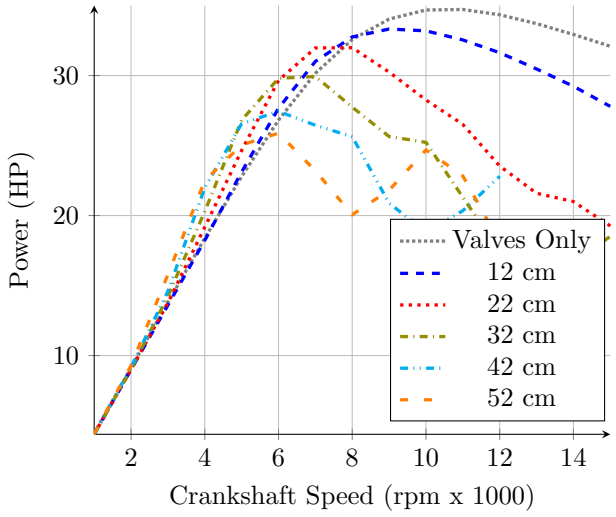

(A) Variation of Power with Intake Runner Length

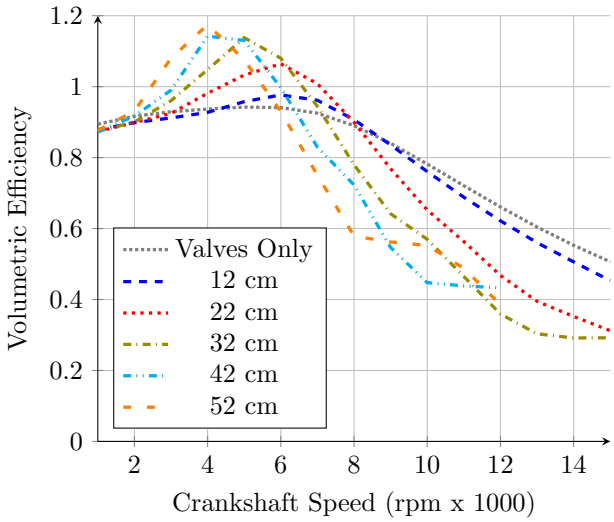

(B) Variation of Volumetric Efficiency with Intake Runner Length

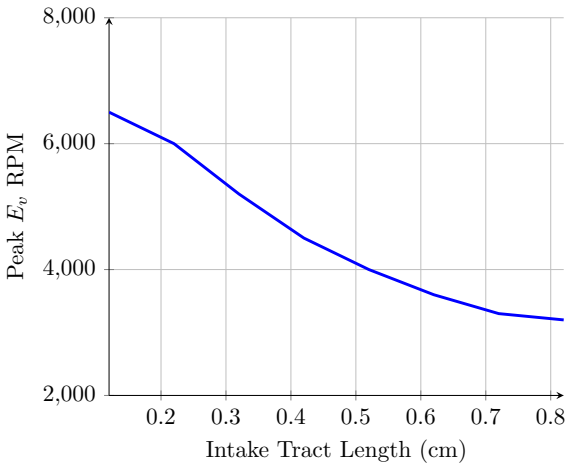

(C) Variation of Peak Volumetric Efficiency RPM with Intake Runner Length

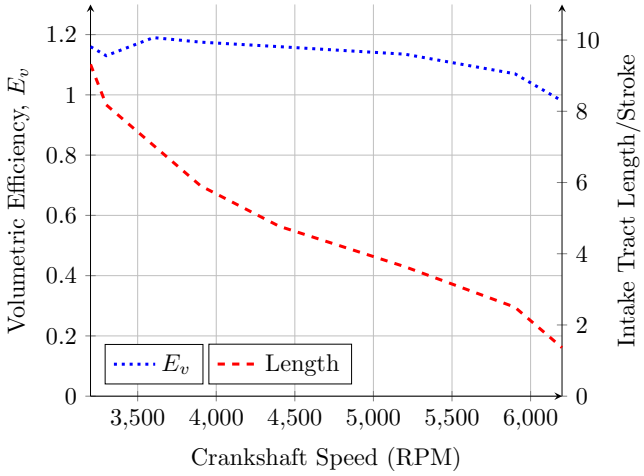

(D) Optimized Intake Runner Length for Maximum E_v

FIGURE 7.39. The Effect of Intake Runner Length on Engine Performance

The working system allows us to delve deeper into the engine responses. We can vary parameters and see how they effect the operation of the engine. For these runs, the working fluid is frozen, standard air. Drag coefficients are set as above and the loss models are all turned off. Combustion is finite-rate Wiebe. Figure 7.39 shows how the engine responds

when the exhaust valve is left open to the atmosphere and a straight pipe is connected to the intake valve. In Figure 7.39a, the densely dotted curve shows the valves-only response. When a 10 cm pipe is added (for a total flowpath length of 12 cm), simulating the presence of the intake port, the ascending portion of the curve gets steeper and the power peak moves down and to the left. With the lengthening of the pipe from 20 through 50 cm, the front of the curve gets even steeper and the peak continues moving down and to the left. These are qualitatively very realistic results, what one would expect to see from a real engine on a dynamometer.

Figure 7.39b shows the reason for the power peak shift. With increasing intake runner length, the volumetric efficiency peak moves up and to the left. For a given intake runner length, the point of maximum volumetric efficiency is also the point of maximum torque. And so as the intake runner is lengthened, the torque peak is moving to a lower RPM. Figure 7.39c shows the relationship between intake runner length and the crankshaft speed where peak volumetric efficiency occurs. This takes us back to Engleman's equation, 7.86. The relationships are close:

$$\text{Engleman: } N = 2,976\,(L_{\text{intake}})^{-0.5} \tag{7.87}$$

$$\text{Model: } N = 2,990\,(L_{\text{intake}})^{-0.46} \tag{7.88}$$

But the small difference in exponents makes for a significant difference in the results. The cylinder and intake tract together don't quite form a perfect Helmholtz resonator.

Figure 7.39d shows what would happen if we could adjust the length of the intake tract with RPM. We would be able to maximize volumetric efficiency and torque across the entire

RPM range. In the case of this engine, E_v can be kept above 1 from 3,200 to 6,300 RPM. The intake tract length required varies with the same $(L_{\text{intake}})^{-0.46}$ relationship that we see above. The intake length is non-dimensionalized by the engine stroke.

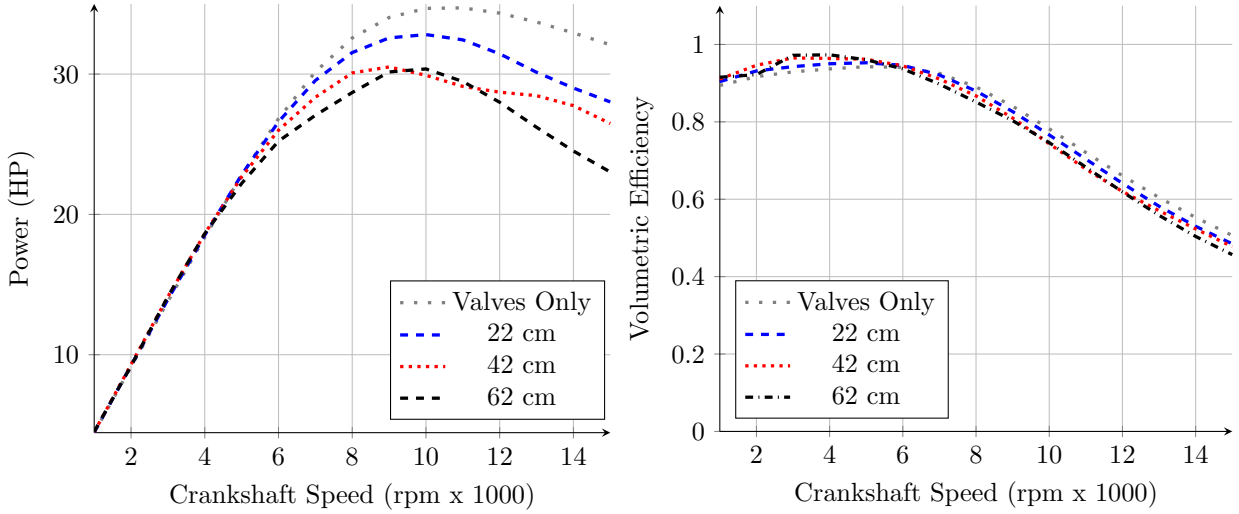

(A) Variation of Power with Exhaust Header Length

(B) Variation of Volumetric Efficiency with Exhaust Header Length

FIGURE 7.40. The Effect of Exhaust Header Length on Engine Performance

Figure 7.40 shows the situation reversed. Here, the intake valve is left open to the atmosphere and the exhaust header length is varied. Figure 7.40a shows that, if the exhaust flow has any dynamic interaction with the charge, that effect doesn't, in turn, affect the intake stroke. Instead, as the length of the header is increased, exhaust pumping losses grow and the height of the center and back of the power curve is reduced. For a given header length, pumping losses increase with RPM, and so in addition to the back end of the curve dropping, the power peak is also displaced slightly to the left. Figure 7.40b shows little variation in volumetric efficiency with header length, confirming that the exhaust flow has little effect on the intake stroke. Consider the freedom this provides the engine designer. Adjustments to either the intake or exhaust system length are relatively independent.

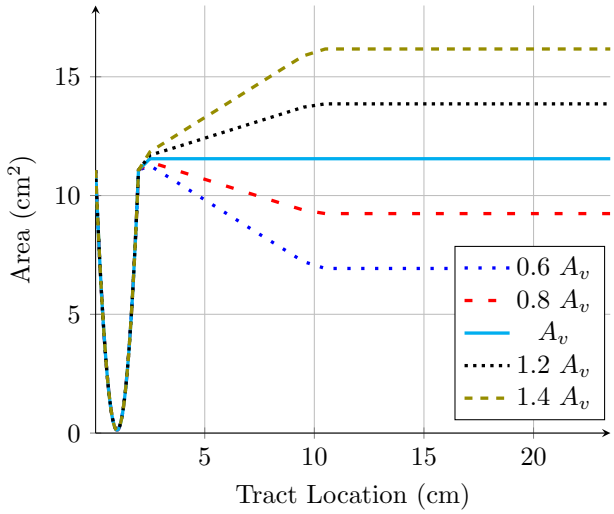

(A) Intake Tract Area Profiles (Flow *in* is right to left.)

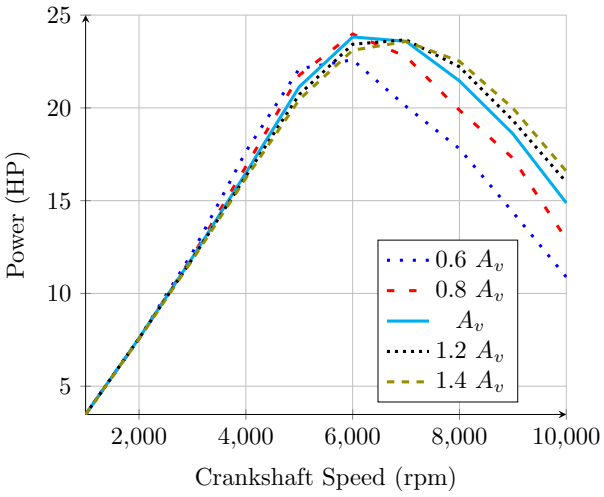

(B) Variation of Power with Intake Area

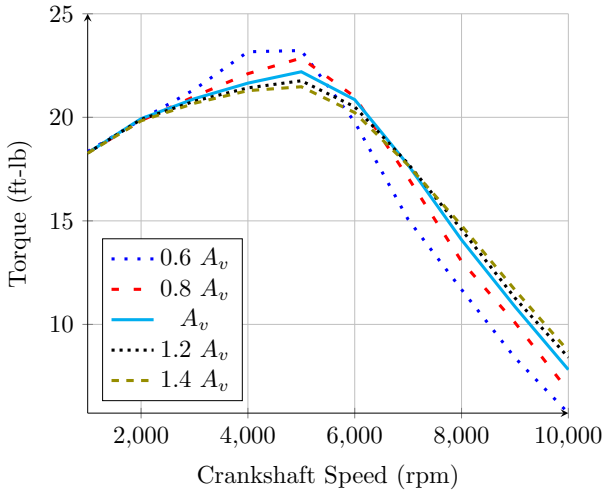

(C) Variation of Torque with Intake Area

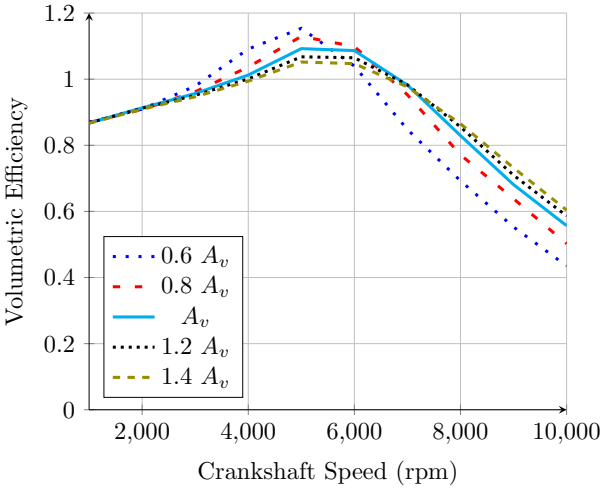

(D) Variation of Volumetric Efficiency with Intake Area

FIGURE 7.41. The Effect of Intake Area on Engine Performance

Figure 7.41 shows that the cross-sectional flowpath area of the intake tract has a significant effect on engine performance. In this scenario, the intake valve connects to an intake port 8 cm long. The port varies linearly with area to match the Nth end of the valve with the 0th end of the intake runner, which is 14 cm long. The total length of the intake tract is 24 cm. The area of the runner is varied from 60% to 140% of the valve area. Figure 7.41a shows the area profiles of the five cases. A_v is the skirt area of the valve. Figure 7.41b shows

the strong effect intake tract area has on the power curve. As the area is reduced from A_v, the power peak moves first up and to the left, then down and to the left. As the area is increased from A_v, the power peak moves down slightly and to the right. Importantly, *there is an optimum intake tract area.* When the area is reduced to 0.8 A_v, we see an absolute power peak. As an added benefit, the peak moves down in the RPM range, steepening the front of the curve. This is a significant finding for engine tuning. Figure 7.41c shows that reducing the intake tract area moves the torque peak up and to the left. If low RPM torque is a requirement, this provides a way to deliver it. As always, volumetric efficiency responds as torque does, with the peak moving up and to the left as area is reduced.

The cross-sectional exhaust flowpath area also has a significant effect on engine performance. Figure 7.42 shows what happens when the area of the exhaust header is increased and decreased, just as the intake runner was. The exhaust port length is 8 cm and the port varies in area linearly from the valve to the header. The header is 29 cm long, making for a total exhaust tract length of 39 cm. Figure 7.42a shows the profiles of the exhaust tract for the five cases, with the header varying from 0.6 A_v through 1.4 A_v. Figure 7.42b shows the effect varying the exhaust area has on power. If the area is reduced from A_v, the entire power curve shifts down, presumably because of increased pumping losses. But when the area is increased from A_v, the power peak rises and shifts slightly to the left, both beneficial responses. The 1.2 and 1.4 A_v curves are coincident, so there is a tract area beyond which there is no improvement. And so, just as there is for the intake, *there is an optimum exhaust tract area.* The effect on torque is interesting. Reducing the area below A_v moves the torque peak down the RPM range, but also reduces its magnitude. Enlarging the area above A_v

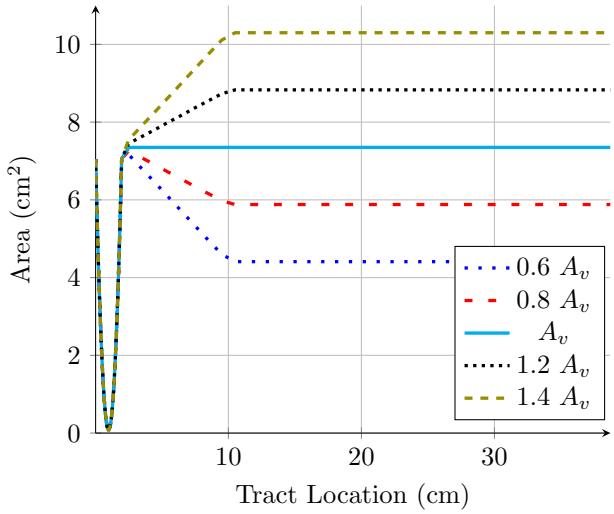

(A) Exhaust Tract Area Profiles (Flow *out* is left to right.)

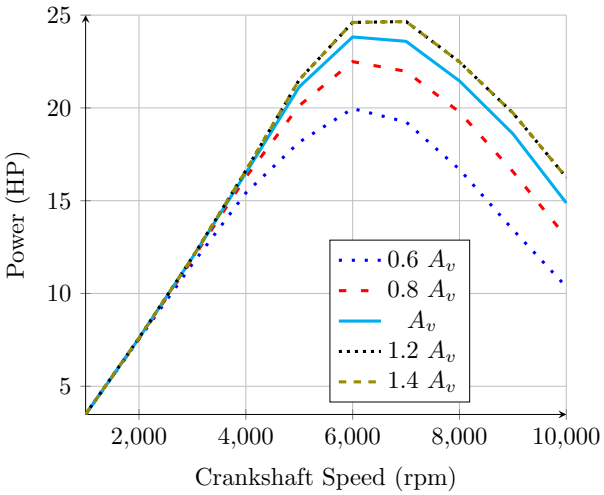

(B) Variation of Power with Exhaust Area

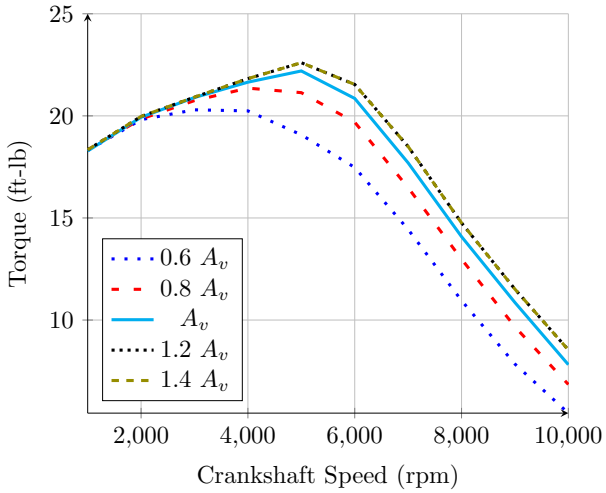

(C) Variation of Torque with Exhaust Area

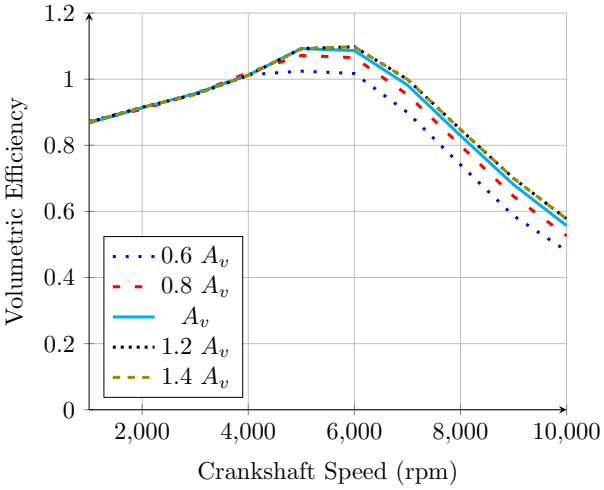

(D) Variation of Volumetric Efficiency with Exhaust Area

FIGURE 7.42. The Effect of Exhaust Area on Engine Performance

raises the peak and moves it slightly to the right. We see the same effect on volumetric efficiency.

Next let's examine the effect of valve timing. Going back to the complete engine with drag coefficients and all loss models turned on, Figure 7.43 shows the effect of advancing and retarding the timing of the intake valve. Figure 7.43a shows the valve area profiles. The exhaust valve timing is maintained while the intake valve timing is being advanced

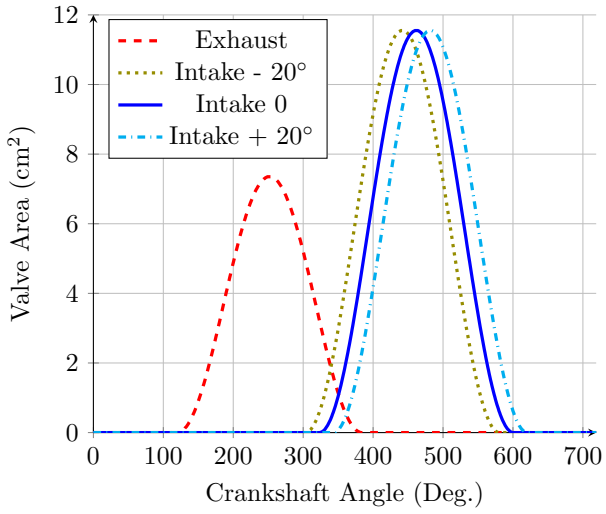

(A) Advanced and Retarded Intake Valve Timing

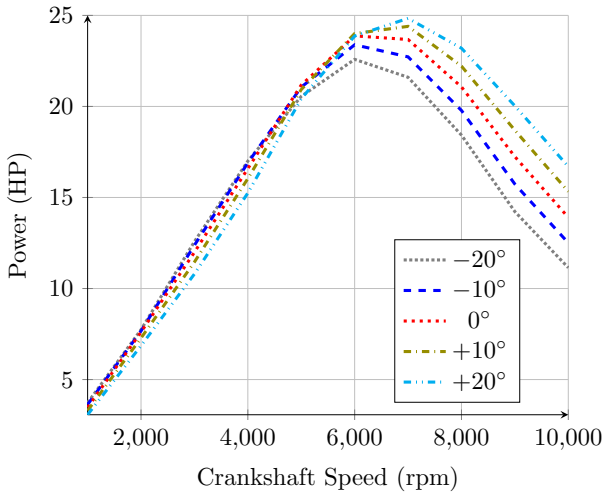

(B) Variation of Power with Intake Cam Timing

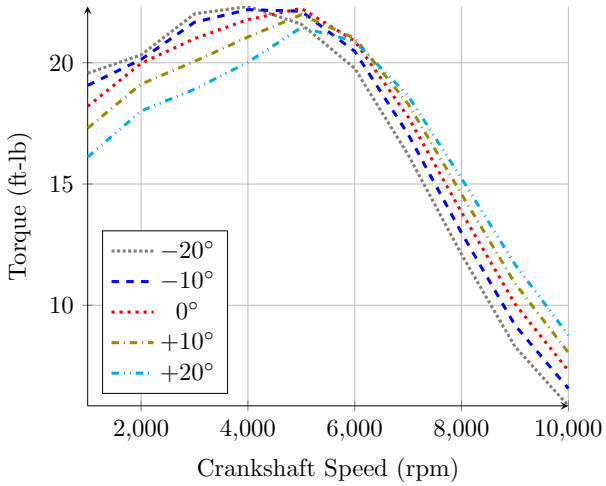

(C) Variation of Torque with Intake Cam Timing

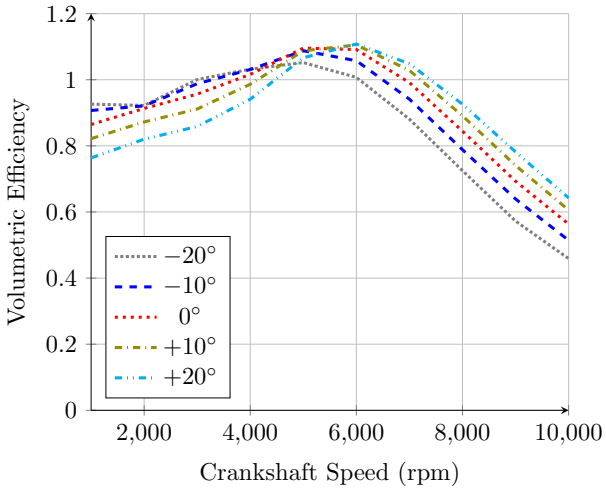

(D) Variation of Volumetric Efficiency with Intake Cam Timing

FIGURE 7.43. The Effect of Intake Cam Timing

(-) and retarded (+) with constant duration. Figure 7.43c shows that intake valve timing has a significant effect on low- and high-RPM torque. As the timing is advanced from the standard value of 0° (-10° and -20° curves), low RPM torque increases and high RPM torque decreases. As the timing is retarded from the standard value (+10° and +20° curves), low RPM torque decreases significantly and high RPM torque increases. This trend results in an

increase in the height of the power peak in Figure 7.43b, with a shift in the peak to higher RPM as intake valve timing is retarded. Volumetric efficiency responds much like torque.

EFFECTS OF ALTERING CAMSHAFT TIMING	
Advancing	Retarding
Begins Intake Event Sooner	Delays Intake Closing Event
Open Intake Valve Sooner	Keeps Intake Valve Open Later
Builds More Low-End Torque	Builds More High-RPM Power
Decrease Piston-Intake Valve Clearance	Increase Piston-Intake Valve Clearance
Increase Piston-Exhaust Valve Clearance	Decrease Piston-Exhaust Valve Clearance

FIGURE 7.44. Comp Cams' Experience on Intake Cam Timing

Comp Cams [67], a cam manufacturer, has many years of experience testing its cams in real engines on the dynamometer. On its website it offers its customers the advice offered in Figure 7.44. They find that advancing the cam "builds more low-end torque" and retarding the cam "builds more high-RPM power". These are exactly the trends the simulation has revealed above.

Next we look at the effect of changing exhaust cam timing. Figure 7.45a shows the intake valve timing maintained while the exhaust valve timing is advanced (-) and retarded (+). Figure 7.45c shows that advancing the timing of the exhaust valve shifts the entire torque curve down. Retarding the timing raises the entire curve. This might be due to the greater length of time that the expanding charge is retained over the power stroke. Figure 7.45b shows that retarding the timing makes a significant change to the power curve, raising the power peak while shifting it slightly to the right. From the plots, it appears the power curve is arriving at an asymptote, and there is likely an optimal timing setting. Exhaust timing also has a significant effect on volumetric efficiency. As the timing is retarded, overall volumetric efficiency rises significantly.

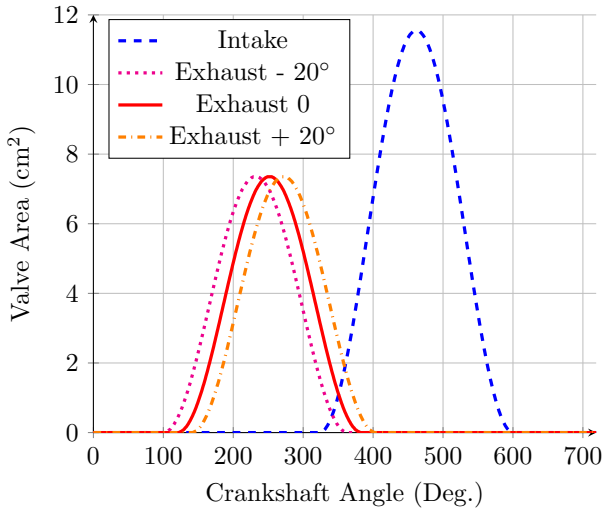

(A) Advanced and Retarded Exhaust Valve Timing

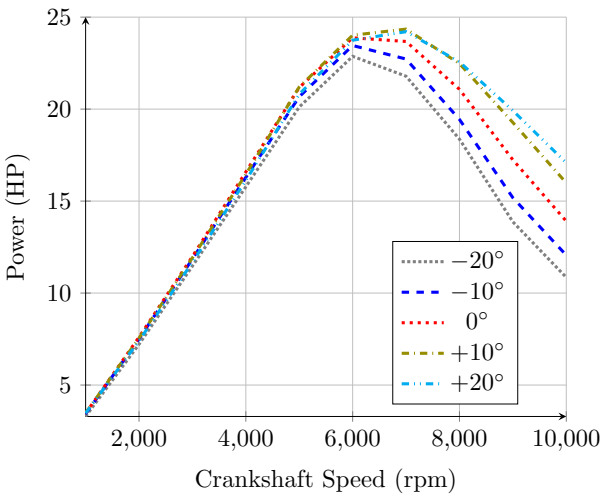

(B) Variation of Power with Exhaust Cam Timing

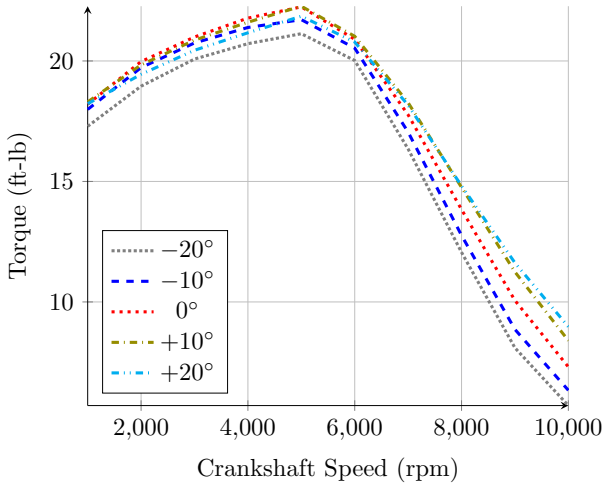

(C) Variation of Torque with Exhaust Cam Timing

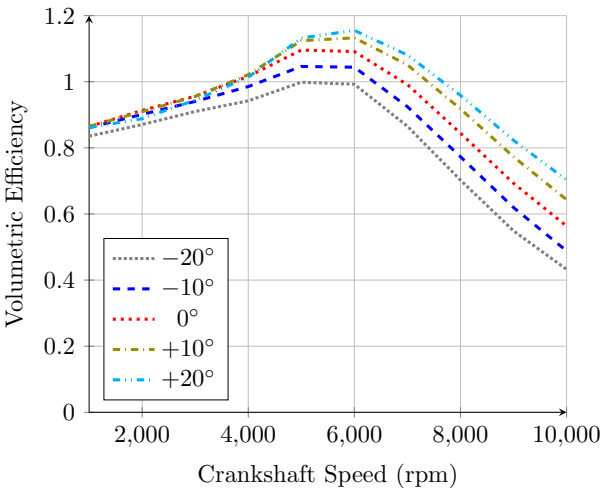

(D) Variation of Volumetric Efficiency with Exhaust Cam Timing

FIGURE 7.45. The Effect of Exhaust Cam Timing

CHAPTER 8

Comparisons and Conclusions

8.1. Introduction

In this chapter, we'll make comparisons to determine the significance of each of the submodels that we've included in the overall engine model. We'll decide whether or not each embodies dominant physics. Then we will collect the conclusions that we have drawn from this and the previous chapters.

8.2. Simple Valve Model

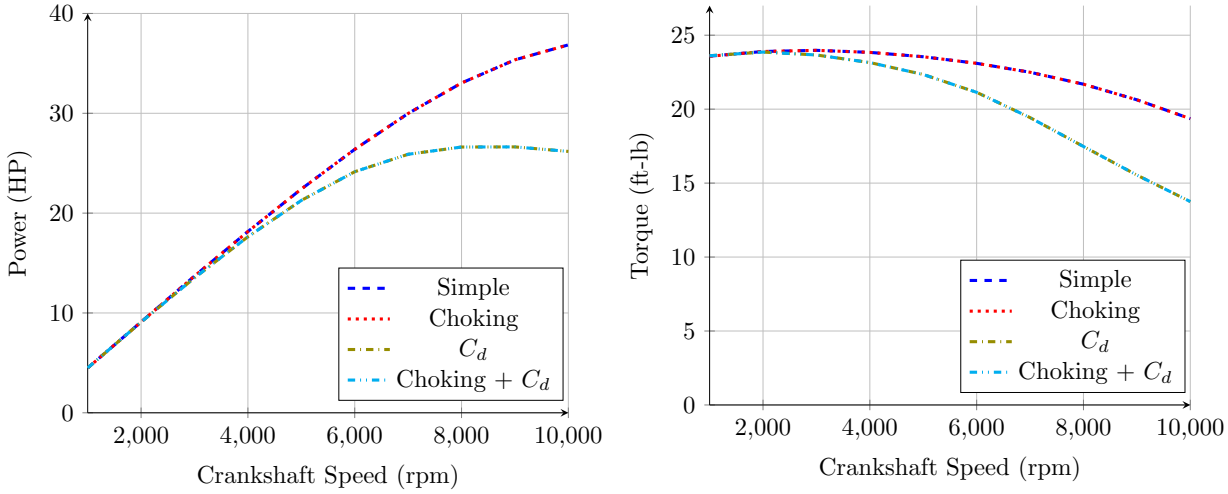

(A) Predicted Power

(B) Predicted Torque

Figure 8.1. Performance Predictions with the Simple Valve Model

Figure 8.1 shows the simulation's predictions of the performance of our test engine, as configured in Table 7.6. In this case, the simulation is using the simple valve model. All loss models are turned off and combustion is finite-rate, Wiebe. In Figure 8.1a there are four power curves. The curve labeled "Simple" is the bare simple valve model with choking

detection and discharge coefficients (C_d) turned off. "Choking" is the result with choking detection turned on and C_d off. Note how this and the previous curve are identical. This shows that choking is intrinsically accounted for in the isentropic flow equations. No explicit detection, with separate equations, is necessary. "C_d" is the result with C_d turned on and choking detection turned off. Note the significant difference between this and the previous curves. With only isentropic flow equations in place, the flow through the intake valve experiences no throttling or restriction unless the flow chokes. Likewise, there is no pumping work on the flow through either valve unless the flows choke. This happens with varying degrees during the exhaust stroke, the duration increasing with RPM. The intake flow doesn't choke until extremely high RPM. With discharge coefficients turned on, the extent of choking through the strokes is greatly increased. This acts to limit the intake mass flow rate and total intake mass transfer, reducing volumetric efficiency, torque and power. The increased level of choking also magnifies pumping losses, reducing power output. The pumping losses increase with RPM, causing the power curve to reach a peak, then drop as RPM rises even further. In the fourth curve, "Choking + C_d", both options are on and we see that adding choking to C_d makes no difference. When using the isentropic flow equations, the detection of choking is redundant. Note the same behavior in the Torque curves.

8.3. Comparing the Simple and Q1D Valve Models

Figure 8.2 compares the simulation's performance predictions with the simple and Q1D flow models. Here, the simulation is operating at its maximum level of detail. The intake and exhaust tracts are modeled to match those of the real engine. The total intake length is 24 cm and the total exhaust length is 40 cm. The working fluid is equilibrium intake and

exhaust gases. Blowby, ring and skirt friction, and Woschni heat transfer are all turned on. Discharge coefficients are turned on for the simple valve model. The Q1D model is operated with both discharge coefficients ("C_d" curves) and drag coefficients ("C_D" curves).

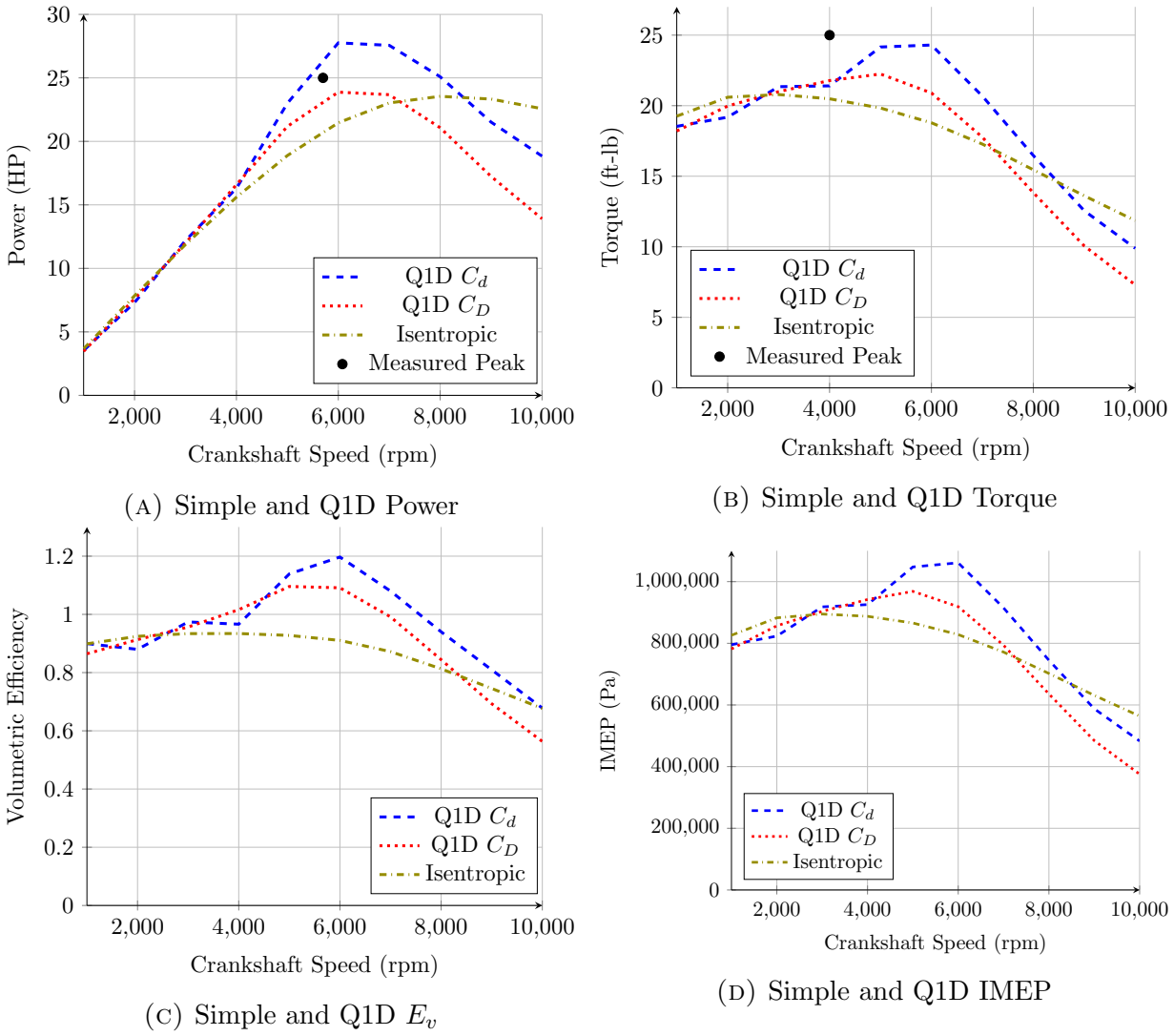

(A) Simple and Q1D Power

(B) Simple and Q1D Torque

(C) Simple and Q1D E_v

(D) Simple and Q1D IMEP

FIGURE 8.2. Performance Predictions from Both Models

Figure 8.2a shows the power predictions for the two models. As we saw in the previous chapter, the Q1D results straddle the measured power peak. The simple model is well below the peak, about 20% low, at 5,700 RPM, and has its own peak just above 8,000 RPM, much too high to be considered a reasonable estimate. The reason for the difference is shown in

Figure 8.2c. Note the difference in the nature of the volumetric efficiency (E_v) estimates. The Q1D model accounts for the so-called ram effect of the intake flow, predicting volumetric efficiencies above 1 at around 5,500 RPM, thus the torque peak at the same crankshaft speed. The simple model, neglecting the momentum of the intake and exhaust flows, predicts a fully sub-unity E_v curve with a peak around 3,000 RPM. Both its E_v and torque peaks are misplaced low. The Q1D model reproduces the dynamic interaction between the charge and the intake flow that leads to the strong rolloff in E_v and torque after the peak. The simple prediction leads to a much less severe decrease in E_v and torque after the peak, leading to the power peak residing at an elevated RPM. The Indicated Mean Effective Pressure curve is included for detail. Note how it follows the E_v curves.

The real beauty of the simple valve model is that it is computationally simple. With piston and ring friction turned off, the set of curves here can be calculated in 7 seconds on one processor of a 2.13 GHz Pentium P6200 laptop. With piston and ring friction turned on, the same run takes about a minute. In contrast, the Q1D model is highly computationally intensive, and requires on the order of 10 minutes to generate this set of curves, regardless of piston and ring friction state. But speed and convenience aren't everything. Imagine if we were to compare the two models in the varying intake runner test of the previous chapter. We already saw the positive effect changing runner length has on the Q1D model. The simple model is completely insensitive to intake and exhaust length and on those plots its responses would comprise a single, unchanging curve. That comparison by itself eliminates the simple valve model as a useful tool. Momentum of the intake and exhaust flows is dominant physics and can't be neglected.

Since the simulation's predictions with the simple valve model vary significantly from reality, we will drop that model. From this point on, we will only use the Q1D model for comparisons. Let's look into the submodels and see what effect each of them has on the high-level predictions of the engine model. In Chapter 7 we showed that fluid drag is dominant physics. So our discussion here will begin with the baseline engine model set up as above and with the Q1D model operating with the valve drag coefficient set to $C_D = 0.85$ and the pipe drag coefficient set to $C_D = 0.05$. To avoid masking any model effects, the baseline configuration will have all of the loss models turned off. Figure 8.3 shows the system's predictions for the engine in the baseline configuration. Note how much closer the power and torque predictions are to the measured peak values. The volumetric efficiency curve is included, but the observant reader will see that it doesn't differ from that with losses included.

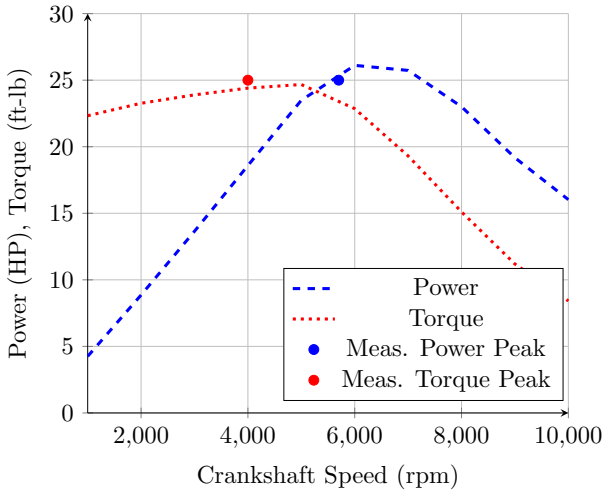

(A) Baseline: Loss-Free Power and Torque

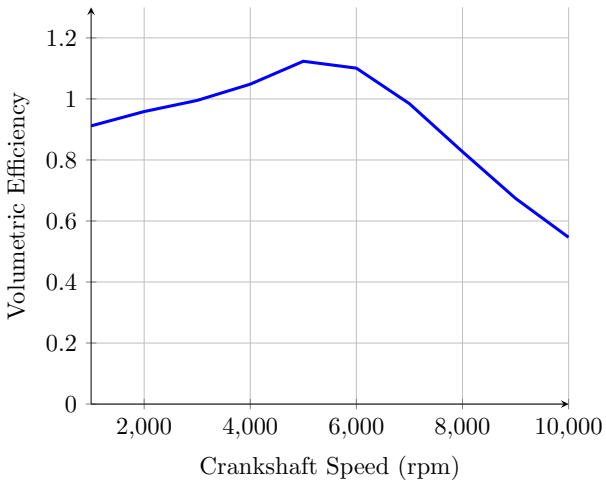

(B) Baseline: Loss-Free Volumetric Efficiency

Figure 8.3. The Baseline Model

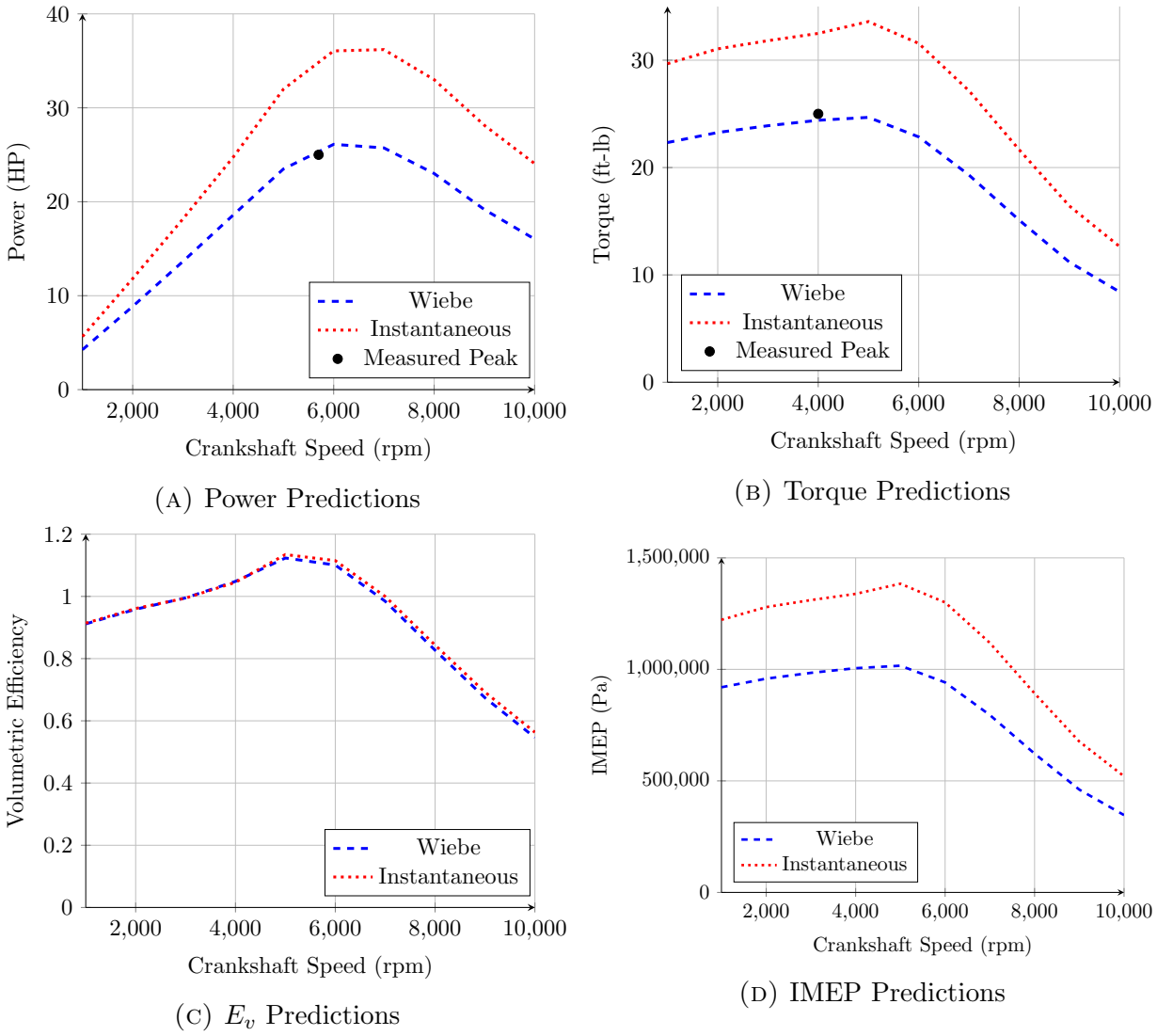

(A) Power Predictions

(B) Torque Predictions

(C) E_v Predictions

(D) IMEP Predictions

Figure 8.4. Performance Predictions with Finite-Rate and Instantaneous Combustion

Figure 8.4 compares the simulation's predictions with Wiebe, finite-rate combustion and instantaneous combustion. The Wiebe model begins releasing combustion energy at 20° BTDC and has a duration of 60°. The instantaneous model releases the entirety of the charge's combustion energy at TDC. In closed-form analyses, this is referred to as "constant-volume" combustion. There is a very significant difference in the results. Figures 8.4a and

8.4b show the instantaneous power and torque peaks to be about 38% higher than the finite-rate peaks. Figure 8.4c shows the volumetric efficiency to be nearly unchanged, and so the increase in power and torque are due to more energy being extracted from the hot, high-pressure charge when combustion is instantaneous. While the difference in results unfortunately eliminates instantaneous combustion as a useful model, it also shows us that accelerating the rate of combustion in a real engine could make the engine deliver more power for its size (greater Indicated Mean Effective Pressure—IMEP) and return greater efficiency—a note for future research.

8.4.2. Working Fluid Models

Figure 8.5 shows the simulation's performance predictions using three different working fluid models. Figure 8.5a shows the power delivery when the simulation models frozen, standard air, equilibrium air and equilibrium intake/exhaust gases. For the frozen air model, all of the gas properties, in the intake and exhaust systems and in the in-cylinder charge, are those of frozen, standard air. For the equilibrium air model, the intake gas properties are those of air at standard temperature, so identical to frozen, standard air. The exhaust gas properties are those of air, frozen at 800 K. The gas properties of the in-cylinder charge are those of air at the charge temperature. For the equilibrium intake/exhaust model, the intake gas properties are those of the intake octane/air mixture at standard atmospheric temperature. The exhaust gas properties are those of the combustion product mixture, frozen at 800 K. The properties of the in-cylinder charge switch back and forth. From intake valve opening to TDC of the compression stroke, the gas properties are those of the intake octane/air mixture at charge temperature. From TDC of the compression stroke to intake

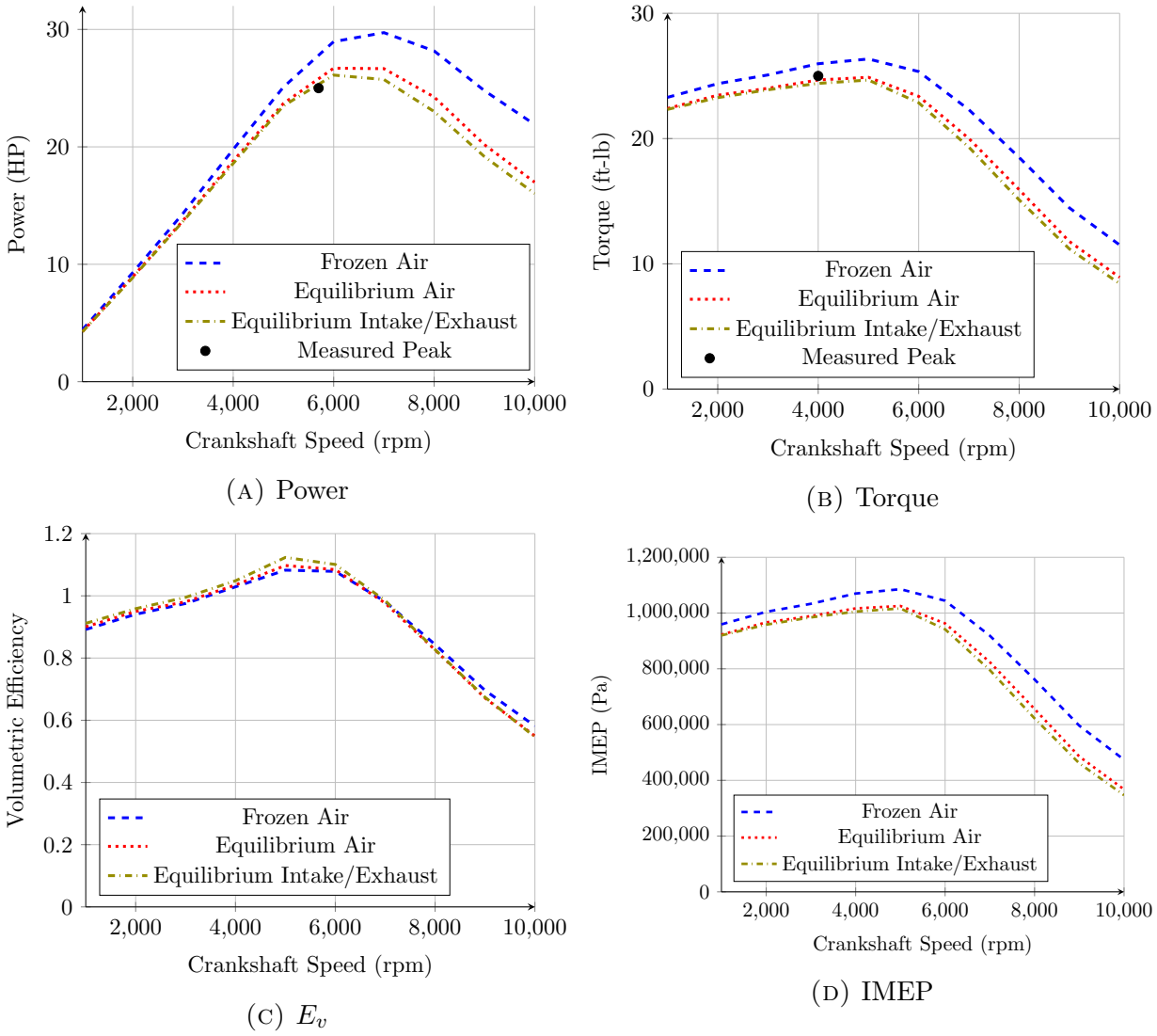

(A) Power

(B) Torque

(C) E_v

(D) IMEP

FIGURE 8.5. Performance Predictions with Three Working Fluid Models

valve opening, the properties are switched to those of the combustion products at charge temperature. As we saw in Chapter 5, frozen air stores no energy in the extended modes, instead manifesting all of its internal energy as temperature. This increases cylinder pressures and results in significantly higher torque and power predictions. It appears that energy storage dominates over species properties, as the equilibrium air curves don't fall far from the equilibrium intake/exhaust curves. Note that in Figure 8.5c, the volumetric efficiency using the three fluid models doesn't vary much. We can conclude that the differences in the power,

torque and IMEP curves are almost all thermodynamic. At the temperatures experienced in the charge after combustion, energy storage in the extended modes is dominant physics. With significant differences caused by energy storage, and minor differences caused by gas species, it seems prudent to apply equilibrium intake and exhaust mixtures if one wants to make accurate predictions.

8.4.3. Blowby

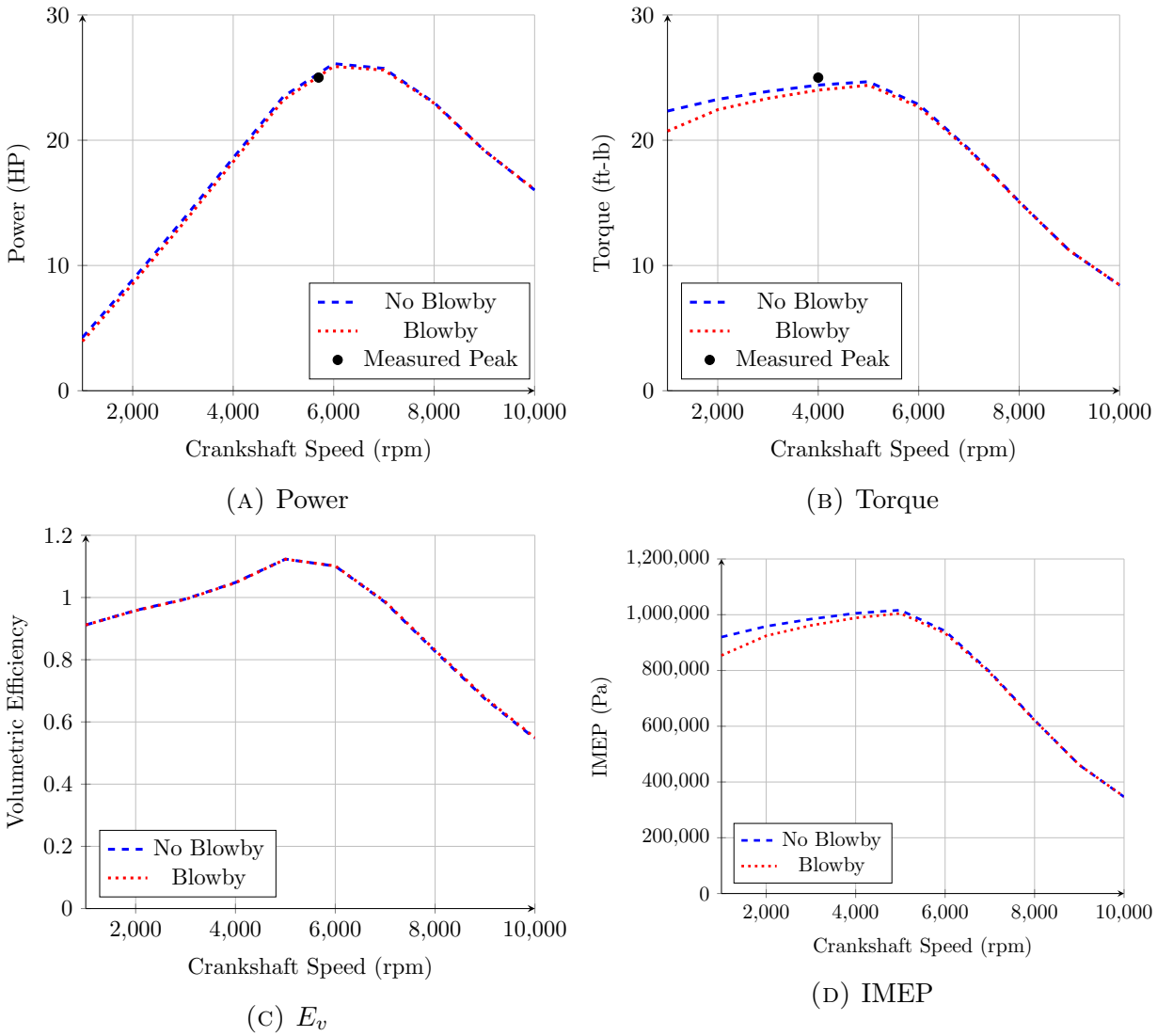

(A) Power

(B) Torque

(C) E_v

(D) IMEP

Figure 8.6. Performance Predictions with and without Blowby

Figure 8.6 shows the simulation's predictions of engine performance with and without blowby. Figure 8.6a shows little change to the power curve with the blowby model turned on. There is a slight loss of power in the low RPM range, but not a significant amount. Volumetric efficiency, Figure 8.6c isn't affected at all. This makes sense, since there is little pressure differential between the charge and the atmosphere over the intake stroke and blowby mass flow is tiny compared to the mass flow through the intake tract. But Figure 8.6b shows a significant loss of torque at low RPM—almost 8% at 1,000 RPM—decreasing toward the torque peak. This is caused by the loss of working fluid, and therefore charge pressure, over the power stroke. The pressure differential between the charge and the crankcase during the power stroke is always high enough to choke the flow through the blowby passage, putting an upper limit on the blowby mass flow rate. As RPM increases, the duration of loss through the blowby decreases, resulting in a decreasing loss of working fluid and torque with RPM. Figure 8.6d shows these same phenomenon manifest in IMEP. While a look at the power curve suggests blowby could be neglected, if we're interested in predicting torque correctly, we need to account for blowby. We'll call blowby dominant physics.

8.4.4. Heat Transfer

Figure 8.7 shows the simulation's predictions of engine performance with three heat transfer models and with no heat transfer. Comparing Figures 8.7a and 8.7b, we can see that heat loss is greatest at low RPM for all three models and decreases with increasing RPM. This makes intuitive sense, as there is less time for heat to transfer from the charge to the cylinder, and vice-versa, as RPM increases. The Chang modification of the Woschni correlation realizes the least amount of energy loss. The Woschni correlation loses noticeably

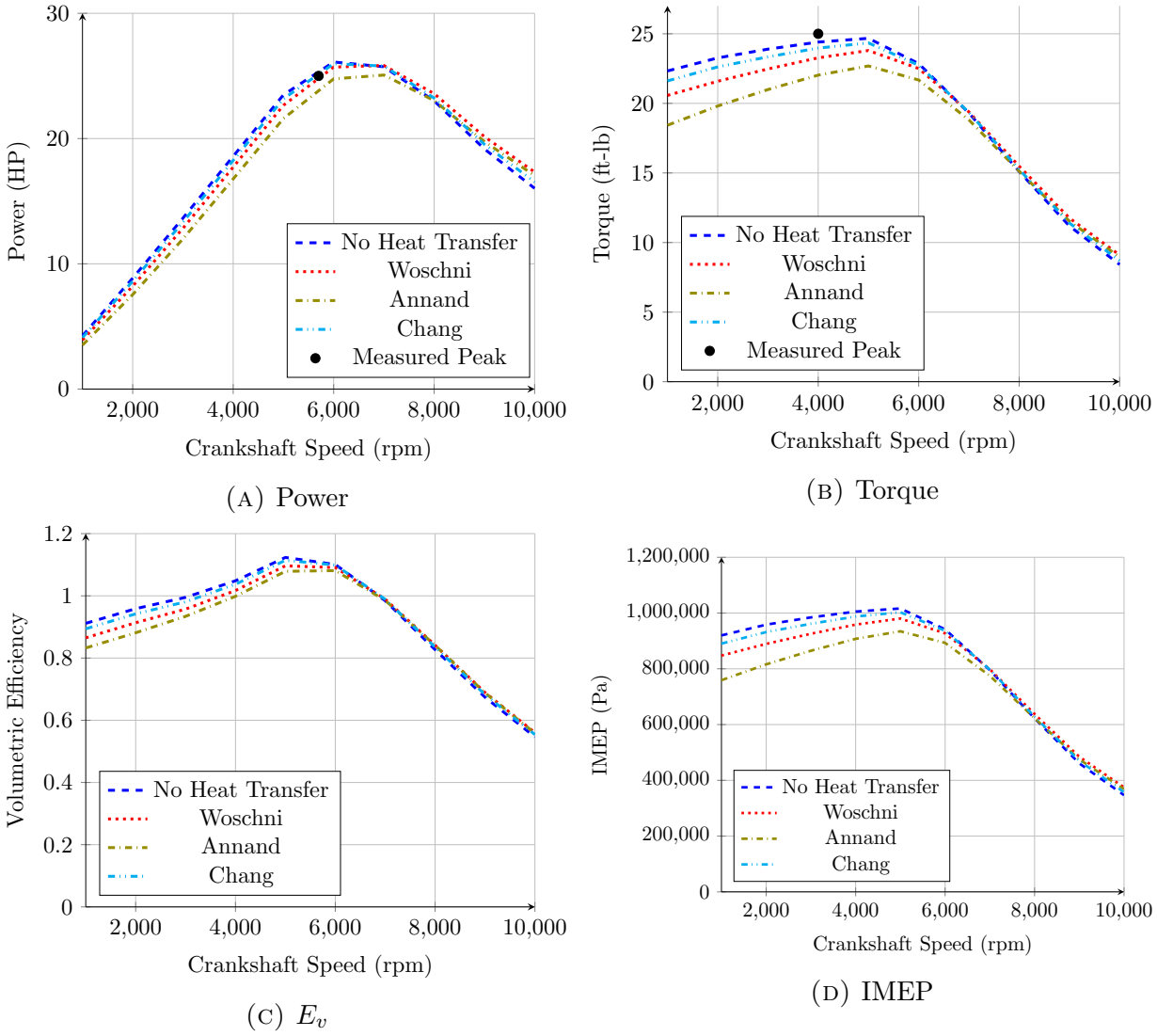

(A) Power

(B) Torque

(C) E_v

(D) IMEP

FIGURE 8.7. Performance Predictions with Selected Heat Transfer Models

more. The Annand correlation is the simplest of the three and predicts the greatest level of energy loss. The effect of heat transfer on the power curve could be significant. Annand sees a maximum loss of 9.7%, Woschni loss is 4.6% and Chang is 1.7%. Which model is most accurate? It's difficult to say without a great deal more investigation. The Chang model uses the Woschni framework with updated parameters to match modern engines. That makes it seem like it may be the most trustworthy. With our limited data set, we have no way of determining which is best. The torque curves, Figure 8.7b show much stronger heat

transfer effects. Note the effect heat transfer has on volumetric efficiency. When considering heat transfer, we tend to think only of the "forward" transfer from the hot charge to the cooler cylinder during combustion and the power stroke, when temperature differentials are greatest. But it's clear there is also activity, in reverse, during the intake stroke. We can envision that, as cool intake charge enters the cylinder, heat is transfered from the cylinder to charge, heating it up and causing it to lose density. The more heat transfered, the lower the E_v will be. Clearly, if we wish to predict power, torque and E_v accurately, we must take heat transfer into account. It is dominant physics.

8.4.5. Piston Ring and Skirt Friction

Figure 8.8 shows the simulation's performance predictions with the ring and skirt friction models turned on. In Figures 8.8a and 8.8b the effect of ring friction ("Ring" plots) is surprisingly limited. At peak power, the engine loses only 2.1% of its power to ring friction. The power lost increases with RPM. At peak torque, the engine loses 2.0% of its torque to ring friction. But note the opposite trends. Torque lost to ring friction *decreases* with RPM. Skirt friction ("Skirt" plots) is more significant. At peak power the engine loses 3.9% of its power to skirt friction. And at peak torque the engine loses 3.1% of its torque to skirt friction. Power lost to skirt friction increases with RPM, while torque lost to skirt friction appears to decrease slightly with RPM. Combined ("Both" plots), we see 6% power lost to piston friction at peak power. But luckily, at low RPM piston friction losses are minimal. Thus if we can arrange for an engine to operate at reasonably low RPM, we can avoid expending fuel on, and creating emissions due to, piston friction. Approaching peak, friction losses become significant. Above peak they become severe. This is something that

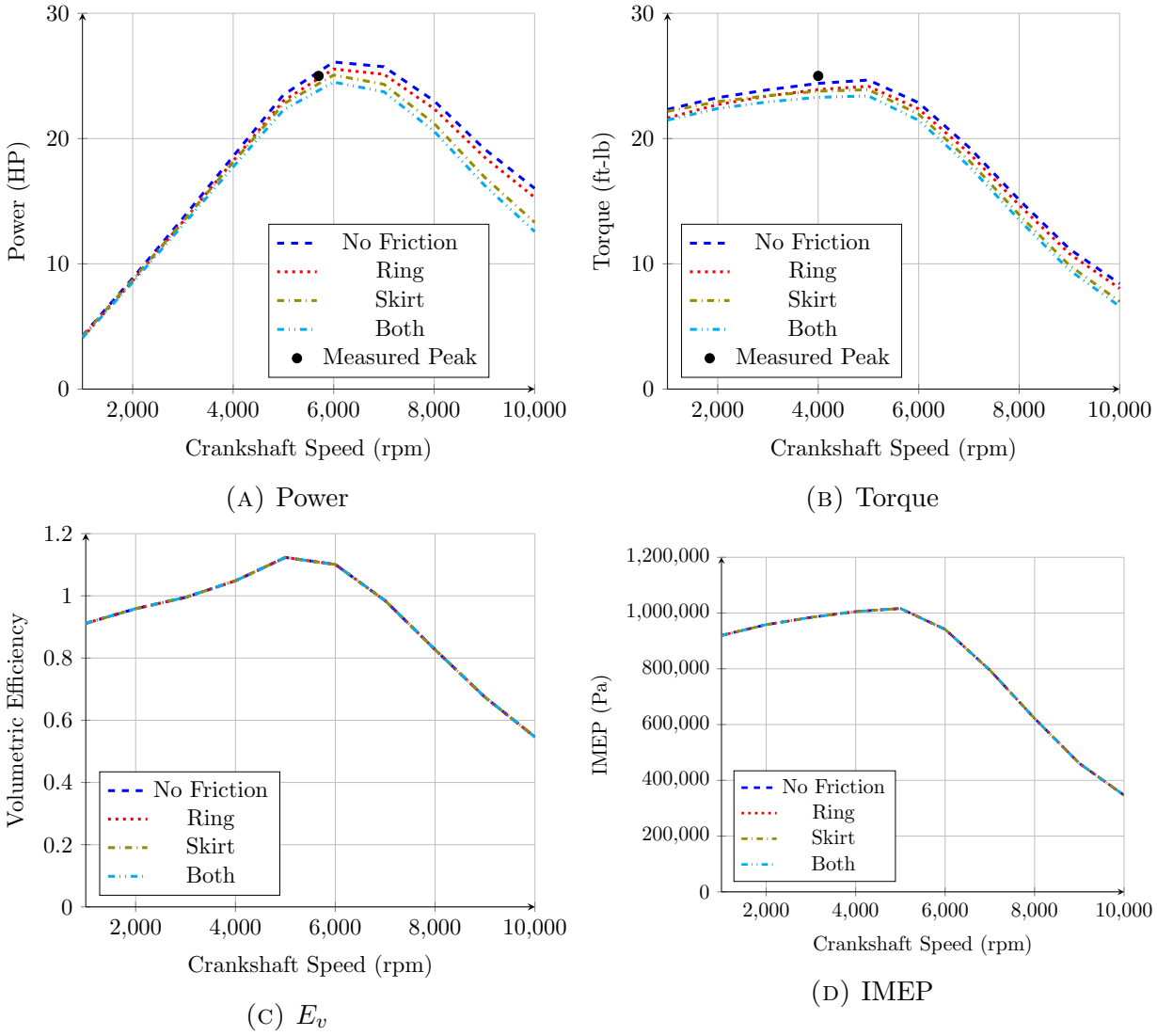

(A) Power

(B) Torque

(C) E_v

(D) IMEP

FIGURE 8.8. Performance Predictions with Piston Ring and Skirt Friction

should be considered in the design of a racing or marine engine. Note that piston friction has no effect at all on engine volumetric efficiency or IMEP. Piston friction is dominant physics. If an engine is being operated at low RPM, it can be neglected. If an engine is operating at high RPM or if torque prediction is important, it can't be neglected.

8.5. Conclusions

(1) Modeling the intake and exhaust flows of a four-stroke, internal combustion engine using the isentropic flow equations supplemented with discharge coefficients doesn't capture all of the dominant physics of the flows and is insufficient to produce accurate results.

(2) A four-stroke, internal combustion engine can be modeled using a single-volume, time-domain representation of the charge, coupled with time-accurate, compressible, Quasi-One-Dimensional models of the intake and exhaust flows.

   (a) The charge can be modeled as a homogeneous, isotropic, non-adiabatic mass of gas with equilibrium gas properties. Mass and energy conservation are the dominant physics of the charge. Momentum can be neglected.

   (b) The intake and exhaust flows can be modeled as Quasi-One-Dimensional flows, with mass, momentum and energy conservation comprising the dominant physics. A Runge-Kutta, four-stage integration technique can be used to time-march the flow solutions. Artificial viscosity can be used to stabilize the solution without adversely affecting the results. A minimum of 46 cells are required in a valve that closes to 1% opening. Solving the intake and exhaust flows separately, each with its own timestep, minimizes the growth of error. Non-reflective boundary handling adds a level of realism to the flows and helps to stabilize the solution, especially at high RPM.

   (c) A model constructed in this manner is sensitive to intake and exhaust geometry as well as intake and exhaust valve timing.

(3) Drag, resulting from boundary layer and separated flow, is dominant physics in the intake and exhaust flows. It can be modeled with both discharge and drag coefficients. Separated flow in the valves is an order of magnitude more significant than laminar flow through the pipes. Further research into sub-grid scale modeling of separated flow would be very useful and could result in highly accurate performance predictions using the Q1D approach.

(4) Modeling of combustion as an instantaneous process provides erroneous results. The rate of heat release is dominant physics. The Wiebe combustion model seems to provide realistic results. A study comparing the simulation's predictions to full dynamometer data could yield a "best" range of values for the Wiebe parameters of ignition start time and combustion duration.

(5) Working fluids must be chosen carefully. Frozen models can't account for energy storage in the extended modes and result in artificially high power and torque predictions. With the high temperatures of combustion, energy storage is dominant physics. Equilibrium gas models return acceptable results. Accounting for the composition and gas properties of the intake and exhaust mixtures makes for even more accurate predictions, but is less dominant physics.

(6) Charge blowby plays an insignificant role in power prediction. If accurate torque or IMEP predictions are required across the RPM range, then blowby is dominant physics. Otherwise, it can be neglected.

(7) Heat transfer from the charge to the cylinder and vice-versa is dominant physics. It significantly affects the prediction of power, torque, volumetric efficiency and IMEP.

(8) Piston ring and skirt friction are dominant physics. First-principle models based on the Reynolds equation and Newtonian fluid principles provide highly accurate results. The temperature rise of the fluid in the lubrication gap is also dominant physics and must be taken into account for accurate results.

(9) Intake and exhaust tract geometry (length and cross-sectional area), as well as intake and exhaust valve timing, affect engine performance strongly.

Bibliography

[1] G. Borgeson, *The Golden Age of the American Racing Car*. 1965.

[2] F. Markus, "Cadillac sixteen concept v-16 engine." Online. `http://www.caranddriver.com/features/cadillac-sixteen-concept-v-16-engine-feature`.

[3] D. Bortoluzzi, V. Cossalter, and A. Doria, "The effect of tunable resonators on the volumetric efficiency of an engine," *Motorsports Engineering Conference and Exposition*, 1998. SAE Technical Paper 983045.

[4] M. Chapman, J. M. Novak, and R. A. Stein, "A nonlinear acoustic model of inlet and exhaust flow in multi-cylinder internal combustion engines," *Flows in internal combustion engines*, vol. 83, pp. 1–8, 1983.

[5] R. J. Tabaczynski, "Effects of inlet and exhaust system design on engine performance," *SAE Journal*, vol. 82, pp. 71–81, 1982. SAE Technical Article 821577.

[6] S. de Morais Hanriot, R. M. Valle, J. R. Sodre, and J. M. Queiroz, "Helmholtz resonator effects on engine intake air mass flow rate," *Proceedings of the 22nd International Congress of Mechanical Engineering*, pp. 3925–3933, November 2013.

[7] P. C. Vorum, "Short pipe manifold design for four-stroke engines: Part ii," *Transactions of the ASME*, vol. 102, pp. 836–841, October 1980.

[8] D. Chalet, P. Chesse, X. Tauzia, and J.-F. Hetet, "Comparison of different methods for the determination of pressure wave in the inlet and exhaust systems of internal combustion engines," *SAE World Congress*, 2006. SAE Paper 2006-01-1542.

[9] R. J. Pearson and D. E. Winterbone, "A rapid wave action simulation technique for intake manifold design," *SAE Journal*, pp. 1–10, 1990. SAE Technical Article 900676.

[10] H. Mezher, D. Chalet, J. Migaud, and P. Chesse, "Frequency based approach for simulating pressure waves at the inlet of internal combustion engines using a parameterized model," *Applied Energy*, vol. 106, pp. 275–286, 2013.

[11] M. F. Harrison and P. T. Stanev, "A linear acoustic model for intake wave dynamics in ic engines," *Journal of Sound and Vibration*, vol. 269, pp. 361–387, 2004.

[12] D. Chalet, A. Mahe, J. Migaud, and J.-F. Hetet, "A frequency modelling of the pressure waves in the inlet manifold of internal combustion engine," *Applied Energy*, vol. 88, pp. 2988–2994, 2011.

[13] R. S. Benson, R. D. Garg, and W. A. Woods, "Unsteady flow in pipes with gradual or sudden area changes," *Proceedings of the Institution of Mechanical Engineers*, vol. 178, pp. 1–23, 1963.

[14] T. Bulaty and H. Niessner, "Calculation of 1-d unsteady flows in pipe systems of i. c. engines," *Journal of Fluids Engineering*, vol. 107, pp. 407–412, September 1985.

[15] M. Chapman, J. M. Novak, and R. A. Stein, "Numerical modeling of inlet and exhaust flows in multi-cylinder internal combustion engines," *Flows in internal combustion engines*, pp. 9–19, 1982.

[16] Y. Shinamoto, M. Oka, and Y. Tanaka, "A research on inertia charging effect of intake system in mult-cylinder engines," *Bulletin of the JSME*, vol. 21, pp. 502–510, March 1978. Paper No. 153-19.

[17] M. Takizawa, T. Uno, and T. Yura, "A study of gas exchange process simulation of an automotive multi-cylinder internal combustion engine," *International Congress & Exposition*, pp. 1–14, February 1982. SAE Paper 820410.

[18] G. Q. Zhang and D. N. Assanis, "Manifold gas dynamics modeling and its coupling with single-cylinder engine models using simulink," *Journal of Engineering for Gas Turbines and Power*, vol. 125, pp. 563–571, April 2003.

[19] G. P. Blair, *Design and Simulation of Four-Stroke Engines*. Society of Automotive Engineers, Inc., 1999.

[20] S. Stockar, M. Canova, Y. Guezennec, A. D. Torre, G. Montenegro, and A. Onorati, "Modeling wave action effects in internal combustion engine air path systems: comparison of numerical and system dynamics approaches," *International Journal of Engine Research*, vol. 14, pp. 391–408, 2013.

[21] D. Chalet, P. Chesse, J.-F. Hetet, and X. Tauzia, "Inflow boundary condition for one-dimensional gas dynamics simulation code of internal combustion engine manifolds," *Proceedings of the Institution of Mechanical Engineers, Part D: Journal of Automobile Engineering*, pp. 953–965, 2009.

[22] G.-H. Kim, A. Kirkpatrick, and C. Mitchell, "Supersonic virtual valve design for numerical simulation of a large-bore natural gas engine," *Journal of Engineering for Gas Turbines and Power*, vol. 129, pp. 1065–1071, October 2007.

[23] C. R. Ferguson and A. T. Kirkpatrick, *Internal Combustion Engines; Applied Thermosciences*. John Wiley and Sons, Ltd., 2016.

[24] J. D. Anderson, *Fundamentals of Aerodynamics*. McGraw-Hill Inc., 1984.

[25] M. M. Abbott and H. G. Van Ness, *Thermodynamics with Chemical Applications*. The McGraw-Hill Companies, Inc., 1989.

[26] E. Fermi, *Thermodynamics*. Dover Publications, Inc., 1956.

[27] G. J. Van Wylen and R. E. Sonntag, *Fundamentals of Classical Thermodynamics*. John Wiley and Sons, Inc., 1978.

[28] "Nist chemistry webbook." Online. `http://webbook.nist.gov/chemistry/`.

[29] J. D. Anderson, *Modern Compressible Flow with Historical Perspective*. McGraw-Hill Inc., 1982.

[30] A. Dobos, *Quasidimensional Modeling of Reacting Fuel Sprays Using Detailed Chemical Kinetics*. PhD thesis, Colorado State University, Department of Mechanical Engineering, 2016.

[31] J. I. Ghojel, "Review of the development and applications of the wiebe function: a tribute to the contribution of ivan wiebe to engine research," *International Journal of Engine Research*, vol. 11, pp. 297–312, May 2010.

[32] M. A. Cevis and I. Kaymaz, "Temperature and airfuel ratio dependent specific heat ratio functions for lean burned and unburned mixture," *Energy Conversion and Management*, vol. 46, pp. 2387–2404, February 2005.

[33] T. Tian, L. B. Noordzij, V. W. Wong, and J. B. Heywood, "Modeling piston-ring dynamics, blowby and ring-twist effects," *Journal of Engineering for Gas Turbines and Power*, vol. 120, pp. 843–854, October 1998.

[34] Goetze, "Goetze piston ring handbook," 2003. Online: `http://korihandbook.federalmogul.com/en/index.htm`.

[35] A. H. Rose, Jr and R. C. Stahman, "The role of engine blowby in air polution," *Journal of the Air Pollution Control Association*, pp. 114–144, May 1961.

[36] R. Keribar, Z. Dursunkaya, and M. F. Flemming, "An integrated model of ring pack performance," *Journal of Engineering for Gas Turbines and Power*, vol. 113, pp. 382–389, July 1991.

[37] R. C. Wagner, "Fluid dynamics and aerodynamics notebook." Unpublished, 2017.

[38] W. J. D. Annand, "Heat transfer in the cylinders of reciprocating internal combustion engines," *Proceedings of the Institution of Mechanicsl Engineers*, vol. 177, pp. 973–990, 1963.

[39] G. Woschni, "A universally applicable equation for the instantaneous heat transfer coefficient in the internal combustion engine," 1967. SAE Paper 670931.

[40] I. N. Bishop, "Effect of design variables on friction and economy," *SAE Automotive Engineering Congress*, pp. 334–358, January 1964.

[41] K. J. Patton, R. G. Nitschke, and J. B. Heywood, "Development and evaluation of a friction model for spark-ignition engines," *International Congress and Exposition*, pp. 1–22, 1989. SAE Technical Paper 890836.

[42] D. Sandoval and J. B. Heywood, "An improved friction model for spark-ignition engines," 2003. SAE Paper 2003-01-0725.

[43] A. Kirkpatrick, "Couette flow notes." Unpublished, 2017.

[44] K. L. Johnson, J. A. Greenwood, and S. Y. Poon, "A simple theory of asperity contact in elastohydrodynamic lubrication," *Wear*, vol. 19, pp. 91–108, July 1972.

[45] J. Jocsak, "The effects of surface finish on piston ring-pack performance in advanced reciprocating engine systems," Master's thesis, Massachusetts Institute of Technology Department of Mechanical Engineering, 2005.

[46] I. Sherrington and E. H. Smish, "Experimental methods for measuring oil-film thickness between the piston-rings and cylinder-wall of internal combustion engines," *Tribology International*, pp. 315–320, 1986.

[47] S. Furuhama, C. Asahi, and M. Hiruma, "Measurement of piston ring oil film thickness in an operating engine," *ASLE Transactions*, vol. 26, pp. 325–332, October 1982.

[48] M. Sjoderfjall, A. Almqvist, and R. Larsson, "Component test for simulation of piston ring-cylinder liner friction at realistic speeds," *Tribology International*, pp. 57–63, August 2016.

[49] Y. Wakuri, T. Hamatake, M. Soejima, and T. Kitahara, "Piston ring friction in internal combustion engines," *Tribology International*, pp. 299–308, 1992.

[50] B. J. Hamrock, *Fundamentals of Fluid Film Lubrication*. National Aeronautics and Space Administration, 1991. NASA Reference Publication 1255.

[51] L. S. Andres, *Derivation of the Classical Reynolds Equation for Thin Film Flows*. Luis San Andres, 2010. Online: `http://rotorlab.tamu.edu/me626/Notes_pdf/Notes02%20Classical%20Lub%20Theory.pdf`.

[52] C. C. Mei, *Lecture Notes on Fluid Dynamics*, ch. 2.2 Lubrication approximation for flow in a thin layer.

[53] R. I. Taylor, M. A. Brown, D. M. Thompson, and J. C. Bell, "The influence of lubricant rheology on friction in the piston ring-pack," *SAE Technical Paper Series*, vol. 103, pp. 65–74, 1994. SAE Technical Paper 941981.

[54] "Dichta-katalog-semeringov." Online. `https://www.mm-intercom.si/wp-content/uploads/2015/08/DICHTA-KATALOG-SEMERINGOV.pdf`.

[55] S. Yagi, A. Ishizuya, and I. Fujii, "Research and development of high-speed, high-performance, small displacement honda engines," 1970.

[56] J. D. Anderson, "A time-dependent analysis for vibrational and chemical nonequilibrium nozzle flows," *AIAA Journal*, vol. 8, pp. 545–550, March 1970.

[57] A. Jameson, W. Schmidt, and E. Turkel, "Numerical solution of the euler equations by finite volume methods using runge-kutta time-stepping schemes," in *AIAA 14th Fluid and Plasma Dynamic Conference*, American Institute of Aeronautics and Astronautics, June 1981. AIAA Paper 1981-1259.

[58] C. Hirsch, *Numerical Computation of Internal & External Flows*. Butterworth-Heinemann, 2007.

[59] J. D. Anderson, *Computational Fluid Dynamics, The Basics with Applications*. McGraw-Hill, Inc., 1995.

[60] H. Lomax, T. H. Pulliam, and D. W. Zingg, *Fundamentals of Computational Fluid Dynamics*. Springer-Verlag, 2003.

[61] R. C. Wagner, "Mech 651 class notes." 2015.

[62] R. C. Wagner, "Engine simulation notebook." Unbpublished, 2003.

[63] F. M. White, *Fluid Mechanics*. McGraw-Hill, 1979.

[64] R. C. Wagner, "Mech 661 class notes." Unpublished, 2017.

[65] S. Yin, "Volumetric efficiency modeling of a four stroke ic engine," Master's thesis, Colorado State University Department of Mechanical Engineering, 2017.

[66] G. Sammut and A. C. Alkidas, "Relative contributions of intake and exhaust tuning on si engine breathing–a computational study," *SAE World Congress and Exhibition*, 2007. SAE Paper 2007-01-0492.

[67] "Comp cams website." Online, 2017. http://www.compcams.com/Pages/413/cam-timing-lobe-separation-angle.aspx.

[68] E. Abu-Nada, L. Al-Hinti, A. Al-Sarkhi, and B. Akash, "Effect of piston friction on the performance of si engine: A new thermodynamic approach," *Journal of Engineering for Gas Turbines and Power*, vol. 130, pp. 1–8, March 2008. Paper 022802.

[69] O. Akalin and G. M. Newaz, "Piston ring-cylinder bore friction modeling in mixed lubrication regime part i: Analytical results," *Journal of Tribology*, vol. 123, pp. 211–218, January 2001.

[70] M. F. Harrison and P. T. Stanev, "Measuring wave dynamics in ic engine intake systems," *Journal of Sound and Vibration*, vol. 269, pp. 389–408, 2004.

[71] J. W. Kim and D. J. Lee, "Generalized characteristic boundary conditions for computational aeroacoustics," *AIAA Journal*, vol. 38, pp. 2040–2049, November 2000.

[72] G.-H. Kim, *Computational fluid dynamics modeling of a large bore two-stroke natural gas engine*. PhD thesis, Colorado State University, Department of Mechanical Engineering, 2004.

[73] E. Gutierrez-Miravete, *Chapter 7 Lubrication*. Ernesto Gutierrex-Miravete, 2012. Online: http://www.ewp.rpi.edu/hartford/~ernesto/F2012/FWM/Notes/ch07.pdf.

[74] A. Ohata and Y. Ishida, "Dynamic inlet pressure and volumetric efficiency of four cycle four cylinder engine," *SAE Journal*, pp. 1637–1647, 1982. Technical Paper 820407.

[75] T. J. Poinsot and S. K. Lele, "Boundary conditions for direct simulation of compressible viscous flows," *Journal of Computational Physics*, pp. 104–129, 1992.

[76] G. Ryk, Y. Kligerman, I. Etsion, and A. Shinkarenko, "Experimental investigation of partial laser surface texturing for piston-ring friction reduction," *Tribology Transactions*, vol. 48, pp. 583–588, 2005.

[77] D. Saravanan, A. Gokhale, and N. Karthikeyen, "Design and development of a novel charge boosting system for a single cylinder si engine," *SAE Journal*, April 2014. Paper 2014-01-1707.

[78] L. Selle, F. Nicoud, and T. Poinsot, "Actual impedance of nonreflecting boundary conditions: Implications for computational resonators," *AIAA Journal*, pp. 958–964, 2004.

[79] K. W. Thompson, "Time dependent boundary conditions for hyperbolic systems," *Journal of Computational Physics*, vol. 68, pp. 1–24, January 1987.

[80] R. C. Wagner, "Computational fluid dynamics notebook." Unpublished, 2001 - present.

APPENDIX A

Derivation and Application of Quasi-One-Dimensional, Non-Reflective Boundary Handling

We can derive a set of Q1D, non-reflective boundary conditions by applying a characteristic decomposition to the Q1D governing equations. To begin, we must have the equations in differential form. They are presented here without derivation:

$$\frac{\partial}{\partial t}(\rho A) + \frac{\partial}{\partial x}(\rho A u) = 0 \tag{A.1}$$

$$\frac{\partial}{\partial t}(\rho A u) + \frac{\partial}{\partial x}\left(\rho A u^2\right) = -A\frac{\partial P}{\partial x} \tag{A.2}$$

$$\frac{\partial}{\partial t}\left[\rho A\left(C_v T + \frac{u^2}{2}\right)\right] + \frac{\partial}{\partial x}\left[\rho A u\left(C_v T + \frac{u^2}{2}\right)\right] = -\frac{\partial}{\partial x}(P A u) \tag{A.3}$$

Equation A.1 is the continuity equation, equation A.2 is the momentum equation and equation A.3 is the energy equation. They are in conservation form and must be converted to non-conservation form. We do this by carrying through the derivatives of products. Where possible, we also apply the perfect gas equation of state, $P = \rho R T$, and the speed of sound, $c^2 = \gamma R T$, yielding:

$$\frac{\partial \rho}{\partial t} + u\frac{\partial \rho}{\partial x} + \rho\frac{\partial u}{\partial x} + 0\,\frac{\partial P}{\partial x} + \frac{\rho u}{A}\,\frac{\partial A}{\partial x} = 0 \tag{A.4}$$

$$\frac{\partial u}{\partial t} + 0\,\frac{\partial \rho}{\partial x} + u\,\frac{\partial u}{\partial x} + \frac{1}{\rho}\frac{\partial P}{\partial x} + 0\,\frac{\partial A}{\partial x} = 0 \tag{A.5}$$

$$\frac{\partial P}{\partial t} + 0\,\frac{\partial \rho}{\partial x} + \rho c^2\frac{\partial u}{\partial x} + u\frac{\partial P}{\partial x} + \frac{\rho c^2 u}{A}\,\frac{\partial A}{\partial x} = 0 \tag{A.6}$$

We can write a generic equation that represents the system of three equations:

$$\frac{\partial U}{\partial t} + a\,\frac{\partial U}{\partial x} + J = 0 \tag{A.7}$$

where U and J are the vectors,

$$U = \begin{bmatrix} \rho \\ u \\ P \end{bmatrix} \begin{matrix} U_1 \\ U_2 \\ U_3 \end{matrix} \qquad J = \begin{bmatrix} \frac{\rho u}{A}\frac{\partial A}{\partial x} \\ 0 \\ \frac{\rho c^2 u}{A}\frac{\partial A}{\partial x} \end{bmatrix} \begin{matrix} J_1 \\ J_2 \\ J_3 \end{matrix} \tag{A.8}$$

and the matrix a is a Jacobian matrix. Since it is applied to the flux (spatial) derivative, it is often called the "flux Jacobian":

$$a = \begin{bmatrix} u & \rho & 0 \\ 0 & u & \frac{1}{\rho} \\ 0 & \rho c^2 & u \end{bmatrix} \tag{A.9}$$

Note how the generic equation (A.7) is in the form of a wave equation. If we had no knowledge of the contents of matrix a, we might even think it is linear.

The a matrix can be decomposed into its eigenvalues and eigenvectors,

$$a = R\,\Lambda\,L \qquad \text{or} \qquad \Lambda = L\,a\,R \tag{A.10}$$

Where Λ is a matrix of a's eigenvalues, L is the left eigenvector matrix and R is the right eigenvector matrix. The left eigenvector matrix is the inverse of the right, so $RL = 1$. I have come to call the following procedure the "black magic, left eigenvector trick". I haven't been able to find the origin of the procedure, but it is commonly used to decompose a system of equations into its characteristic components. Returning to the generic equation, A.7, we find that, some time in the past, an ingenious person noticed that a could be multiplied on the right by $RL = 1$ [79, 61]:

$$\frac{\partial U}{\partial t} + a\,R\,L\,\frac{\partial U}{\partial x} + J = 0 \tag{A.11}$$

Then, pre-multiplying the whole equation by the left eigenvector matrix,

$$L\,\frac{\partial U}{\partial t} + L\,a\,R\,L\,\frac{\partial U}{\partial x} + L\,J = 0 \tag{A.12}$$

or,

(A.13)
$$\boxed{L\,\frac{\partial U}{\partial t} + \Lambda L\,\frac{\partial U}{\partial x} + L\,J = 0}$$

a's eigenvalues are

$$\lambda_1 = u - c, \qquad \lambda_2 = u + c, \qquad \lambda_3 = u$$

And a's eigenvalue matrix is:

(A.14)
$$\Lambda = \begin{bmatrix} u-c & 0 & 0 \\ 0 & u+c & 0 \\ 0 & 0 & u \end{bmatrix}$$

Note that the eigenvalues of the Jacobian are the characteristics of the flow. And thus, the eigenvalue matrix substitution has converted our original generic equation in to a true wave equation, based on the characteristics of the flow. Equation A.13 is a "characteristic" representation of the generic equation, A.7.

a's left and right eigenvector matrices are:

(A.15)
$$L = \begin{bmatrix} 0 & -\frac{\rho}{2c} & \frac{1}{2c^2} \\ 0 & \frac{\rho}{2c} & \frac{1}{2c^2} \\ 1 & 0 & -\frac{1}{c^2} \end{bmatrix} \qquad R = \begin{bmatrix} 1 & 1 & 1 \\ -\frac{c}{\rho} & \frac{c}{\rho} & 0 \\ c^2 & c^2 & 0 \end{bmatrix}$$

Note that, like the generic equation, equation A.13 is a vector equation. Let's compute each term.

$$L\,\frac{\partial U}{\partial t} = \begin{bmatrix} -\frac{\rho}{2c}\,\frac{\partial u}{\partial t} + \frac{1}{2c^2}\,\frac{\partial P}{\partial t} \\ \frac{\rho}{2c}\,\frac{\partial u}{\partial t} + \frac{1}{2c^2}\,\frac{\partial P}{\partial t} \\ \frac{\partial \rho}{\partial t} - \frac{1}{c^2}\,\frac{\partial P}{\partial t} \end{bmatrix} \tag{A.16}$$

$$L\,\frac{\partial U}{\partial x} = \begin{bmatrix} -\frac{\rho}{2c}\,\frac{\partial u}{\partial x} + \frac{1}{2c^2}\,\frac{\partial P}{\partial x} \\ \frac{\rho}{2c}\,\frac{\partial u}{\partial x} + \frac{1}{2c^2}\,\frac{\partial P}{\partial x} \\ \frac{\partial \rho}{\partial x} - \frac{1}{c^2}\,\frac{\partial P}{\partial x} \end{bmatrix} \tag{A.17}$$

$$L\,J = \begin{bmatrix} \frac{\rho u}{2A}\,\frac{\partial A}{\partial x} \\ \frac{\rho u}{2A}\,\frac{\partial A}{\partial x} \\ 0 \end{bmatrix} \tag{A.18}$$

Inserting these vectors into equation A.13, we obtain three equations:

$$-\frac{\rho}{2c}\,\frac{\partial u}{\partial t} + \frac{1}{2c^2}\,\frac{\partial P}{\partial t} + (u-c)\left(-\frac{\rho}{2c}\,\frac{\partial u}{\partial x} + \frac{1}{2c^2}\,\frac{\partial P}{\partial x}\right) + \frac{\rho u}{2A}\,\frac{\partial A}{\partial x} = 0 \tag{A.19}$$

$$\frac{\rho}{2c}\,\frac{\partial u}{\partial t} + \frac{1}{2c^2}\,\frac{\partial P}{\partial t} + (u+c)\left(\frac{\rho}{2c}\,\frac{\partial u}{\partial x} + \frac{1}{2c^2}\,\frac{\partial P}{\partial x}\right) + \frac{\rho u}{2A}\,\frac{\partial A}{\partial x} = 0 \tag{A.20}$$

$$\frac{\partial \rho}{\partial t} - \frac{1}{c^2}\,\frac{\partial P}{\partial t} + u\left(\frac{\partial \rho}{\partial x} - \frac{1}{c^2}\,\frac{\partial P}{\partial x}\right) = 0 \tag{A.21}$$

Note how each spatial term is multiplied by a flow characteristic. Each of these equations functions as a component, accounting for the propagation of influences through the flow, one in the positive-x direction at the speed of sound through the fluid, $u + c$, one in the negative-x direction at the speed of sound through the fluid, $u - c$ and one with the motion of the fluid, u. We can clean these equations up a bit by multiplying by c^2 and $2c^2$:

$$-\rho c \frac{\partial u}{\partial t} + \frac{\partial P}{\partial t} + (u - c)\left(-\rho c \frac{\partial u}{\partial x} + \frac{\partial P}{\partial x}\right) + \frac{\rho u c^2}{2A}\frac{\partial A}{\partial x} = 0 \tag{A.22}$$

$$\rho c \frac{\partial u}{\partial t} + \frac{\partial P}{\partial t} + (u + c)\left(\rho c \frac{\partial u}{\partial x} + \frac{\partial P}{\partial x}\right) + \frac{\rho u c^2}{2A}\frac{\partial A}{\partial x} = 0 \tag{A.23}$$

$$c^2 \frac{\partial \rho}{\partial t} - \frac{\partial P}{\partial t} + u\left(c^2 \frac{\partial \rho}{\partial x} - \frac{\partial P}{\partial x}\right) = 0 \tag{A.24}$$

To simplify the following algebra, we'll name each of the spatial terms:

$$\boxed{\begin{aligned} \mathcal{L}_1 &= (u - c)\left(-\rho c \frac{\partial u}{\partial x} + \frac{\partial P}{\partial x}\right) \\ \mathcal{L}_2 &= (u + c)\left(\rho c \frac{\partial u}{\partial x} + \frac{\partial P}{\partial x}\right) \\ \mathcal{L}_3 &= u\left(c^2 \frac{\partial \rho}{\partial x} - \frac{\partial P}{\partial x}\right) \end{aligned}} \tag{A.25}$$

Then the characteristic governing equations are:

$$-\rho c \frac{\partial u}{\partial t} + \frac{\partial P}{\partial t} + \mathcal{L}_1 + \frac{\rho u c^2}{2A} \frac{\partial A}{\partial x} = 0 \tag{A.26}$$

$$\rho c \frac{\partial u}{\partial t} + \frac{\partial P}{\partial t} + \mathcal{L}_2 + \frac{\rho u c^2}{2A} \frac{\partial A}{\partial x} = 0 \tag{A.27}$$

$$c^2 \frac{\partial \rho}{\partial t} - \frac{\partial P}{\partial t} + \mathcal{L}_3 = 0 \tag{A.28}$$

When we consider the application of these equations at a boundary, we can see where one or two of the characteristics will be entering the domain from the outside. In that case, the influence entering the domain will be truly one-dimensional [75]. And so, following the Locally One-Dimensional, Inviscid [75] pattern, we'll make an assumption that at the boundary, the flow is one-dimensional. Then $\frac{\partial A}{\partial x} = 0$ and we can eliminate the source (J) terms:

$$-\rho c \frac{\partial u}{\partial t} + \frac{\partial P}{\partial t} + \mathcal{L}_1 = 0 \tag{A.29}$$

$$\rho c \frac{\partial u}{\partial t} + \frac{\partial P}{\partial t} + \mathcal{L}_2 = 0 \tag{A.30}$$

$$c^2 \frac{\partial \rho}{\partial t} - \frac{\partial P}{\partial t} + \mathcal{L}_3 = 0 \tag{A.31}$$

If we add equations A.29 and A.30, we have:

$$\boxed{\frac{\partial P}{\partial t} + \frac{1}{2}(\mathcal{L}_1 + \mathcal{L}_2) = 0} \tag{A.32}$$

Then, substituting equation A.32 into equation A.31, we have:

(A.33)
$$\boxed{\frac{\partial \rho}{\partial t} + \frac{1}{c^2}\left[\frac{1}{2}\left(\mathcal{L}_1 + \mathcal{L}_2\right) + \mathcal{L}_3 = 0\right]}$$

Last, subtracting equation A.30 from A.29 we have:

(A.34)
$$\boxed{\frac{\partial u}{\partial t} + \frac{1}{2\rho c}\left(\mathcal{L}_2 - \mathcal{L}_1\right) = 0}$$

These equations give us the time-rates of change of the original state variables, ρ, u and P based on the gradients of the state variables and the characteristic velocities. We can integrate these values to calculate the state values. Problem: the Q1D CFD model we've constructed has conservation-form flux variables—and with different primitive variables at that! But we can calculate the flux variables from these primitives. For continuity, referring back to Chapter 7,

$$\frac{\partial U_1}{\partial t} = \frac{\partial}{\partial t}\left(\rho A\right) = A\frac{\partial \rho}{\partial t}$$

(A.35)
$$\boxed{\frac{\partial U_1}{\partial t} = A\frac{\partial \rho}{\partial t}}$$

$$\frac{\partial U_2}{\partial t} = \frac{\partial}{\partial t}\left(\rho u A\right) = A\left(u\,\frac{\partial \rho}{\partial t} + \rho\,\frac{\partial u}{\partial t}\right)$$

(A.36)
$$\boxed{\frac{\partial U_2}{\partial t} = A\left(u\frac{\partial \rho}{\partial t} + \rho\frac{\partial u}{\partial t}\right)}$$

$$\frac{\partial U_3}{\partial t} = \frac{\partial}{\partial t}\left(\rho e' A\right) = A\left(e'\frac{\partial \rho}{\partial t} + \rho\frac{\partial e'}{\partial t}\right)$$

where $e' = C_v T + \frac{u^2}{2}$ and

$$\frac{\partial e'}{\partial t} = \frac{C_v}{R}\left(\frac{1}{\rho}\frac{\partial P}{\partial t} - \frac{P}{\rho^2}\frac{\partial \rho}{\partial t}\right) + u\frac{\partial u}{\partial t}$$

Then,

(A.37)
$$\boxed{\frac{\partial U_3}{\partial t} = A\left[\left(C_v T + \frac{u^2}{2}\right)\frac{\partial \rho}{\partial t} + \frac{C_v}{R}\left(\frac{\partial P}{\partial t} - \frac{P}{\rho}\frac{\partial \rho}{\partial t}\right) + \rho u\frac{\partial u}{\partial t}\right]}$$

Using equations A.32, A.33, A.34, A.35, A.36 and A.37 we can calculate the time-rates of change of the Q1D flux variables at the boundaries. We can calculate them at the same time that we calculate the rates of the flux variables for the field cells, and then march them forward in time by integrating them along with the field values.

The real beauty of the characteristic approach is that the characteristics of the equations tell us where to find the data that feeds the equations. We will always be calculating the values of $\frac{\partial P}{\partial t}$, $\frac{\partial \rho}{\partial t}$, $\frac{\partial u}{\partial t}$, $\frac{\partial U_1}{\partial t}$, $\frac{\partial U_2}{\partial t}$ and $\frac{\partial U_3}{\partial t}$, but the way we calculate $\mathcal{L}_1$, $\mathcal{L}_2$ and $\mathcal{L}_3$ will vary depending on the direction and speed of the flow at each boundary. Figure A.1 shows cell 0 and the characteristics of the flow entering the cell. The characteristics are drawn from

their terminus, the center of cell 0, to their origin, the point from which they carry physical influences.

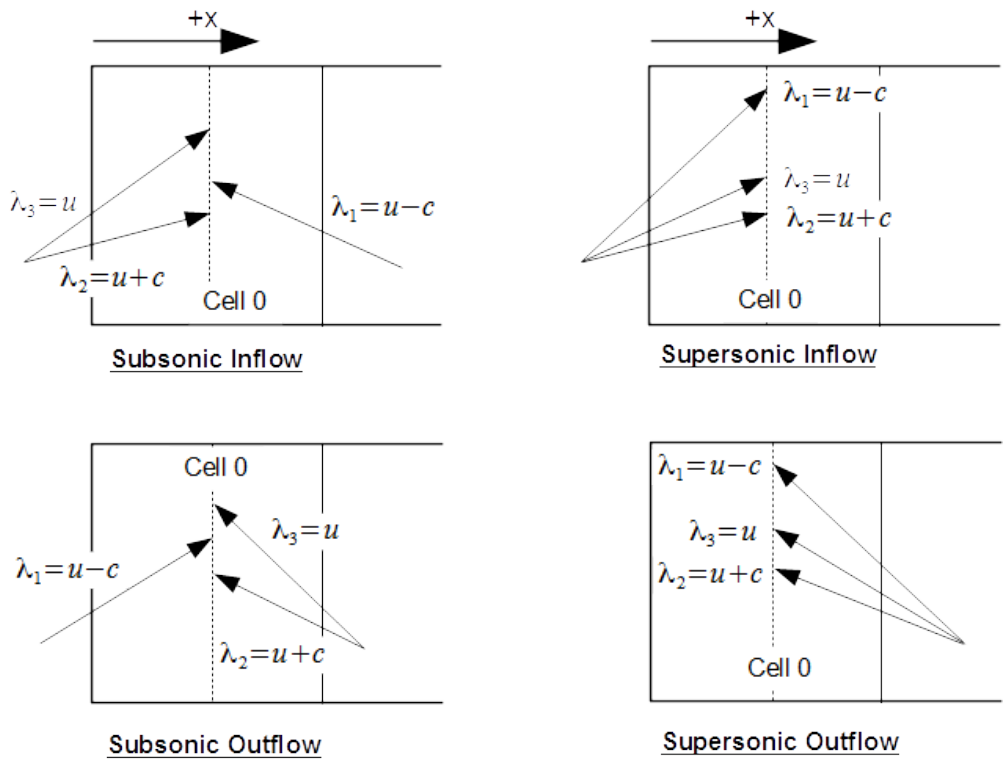

FIGURE A.1. Cell 0 Characteristics

For a subsonic inflow, λ_1 $(u - c)$, propagates from cell 1, λ_2 $(u + c)$ enters from beyond the boundary, and λ_3 (u) also enters from beyond the boundary. The origin of each characteristic determines how $\mathcal{L}_1$, $\mathcal{L}_2$ and $\mathcal{L}_3$ will be calculated. We will calculate $\mathcal{L}_1$ from the field, calculating the values of $\frac{\partial u}{\partial x}$ and $\frac{\partial P}{\partial x}$ using second-order, one-sided, finite-difference quotients between cells 0, 1 and 2. But what shall we do about $\mathcal{L}_2$ and $\mathcal{L}_3$? The domain ends and we have no way to calculate the derivatives beyond it. Poinsot and Lele [75] suggest a Linear Relation Method (LRM), where we will calculate:

(A.38)
$$\boxed{\begin{aligned} \mathcal{L}_2 &= K\left(P_0 - P_\infty\right) \\ K &= \sigma\left(1 - M_0^2\right)\frac{c_0}{L} \end{aligned}}$$

where P_0 is the pressure in cell 0, P_∞ is the pressure outside the boundary, M is the Mach number in cell 0, c_0 is the speed of sound in cell 0, L is the length of the tract from 0th boundary to Nth boundary and σ is a multiplier.

The $\mathcal{L}$ functions have units $\left\langle \frac{kg}{m-sec^3} \right\rangle$ and Poinsot and Lele have created their LRM value to have the same units. We need to create a value to replace $\mathcal{L}_3$ for an outside influence. Following Poinsot and Lele's lead, we'll create a similar value based on density that has the same units:

(A.39)
$$\boxed{\begin{aligned} \mathcal{L}_3 &= Kc_0^2\left(\rho_0 - \rho_\infty\right) \\ K &= \sigma\left(1 - M_0^2\right)\frac{c_0}{L} \end{aligned}}$$

These two functions will provide the non-reflective condition, allowing both the pressure and density in cell 0 to fluctuate, but always seek the far-field values. Note that σ, by way of the K function, sets the "stiffness" with which the boundary values are held. An infinite value of σ gives us back hard boundary handling. A value of zero allows the pressure and density to float freely.

Now return to Figure A.1 and consider the case of a supersonic inflow. This scenario is physically impossible. Given a pipe with a minimum area somewhere along its length, that point becomes the sonic point and the inflow must therefore be subsonic. The characteristic

boundary conditions allow us to handle this situation with great elegance. If we simply don't allow λ_1 to come in from outside of the boundary, the cell *can't* go supersonic. It can only reach Mach 1. So we will always calculate $\mathcal{L}_1$ from the field.

Now consider the two outflow cases. For subsonic outflow, we can calculate $\mathcal{L}_2$ and $\mathcal{L}_3$ from the field. But we must calculate $\mathcal{L}_1$ using the LRM method:

$$\boxed{\begin{aligned} \mathcal{L}_1 &= K\left(P_0 - P_\infty\right) \\ K &= \sigma\left(1 - M_0^2\right)\frac{c_0}{L} \end{aligned}} \tag{A.40}$$

For a supersonic outflow, we simply switch and calculate $\mathcal{L}_1$ from the field. This indicates that we must have some logic in the boundary handling. We must monitor λ_1 $(u - c)$ on the outflow and when it goes less than or equal to zero, switch from LRM to field calculation.

Now consider the Nth boundary, shown in Figure A.2. For an inflow, we will calculate $\mathcal{L}_2$ from the field using second-order, one-sided, finite-difference quotients between cells N, $N-1$ and $N-2$ for the $\frac{\partial P}{\partial t}$ and $\frac{\partial u}{\partial t}$ derivatives. We'll calculate $\mathcal{L}_1$ and $\mathcal{L}_3$ using LRM:

$$\boxed{\begin{aligned} \mathcal{L}_1 &= K\left(P_N - P_\infty\right) \\ K &= \sigma\left(1 - M_N^2\right)\frac{c_N}{L} \end{aligned}} \tag{A.41}$$

$$\boxed{\begin{aligned} \mathcal{L}_3 &= K c_N^2\left(\rho_N - \rho_\infty\right) \\ K &= \sigma\left(1 - M_N^2\right)\frac{c_N}{L} \end{aligned}} \tag{A.42}$$

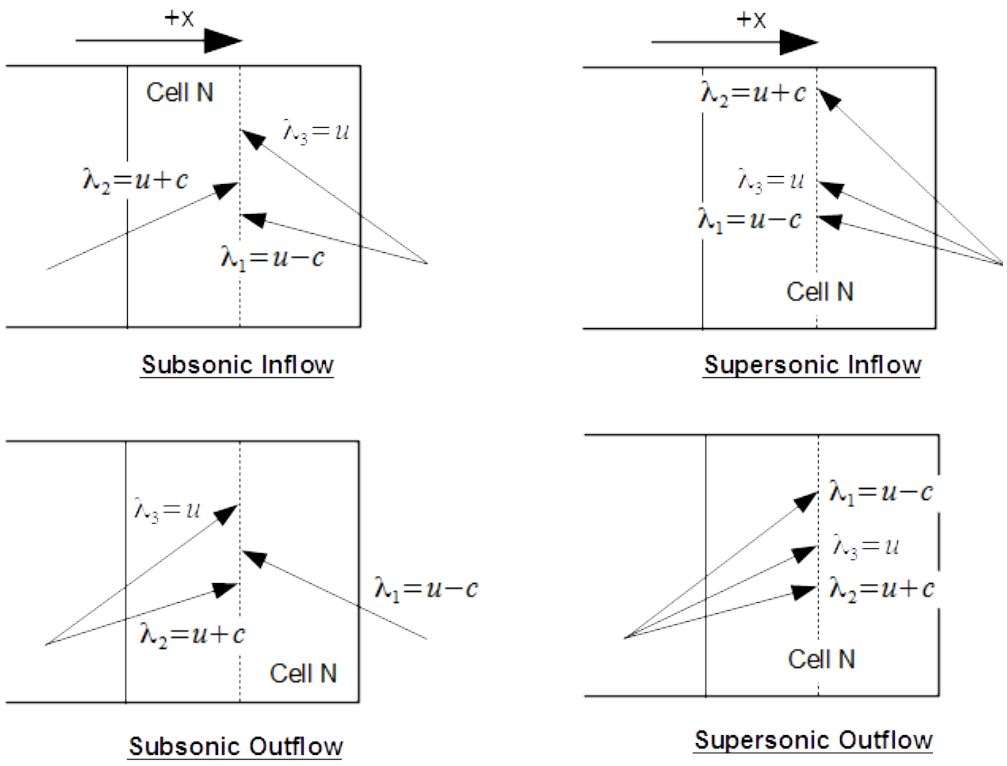

FIGURE A.2. Cell N Characteristics

Again, we will always calculate $\mathcal{L}_2$ from the field to limit the inflow velocity to Mach 1. For a subsonic outflow, we will calculate $\mathcal{L}_2$ and $\mathcal{L}_3$ from the field and $\mathcal{L}_1$ using LRM. We will monitor λ_1 $(u - c)$ and when it becomes equal to or greater than zero, indicating a supersonic outflow, we will switch to calculating $\mathcal{L}_1$ from the field.

While we mentioned it a short time back, we left out an extremely important detail. To what value shall we set σ? In his seminal paper, Thompson [79] essentially set σ to zero, eliminating any influences from beyond the boundary. His paper considered simulations of steady, external flows and applied the non-reflective handling to the single outflow boundary of the domain, located a very large distance from the body, where one need not worry about reversed flow. In marching to the steady state, time-accuracy is also not a consideration, so in Thompson's case, loss of the possible incoming influences at the outflow boundary isn't

a major detriment. It appears there may be no exact value for σ in the simulation of an external flow. But Selle et.al. [78] found an analytical path allowing them to establish an exact value of σ for pipes. A value of $\sigma = \pi$ ensures that a quarter-wave pipe will couple to the atmosphere correctly and produce acoustically accurate responses. It also allows frequencies above the pipe's fundamental to escape into the atmosphere, as happens with real pipes, and allows shock waves to pass through the boundary, into the atmosphere. Following their analysis, we see that, for a half-wave pipe, a value of $\sigma = 2\pi$ is correct.

(A.43)

$\sigma = \pi$	One end open.
$\sigma = 2\pi$	Both ends open.

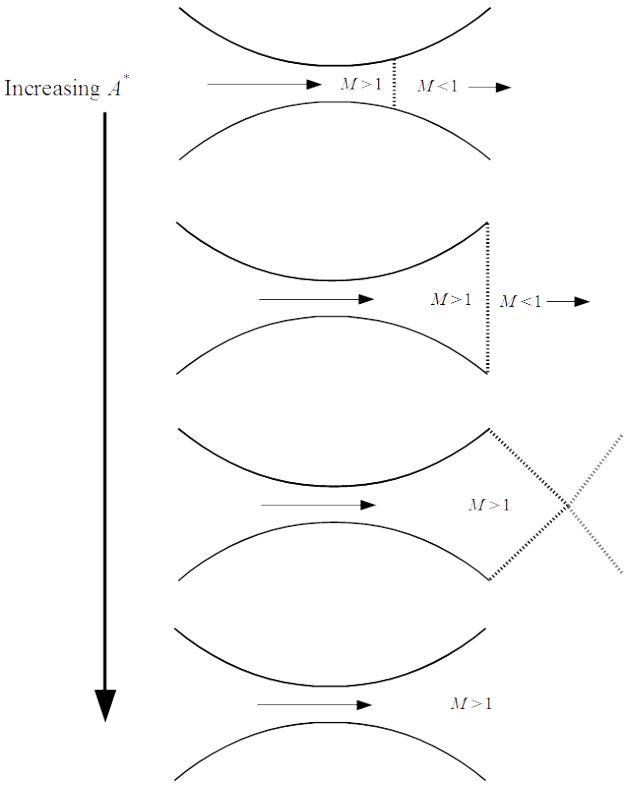

FIGURE A.3. Nozzle Shock Wave Progression

We seem to have a complete boundary handling strategy devised at this point. But let's consider an operational scenario for a moment. Let's say that the Q1D nozzle, the valve of the engine model, is opening with constant inlet and exit pressures. The nozzle is exhausting into air at "ambient" pressure, P_a. As the valve opens and the throat area, which we'll refer to as A^*, increases, the flow will accelerate to sonic speed at the throat, continue accelerating to supersonic speed and then, in the expanding section of the nozzle, decelerate through a normal shock wave. This is the top case in Figure A.3. Downstream of the shock wave the velocity will be subsonic and decelerating to the exit, where the pressure of the flow will be equal to P_a. As the valve opens wider and A^* grows, the shock wave will move downstream. At some A^* the shock wave will be at the nozzle exit, the second case in the figure. In this case, the flow is supersonic from the throat to just before the exit. The normal shock takes the flow from a low pressure directly to P_a. As the throat opens still further, the shock wave will expand out and transition to a cone with a trail of diamond shaped shock waves behind it that bring the flow up to ambient pressure externally. This is the third case in the figure. Note the significance of the transition from the second to third case. In cases one and two, the flow at the exit is subsonic. In our simulation, for this case at the Nth boundary, we calculate λ_2 and λ_3 from the field. $\lambda_1 = u - c < 0$ and so we calculate $\mathcal{L}_1$ using the LRM method. In case three, the flow at the exit is supersonic, $\lambda_1 = u - c > 0$ and so we must switch our handling and calculate $\mathcal{L}_1$ from the field. Now what happens if the nozzle begins to close back down? The flow at the exit is already supersonic. No influences can enter the domain from the exit to change the flow state. If we continue calculating $\mathcal{L}_1$ from the field, we'll reach a point where A^* is back in the range for cases one and two, but our handling, instead of allowing the shock wave to form, will instead give us the isentropic solution for

those A^* values, which we don't want. When the flow at the exit is supersonic, we must include some sensing mechanism that can tell us when to switch from calculating $\mathcal{L}_1$ from the field to calculating it using LRM.

We know the nozzle is operating overexpanded when the Mach number at the exit, $M_N >= 1$ and the pressure is below atmospheric, $P_N < P_a$. We'll test for this condition on each Q1D computational step. If it's true, then we'll *assume* that there is a shock standing in the exit. We'll calculate the pressure rise across the shock using the normal shock relation:

$$\boxed{\frac{P_e}{P_N} = 1 + \frac{2\gamma}{\gamma + 1}\left(M_N^2 - 1\right)} \tag{A.44}$$

where P_N is the pressure in cell N, P_e is the pressure on the downstream side of the shock, and M_N is the Mach number in cell N. If $P_e > P_a$ there can be no shock in the exit nor upstream. There must be a shock train. So we know the exit velocity is still supersonic and we continue calculating $\mathcal{L}_1$ from the field. If $P_e <= P_a$ we know that the shock is either in the exit or upstream, in the diverging section of the nozzle. In that case, we switch and calculate $\mathcal{L}_1$ using the LRM method, forcing the flow at the exit to become subsonic. This logic will allow the shock train to collapse into a normal shock at the exit, then enter the nozzle and begin moving upsteam as necessary.

But note, the computation of K becomes problematic. As we switch from calculating $\mathcal{L}_1$ from the field to LRM, the Mach number in the end cell will exceed 1, and this will cause K to go negative. We can clip the Mach number to 1, but then K simply goes to zero and the influences that we want to introduce from beyond the boundary get smothered—nothing

happens. Instead, we'll limit the square of the Mach number to 0.95 in the equation. This provides the results we're looking for:

$$\boxed{K = \sigma \left[1 - min\left(M_N^2, 0.95\right)\right] \frac{c_N}{L}} \tag{A.45}$$